Pathfinder for a Neutral Hydrogen Dark Energy Survey

by

Kevin Bandura

Submitted in partial fulfillment of the
requirements for the degree of
Doctor of Philosophy
at
Carnegie Mellon University
Department of Physics
Pittsburgh, Pennsylvania

Advised by Professor Jeff Peterson

June 19, 2011

Abstract

This thesis presents experimental progress towards constraining cosmology with 21cm radio observations. In particular, dark energy can be constrained by mapping out the cosmic web on large scales (> 10 Mpc) to see the evolution of the baryon acoustic oscillation (BAO) scale. 21cm Hydrogen has been detected at redshift 0.8 in cross-correlation using the Green Bank Telescope. The Pittsburgh Cylinder Prototype Telescope was built to investigate the use of a modern cylindrical paraboloid interferometer as a survey instrument and its first results are presented.

Acknowledgments

I would like to thank my advisor Professor Jeffrey Peterson for his incredible guidance and wealth of information and ideas. I thank my thesis committee for critiquing this thesis, improving my work.

A thank you to all the people who have made the Pittsburgh Cylinder Prototype possible. Thank you to Bruce Taylor for all the irreplacible help you've given me. Thank you to all the undergraduates who helped dig, drill, solder and weld: Jim McGee, Stephen Schweizer, Derrick McKee, Deena Kim, Florence Lui, Amy Stetten and Ben Maruca.

Thank you Laura for your support and love in this long graduate process. And thank you Eliza for brightening every day. Special thanks to all my family who are always there for me.

And many thanks to all my editors, Bruce, Laura, and Dorothy, although all errors remain mine.

Contents

List of Tables

List of Figures

1

Introduction

Understanding dark energy is one of the great drivers of cosmology today. General relativity brought about a testable model of the Universe. The discovery that the universe was expanding established a model. The cosmic microwave background (CMB) measurement of a pristine blackbody at a redshift of 1100 confirmed the universe started with a hot big bang. These measurements established a standard model of big bang cosmology with the following components. The universe has a flat space metric. It is comprised of 4% baryonic matter. 23% is dark matter, which appears to interact with baryonic matter only via the force of gravity. The remaining 73% of the universe is comprised of an even more mysterious dark energy. This repulsive-gravity agent could most simply be a cosmological constant, though there is no known theoretical cause for such a force at such a weak level.

1.1 Dark Energy

In order to measure something about the evolution of dark energy, we must start with a model. The usual parameter used to define dark energy is the equation of state:

$$w = \frac{P_\Lambda}{\rho_\Lambda} \tag{1.1}$$

where P is the pressure and ρ is the energy density using units with $c = 1$. In the cosmological constant model, $w = -1$ for all z, but other models can have an evolution of w with z.

In a flat universe, the Hubble parameter, $H(z)$ and the angular diameter distance, $D_A(z)$ are given by:

$$H(z) = H_o\sqrt{\Omega_m\,(1+z)^3 + \Omega_\Lambda e^{\left[3\int_0^z \frac{1+w(z)}{1+z}dz\right]}} \tag{1.2}$$

$$D_A(z) = \frac{c}{1+z}\int_0^z \frac{dz}{H(z)} \tag{1.3}$$

A comoving object with observable Δz along the line of sight ($r_{||}$) and features of size $\Delta\theta$ perpendicular to the line of sight, ($r_\perp$) are related by:

$$r_{||} = c\int_z^{z+\Delta z} \frac{dz}{H(z)} \approx \frac{c\Delta z}{H(z)} \tag{1.4}$$

$$r_\perp = (1+z)D_A(z)\Delta\theta = c\Delta\theta \int_0^z \frac{dz}{H(z)} \tag{1.5}$$

Measuring a comoving feature's angular and radial evolution, $\Delta z(z)$ and $\Delta\theta(z)$ will then constrain $H(z)$, Ω_Λ, and w.

1.1.1 Cosmological Model

See Frieman et al. [27] for an excellent review of the current cosmological model and the near term prospects for observational progress. An excellent textbook on the subject is Modern Cosmology by Dodelson [21]. Following the analysis in these two reference the key equations needed for this thesis are as follows:

On scales larger than 100 Mpc, the Universe is extremely isotropic and homogeneous. Assuming isotropy leads to the Friedman-Robertson-Walker metric:

$$ds^2 = dt^2 - a^2(t)\left(\frac{dr^2}{1-kr^2} + r^2 d\theta^2 + r^2 sin^2\theta d\phi^2\right) \tag{1.6}$$

with r, θ, ϕ as the comoving spatial coordinates, t is time, a is the scale factor, normalized to 1 today. k is the curvature, with $k > 0$ corresponding to a closed universe, $k < 0$ a open universe, and $k = 0$ a flat universe.

Applying the FRW metric to Einstein's field equations gives the Friedman Equation:

$$H^2 = \left(\frac{\dot{a}}{a}\right) = \frac{8\pi G\rho}{3} - \frac{k}{a^2} + \frac{\Lambda}{3} \tag{1.7}$$

where ρ is the total energy density including baryons, radiation, and dark matter. and:

$$\frac{\ddot{a}}{a} = -\frac{4\pi G}{3}(\rho + 3p) + \frac{\Lambda}{3} \tag{1.8}$$

where p is the total pressure. The equation representing adiabatic expansion, the fluid equation, can be derived from the other two:

$$\dot{\rho} + 3\frac{\dot{a}}{a}(\rho + p) = 0 \tag{1.9}$$

The first law of thermodynamics, $dE = -pdV$ is given by:

$$d(a^3\rho_i) = -p_i da^3 \tag{1.10}$$

and

$$w_i = \frac{P_i}{\rho_i} \tag{1.11}$$

is the equation of state, where $w_m = 0$ for matter, $w_R = \frac{1}{3}$ for radiation. If w is constant, then energy density is:

$$\rho_i \propto (1+z)^{3(1+w_i)} \tag{1.12}$$

and in general:

$$\rho_i \propto e^{3\int_0^z (1+w_i(z'))d\ln(1+z')} \tag{1.13}$$

1.2 Baryon Acoustic Oscillations

1.2.1 CMB

The big bang starts with an initial hot dense state and the universe rapidly expanding and cooling. Once the universe cools to the point Hydrogen atoms form, which happens at a temperature of about 0.25 eV [21], photons no longer Compton scatter off electrons, and light becomes decoupled from the matter. This leaves the light able to free stream to us today. This time is called recombination, and the remnant photons, greatly redshifted, are called the cosmic microwave background.

Before recombination, density structure left from inflation [31] creates pressure-density waves which will propagate at the speed of sound, $c_s^2 = dp/d\rho$. The speed of sound is given in the early universe by

$$c_s = \frac{1}{\sqrt{3}}\left(1 + \frac{3}{4}\frac{\rho_b}{\rho_\gamma}\right)^{-\frac{1}{2}} \tag{1.14}$$

where ρ_b is the baryon density and ρ_γ is the radiation density [42]. The comoving distance this wave will travel before recombination is:

$$s = \int_0^{t_{CMB}} \frac{c_s}{a(t)} dt = \int_{z_{CMB}}^{\infty} \frac{c_s}{H(z)} dz \tag{1.15}$$

This scale has been measured well via the CMB anisotropies power spectrum, and is given by $s = 147 \pm 2$Mpc. In Komatsu et al. [39] what is measured is the location of the peak multipole moment in the angular power spectrum, $l_A = 302.09 \pm 0.76$ and $z_* = 1091.3 \pm 0.91$ with z_* the redshift of recombination and

$$l_A = (1 + z_*) \frac{\pi D_A(z_*)}{s(z_*)} \tag{1.16}$$

which using standard ΛCDM cosmology gives a measurement of the sound horizon scale $s = 147$ Mpc.

This scale is strongly shown as the period of the oscillation in the CMB power spectrum, which is shown in figure 1.1

1.2.2 Standard Ruler

The sound horizon scale that left an imprint in the cosmic microwave background also left an imprint in the baryon density. Since the dark matter was not affected, the signature is smaller. However there is enhanced clustering of matter at 147 Mpc comoving scales. This leads to a peak in the correlation function and a set of oscillations in the power spectrum which are known as Baryon Acoustic Os-

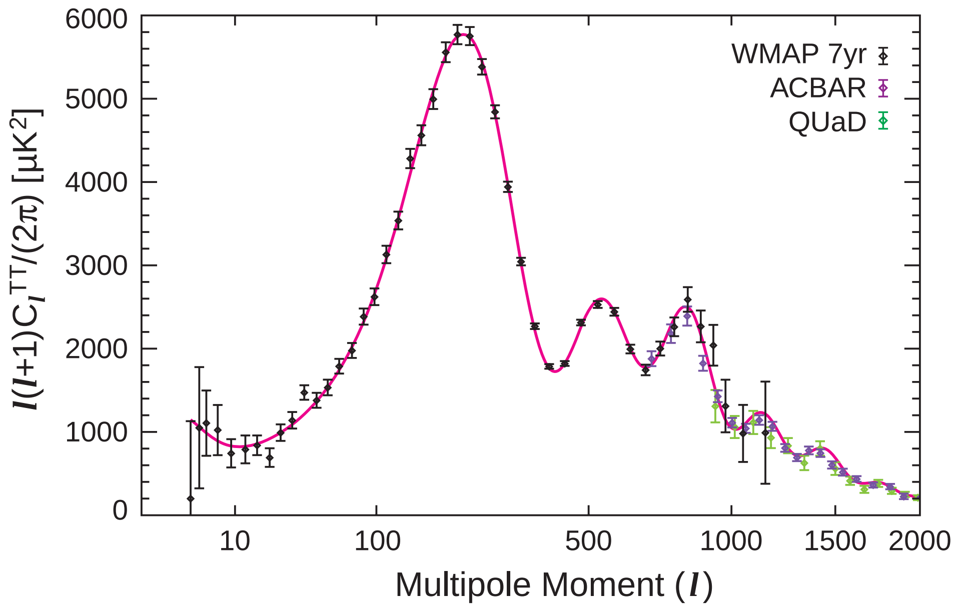

Figure 1.1: CMB power spectrum. Reproduced from [39].

cillations (BAO). The theoretical framework for the anisotropies in the CMB and BAO was first developed by Sunyaev and Zeldovich [65] and Peebles and Yu [51] in 1970, Bond and Efstathiou [10],Bond and Efstathiou [11], and Holtzman [34] in the 1980's. The framework was further developed by Hu and Sugiyama [36] and Eisenstein and Hu [22]. The first proposal that BAO could be used to constrain cosmology was by Eisenstein et al. [23]. More detailed projections for the use of galaxy redshift surveys to measure BAO and constrain cosmological models were established by Seo and Eisenstein [62], Blake and Glazebrook [9], Hu and Haiman [35], Glazebrook and Blake [30], andAmendola et al. [3] although this list is not meant to be exhaustive.

1.2.3 Previous Measurements

The very first marginal BAO detections were done by Percival et al. [52] in the power spectrum of the 2dF survey, and by Miller et al. [48] combining independent smaller surveys. Tegmark et al. [69] independently analyzed the 2dF 100k data set and were not able to detect the BAO with their errors. The first strong detection of BAO was done by [24] using the SDSS LRG sample, and the correlation function reproduced from that paper is in figure 1.2. A weaker detection was by [17] in the 2dF power spectrum, and the Sloan data was combined with the 2dF data to get stronger constraints [53]. The best BAO measurement yet is with more recent Sloan data release 7 [54]. Most results to date do not measure radial and angular directions independently. Instead they measure a total effective volume element with side length:

$$D_V = \left((1+z)^2 D_A^2 \frac{cz}{H(z)} \right) \tag{1.17}$$

These measurements cannot measure $H(z)$ independently from D_A. Recent attempts by Gaztanaga et al. [29] make a BAO detection using only the line of sight direction in the SDSS data release 7 data. From this Gaztanaga et al. [29] are able to make measurements of the Hubble parameter, $H(z)$ at two redshifts.

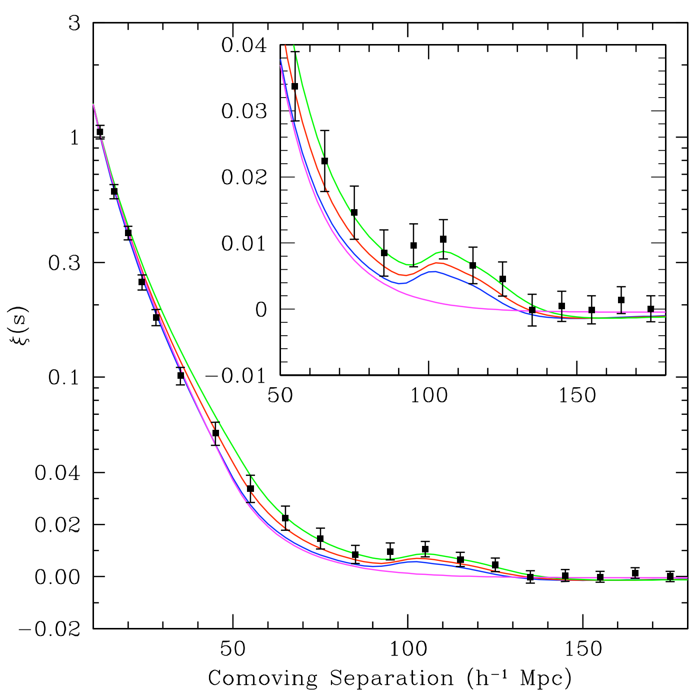

Figure 1.2: Detection of the BAO peak in the SDSS LRG sample. The models are Ω_m h^2 = 0.12 (green line), 0.13 (red line), and 0.14 (blue line), all with Ω_b h^2 = 0.024 and n = 0.98 [24]

1.2.4 Current Constraints on Dark Energy

The current cosmological parameters for the standard ΛCDM cosmology with $\Omega_k = 0$ are listed in table 1.1. These parameters come from combining the measurement of H_0 by Riess et al. [57] and the BAO measurement of $r_s/D_V(z)$ from the SDSS data release 7 [54]. Using the same the same combination the constraint the dark energy equation of state is $w = -1.10 \pm 0.14$[39]. Including the high redshift type Ia supernovae data from Hicken et al. [32] changes the estimate to $w = -0.98 \pm 0.053$[39]. Letting the dark energy equation of state vary, parameterized as $w(a) = w_0 + w_a(1-a)$, the current best constraints are $w_0 = -0.93 \pm 0.12$ and $w_a = -0.38^{+0.66}_{-0.65}$[39] using WMAP, H_0, BAO, SN, and also adding constrains from gravitational lensing by Suyu et al. [66].

1.2.5 21cm Intensity Mapping BAO experiment

The 21cm hydrogen line can be used to create a galaxy redshift survey out to high redshifts and measure the BAO scale. This was proposed by Abdalla and Rawlings [1] as a major SKA science goal. Such a survey's constraints on dark energy are presented in Glazebrook and Blake [30] and more recently in [2].

The intensity mapping technique takes a step further and directly maps the three dimensional specific intensity of the 21 cm line, in voxels of size 5-10 h^{-1} Mpc. Intensity mapping is about 100 times as efficient as the traditional redshift survey, in which galaxies are individually detected, redshifts measured, then

Table 1.1: Current ΛCDM cosmology measured and derived parameters. Reproduced from [37]

. These are derived combining the

Symbol	Description	WMAP + BAO + H_0
t_0	Age of Universe	13.75 ± 0.11 Gyr
H_0	Hubble constant	$70.4^{+1.3}_{-1.4}$ km s^{-1} Mpc^{-1}
Ω_b	Baryon density	0.0456 ± 0.0016
Ω_c	Dark matter density	0.227 ± 0.014
Ω_Λ	Dark energy density	$0.728^{+0.015}_{-0.016}$
$\Delta^2_{\mathcal{R}}$	Curvature fluctuation amplitude, $k_0 = 0.002$ Mpc^{-1}	$(2.441^{+0.088}_{-0.092}) \times 10^{-9}$
σ_8	Fluctuation amplitude at $8h^{-1}$ Mpc	0.809 ± 0.024
n_s	Scalar spectral index	0.963 ± 0.012
z_{eq}	Redshift of matter-radiation equality	3232 ± 87
$d_A(z_{eq})$	Angular diameter distance to z_{eq}	14238^{+128}_{129} Mpc
z_*	Redshift of decoupling	$1090.89^{+0.68}_{-0.69}$
t_*	Age of universe at decoupling	377730^{+3205}_{-3200} yr
$d_A(z_*)$	Angular diameter distance to decoupling	14073^{+129}_{-130} Mpc
$r_s(z_*)$	Sound horizon at decoupling	146.2 ± 1.1 Mpc
$l_A(z_*)$	Acoustic scale at decoupling	302.4 ± 0.73
τ	Reionization optical depth	0.087 ± 0.014
$z_{reionization}$	Redshift of step reionization	10.4 ± 1.2

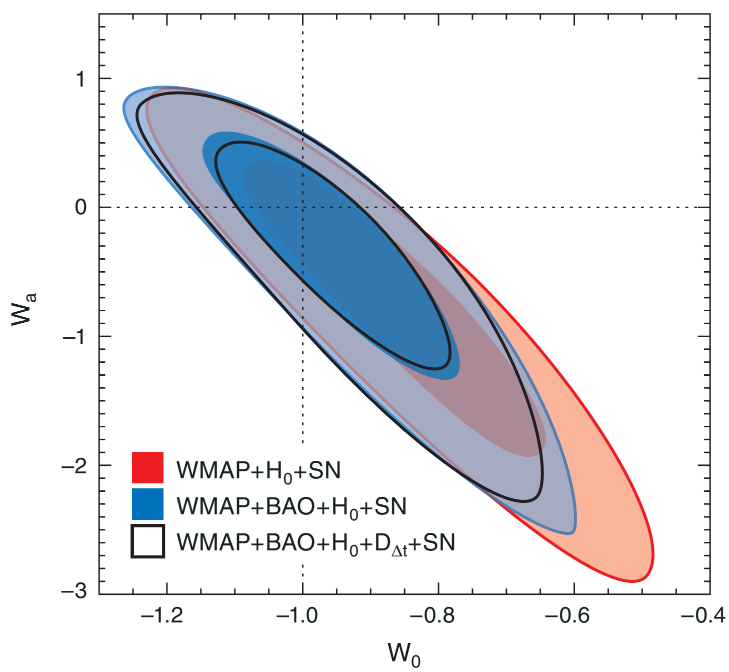

Figure 1.3: Current constraints on a varying dark energy equation of state. Constant with cosmological constant. figure from Komatsu et al. [39]

the galaxy positions are used as a tracer of large scale structure. This is a new technique, recently proposed and experimentally verified (See Peterson et al. [55], Chang et al. [13], Masui et al. [47], and Chang et al. [14], Wyithe [71], Wyithe and Loeb [72]). By measuring the radial and angular size of this BAO scale at each redshift we can probe the expansion history during the time period when dark energy began to dominate the attractive gravitational interactions on the largest scales. The constraints of a future intensity mapping survey in 21cm are compared to other surveys in Chang et al. [13] and Ansari et al. [5]. The dark energy equation of state constraints parameterized as $w(z) = w_0 + w_a \frac{z}{1+z}$ reproduced from Ansari et al. [5] is shown in figure 1.4. Bagla et al. [6] simulate the 21cm signal and project what could be observed using the Giant Metrewave Radio Telescope (GMRT) [1].

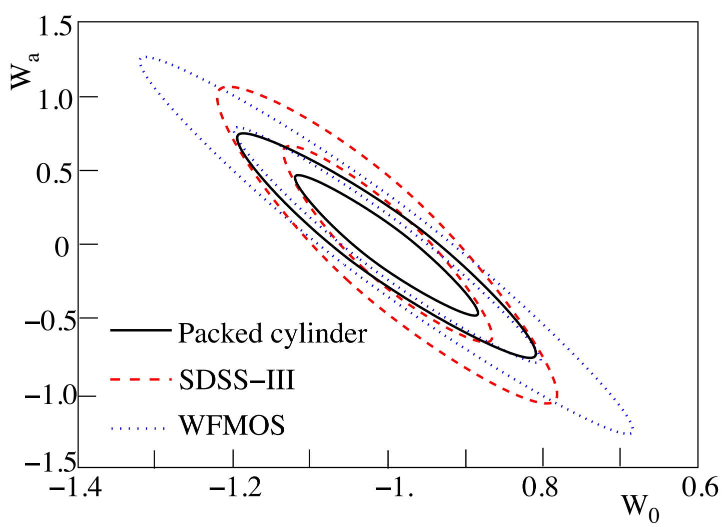

Figure 1.4: Projected constraints on a varying dark energy equation of state. Figure from Ansari et al. [5]

[1] http://gmrt.ncra.tifr.res.in/

1.3 21 cm Hydrogen Line

There have been a number of excellent reviews on the 21 cm line and its use in cosmology. Recent reviews concentrating on the 21cm line are Morales and Wyithe [50], Furlanetto et al. [28], Fan et al. [26],and Barkana and Loeb [7], which all go into great detail. In particular Morales and Wyithe [50] discusses both the epoch of reionization and intensity mapping afterward.

1.3.1 21 cm Emission

The Hydrogen hyperfine splitting of the ground state has a rest frequency $\nu_0 =$ 1420.40575MHz. Due to the expansion of the universe, neutral hydrogen at a red-shift z will be observed at a corresponding frequency $\nu = \nu_0/(1+z)$. The apparent brightness temperature observed will be $T_b(\nu) = T_b(\nu_0)/(1+z)$

The radiative transfer equation can be written as:

$$dP = emission - absorption \tag{1.18}$$

$$dIdAd\Omega = JdAdsd\Omega - KIdAd\Omega ds \tag{1.19}$$

where I is the specific intensity, dA is the unit area perpendicular to the direction of travel, ds is the element of distance along the line of travel, and $d\Omega$ is a unit of solid angle. J is the emissivity of the medium and K is the extinction coefficient.

This leads to a brightness temperature in the Rayleigh-Jeans limit:

$$T_b(\nu) = T_S(1 - e^{-\tau_\nu}) + T_{BG}(\nu)e^{-\tau_\nu} \tag{1.20}$$

where T_S is called the spin temperature of the atomic hydrogen gas cloud, τ_ν is the optical depth, and T_{BG} is the brightness of the background behind the cloud.

The spin temperature T_S is defined as the effective temperature which gives the number population between the two spin states 1 and 2 possible, where state one has total atomic angular momentum of 0, and state 2 has a total angular momentum of 1. T_S is defined by the equation:

$$\frac{n_2}{n_1} = \frac{g_2}{g_1} e^{-\frac{E_{21}}{k_B T_S}} \tag{1.21}$$

where $g_2 = 3$ is the degeneracy of the excited state and $g_1 = 1$ is the degeneracy of the ground state.

The optical depth is defined as

$$\tau_\nu = \int K ds = \int \sigma_{12}(1 - e^{-\frac{E_{21}}{k_B T_S}})\phi(\nu) n_1 \tag{1.22}$$

with

$$\sigma_{12} = \frac{3c^2 A_{21}}{8\pi\nu^2} \tag{1.23}$$

and $A_{21} = 2.85 \times 10^{-15} s^{-1}$ is the spontaneous emmission coefficient, $\phi(\nu)$ is the line shape, and n_1 is the density.

this leads to an optical depth:

$$\tau_{\nu_0} = \frac{3}{32\pi}\frac{hc^3 A_{12}}{k_B T_S \nu_0^2}\frac{x_{HI} n_H}{(1+z)(dv_{\|}/dr_{\|})} \tag{1.24}$$

where $(dv_{\|}/dr_{\|}) \approx H(z)/(1+z)$ is the gradient of the proper velocity along the line of site, x_{HI} is the neutral fraction and $n_H = (1+z)^3 n_{H,0}$ the density of hydrogen.

The 21cm brightness relative to T$_{CMB}$ is then

$$T_B = \frac{T_S - T_{CMB}(z)}{1+z}(1 - e^{-\tau_\nu}) \tag{1.25}$$

and can be parameterized, assuming $\tau_\nu << 1$ and $T_S >> T_{CMB}$ as

$$T_b = 0.3 \left(\frac{1+z}{2.5}\right)^{\frac{1}{2}} (1+\delta) \left(\frac{\Omega_m + (1+z)^{-3}\Omega_\Lambda}{0.29}\right)^{-\frac{1}{2}} \left(\frac{\Omega_{HI}}{10^{-3}}\right) mK \tag{1.26}$$

with $T_b = \bar{T}_b + \Delta T_b$ is the brightness temperature, δ is the normalized HI density $\rho_H/\bar{\rho_H}$, and Ω_{HI} is the neutral hydrogen density over the critical density.

1.4 Outline

In order to make a significant contribution to dark energy constraints a single dish telescope is not enough. However, existing telescopes can be used to develop techniques for intensity mapping, and are availabe to use right now. We use the Green Bank Telescope (GBT) to make first the first detections of HI at a redshift of $\sim$0.8, as described in Chapter 5.

To make a detection with high precision, approximately 500 channels are necessary, see Ansari et al. [4]. In order to do this we will need a dedicated instrument. Peterson et al. [56] propose cylinders as a possible low cost option, but a cylinder design may have calibration advantages to make it the best regardless of cost. An array of dishes might be an excellent option as well. Chapter 2 explores a prototype cylinder telescope option. Chapter 3 discusses imaging with the prototype cylinder. Chapter 4 describes the collapse and rebuilding of the cylinder. Chapter 6 discusses ongoing projects to observe the universe with 21cm intensity mapping.

2

Pittsburgh Cylinder Prototype Telescope Design and Characteristics

2.1 Design

There is a revolution going on in radio astronomy. The early telescopes were single dish designs. Karl Janksy made the first astronomical radio observations in 1931, detecting a radio hiss from the Milky Way galaxy. Grote Reber made the first dish for astronomical observations in 1937 in Illinois. World War II and the development of radar had technology development that crossed-over well into radio astronomy. The first interferometric measurements were made by Ryle in 1946[60]. In the 50's and 60's the parabolic cylinder style of antenna design became popular. The Mills Cross[12], Illinois 400ft[68], Cambridge 4C Mullard[59], Northern Cross, and Ooty[67] Telescopes were all built in that time period. Ooty is still being used and the Mills Cross was upgraded to MOST[49]. However in general cylinders have lost favor. Cooled amplifiers are quiet but expensive. Cryogenic low noise amplifiers favored a large collecting area with low loss before the amplifier as supplied by dishes and difficult to achieve with cylinders. The line feed of a cylinder requires many amplifiers, which becomes prohibitively expensive with a cryogenic system.

Cylinders were initially built to conduct surveys. However, traditionally the feed elements were analog-summed and phase-shifted using adjustable cable lengths and feed rotations to steer the beam. This lead to an unreliable beam which was adjusted by hand for each observation. Returning to the same calibration state was difficult.

Development of room temperature amplifiers for satellite television, and exponential growth of computational power have brought along technologies that make cylinders an attractive technology again. It is possible to integrate an uncooled amplifier with 5K noise temperature into the feed system. It is also possible to sample every single feed element, and adjust phases and amplitudes digitally.

The key program of this thesis is to construct a prototype cylinder telescope that can detect neutral hydrogen from the Milky Way galaxy on large scales. The prototype is used to help determine whether a cylinder telescope designed with today's technology can be calibrated to achieve the dynamic range and stability in order to detect Baryon Acoustic Oscillations in the 21-cm intensity field.

A single dish can only point at a single place in the sky at a time. Advances in focal plane arrays with many feeds have allowed single dishes to look at 7-15 pixels on the sky at once. Such multi-beam arrays are in place at Parkes [64], Arecibo [8], and Green Bank [40]. Off axis distortion limits the focal plane size of most single dish telescopes to tens of beams. In contrast a cylinder can have hundreds or thousands of receivers and beams. Thus a cylinder can conduct a survey of the sky more quickly, since it collects radiation from an entire strip of sky at once. .

A fixed design parabolic cylindrical drift scan telescope was chosen. Given that we want an all-sky survey, steering ability only adds to the cost. The cylinders are oriented along the north-south direction. The feeds are all placed along the parabolic cylinder focal line rather than a single focal point. Using electronic beam-forming the telescope can be used to form many simultaneous beams along the north-south meridian.

2.1.1 Cylinder

The cylinders are oriented in a north-south direction. They are 10m wide and have supports 75 feet long. The surface itself is 68 feet long on the East cylinder and 58 feet long on the West cylinder. The East and West cylinders are spaced 25 m from center to center (15m space between them). See figure 2.1

Figure 2.1: The Pittsburgh cylinders viewed from above looking west. Orange covering is the instrumented feed-line. Each cylinder is 10m wide, 25m long, and spaced 25m East-West.

2.1.1.1 Surface

The surface is a welded and not woven 0.042″ diameter steel wire mesh, galvanized after welding. The welded construction leads to a much stiffer surface than a woven mesh. The mesh is made of continuous sheets transverse to the cylinder axis. The mesh is stiffened by steel 5′ by 6″, 3/16″ galvanized steel flat plates, which we call battens, on top of the mesh. These are bolted to bent mating plates on the bottom.

The East and West cylinders were constructed with slightly different designs in order to test costs and performance.

On the East cylinder the battens were spaced along the mesh such that the projection on the ground would be evenly spaced 1m apart in the east-west direction. Along the mesh, the center to first separation is 39″, the first to second is 43″, the second to third is 44″, and the third to forth is 53″.

On the East cylinder the battens are attached to the mesh by 5 3/8″ carriage bolts, with the bolts on each end overlapping with the adjacent battens. Below, the bent battens overlap so they stiffen the length, but are able to move a bit for adjustment.

The West cylinder used steel 2x4 studs as beams 10 feet long. These were attached with self-drilling screws to the mesh and the flat steel plates on top. Pairs of 10 foot sections were then also attached together and erected as a unit. The steel 2x4's turned out to be a bit flimsy, so the bent battens were then screwed on to add weight and stiffen the structure. The focal length of the east cylinder is 78″ and is 77″ for the west cylinder.

2.1.1.2 Support

The foundation consists of concrete footings poured approximately 3ft deep with rebar crosses and 1/2″ j-bolts protruding from the surface. For guying and attaching the surface mesh, concrete dead-men were poured directly into the ground, with rebar and 3/8″ galvanized steel cable loops extending above ground for attachment.

The support columns are custom weldments made by Vegely Welding. The columns are 12 feet tall schedule 10 (approximately 1/4″ thick) 8 inch pipe with an 18 inch square plate 1/2 inch thick welded to the bottom, and a 12 inch square 1/4″ thick square plate welded to the top. The bottom plates have slotted holes to attach to the J-bolts in the concrete. The top plates have slotted holes to attach to the trusses. The columns were guyed from the top in 4 directions to the bottom of the adjacent columns and the dead-men. The columns were raised with 2-3 people. The column was positioned on the ground at the J-bolts, then one person guided the bottom into place while the others lifted. See figure 2.2

The trusses use heavy duty standard bar joist trusses 25′ long. The trusses have a 6″ pipe welded to their top, precision shimmed to be straight and level. The top of these pipes determines the surface for the mesh to hang from and served as

Figure 2.2: Putting up the columns. Wagon used to bring columns into place before raising. Columns were raised with just 2-3 people and no machinery.

a reference for measurements.

2.1.1.3 Adjustment

The tops of the trusses at each column were measured using a Total Station retro reflector based surveying transit. This allowed for adjustment of the position of the truss height to a few mm accuracy. See figure 2.3. The cylinder heights were adjusted to within 5mm within each cylinder, and the West cylinder is approximately 1cm higher than the East.

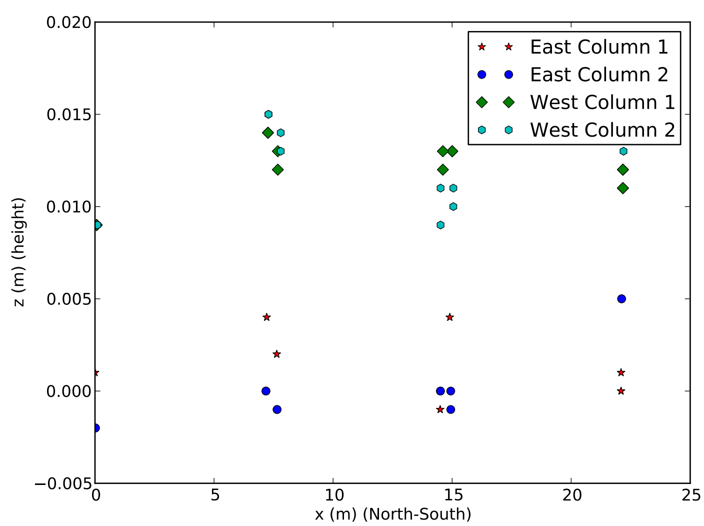

Figure 2.3: Cylinder heights were measured with a Total Station surveying transit. Plotted is the height vs. North-South position for each of the 4 truss line supports. The height of the East and West cylinders independently were within 5mm, and the two cylinders have heights that differed by about 1cm.

The cylinder shape is adjusted with pull-downs attached approximately every 5-10 feet along the length of the cylinder. The cylinders were built upon a slag material, which was acted like solid, brittle rock when trying to dig. In softer soil concrete curbs or a drilled or driven anchor in the ground would serve as attachment points for the pull-downs. Since the slag matrix was so hard below our cylinders, we attached out pull-downs to steel 4x4's bolted to the base of the columns. We also used 3/8″ steel cables run underneath each line of battens. The pull-downs were made from steel cables connecting the battens to the 3/8″ steel cables running underneath. We used adjustable turnbuckles with 3″ range on each pull-down.

2.1.1.4 Feedline Support

The feed line support structure was made from Rohn 25G tower sections. The sections were welded together so that no bolt heads would stick out. This allowed for a rolling Antenna feed support. However, the rolling feed never actually worked smoothly, and the feed system was attached with u bolts instead. 1″ square steel bar were welded to the tower to have attach points holding up the tower. The feedline was supported using marine grade spectra polyethylene rope which has very little stretch and a tensile strength to weight ratio larger than steel.

2.1.2 Feed System

The analog feed system integrates four antennas and LNA channels onto one circuit board. Each channel is connected to a receiver box which amplifies, mixes down and filters the signal to a band in the range 50-100MHz. This intermediate frequency (IF) signal is then carried on coax 100m into the "white house" where it arrives at a filter box, which then leads into the ADC. See figure 2.4 for a block view of the system.

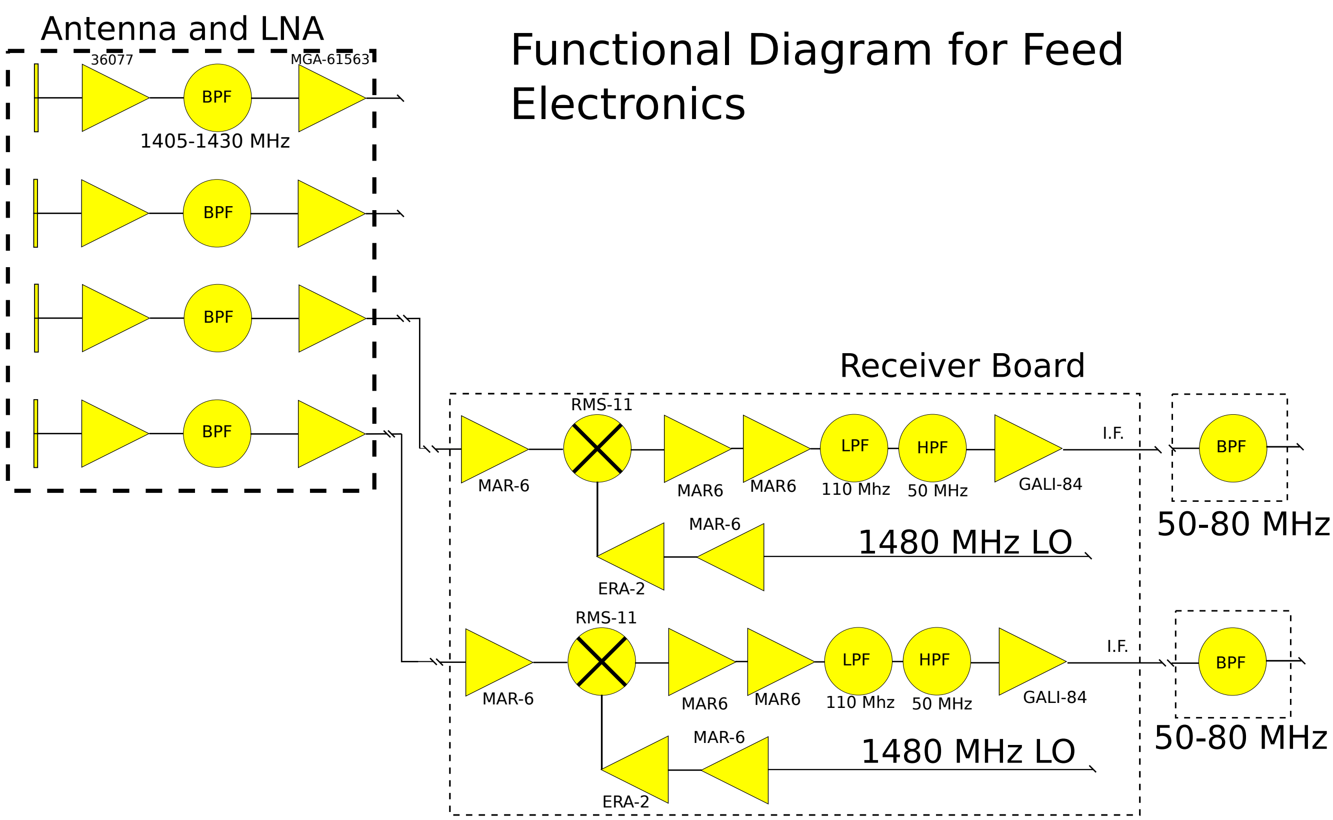

Figure 2.4: Block diagram of the feed system. Each box represents a unit. The antenna, LNA and receiver board are all at the prime focus line of the cylinders. The final band pass filter is placed immediately before the ADC boards.

2.1.2.1 Integrated Antenna

For the longitudinal polarization the antenna lies in the plane of the circuit board. For the transverse polarization small antennas printed on FR-4 were soldered to the main circuit board. This allowed for the LNA circuit to start right at the antenna, minimizing system temperature. See figure 2.5 for an image of the antenna and LNA boards.

2.1.2.2 LNA

The need for smaller satellite TV dishes brought about development of very low noise amplifiers at room temperature. These are high electron mobility transistor(HEMT) devices.

I designed a low noise amplifier (LNA) around the Avago ATF-36077 which was the lowest noise figure device at the time. Lab tests of the LNA show a 0.3 db (21K) noise figure, see figure 2.6.

It was found that the RFI in Pittsburgh was overloading the LNA. To prevent this, the LNA circuit was then re-designed with a 9 element High-pass filter at 1200 MHz before the amplifier. These filter elements were also included in optimization of the noise matching of the amplifier to the antenna.

Immediately following the first gain block is a Neosid helical filter. It has a tunable frequency range approximately 30 MHz wide. A second gain stage follows the first using a MGA61563. It has a 1 dB noise figure and 20dB of gain, see figure

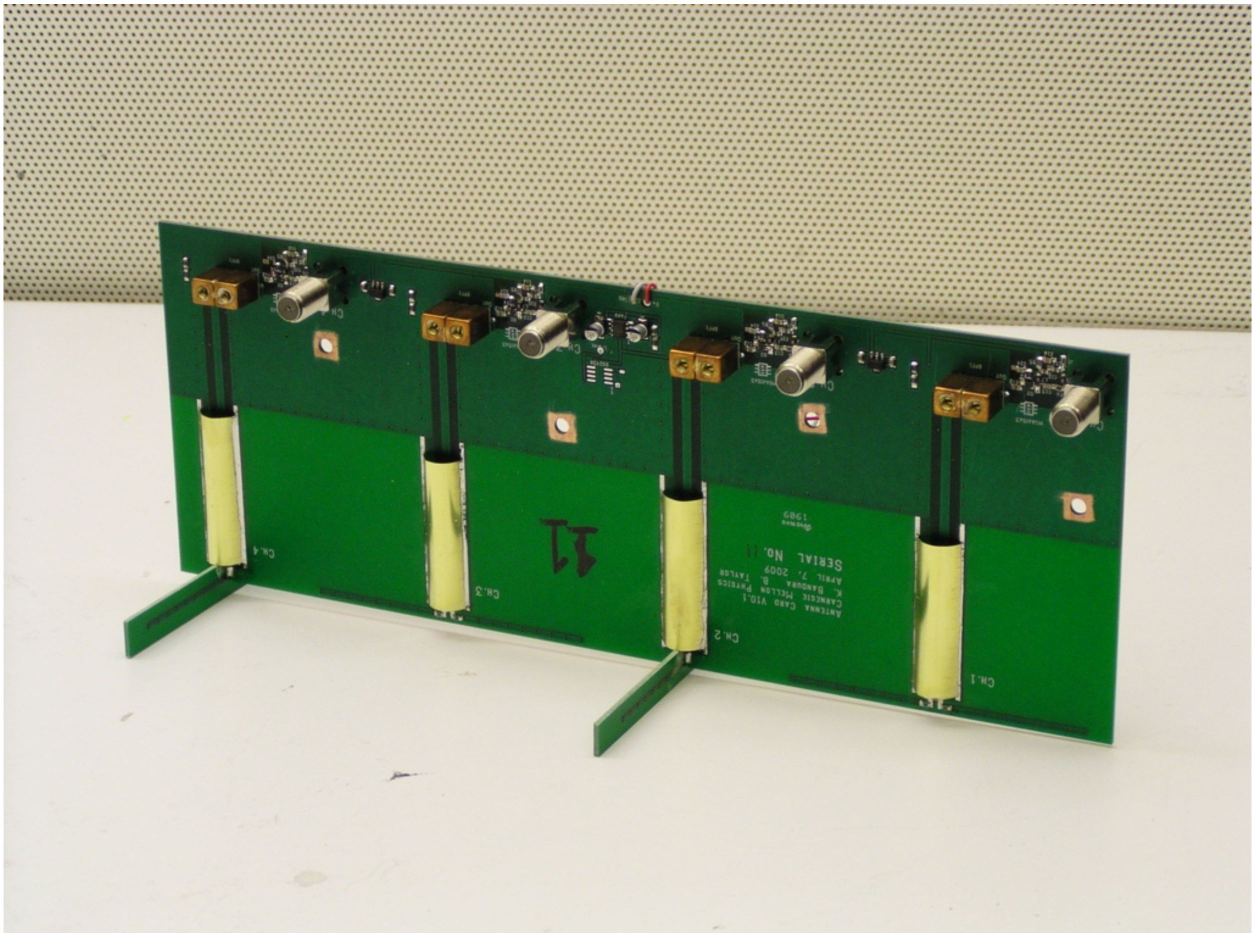

Figure 2.5: View of the antenna circuit board used. Transverse and longitudinal polarizations are interleaved, offset by 0.35λ. The longitudinal antennas are built into the circuit board. The transverse antennas are soldered to the board. The first LNA is covered by the brass shields. The space between the shields and the filter is for attachment of the ground plane. The RF is filtered by a Neosid Helical filter to a 30MHz passband and then amplified by a second LNA before coming out the F connector.

2.7.

The entire circuit was simulated using Agilent's Advanced Design System (ADS). The schematic is shown in figure 2.8, and the simulated results are shown in figure 2.9. The simulated gain of the system is 32 dB, and the simulated noise figure is 1 dB. For some tests we used aircoil inductors which lowered the noise figure to 0.75dB. The LNA was unconditionally stable in simulation. The simulation has the Neosid helical filter set at 1425MHz center. In actuality the filter is continuously tunable, and was set to have the gain maximum between 1410MHz and 1415MHz.

We built over 100 of these LNA's. The best channels did approach the model predictions. See figure 2.10 where the measured noise figure was 0.8dB. Most channels had a noise figure at about 1dB, see figure 2.11a and figure 2.11b

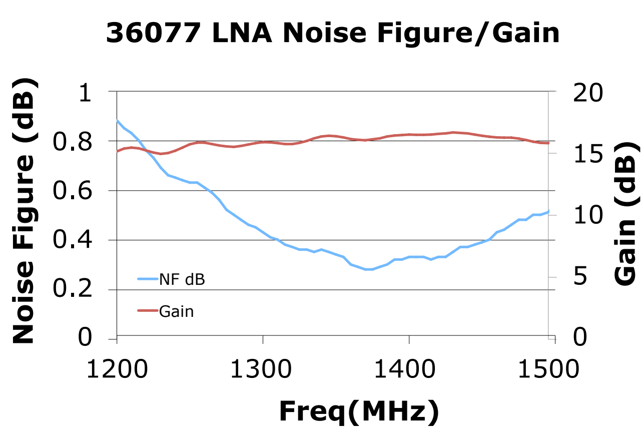

Figure 2.6: Measured noise figure and gain of Avago ATF-36077 LNA. The LNA has a 20K (0.3dB) noise temperature using room temperature components. Design had to be refined to use a high-pass filter to attenuate the cell phone band.

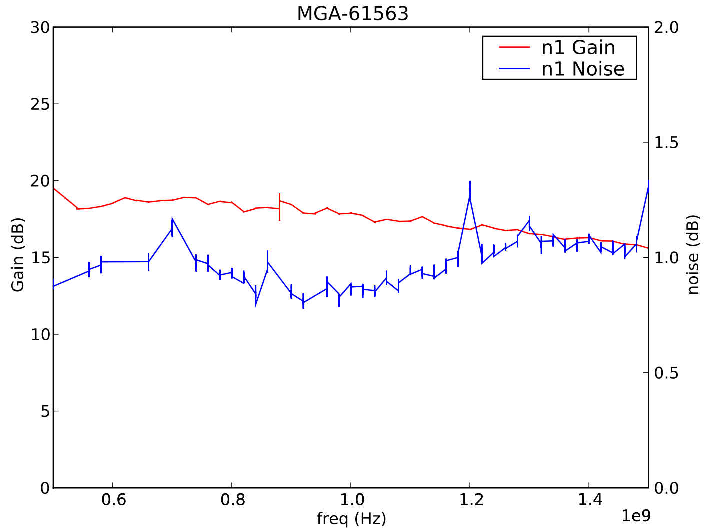

Figure 2.7: Measured noise figure and Gain of Avago MGA61563 second stage LNA. The amplifier has an approximately 1dB noise figure and 15-20dB gain across a wide band. Gain is about 15dB in the region of interest.

2.1.2.3 Receiver

The receiver mixes the signal down to 50MHz-100MHz. The actual bandpass filter ranges from 50-110MHz at the 3db point, and has 65-70db of gain. There is 20db of RF gain before the mixer, 50db after mixing. The LO is injected at 1380MHz, at a power level of -18dbm going into the receiver box. Each receiver box has 2 independent channels. The schematic for a receiver box is shown in figure 2.12, and one of the boards can be seen in figure 2.13. The receiver has a measured noise figure of $\sim$ 6db.

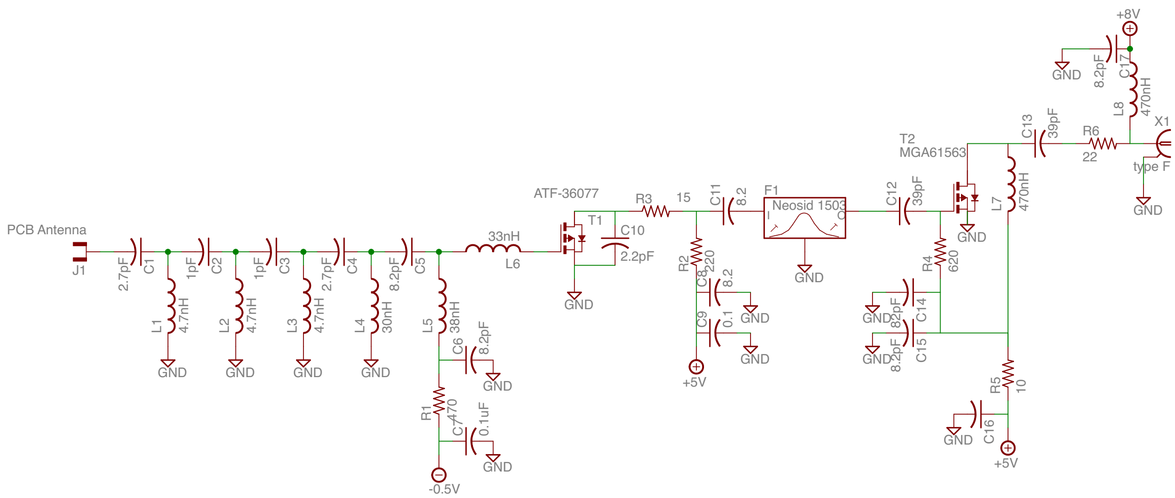

Figure 2.8: Schematic of one LNA channel. The signal first passes through a high pass filter and into a matched LNA. The signal is further filtered and amplified again before being transmitted on 75Ω coax.

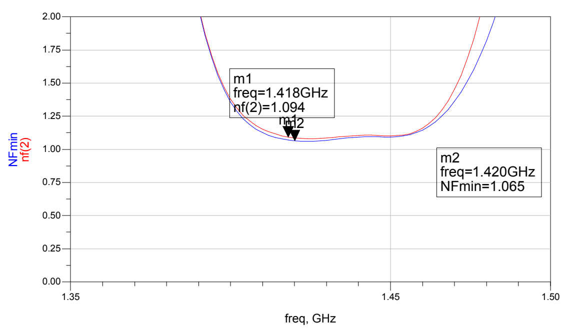

(a) Noise Figure

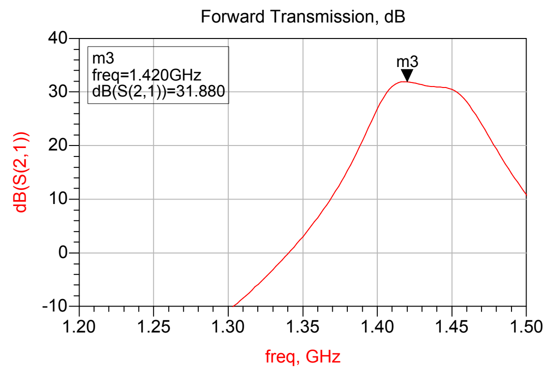

(b) Gain

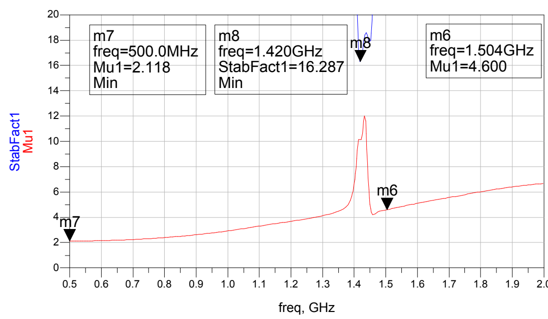

(c) Stability

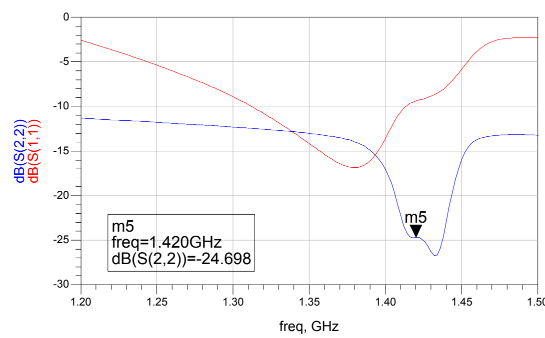

(d) Match

Figure 2.9: Simulated performance of an LNA channel. Figure (a) shows a simulated noise figure of 1dB. Figure (b) shows a simulated gain of 32db. Figure (c) plots the stability of the amplifier, which is > 1 for all frequencies, and therefore unconditionally stable. Figure (d) shows the input and output match. The input match is designed for noise figure. The output is matched for 75 ohms impedance.

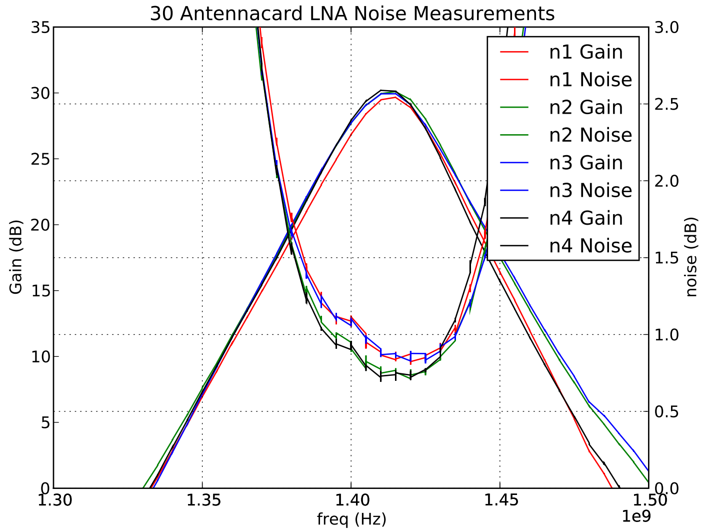

Figure 2.10: Measured performance of one of the best LNA antenna cards. Noise figure at 0.8dB, gain at 30dB. Shows all four channels on a card.

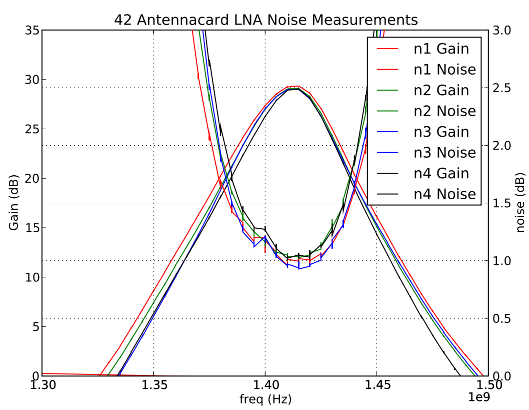

(a)

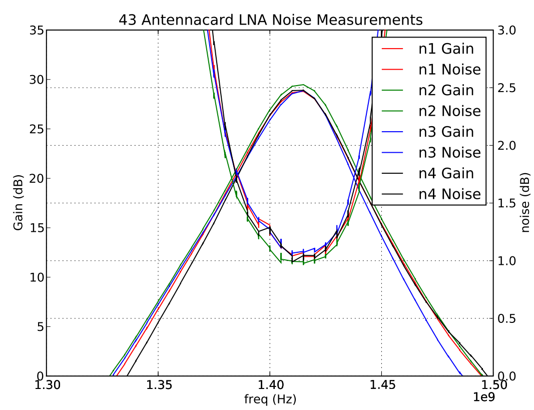

(b)

Figure 2.11: Measured performance of a typical LNA's antenna card. Noise figure at 1dB, gain from 28dB to 29dB for different channels. Matches very closely to the simulated circuit performance in figure 2.9 on the previous page.

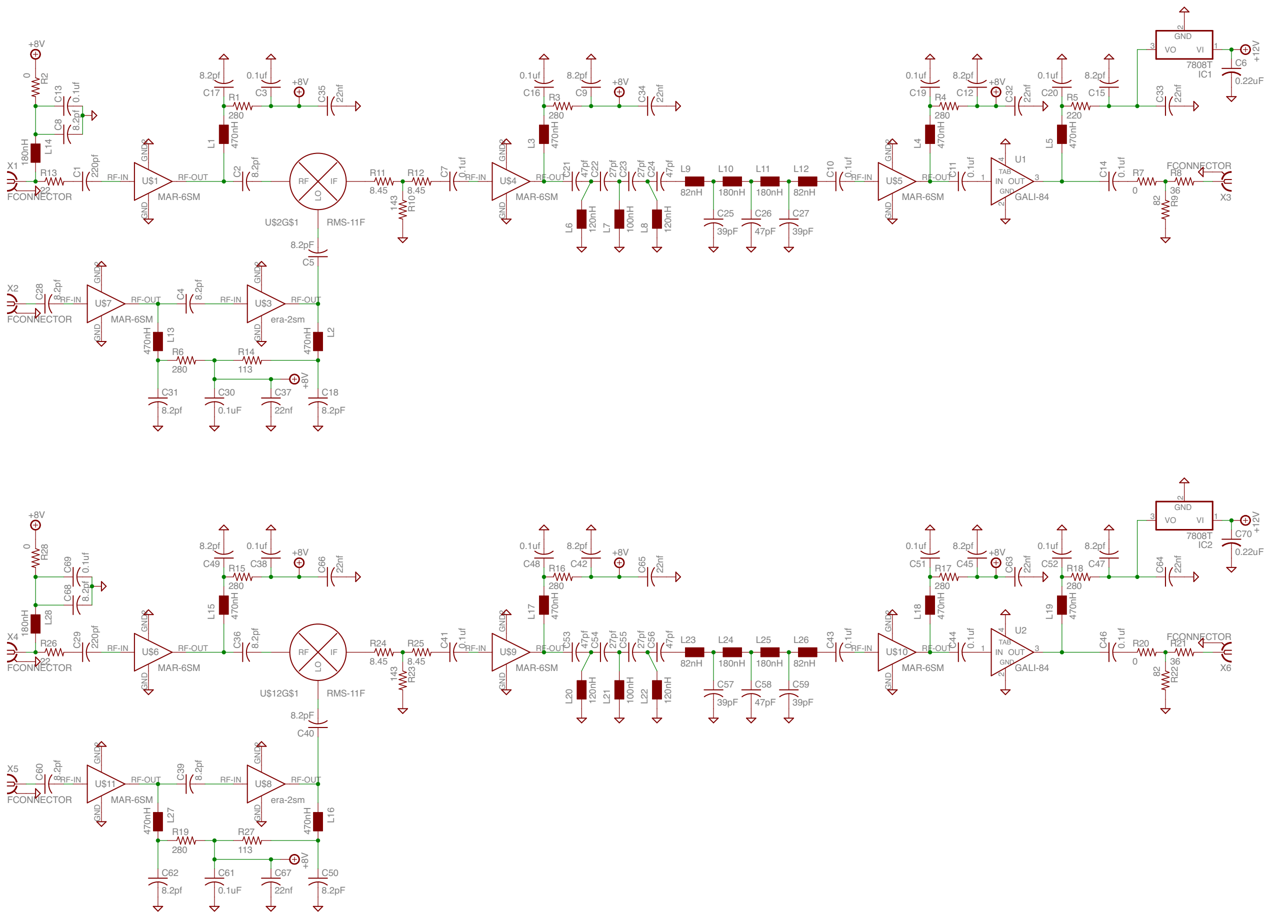

Figure 2.12: View of the receiver schematic. Shows the exact components used. Two channels shared a box but were completely independent of each other.

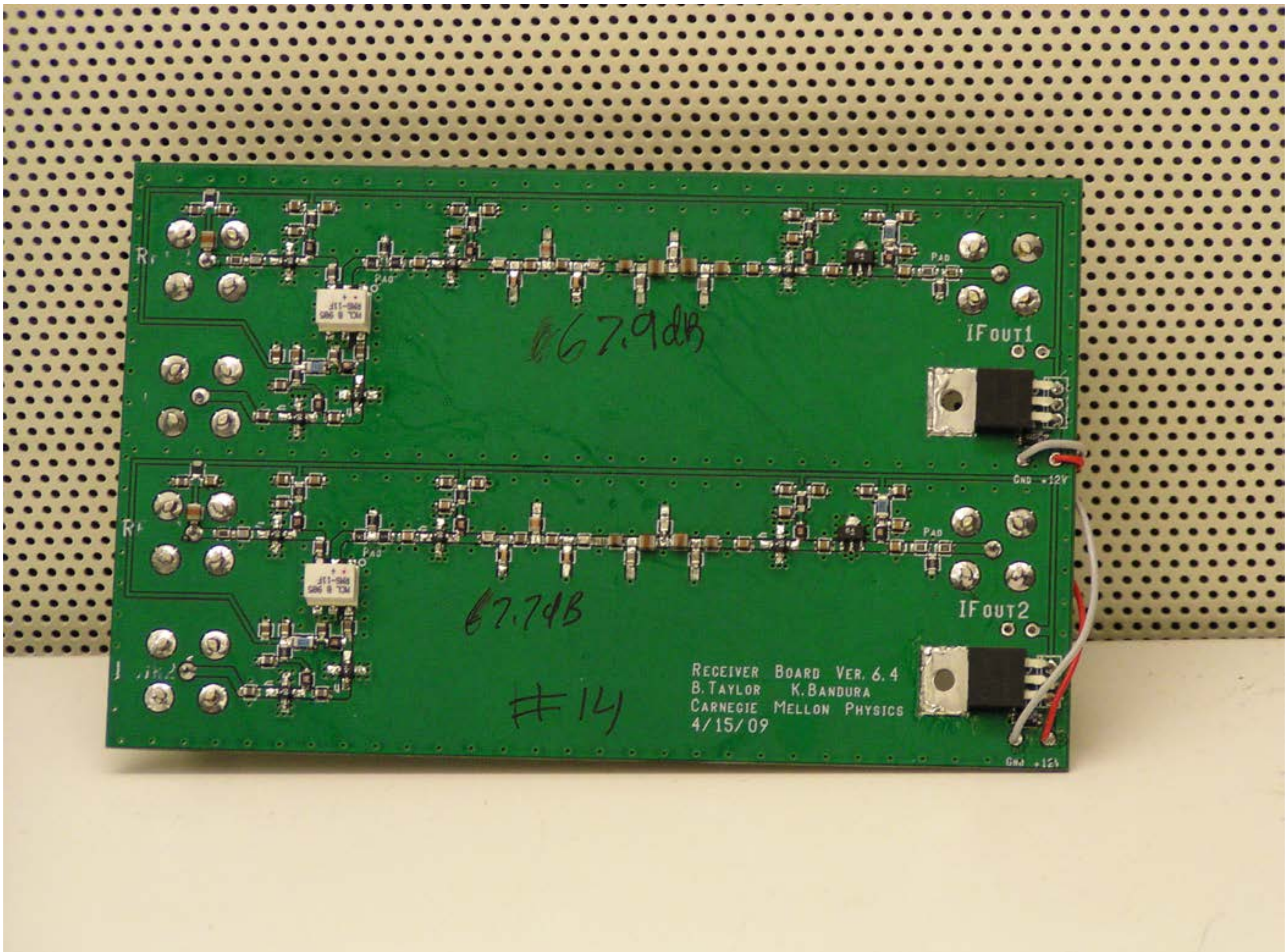

Figure 2.13: Image of the receiver board. Shows the two channels are just exact copies, and the layout of the components.

2.1.2.4 Final filter

Immediately before analog to digital conversion, there is a final anti-aliasing filtering stage. This stage has a sharp filter with a pass-band from ~55MHz to 85MHz. There is also a gain stage, and resistive 75ohm to 50 ohm impedance transformation to go into the adc's. See figure 2.14 for a view of the circuit board, and figure 2.15 for the schematic. This board is also meant to be protection for the ADC from lightening. The anti-aliasing filters are housed in a rack mounted box, 24 channels to a box. This box can be seen in the image in 2.18

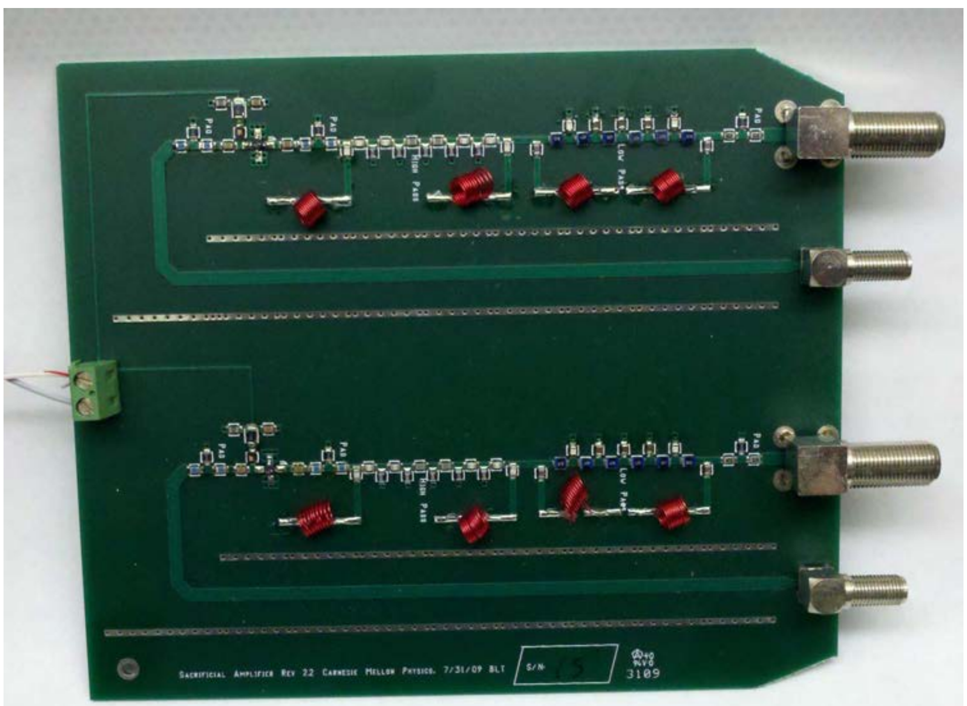

Figure 2.14: View of the final filter board. Was designed as a low-pass filter followed in series by a high pass filter. Included impedance matching and gain such that the overall gain was zero. Each board again had two completely independent channels.

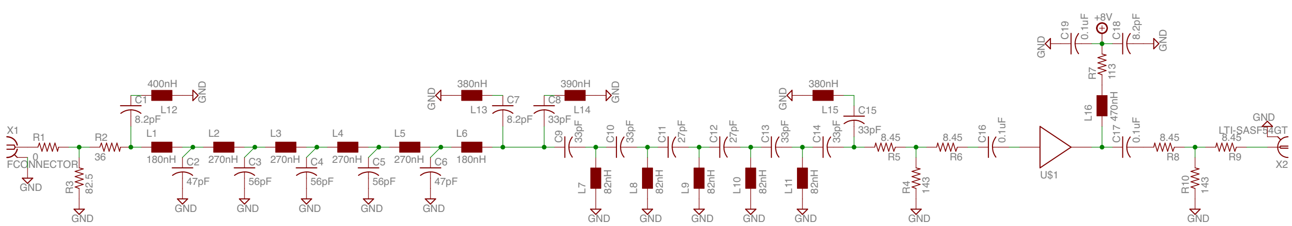

Figure 2.15: Schematic for the final filtering stage. Only a single channel is shown. Used matching for 75Ω input and 50Ω output. Amplifier to make the board have zero gain in band overall.

2.1.3 Correlator

The correlator is a software based correlator, following the design used at GMRT [58]. The analog to digital converter (ADC) used is an acquisition logic AL81004C, with customized firmware and linux drivers. The card has four synchronized channels sampled at 100Msps. Each card receives a 10 MHz external clock signal from a global positioning system disciplined oscillator (GPSDO) [1]. One ADC board acts as the master, sending a triggering signal to itself as well as to all the other ADC's when all boards report that they have an empty buffer and are ready for a trigger. The ADC cards have 256 MB of onboard buffer space shared between the channels. We only use a 32MB buffer, giving 8MB for each channel. The data buffer is sent out the pci bus via DMA transfer to the system memory while the next buffer is filled. The time-stream buffer is split into two pieces, and the first half is Fourier transformed in blocks of 4096 on the acquisition nodes, the second half is sent to another 16 nodes which perform the Fourier transform on that half, and then truncate the signal to 4 bits. The channels are then broken into 16 frequency chunks and each frequency slice is sent to a different correlation node, such that each correlation node has 1/16th of the frequencies from every antenna. These nodes then multiply all correlation pairs and average(accumulate) an entire buffer, which then gets saved to disk using only 16bits for each complex number. Each buffer is stored as an overall integer multiplicative factor times the square

[1] http://www.jackson-labs.com/products_fury.html

root turned into an 8bit number. $n = sign(A_f)\sqrt{|A_f|}/N$. The FFT uses the intel Fourier transform as well as low level register shifting. The correlation also uses specific Intel SSE instructions to vectorize the multiply and accumulate. See figure 2.16 for a block diagram of the correlator.

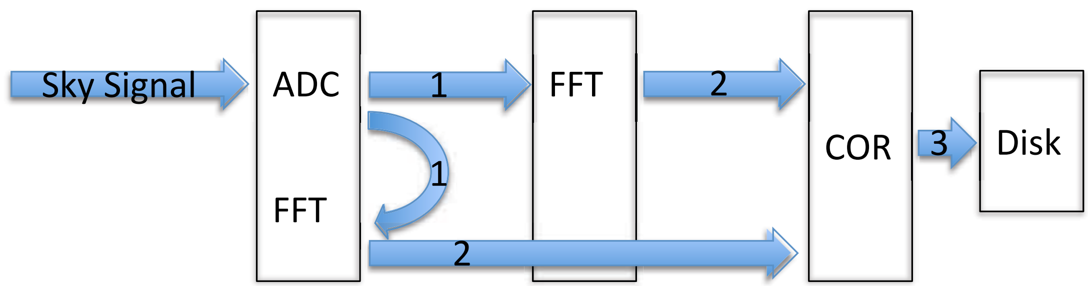

Figure 2.16: Block representation of the correlator. The sky signal is digitized by a set of 16 nodes. The digital time-stream is split in half, with one half Fourier transformed on the acquisition nodes. The other half is sent to another 16 nodes to be Fourier transformed. The resultant spectra are truncated to 4 bits and 1/16th of the frequencies are transferred to each of the 16 correlation nodes. All correlation pairs are calculated, and the spectra are averaged and saved to disk for every 0.08 seconds of data. It takes 0.3 seconds total to process the 0.08 seconds of data, including the sampling time.

For the 64 channels we have each buffer takes approximately 0.30 seconds to process. An 8MB buffer of 8 bit samples at 100Msps takes ideally 0.08 seconds to fill. The correlation is computed at a ~20% duty cycle. The main bottleneck is the transfer of data off the acquisition card into the PC memory.

The acquisition boards are all in dual xeon single core 2.4GHz computers. The compute nodes are dell r410 machines with dual quad-core 2.0 GHz Xeon Nehalem processors. The nodes are all connected through two independent 48 port Dell switches. Disk storage is through two Dell MD1000's hosted by a Dell r710. The disk server and other auxiliary services are connected to another 24 port gigabit switch, along with one of the compute nodes. See figure 2.17 and figure 2.18 for images of the setup.

Figure 2.17: The PC cluster of correlator machines. The 16 machines on the far left contain the ADC's. They were used for sampling and FFT. 32 of the dual CPU quad core machines are used for FFT and correlation. The data is stored on the RAID boxes at the top of the image.

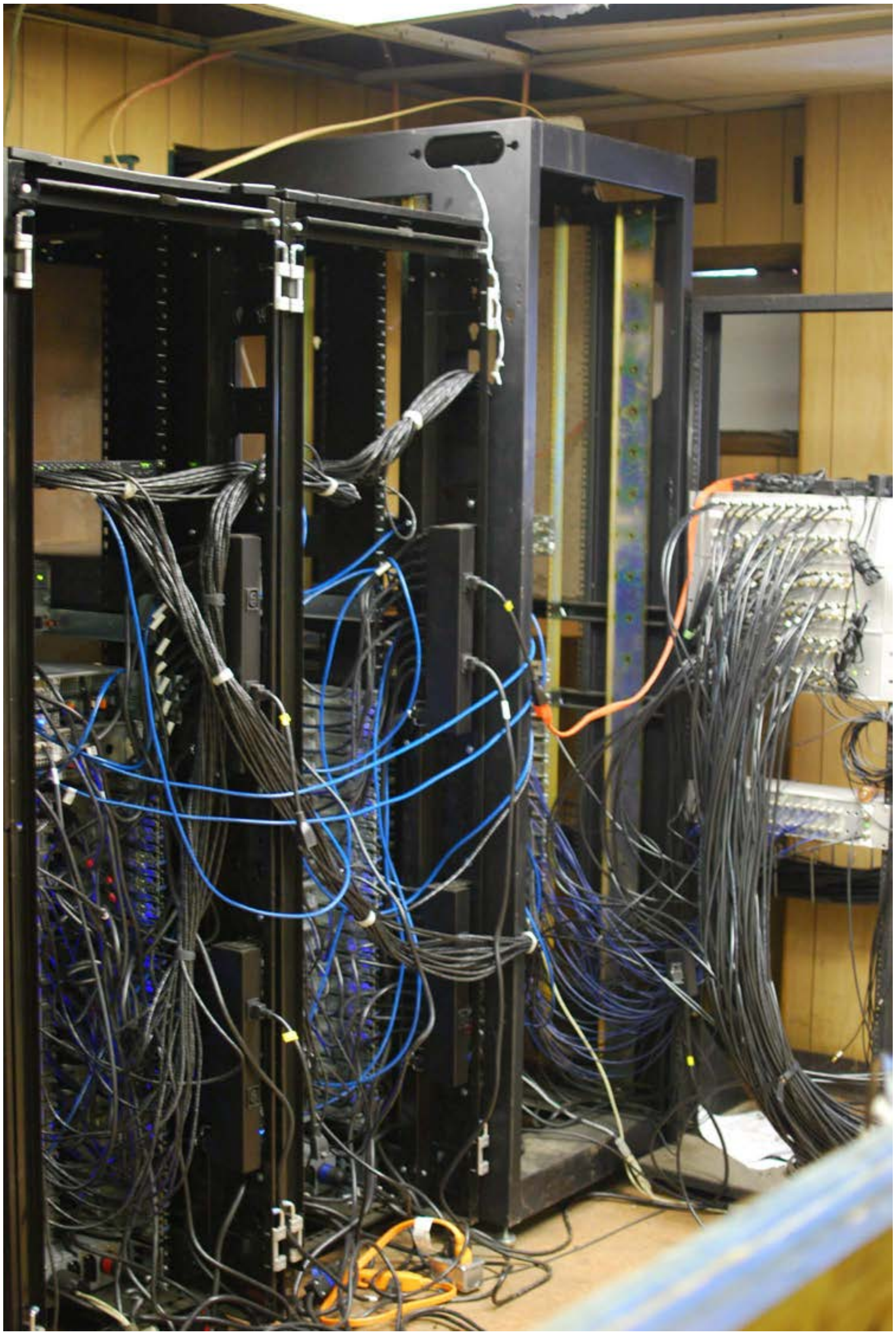

Figure 2.18: Image of the correlator machines from the back. The rack on the right has the 64 channels coming from the telescope, contain the final filtering and then connect to the ADC boards. The bottom box of the rack contains the clock and trigger distribution.

2.2 Cylinder Shape

The cylinder is made by hanging a mesh between two columns. A constant weight object hanging between two points will form a catenary. By pulling down at even points along the length with equal force, this catenary will turn into a better focusing parabola. The telescope was designed to do exactly this. However, equal spacing across the 'x' direction will also cause it to be an equal spacing across the aperture plane. For this reason one of the cylinders has this spacing, the other has the pull-downs spaced equally along the length, naturally forming a catenary. Pulling on these points with different weights will still turn the catenary into a parabola.

The cylinder shape was determined in a two step process.

2.2.0.1 physical technique

First the feed line was leveled using a water level, so that it was at a known height. The feed line was then made straight using a laser line. The distance of each end of the feed line was measured to each set of columns, and was made to be within about a half inch of centered and level. The surface was then adjusted to this feed position.

Cables were attached to the feed line at exactly the ground plane height, and each was measured out and marked a length for a specific parabolic arc length distance along the mesh. The cables were then dropped through the mesh at these positions, and the mesh was adjusted to the feed to get the desired focus position and shape. The East cylinder was fit to a 78 inch focus; the West to a 77 inch focus.

2.2.0.2 Optical Technique

The shape was determined using an optical technique. We set up a camera with a zoom lens about 150m away down the center line of the cylinder. Florescent flags were set up all along the cylinder, with different colors for each row. See examples in figure 2.19 and 2.20. The fits of the cylinder shapes are shown in figure 2.22 and 2.21.

Figure 2.19: East cylinder image used to fit the parabolic cylinder shape. The bottom of each florescent marker is marked with software and then fit to a parabola, assuming a 78 or 77 inch focus depending on the cylinder. The best fit focus is then marked on the image.

2.3 Focusing

The feed used has an expected focus center a bit behind the ground plane. This was calculated from nec2 simulations using cocoaNEC. In simulation the phase center

Figure 2.20: West cylinder image used to fit the parabolic cylinder shape. Camera is centered at the feed height.

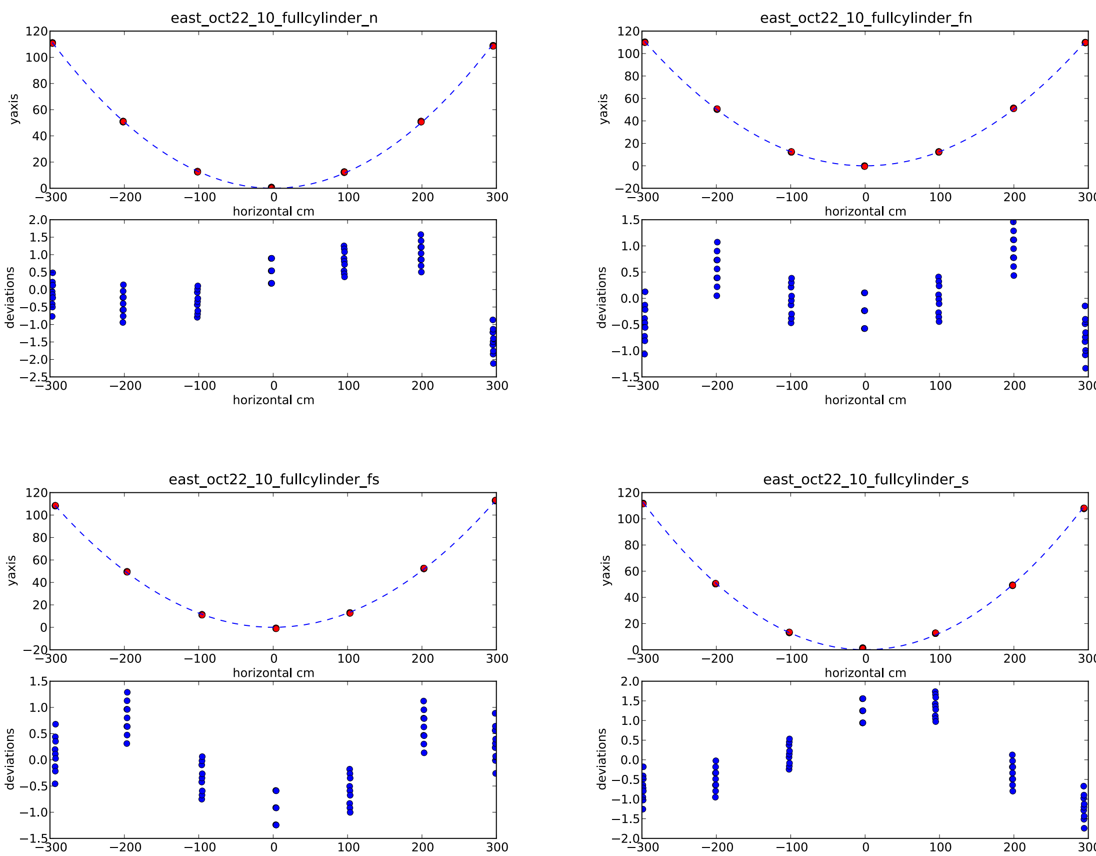

Figure 2.21: Fits to a 78 inch focus parabola for the east cylinder at 4 different locations along the North-South direction. Deviations are in centimeters. RMS less than a centimeter for these points.

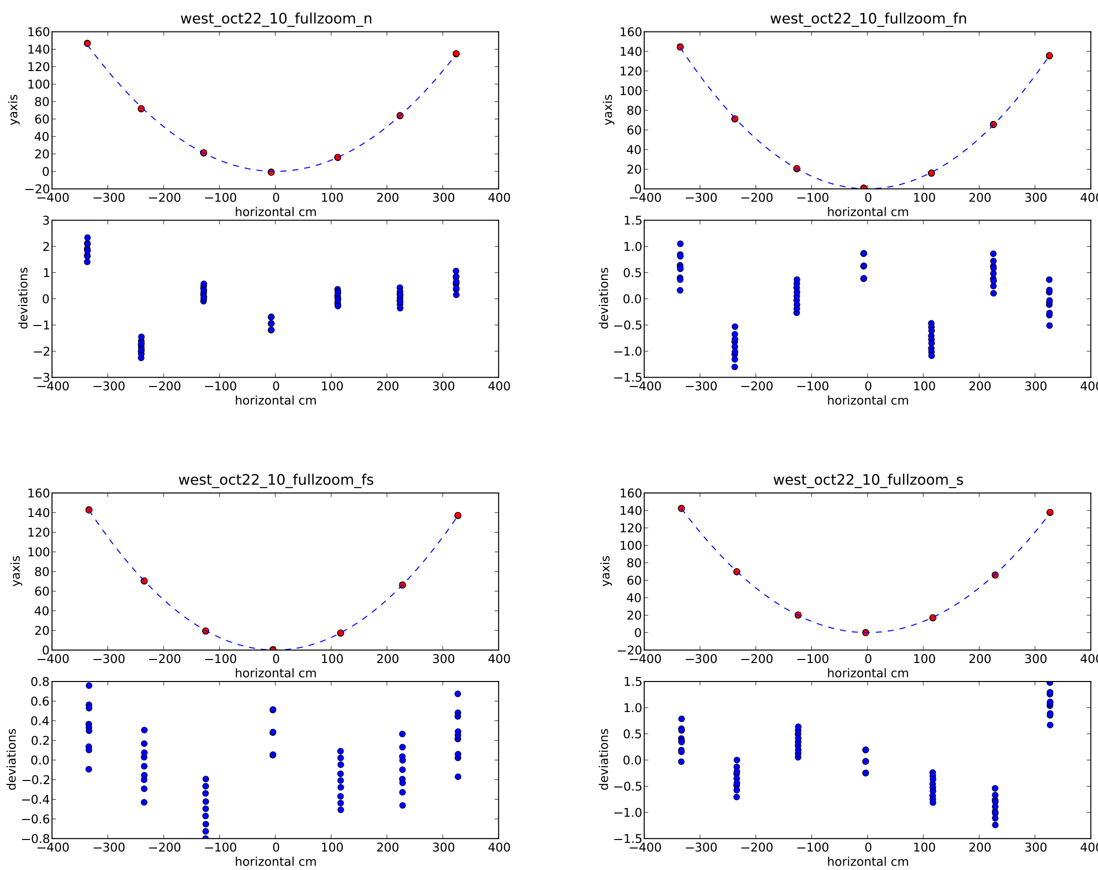

Figure 2.22: Fits to a 77 inch focus parabola for the west cylinder at 4 different locations along the North-South direction.

is 0.09λ behind the groundplane, however it was also relatively insensitive to the exact position. The output of the simulation gives a phase shift with angle from the center assuming that the phase center was the groundplane (the 0,0 coordinate of the simulation). The phase center from that point can then be calculated using:

$$d = \frac{\Delta\phi\lambda}{2\pi(1 - cos(\theta)} \tag{2.1}$$

where $\Delta\phi$ is the relative phase of that particular angle relative to the 0 angle phase, and θ is the angle from zero, see [25]. Using the average of this value over a given set of angles (Included angle of the dish) gives the phase center. I used $\pm 60^\circ$ to get the phase center of 0.09λ behind the ground plane, and was approximately the same for the longitudinal and transverse polarizations. figure 2.23 shows the phase variation when at the phase center. A general rule is that the phase changes less than 1/20th, or 18° to actually be contributing to collecting area.

A focus sweep was performed, and it was found that the transverse and longitudinal dipoles seemed to have different focus centers. In the end the focus was placed such that the transverse and longitudinal polarizations had equivalent gain.

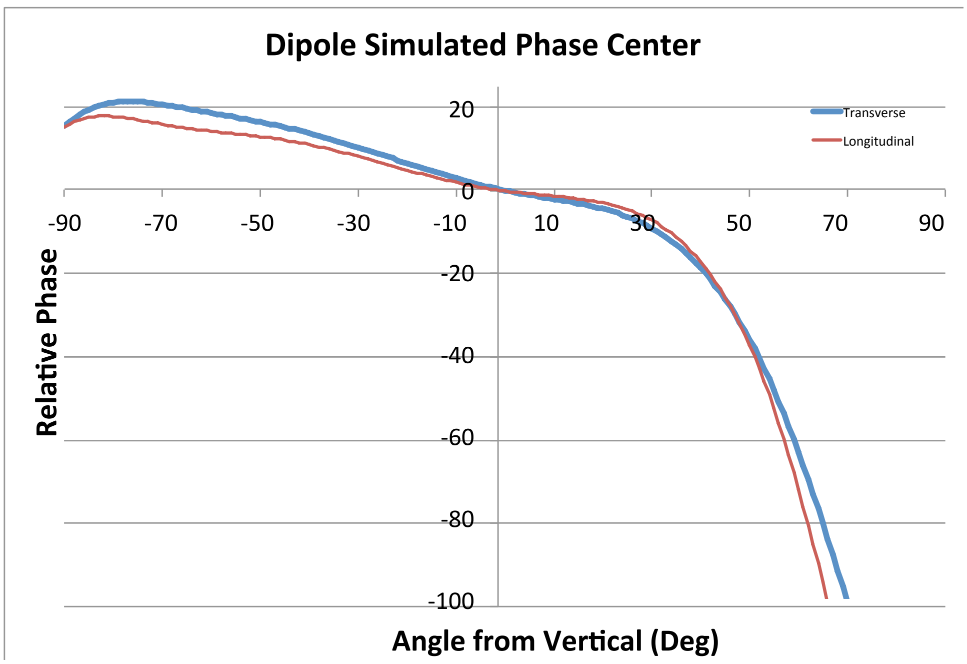

Figure 2.23: Phase change across angle given the simulated feed in figure 2.24a and 2.24b with the focus placed 0.09λ behind the ground-plane. A phase shift of $< 18^\circ$ is considered good. $\pm 45^\circ$ is well illuminated.

2.4 Cylinder and Feed Antenna Patterns

2.4.1 Feed Antenna Pattern

The feed antenna was modeled using cocoaNEC, which is a Numerical Electromagnetics Code (NEC) method of moments based os x application[2]. All elements were simulated using a mesh of wires. Simulations were done assuming an excitation current and transmission of the antenna, but due to reciprocity the receiving pattern is the same. An attempt was made to simulate accurately the geometry of the ground-plane and grounded cover of the LNA, and the differences between the longitudinal and transverse antennas. The feed dipole was tested in an anechoic chamber at CMU[3].

The model of the longitudinal antenna is shown in figure 2.24a. The transverse antenna is shown in figure 2.24b. An individual dipole was measured as shown in figure 2.25. The simulated antenna pattern is shown in figure 2.26b for the transverse dipole and in figure 2.26a for the longitudinal dipole. The measurement of the E-Plane response is shown in figure 2.27a, and the H-Plane response is shown in figure 2.27b. The simulated and measured patterns qualitatively match up well.

The impedance was also simulated and measured. The transverse and longitudinal simulated impedances are shown in figure 2.28. The measured antenna

[2] http://homepage.mac.com/chen/w7ay/cocoaNEC/index.html

[3] http://www.preal.ece.cmu.edu/

impedance is shown in figure 2.29. The dipole as tested is 9.5cm long and 5.28cm above the groundplane. No balun was used, the dipole is fed unbalanced. Measured performance matched well to simulations.

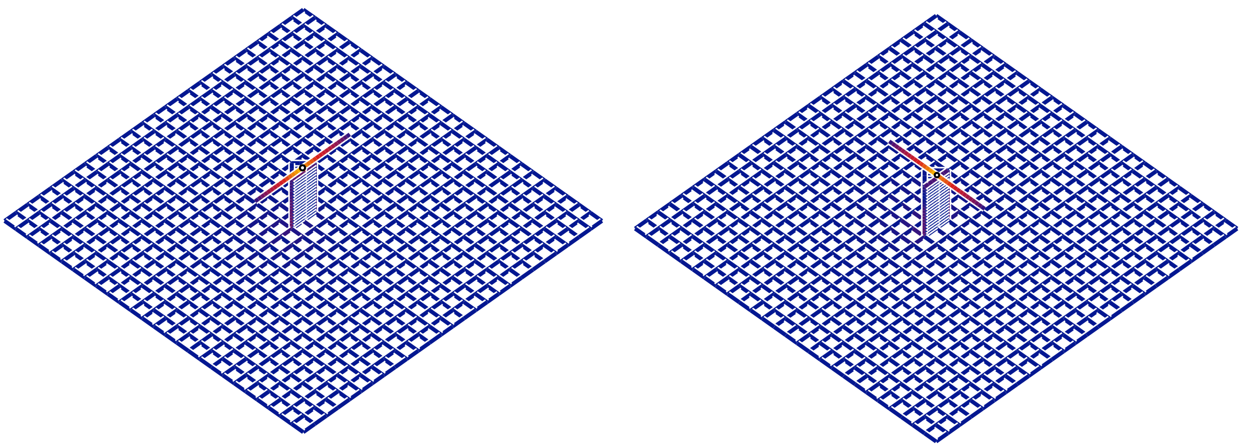

(a) longitudinal (b) transverse

Figure 2.24: Single dipole above ground-plane simulation layouts for a longitudinal (the dipole is aligned in the East-West direction) and transverse (the dipole is aligned North-South). The difference between the two polarizations is how the dipole interacts with the LNA ground shield.

The feed was also measured in an array configuration as used on the feed line. The full antenna with LNA was tested as used on the feedline. The system could not be calibrated for an absolute gain measurement since it was being used in reverse from standard, with the antenna under test receiving and the chamber antenna transmitting. The setup used is shown in figure 2.30. The antennas are set up with two polarizations, spaced 0.7λ apart, and the polarizations interleaved, such that spacing between channels is 0.35λ, where 1420 MHz was used as the reference frequency. The longitudinal polarization is the dipole which lies in the

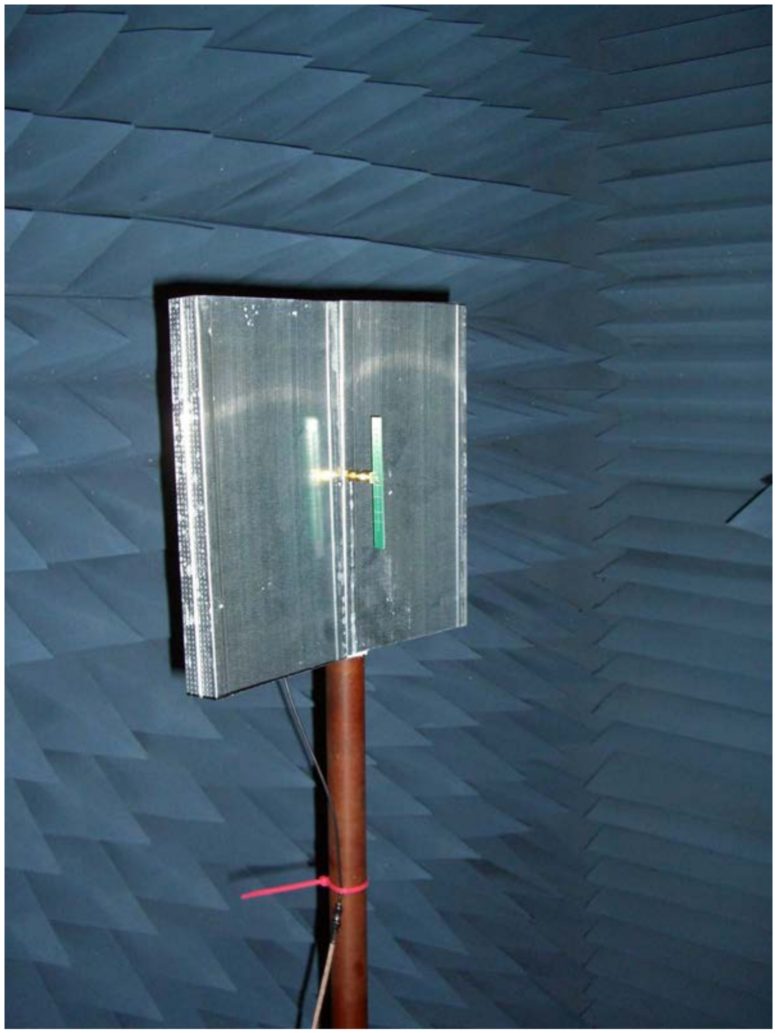

Figure 2.25: Single dipole above ground-plane in anechoic chamber. Shown in H-Plane measurement configuration. The antenna is rotated left-right. This setup was used to measure the pattern and impedance of a single dipole.

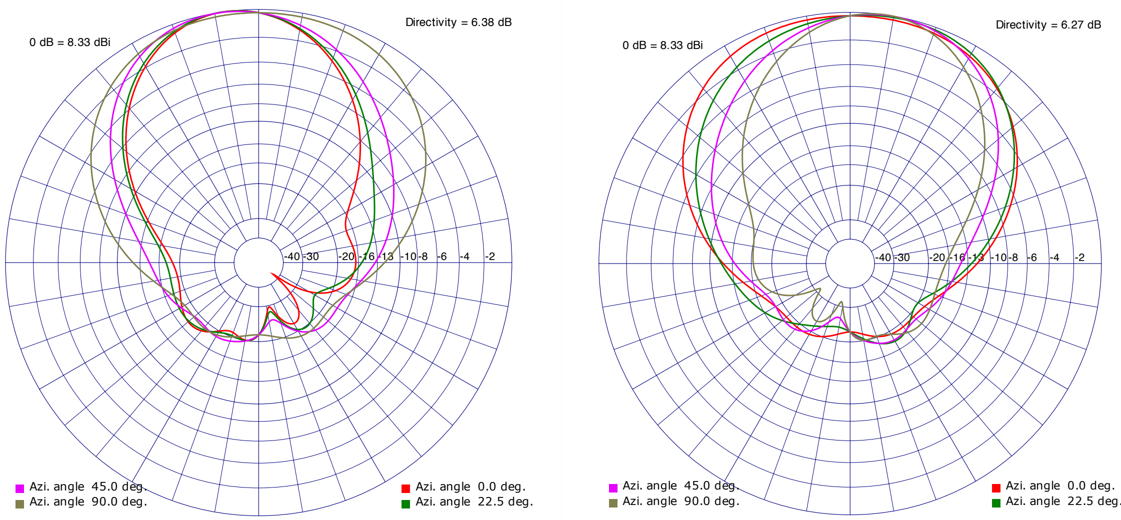

(a) longitudinal

(b) transverse

Figure 2.26: Simulated antenna pattern of a single dipole above ground-plane in the transverse and longitudinal direction. The simulation used an unbalanced dipole feed. The 0° angle is the E-plane, the 90° angle is the H-plane. Skewed pattern due to the feed being unbalanced and the asymmetry due to the LNA cover.

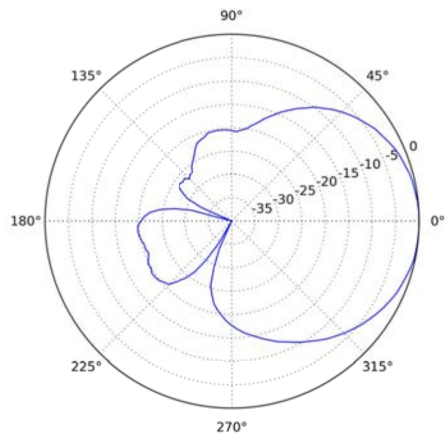

(a) E plane

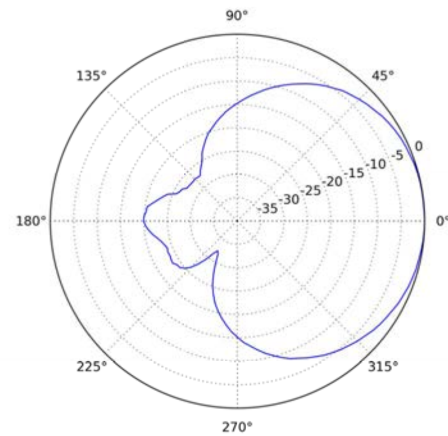

(b) H plane

Figure 2.27: Single dipole above ground-plane E-plane and H-plane pattern at 1.41 GHz. Testing the antenna shown in figure 2.25 but with the antenna rotated 90°(E-plane) or as shown (H-plane). The slight asymmetry in the pattern is due to the unbalanced feed. At 45° the pattern is down by 5db on one side, 7db on the other for the E-plane, 5db on both for the H-plane.

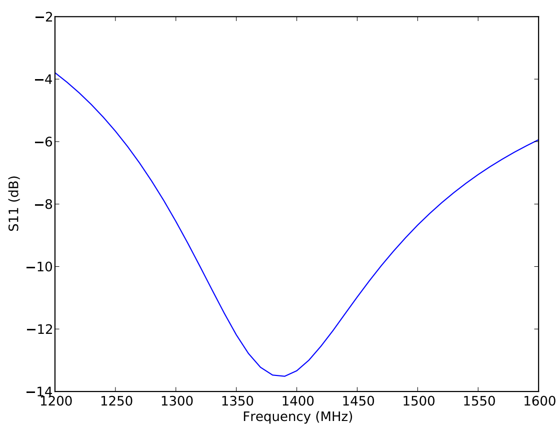

(a) longitudinal

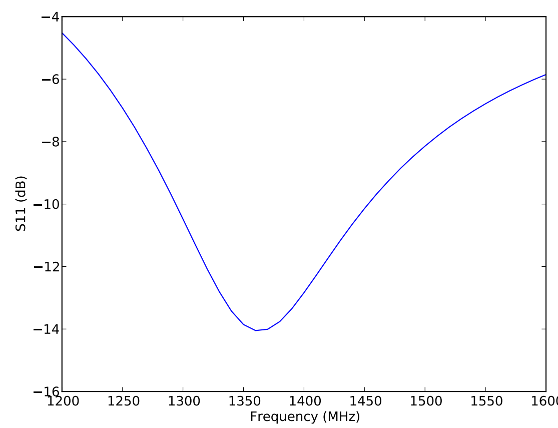

(b) transverse

Figure 2.28: Single dipole above ground-plane simulation input impedance for longitudinal and transverse orientations. We intentionally used a thin dipole to have a narrow response band. This helps immediately reject RFI at frequencies below 1 GHz. This impedance matches well to that measured as shown in figure 2.29

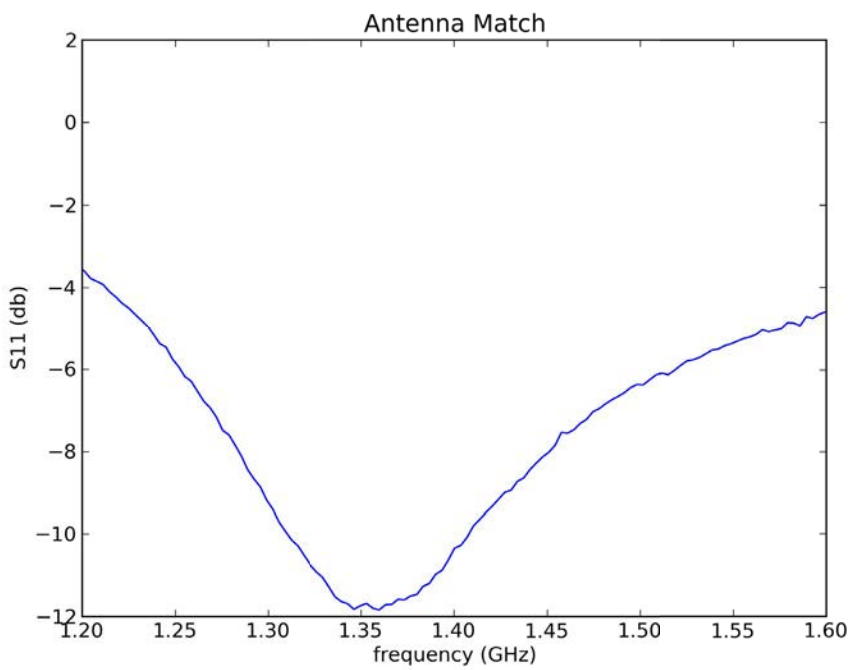

Figure 2.29: Single dipole above ground-plane impedance match (S11). Good performance from 1.30GHz to 1.42GHz

plane of the circuitboard. The transverse polarization is the one which lies transverse to the antenna circuit board. The transverse E-plane pattern is in figure 2.32. Figure 2.31 shows the transverse H-plane pattern. The longitudinal E-plane and H-plane patterns are in figure 2.34 and figure 2.33 respectively.

2.4.2 Modelled Cylinder Pattern

To model the cylinder pattern in the east-west direction, a 1-d model was used. The simulated feed pattern was assumed to be at the exact focus of the cylinder. Then a physical optics approximation ray tracing was done assuming a perfect parabola to an aperture plane. At many points along the aperture plane spherical waves were placed with amplitude and phase based on the ray-tracing and amplitude of the feed. For each angle the far field pattern was then calculated. For the perfect parabola with a blocked feed, the expected east-west pattern is shown in figure 2.35. The 3dB full width is $\sim 2^{\circ}$

To model the cylinder in the north-south direction, a phasing of dipoles above a ground-plane spaced by 0.7λ was simulated in cocoaNEC. The dipoles were phased together with a shift. The dipole gains were considered all the same value. This leads to the pattern shown in figure 2.36. The synthesized beam has a 3db full width of $\sim 5^{\circ}$. As can be seen from the figure, beyond $\pm 45^{\circ}$ from the zenith, the alias is in fact stronger than the pointing direction, and what will be seen in the image is not what is at the phased to pointing, but instead a point

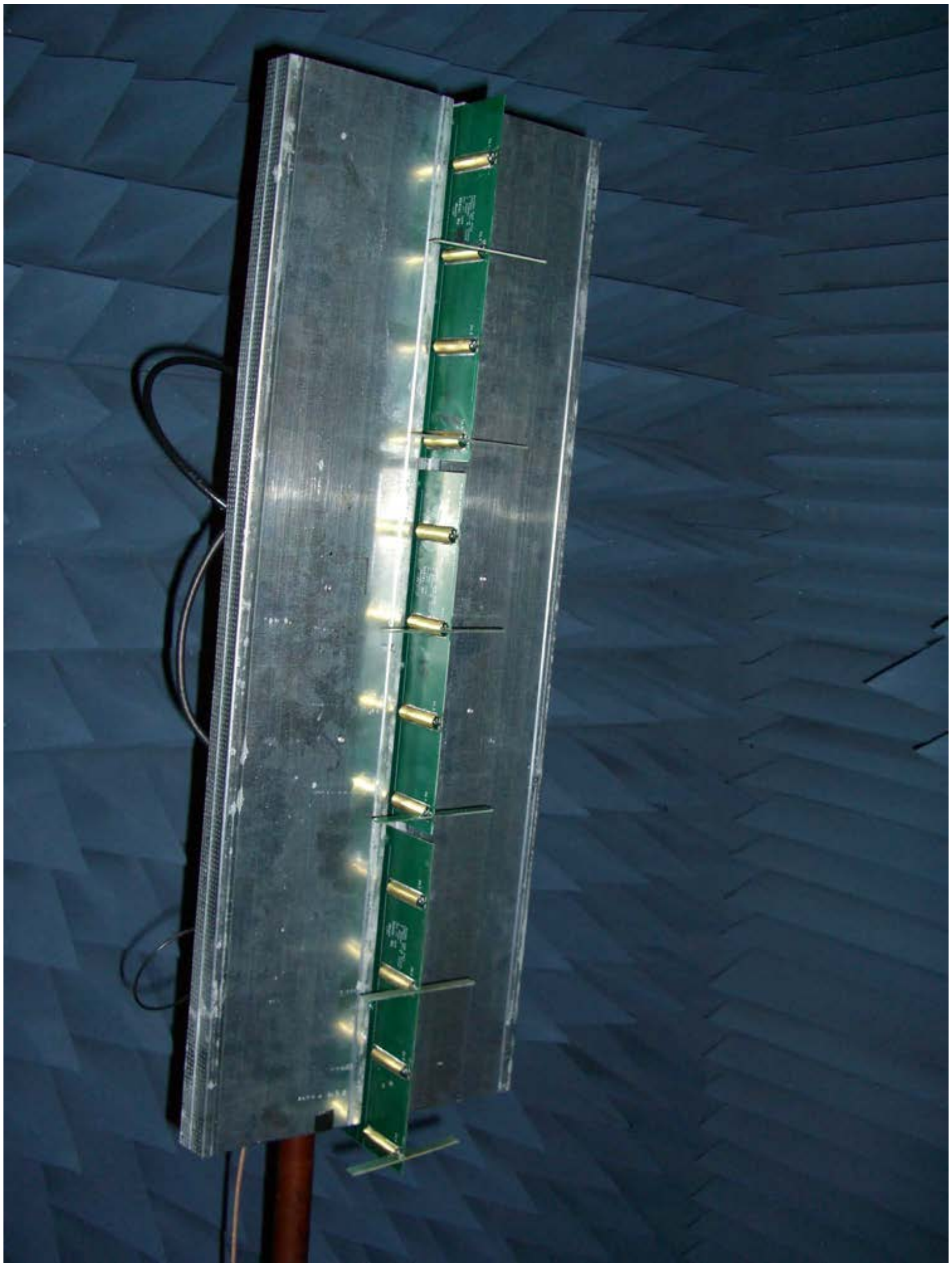

Figure 2.30: Antenna array in the anechoic chamber. The central antennas were tested (one of each polarization). The LNA was powered with a 9V battery for the test. The setup as shown was for the transverse polarization E-plane and the longitudinal polarization H-plane. The entire setup was rotated to test the transverse H-plane and longitudinal E-plane.

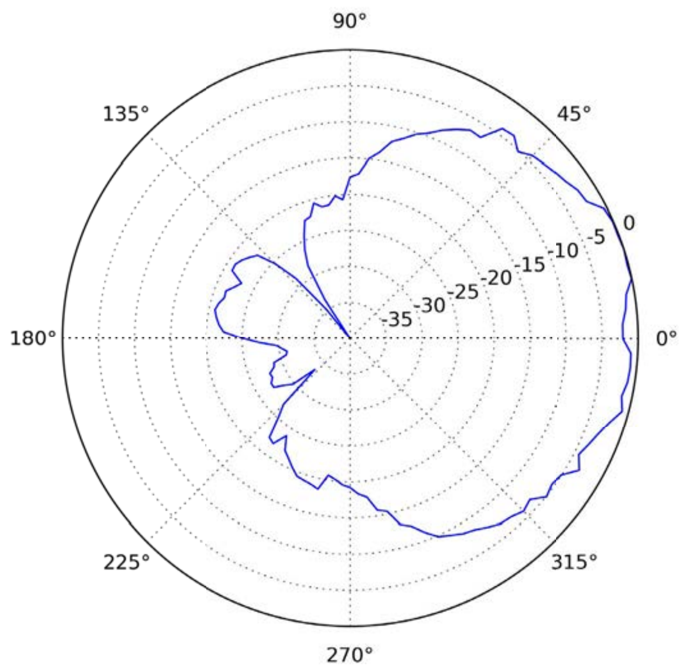

Figure 2.31: H-plane measurement of the antenna array transverse antenna . This configuration was physically rocking in the chamber as data was taken. This caused quite a bit of raggedness to the pattern. This raggedness is believed to be completely due to the setup of the chamber.

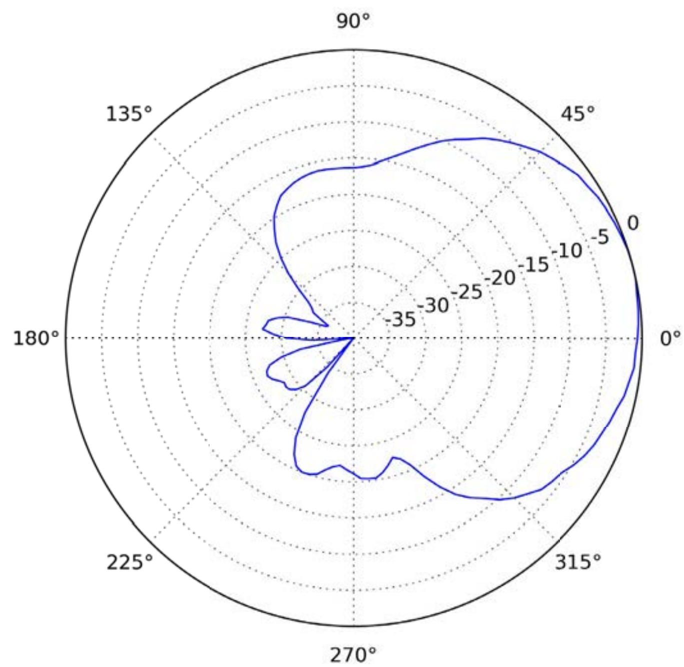

Figure 2.32: E-plane measurement of the antenna array transverse antenna . Pattern is slightly skewed. 5 dB down at 50° on one side and 35° on the other.

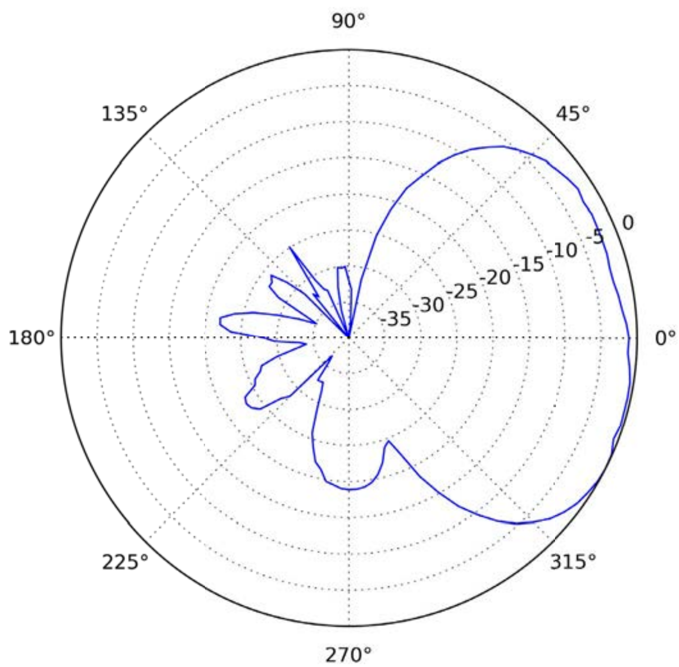

Figure 2.33: E-plane measurement of the antenna array longitudinal antenna . Slightly broader than the E-plane of the transverse antenna. Slightly broader than $\pm 45^{\circ}$ at the 5dB point.

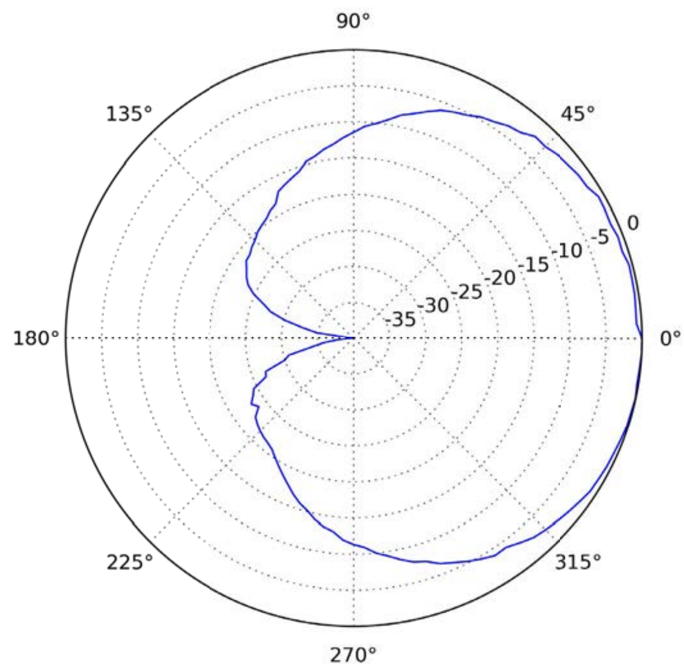

Figure 2.34: H-plane measurement Antenna array longitudinal antenna. Broadest pattern measured.

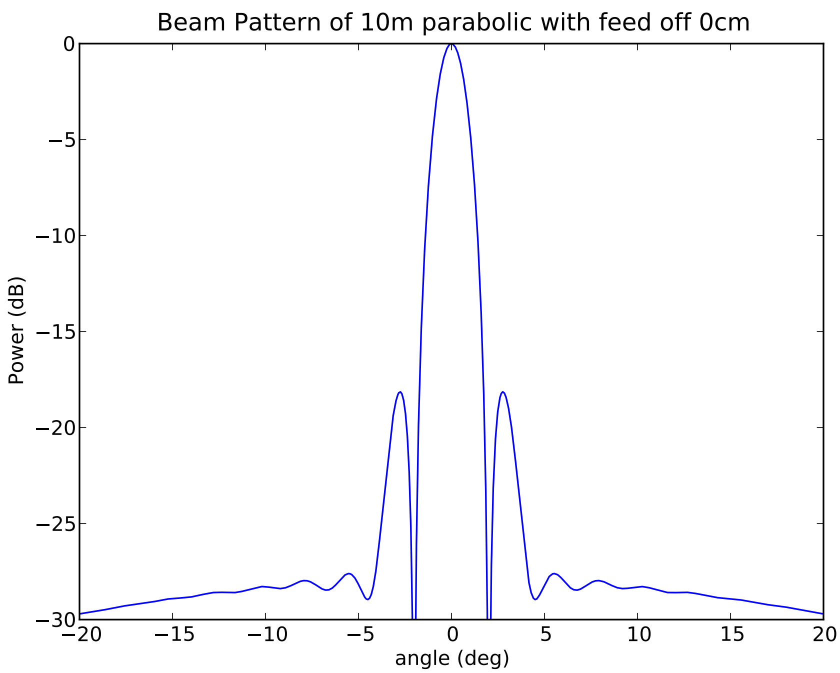

Figure 2.35: Simulated cylinder east-west response of a perfect parabola illuminated with the simulated feed pattern and with feed blockage. First side-lobes are ∼18 dB down, and the pattern hits a floor at ∼ -30 dB due to the blockage of the feed.

closer to the zenith on the opposite side. Thus the image in the center is aliased to the top and bottom of the image.

2.4.2.1 Window Function

The expected window function of a cos^2 illumination of two 10m cylinders 25m apart with the feed blocked is shown in figure 2.37, and the corresponding sky pattern is shown in figure 2.38. The north-south beam with cos^2 apodization of 16 elements with 0.7λ separation is shown in figure 2.39. The full 2d beam with 16 elements placed along the feed line 0.7λ apart is shown in figure 2.40.

2.4.3 Measured Cylinder Pattern and System Temperature

The East-West pattern of each individual dipole was measured with a total power measurement on the sun. The pattern of each dipole is shown in figure 2.47. These total power measurements are very sensitive to both RFI and gain fluctuations. As can be seen in many of the plots, there are gain jumps, which are generally due to strong RFI turning on and off.

This technique shows an enhancement of the noise from the sun on the level of 0.5 to 1dB. The half-power beamwidths range from about 1.7 degrees to 2.7 degrees. This range really is most likely due to the true cylinder pattern range from the shape of the cylinder at different locations. Those beamwidths correspond to an effective width using $W = \frac{\lambda}{\theta}$ of 7.2m to 4.5m. The system temperature was cal-

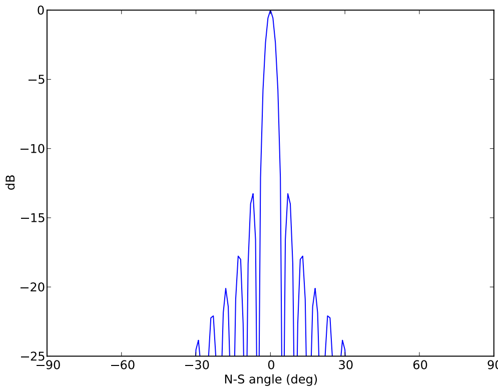

(a)

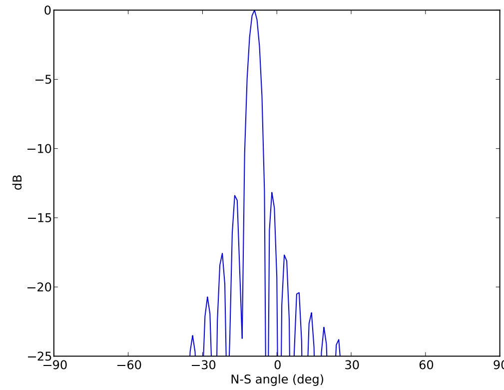

(b)

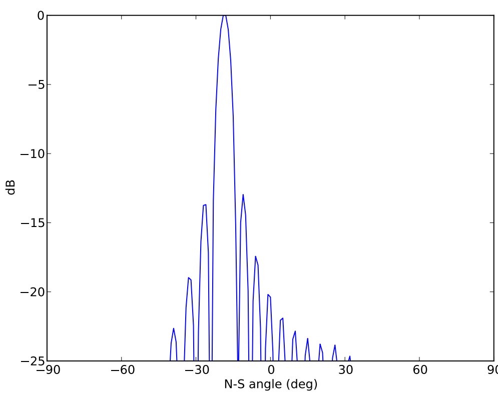

(c)

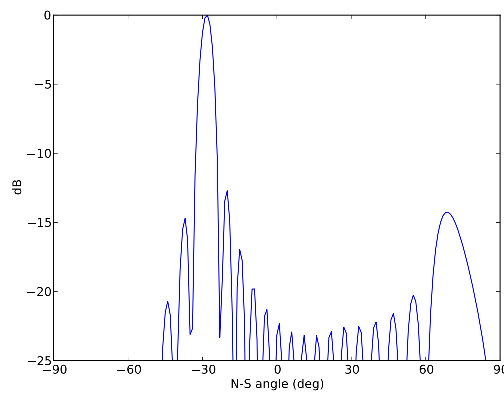

(d)

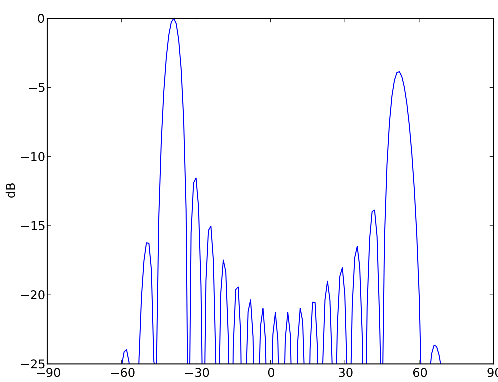

(e)

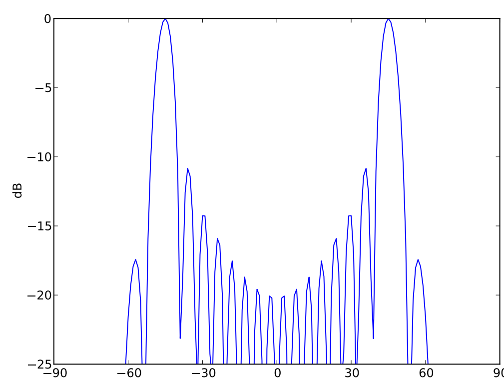

(f)

Figure 2.36: North-south simulated beam pattern. Simulated set of 16 dipoles phased together. Each plot shows a phase step of 40°. Steering the beam more than 45° away from the zenith results in an alias of the sky in the opposite direction.

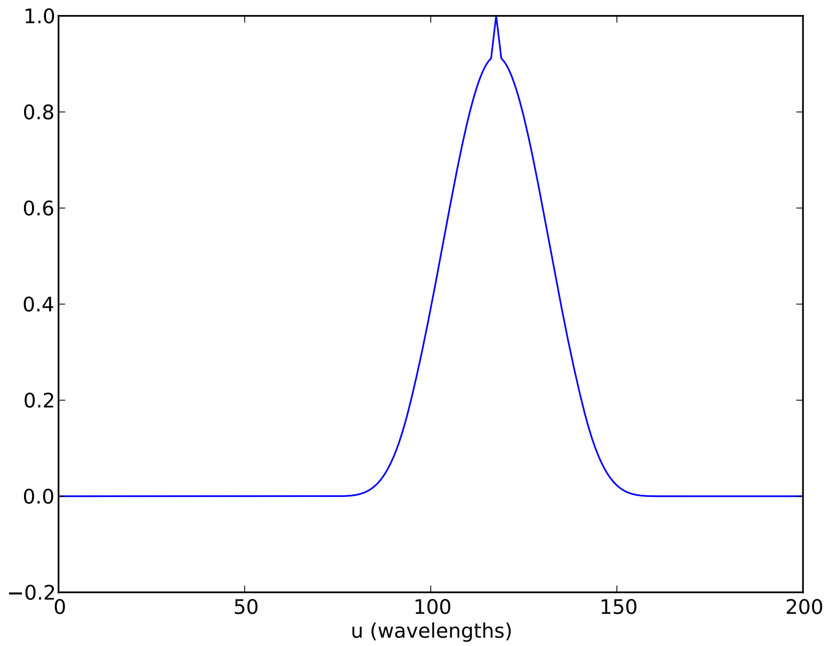

Figure 2.37: Window function of two cylinders 25m apart, with the feed blocking the aperture. Cylinders illuminated with cos^2 function and not the exact dipole pattern.

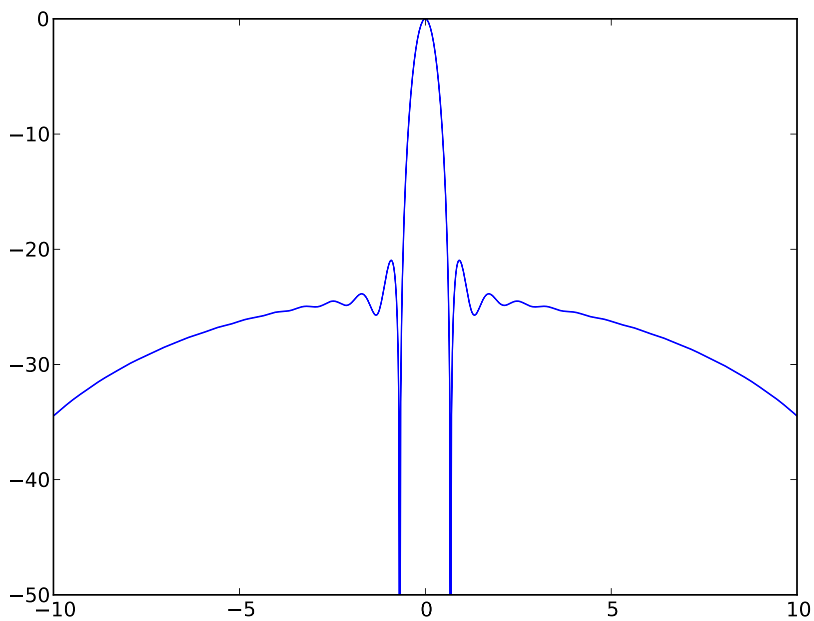

Figure 2.38: Fourier transform of window function east-west. Dirty beam in the east-west direction presuming a cos^2 illumination and not the actual dipole pattern. Very similar to the more accurate calculation in figure 2.35.

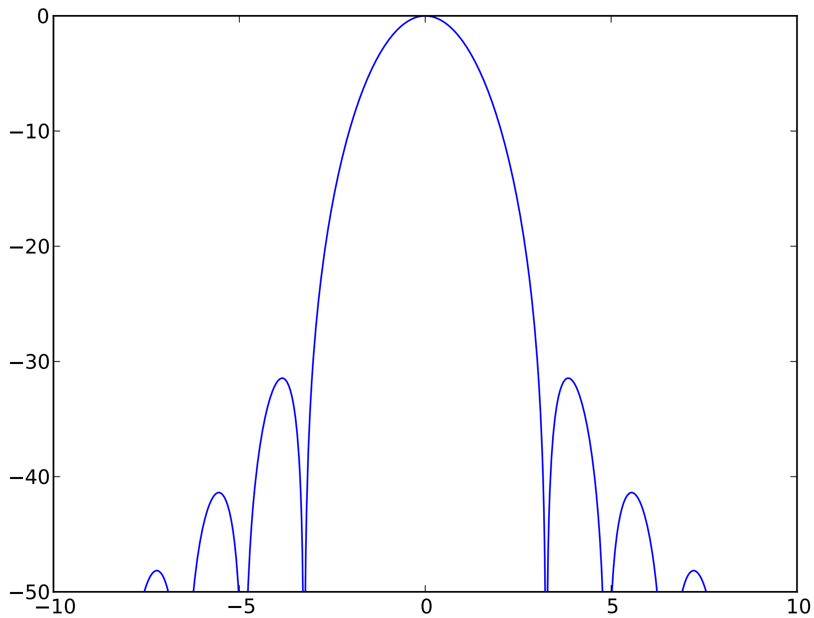

Figure 2.39: Fourier transform of window function in the North-South direction. Dirty beam North-South with cos^2 apodization. Broadens the beam but reduces the side-lobes.

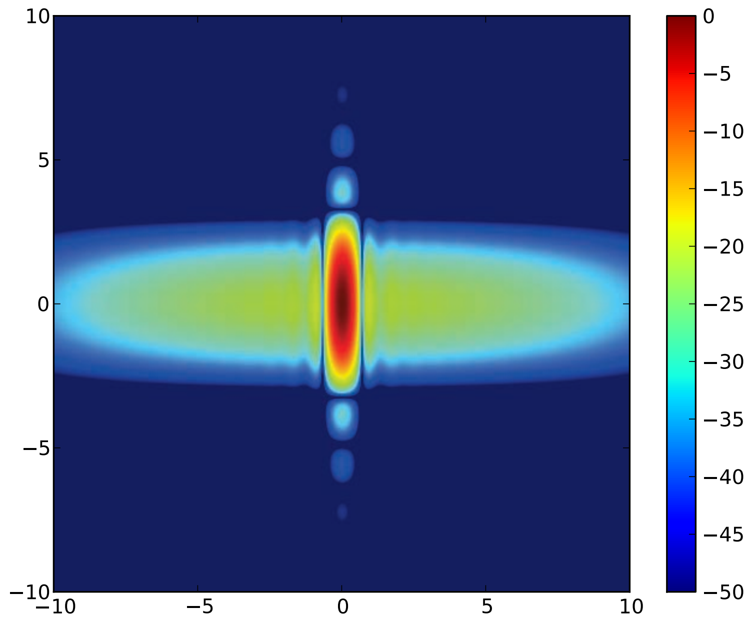

Figure 2.40: Fourier transform of window function. 2-D dirty beam of simulated aperture. Has a cos^2 apodization applied in the North-South direction, and an assumed cos^2 feed pattern in each cylinder.

culated in two ways for each autocorrelation. It was calculated using the deflection in total power from the sun:

$$T_{sys} = T_{sun}\left(\frac{off}{on - off}\right) \tag{2.2}$$

with on being time on the sun, off data taken off the sun, $T_{sun} = \frac{\lambda^2}{\Omega_{PB}2776}S_{sun}$, where λ is the wavelength, Ω_{PB} is the solid angle of the primary beam, S_{sun} is the flux of the sun in Janskys multiplied by the attenuation of the primary beam off center (I used 1.21×10^5 for the sun on that particular day). Using this method gets a T_{sys} in the 100K to 500K range.

The reason why the system temperature varies so much from channel to channel is not well understood. The bench measurements of every channel showed a similar noise figure for every channel, and at the level of 75K. Raising the system temperature to $\sim$ 100K is expected from ground-spill and the addition of the sky brightness.

The second method of measuring the system temperature was done using the signal to noise ratio:

$$T_{sys} = T_{sun}\left(\frac{\sqrt{\Delta\nu\Delta t}}{R_{SN}}\right) \tag{2.3}$$

where T_{sun} is the same as derived in the previous equation, $\Delta\nu$ is the bandwidth, Δt is the integration time, and R_{SN} is the ratio of the signal power to the

RMS of the noise level. The system temperature calculated using this method ranged from 300K to 1000K. The reason this noise level is higher is believed to be RFI. This is one area where the cylinder was not performing as well as expected. The Pittsburgh radio environment may well be too severe to get any better performance and system checks. Further tests are discussed in section 2.6.

Further complicating matters, the pointings of the centers of each of the dipoles does not necessarily line up. Seen in the plots in figure 2.47, the red vertical line corresponds to the actual position of where the sun is crossing the meridian. Figures 2.41 and 2.42 plot the pointing center for the East and West cylinders respectively, each plot broken up by polarization. These plots show that the pointing center for the two different polarizations is different by approximately one degree. However, looking at figures 2.43 and 2.44, one can see that this pattern was very repeatable, and the East and West cylinders were both adjusted such that they are both pointed at the same place for a given polarization. As seen in figures 2.45 and 2.46 the beamwidths of the two polarizations were not systematically different, if anything the transverse dipoles have a slightly smaller beamwidth. Looking at the measured beam patterns of the feed, the transverse dipole pattern across the cylinder, shown in figure2.32 has a 3db full width of less than 90°. The longitudinal pattern across the cylinder, shown in figure 2.33 is slightly wider. One would expect the longitudinal dipoles to have a slightly smaller beam pattern than the transverse dipoles, but if anything the opposite is true. This may well be due to

#	T_{sys} via Deflection	T_{sys} via SN	ratio
1	3219.	553.1	5.82
2	368.6	1626.	0.22
3	663.0	1683.	0.39
4	325.0	5336.	0.06
5	120.3	158.3	0.76
6	505.3	850.0	0.59
7	494.2	538.9	0.91
8	168.0	1079.	0.15
9	608.8	916.1	0.66
10	2536.	1067.	2.37
11	348.4	1022.	0.34
12	287.8	1129.	0.25
13	463.6	625.9	0.74
14	482.7	865.0	0.55
15	321.3	324.4	0.99
16	2862.	1607.	1.78
17	1334.	940.0	1.41
18	296.1	1061.	0.27
19	2036.	523.1	3.89
20	862.8	929.0	0.92
21	229.8	417.7	0.55
22	410.9	1217.	0.33
23	413.6	818.1	0.50
24	630.9	1579.	0.39
25	121.0	1325.	0.09
26	855.1	1406.	0.60
27	310.4	609.0	0.50
28	117.8	355.2	0.33
29	240.7	327.8	0.73
30	780.1	676.9	1.15
31	865.7	3083.	0.28
32	405.0	272.7	1.48

Continued on next page

Continued from previous page			
#	T_{sys} via Deflection	T_{sys} via SN	ratio
33	226.0	520.5	0.43
34	1282.	837.4	1.53
35	313.1	635.8	0.49
36	4115.	1243.	3.30
37	356.6	859.4	0.41
38	299.1	698.6	0.42
39	382.7	434.3	0.88
40	331.6	603.0	0.54
41	555.2	559.6	0.99
42	283.4	626.7	0.45
43	6.087	770.2	0.00
44	377.3	409.3	0.92
45	126.3	1747.	0.07
46	179.6	390.8	0.45
47	274.6	510.8	0.53
48	286.8	548.3	0.52
49	264.1	704.1	0.37
50	205.7	779.3	0.26
51	834.2	1162.	0.71
52	167.1	330.2	0.50
53	339.9	268.0	1.26
54	331.0	848.8	0.38
55	1903.	835.5	2.27
56	312.0	470.3	0.66
57	239.4	723.6	0.33
58	244.5	646.8	0.37
59	167.9	397.3	0.42
60	283.7	964.6	0.29
61	181.5	1285.	0.14
62	353.9	577.6	0.61
63	298.8	517.8	0.57
64	370.6	1221.	0.30

Table 2.1: T_{sys} calculated using the deflection from the sun and via the signal to noise. The number calculated from the sun deflection is in general 1/2 to 1/3 that calculated using the signal to noise ratio. This implies the noise floor is dominated by RFI.

the cylinder having a less perfect shape further away from the center, or to slightly different phase centers for the two polarizations.

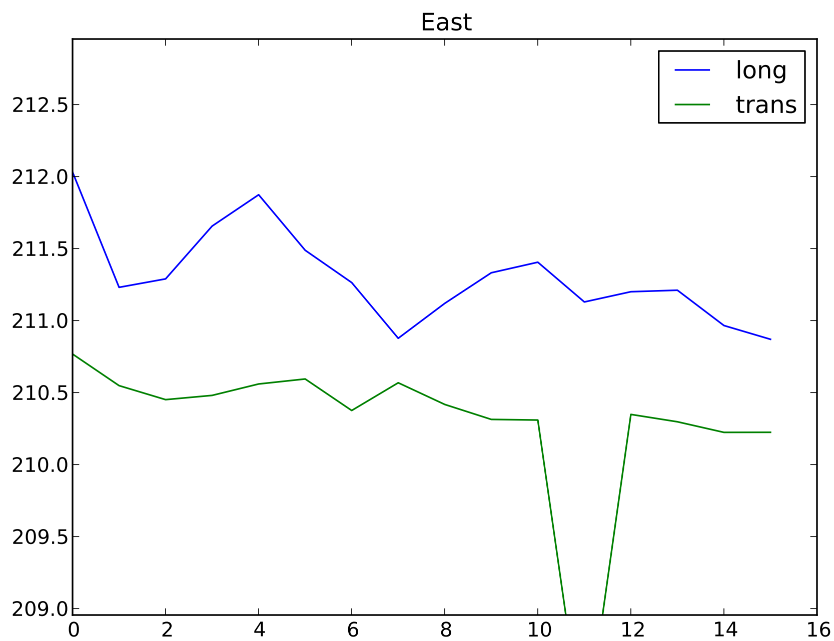

Figure 2.41: Pointing of each dipole on the East cylinder. Broken into transverse and longitudinal polarizations. The transverse and longitudinal pointing centers are a degree off from each other for the same cylinder.

2.5 Pittsburgh RFI Mitigation

Early tests were plagued by RFI contamination. The first attempts at unfiltered LNA's and Receivers were overloaded by tv signals. In the northern direction there are tv towers in direct line of sight of the feeds. These signals are transmitting 1 MWatt power in the 700MHz range, and are required to have harmonics down by

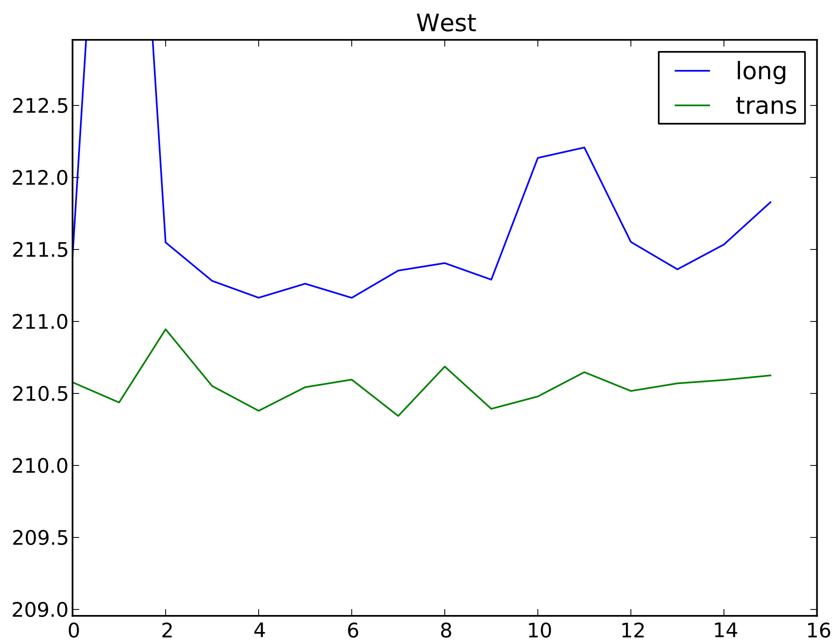

Figure 2.42: Pointing of each dipole on the West cylinder. Broken into transverse and longitudinal polarizations. Again the pointing centers for the two polarizations are different by about one degree in the same way.

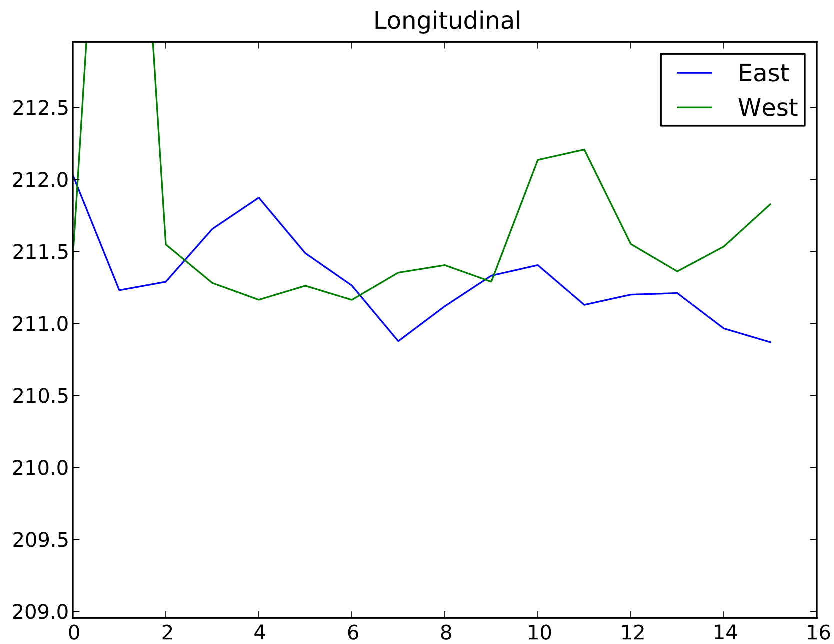

Figure 2.43: Pointing of each longitudinal dipole. Plotting East and West cylinders on top of one another. The within polarization centers are well matched.

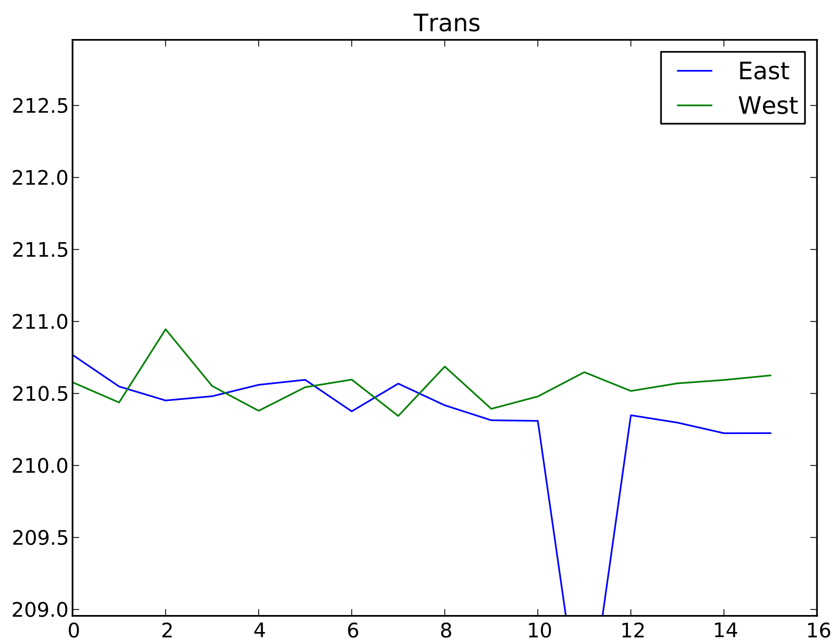

Figure 2.44: Pointing of each transverse dipole. Plotting East and West cylinders on top of one another. Again the pointing of the transverse dipoles are well matched for the east and west cylinders.

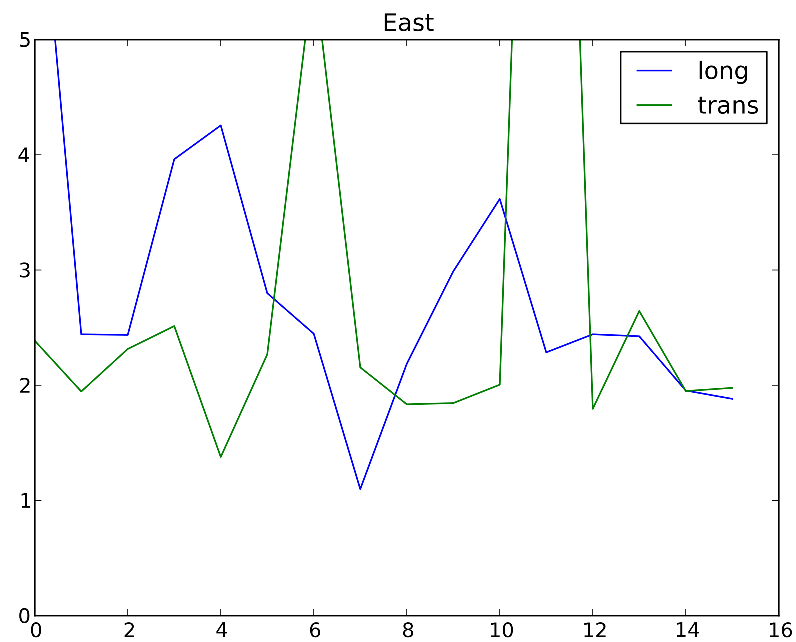

Figure 2.45: Full width half maximum (FWHM) of each dipole on the East cylinder. Broken into transverse and longitudinal polarizations. Both polarizations have a similar beam-width.

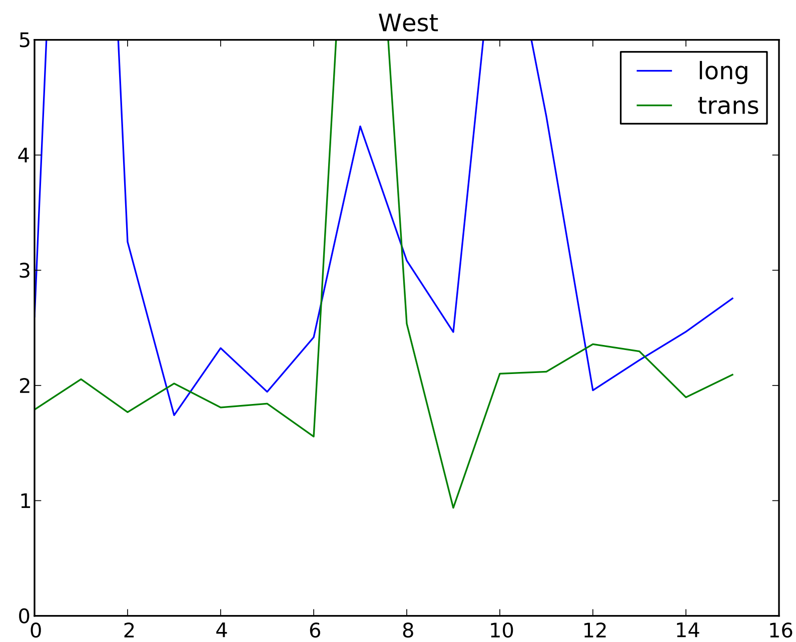

Figure 2.46: Full width half maximum (FWHM) of each dipole on the West cylinder. Broken into transverse and longitudinal polarizations. Again, both polarizations have a similar beam-width.

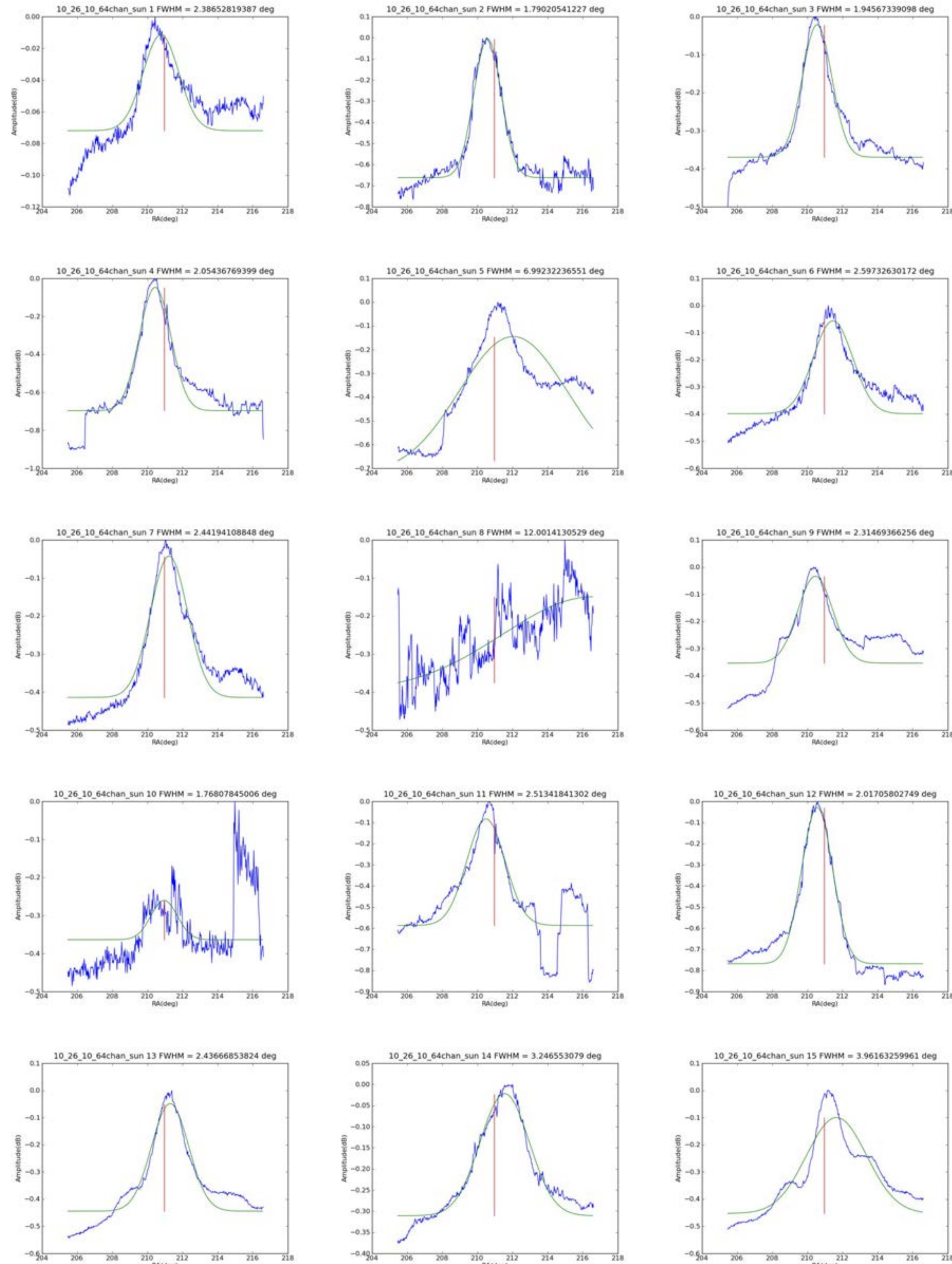
10_26_10_64chan_sun 1 FWHM = 2.38652819387 deg
10_26_10_64chan_sun 2 FWHM = 1.79020541227 deg
10_26_10_64chan_sun 3 FWHM = 1.94567339098 deg
10_26_10_64chan_sun 4 FWHM = 2.05436769399 deg
10_26_10_64chan_sun 5 FWHM = 6.99232236551 deg
10_26_10_64chan_sun 6 FWHM = 2.59732630172 deg
10_26_10_64chan_sun 7 FWHM = 2.44194108848 deg
10_26_10_64chan_sun 8 FWHM = 12.0014130529 deg
10_26_10_64chan_sun 9 FWHM = 2.31469366256 deg
10_26_10_64chan_sun 10 FWHM = 1.76807845006 deg
10_26_10_64chan_sun 11 FWHM = 2.51341841302 deg
10_26_10_64chan_sun 12 FWHM = 2.01705802749 deg
10_26_10_64chan_sun 13 FWHM = 2.43666853824 deg
10_26_10_64chan_sun 14 FWHM = 3.246553079 deg
10_26_10_64chan_sun 15 FWHM = 3.96163259961 deg
Amplitude(dB)
RA(deg)

Figure 2.47

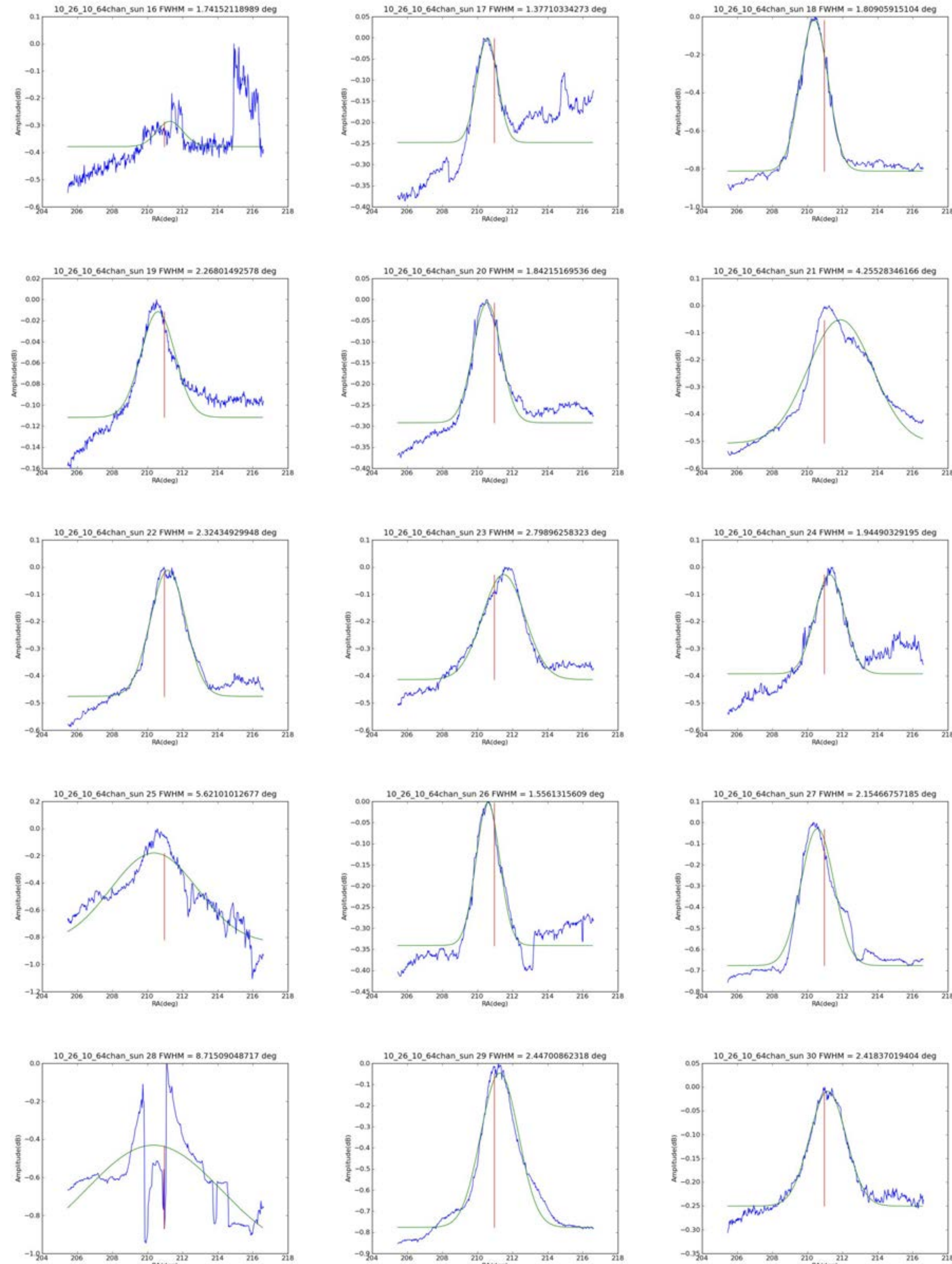
10_26_10_64chan_sun 16 FWHM = 1.74152118989 deg
10_26_10_64chan_sun 17 FWHM = 1.37710334273 deg
10_26_10_64chan_sun 18 FWHM = 1.80905915104 deg
10_26_10_64chan_sun 19 FWHM = 2.26801492578 deg
10_26_10_64chan_sun 20 FWHM = 1.84215169536 deg
10_26_10_64chan_sun 21 FWHM = 4.25528346166 deg
10_26_10_64chan_sun 22 FWHM = 2.32434929948 deg
10_26_10_64chan_sun 23 FWHM = 2.79896258323 deg
10_26_10_64chan_sun 24 FWHM = 1.94490329195 deg
10_26_10_64chan_sun 25 FWHM = 5.62101012677 deg
10_26_10_64chan_sun 26 FWHM = 1.5561315609 deg
10_26_10_64chan_sun 27 FWHM = 2.15466757185 deg
10_26_10_64chan_sun 28 FWHM = 8.71509048717 deg
10_26_10_64chan_sun 29 FWHM = 2.44700862318 deg
10_26_10_64chan_sun 30 FWHM = 2.41837019404 deg
Amplitude(dB)
RA(deg)

Figure 2.47

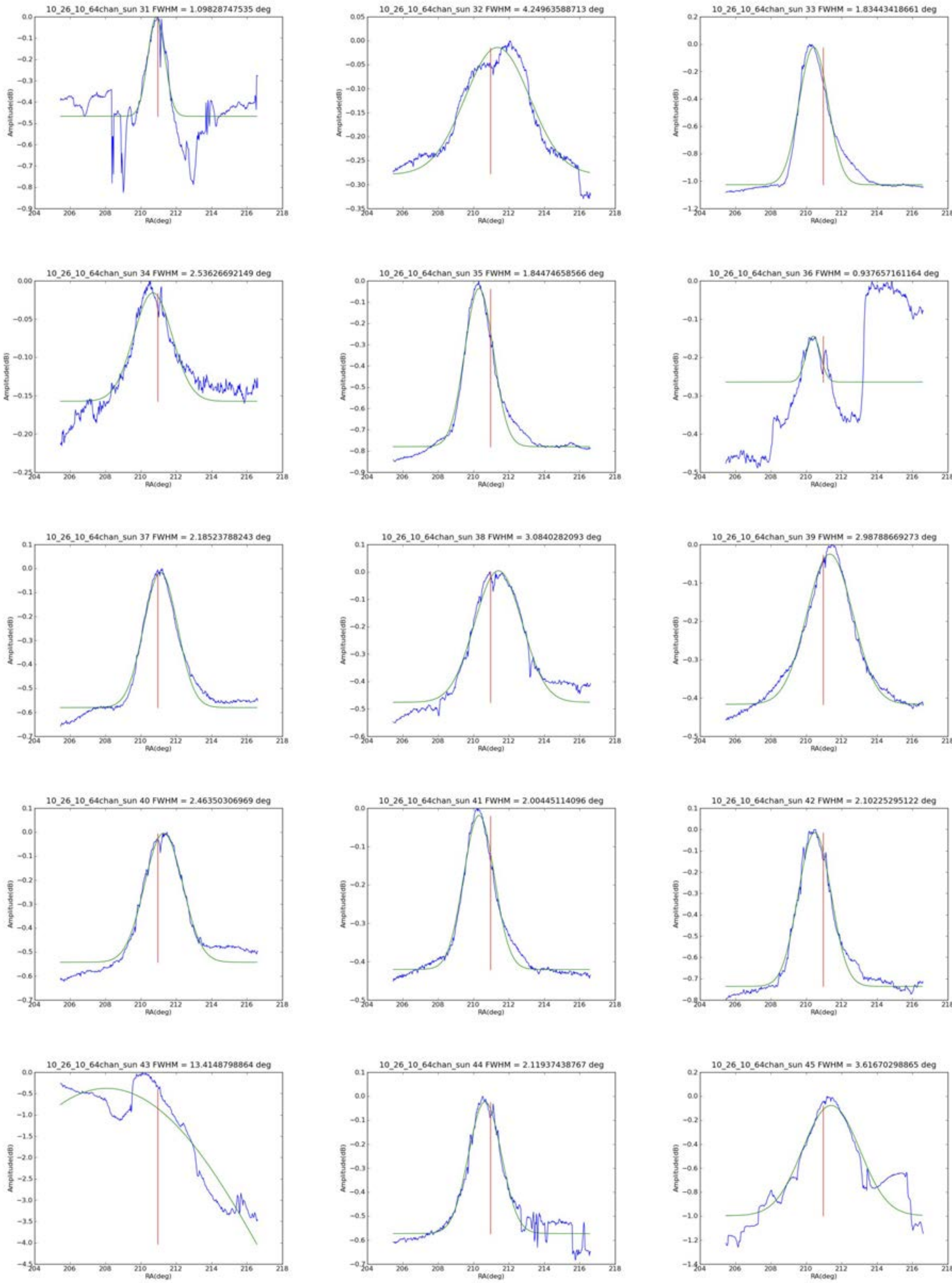
10_26_10_64chan_sun 31 FWHM = 1.09828747535 deg
10_26_10_64chan_sun 32 FWHM = 4.24963588713 deg
10_26_10_64chan_sun 33 FWHM = 1.83443418661 deg
10_26_10_64chan_sun 34 FWHM = 2.53626692149 deg
10_26_10_64chan_sun 35 FWHM = 1.84474658566 deg
10_26_10_64chan_sun 36 FWHM = 0.937657161164 deg
10_26_10_64chan_sun 37 FWHM = 2.18523788243 deg
10_26_10_64chan_sun 38 FWHM = 3.0840282093 deg
10_26_10_64chan_sun 39 FWHM = 2.98788669273 deg
10_26_10_64chan_sun 40 FWHM = 2.46350306969 deg
10_26_10_64chan_sun 41 FWHM = 2.00445114096 deg
10_26_10_64chan_sun 42 FWHM = 2.10225295122 deg
10_26_10_64chan_sun 43 FWHM = 13.4148798864 deg
10_26_10_64chan_sun 44 FWHM = 2.11937438767 deg
10_26_10_64chan_sun 45 FWHM = 3.61670298865 deg
Amplitude(dB)
RA(deg)

Figure 2.47

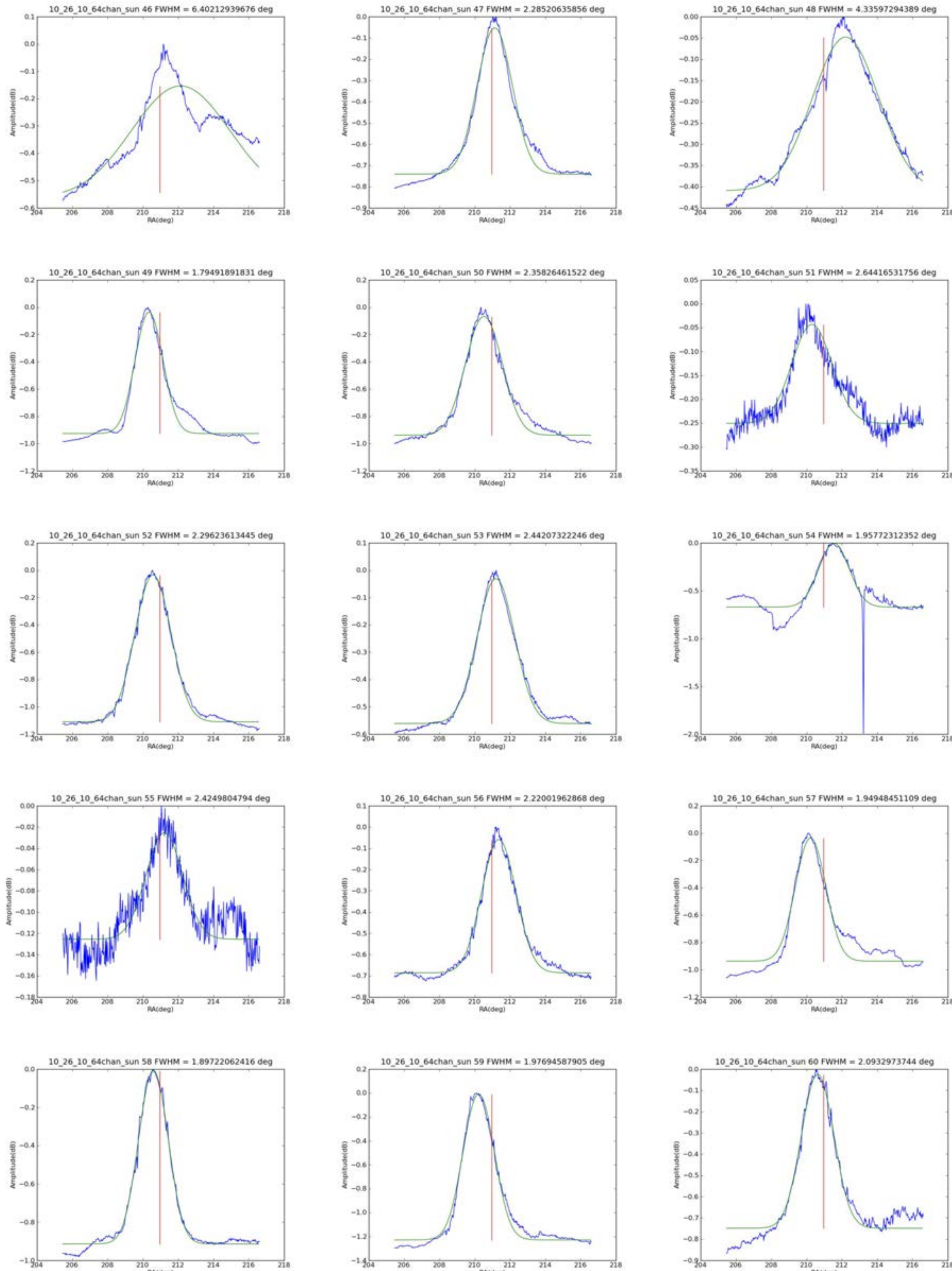
10_26_10_64chan_sun 46 FWHM = 6.40212939676 deg
10_26_10_64chan_sun 47 FWHM = 2.28520635856 deg
10_26_10_64chan_sun 48 FWHM = 4.33597294389 deg
10_26_10_64chan_sun 49 FWHM = 1.79491891831 deg
10_26_10_64chan_sun 50 FWHM = 2.35826461522 deg
10_26_10_64chan_sun 51 FWHM = 2.64416531756 deg
10_26_10_64chan_sun 52 FWHM = 2.29623613445 deg
10_26_10_64chan_sun 53 FWHM = 2.44207322246 deg
10_26_10_64chan_sun 54 FWHM = 1.95772312352 deg
10_26_10_64chan_sun 55 FWHM = 2.4249804794 deg
10_26_10_64chan_sun 56 FWHM = 2.22001962868 deg
10_26_10_64chan_sun 57 FWHM = 1.94948451109 deg
10_26_10_64chan_sun 58 FWHM = 1.89722062416 deg
10_26_10_64chan_sun 59 FWHM = 1.97694587905 deg
10_26_10_64chan_sun 60 FWHM = 2.0932973744 deg
Amplitude(dB)
RA(deg)

Figure 2.47

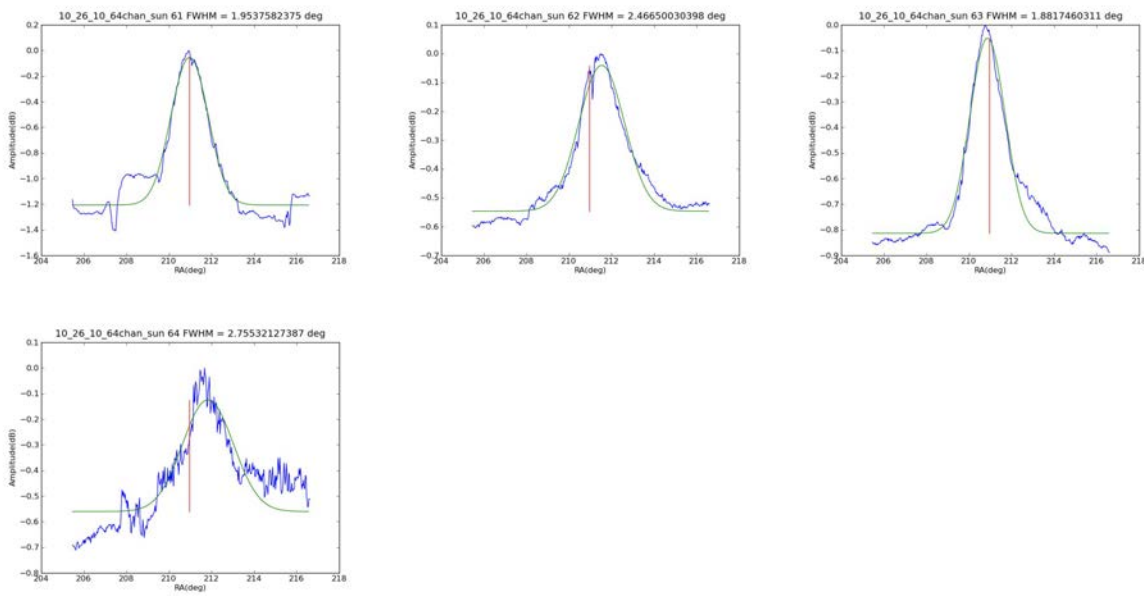

Figure 2.47: East-West beam pattern of each individual dipole. Blue lines are the data. Red line is where the sun passes the meridian and should be the peak of the data. Green line is the gaussian best fit to the data.

10^6, however that is still 1 Watt transmitted directly in our passband.

In order to deal with the RFI two techniques were used. The first was to erect a mesh ground screen on the north end of the cylinders to get rid of line of sight transmission. The second was to put a 1200MHz high pass filter as the first thing before any amplification. This hurts the noise figure, but was required to not overload the first amplifier.

2.6 Correlated Noise and RFI

An experiment was conducted with neighboring feeds. One feed used was a longitudinal dipole built into the antenna card. The other had the antenna removed and an SMA connector attached instead. See figure 2.48 for an image of the setup. During a continuous set of data taking, the SMA connector was open, which gives a close measurement to the amplifier noise contribution, was terminated with a 75Ω load, this gives a ∼300K load on the amplifier, and had an antenna connected, which was approximately $\frac{1}{2}\lambda$ from the groundplane, so did not have a proper match or pattern compared to the others. The continuum averaged result is plotted in figure 2.49. The load measurement was presumed to be 300K, so the amplitude scaling is referenced to that. What can be seen from this plot is an amplifier noise level of $\sim 120K$, which is very flat with time, giving a equivalent noise figure using the signal to noise level. When the antenna is connected, the level of the power goes down, to give a measurement of 200K using the overall power level, but giving a T_{sys} of 1000K using the RMS. This implies that RFI is raising the noise floor, even with only ~ 1 second of integration.

Figure 2.48: Setup for testing the noise figure of the LNA's in the cylinder. Shown with 75Ω load attached to the SMA connecter instead of an antenna.

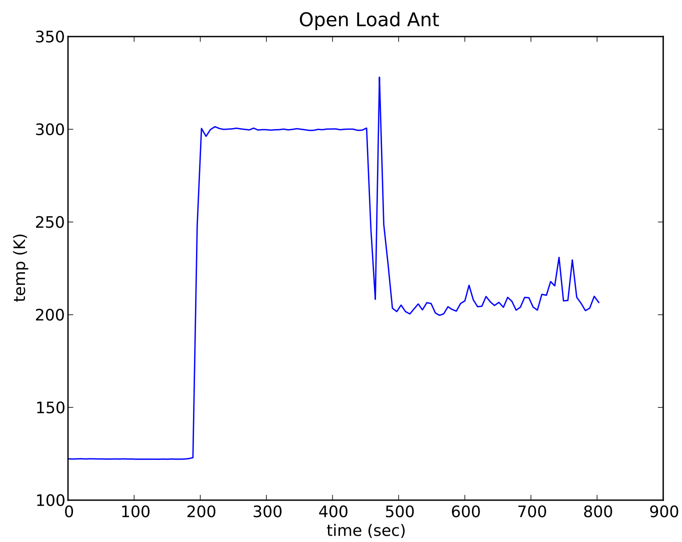

Figure 2.49: Test with LNA open, with 75Ω load, and antenna attached. With the LNA open, the curve is very flat and at a level of $\sim$ 125K. Connecting the load puts the temperature at 300K by definition, but the curve is still very flat. Connecting the antenna, the noise level goes down to about 200K and the fluctuations of the noise become very visible.

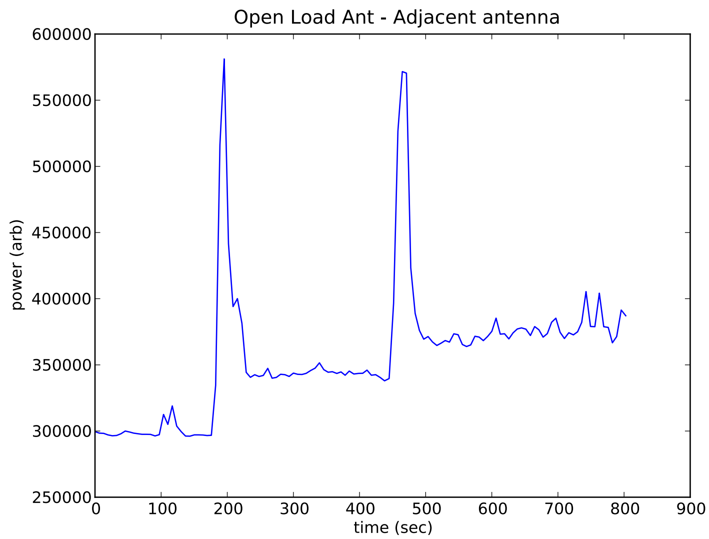

Figure 2.50: Test with LNA open, with 75Ω load, and antenna attached. Measurement with the longitudinal antenna directly adjacent to the channel being manipulated. The power level with time shows visible fluctuations throughout the test. The noise level goes up with the load attached, and up further when the antenna is attached to the adjacent LNA channel. The correlation between the fluctuations is visible when the antenna is attached, implying they are both receiving RFI. Noise increased by 15% when adjacent antenna is attached.

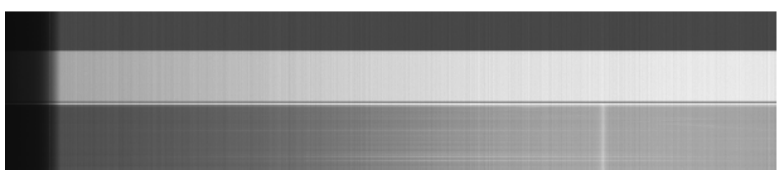

Figure 2.51: Test with LNA open, with 75Ω load, and antenna attached. Waterfall plot with time on the vertical axis and frequency on the horizontal. Broad horizontal structures only visible in the bottom third section when the antenna is connected.

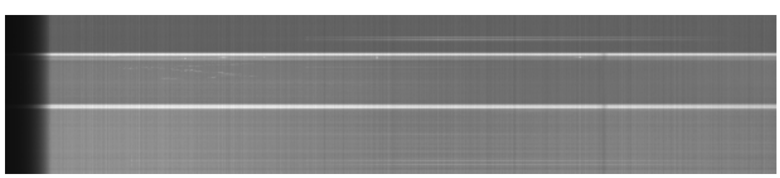

Figure 2.52: Test with LNA open, with 75Ω load, and antenna attached. Measurement with the adjacent antenna. Broad horizontal structures visible in all three sections, presumably broad band RFI.

3

Cylinder Imaging

Synthesis imaging in radio astronomy involves taking a sparsely sampled aperture and turning it into an approximate image expected from sampling the entire aperture.

The electric field at a position $\vec{r}$ from a source at very far distance at location $\vec{r}_p$ is given by:

$$E(\vec{r}) = \int \epsilon(\vec{r}_p) \frac{e^{i2\pi\nu|\vec{r}-\vec{r}_p|/c}}{|\vec{r}-\vec{r}_p|} dS \tag{3.1}$$

with $\epsilon(\vec{r}_p)$ the electric field at the emitted location. The visibility for two receivers at $\vec{r}_1$ and $\vec{r}_2$ is given by:

$$V(\vec{r}_1, \vec{r}_2) = \langle E(\vec{r}_1) E^*(\vec{r}_2) \rangle \tag{3.2}$$

assuming again the source is far away, we write the visibilities as:

$$V = \int_{4\pi} A_N(\boldsymbol{\sigma}) I(\boldsymbol{\sigma}) e^{-i2\pi \mathbf{D}_\lambda \cdot \boldsymbol{\sigma}} d\Omega \tag{3.3}$$

where V is the complex visibility, A_N is the normalized antenna pattern, $I(\mathbf{œ})$ is the source intensity $\langle \epsilon^2 \rangle$, $\mathbf{D}_\lambda$ is the baseline vector between antennas in wavelengths and sigma is the vector to the element of solid angle from the pointing center.

This can be rewritten as:

$$V(u,v) = \int \int A_N(l,m) I(l,m) e^{i2\pi(ul+vm)} dl dm \tag{3.4}$$

and

$$I'(l,m) = A_N(l,m) I(l,m) = \int \int V(u,v) e^{-i2\pi(ul+vm)} du dv \tag{3.5}$$

where l is $\sin(\theta)$ and m is $\sin(\phi)$

We don't actually know a true visiblility, but a measured visibility. The assumed relationship is:

$$\hat{V}_{ij} = g_i g_j^* V_{ij} + n_{ij} \tag{3.6}$$

where $g = ae^{\phi}$ is the complex gain of the telescope and n is the noise term.

solving for the complex gains gives a solution for the true visibilities which is:

$$V_{ij} = \frac{\hat{V}_{ij}}{g_i g_j^*} \tag{3.7}$$

The visibilities can then be used to solve for an intensity pattern on the sky. The gains are either solved for each baseline independently, writing $g_i g_j^* = g_k$, or is $g_i g_j^*$ solved for each gain.

The most straightfoward imaging is:

$$I_D(\theta, \phi) = \sum_{ij} w_{ij} V_{ij} e^{-i2\pi(u_{ij}l + v_{ij}m)} \tag{3.8}$$

where ij is all possible baselines (i and j) and w_{ij} is an apodization function

$I_D = P(\theta, \phi) \otimes I'(\theta, \phi)$ is the sky intensity modified by the antenna beam convolved with the dirty beam defined as:

$$P(l, m) = \sum_{ij} w_{ij} e^{-i2\pi(u_{ij}l + v_{ij}m)} \tag{3.9}$$

3.0.1 Cleaning

The clean algorithm was first developed by Högbom [33], and further refined by Clark [15] and again by Cotton and Schwab [61] [19]. Refinements are still under active developemnt [18]. The algorithm assumes that the images is made of a sum of point sources. Choose the brightest sources, and subtract at a known position:

$$I_R = I_D - \sum_i B_i P_i \tag{3.10}$$

where the sum is over the locations, B is the intensity of the source, and P is the dirty beam of a point source at that location. Can continue to identify and subtract point sources until the entire map left is considered noise like. The map is then the sum of all the identified point sources, usually smoothed with a gaussian of the primary beam.

3.1 Calibration

Cylinder calibration using the point source Cygnus A. This is a least squares matrix method of calibration.

The eigenvalues and eigenvectors of a matrix is usually given by:

$$Ax_k = \lambda_k x_k \tag{3.11}$$

$$(A - \lambda_k I)x_k = 0 \tag{3.12}$$

which is the same as:

$$A = P\Lambda P^{-1} \tag{3.13}$$

where P is the set of Column eigenvectors x_k and Λ is a diagonal matrix with eigenvalues λ_k along the diagonal.

If A is Hermitian then P is a Unitary matrix, and we can write eqn 3.13 as:

$$A = P\Lambda P^{\dagger} = \sum_k \lambda_k x_k x_k^{\dagger} \tag{3.14}$$

for a point source at a at given (l',m') $I = I_S\delta(l', m')$. Looking at eqn 3.4 V is then

$$V(u, v) = A_N(l', m')I_S e^{i2\pi(ul'+vm')} \tag{3.15}$$

Multiplying each visibility by $e^{-i2\pi(ul'+vm')}$ will result in all of the visibilities being a constant. If this point source dominates the Visibilities it can be used for calibraiton. Comparing equation 3.6 and 3.14, the eigenvector corresponding to the largest eigenvalue of the Visibility matrix is the complex gain solution g. The remaining eigenvalues/vectors correspond to the remaining noise. All of this is ambiguous to an overall normalization.

$$\hat{V} = \lambda_1 x_1 x_1^{\dagger} + \sum_{k>1} \lambda_k x_k x_k^{\dagger} = gg^* V + N \tag{3.16}$$

This calibration technique was applied using Cygnus A as the phase center, since it nearly passes overhead at the center of the telescope pointing. For our cylinder telescope the cross-cylinder visibilities are much cleaner than the within cylinder visibilities. For this reason instead of using the measured visibilities for calibrating, they were filled with an initial guess, the complex gains were solved for and subbed back into the equation, and this was iteratively solved until the solution converged on a value, or the solution stopped improving the the residual visibility defined as:

$$r = \sum |V_{ij} - g_i g_j^*| \quad (3.17)$$

This solution was calculated independently for the two different polarizations. The resulting calibration matrix is shown in figure 3.1 for the longitudinal polarization and in figure 3.3 for the transverse polarization. The comparison of the cross-cylinder visibilities direct baseline solution (V_{ij}) and the antenna based solution ($g_i g_j^*$) is shown in figure 3.2 and 3.4 for the longitudinal and transverse polarizations respectively. The spread here shows how well the cylinders are actually calibrated. In the case of the longitudinal polarization the results are quite good. The transverse polarization results are less impressive.

The stability of the calibration is plotted in figures 3.5 and 3.6 for the gain and phase of the two polarizations. For the longitudinal polarization the solutions over multiple days were the same to a few percent. The transverse polarization amplitudes were stable to 5-10%, but the phase had more variation.

By changing the weighting in equation 3.9 one can control the beam shape. The best images are weighted by the gain/noise estimates for each visibility, using all visibilities. Figure 3.7 shows a equal weighting of all visibilities measured, which is close to what the noise weighted image should be. Other possible weights

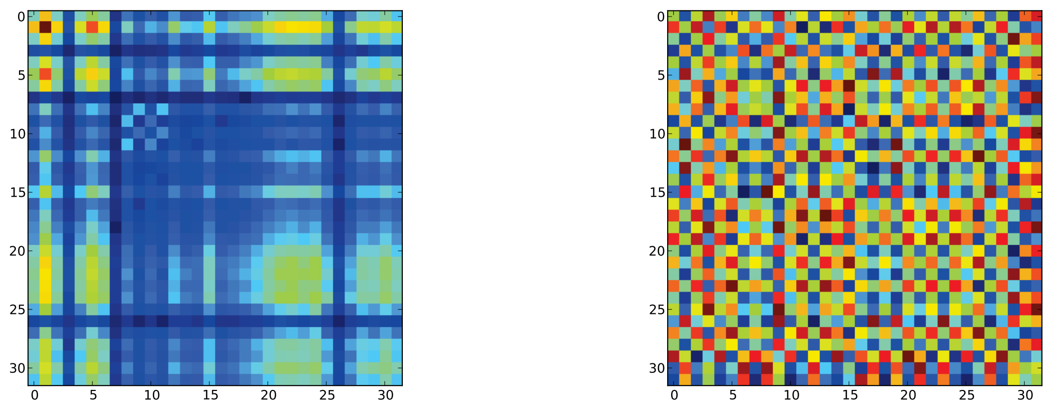

(a) Gain (b) Phase

Figure 3.1: Longitudinal antenna based visibility gain and phase matrix. Is a Hermitian matrix. Ordered alternatively East and West visibility, or within cylinder/cross cylinder visibilities.

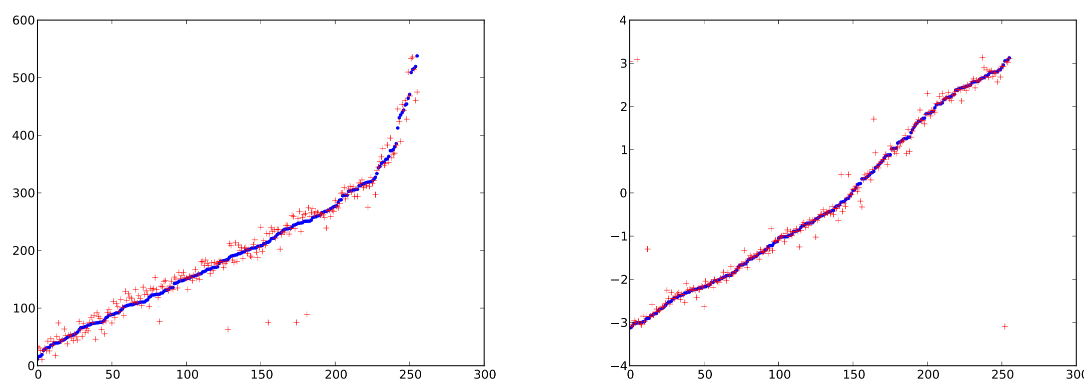

(a) Gain (b) Phase

Figure 3.2: Longitudinal visibility gain and phase antenna based comparison to measured visibilities. Blue points are the gain/phase solved for using an individual baseline. The red points are the computed visibility gain and phase based on that calculated from individual antenna gains and phases.

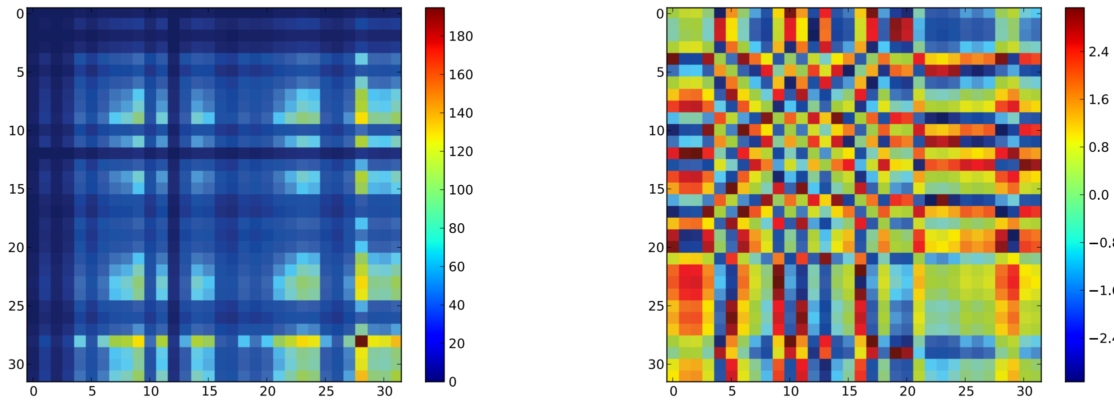

(a) Gain (b) Phase

Figure 3.3: Transverse visibility gain and phase antenna based matrix. Appears to have more phase structure than the longitudinal solution.

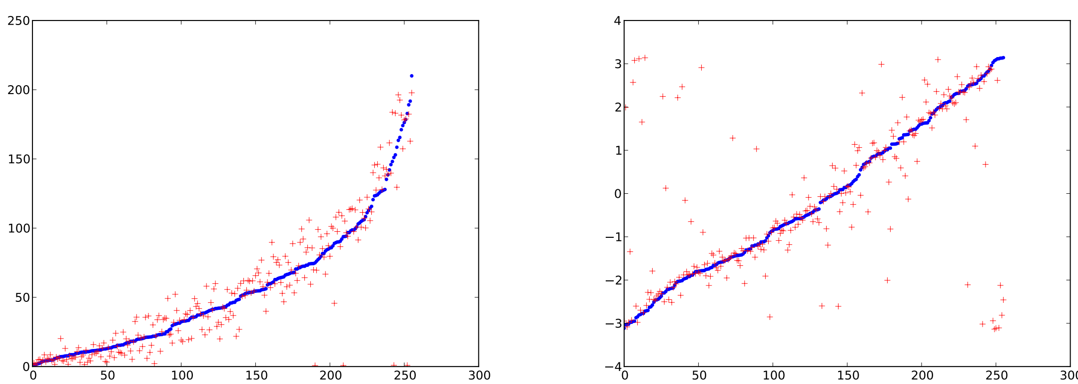

(a) Gain (b) Phase

Figure 3.4: Transverse visibility gain and phase showing the difference between the antenna based visibility gain and phase (red points) to baseline based visibilities (blue points). Much higher spread in the solution compared to the longitudinal polarization.

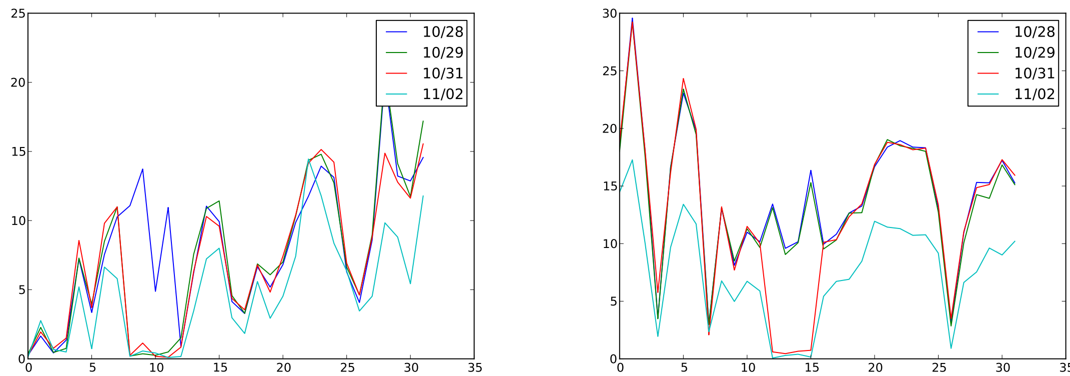

(a) Transverse

(b) Longitudinal

Figure 3.5: Gain vs. dipole number. Solution calculated using Cygnusa A repeated on four successive days. Most feeds in the longitudinal polarization were stable to a few percent. The fourth day the gain for all channels was much lower. The transverse polarization was stable to 5-10 percent.

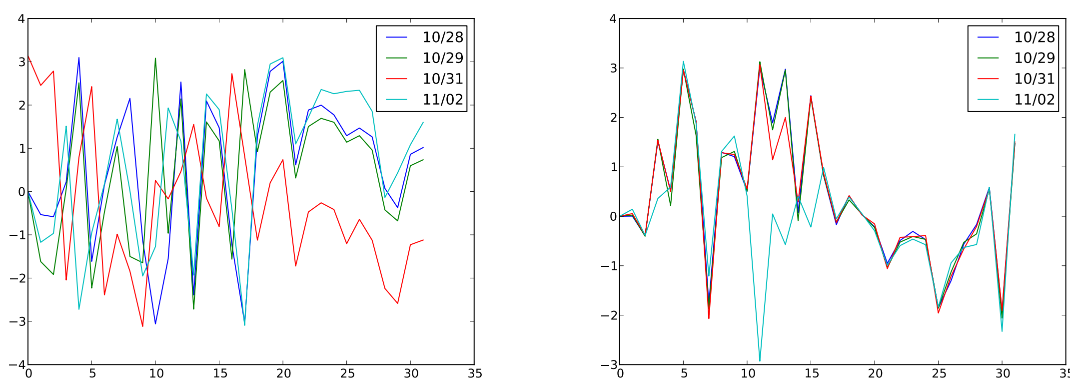

(a) Transverse

(b) Longitudinal

Figure 3.6: Phase (rad) vs. dipole number. Longitudinal phase solutions were again stable to a few percent. Transverse solution was not nearly as stable.

are a $cos^2(v)$, shown in figure 3.9 or what is called natural weighting where each visibility position is weighted equally, shown in figure 3.8. These other weightings can lower the sidelobes or narrow the primary beam, but will increase the noise due to weak visibility pairs.

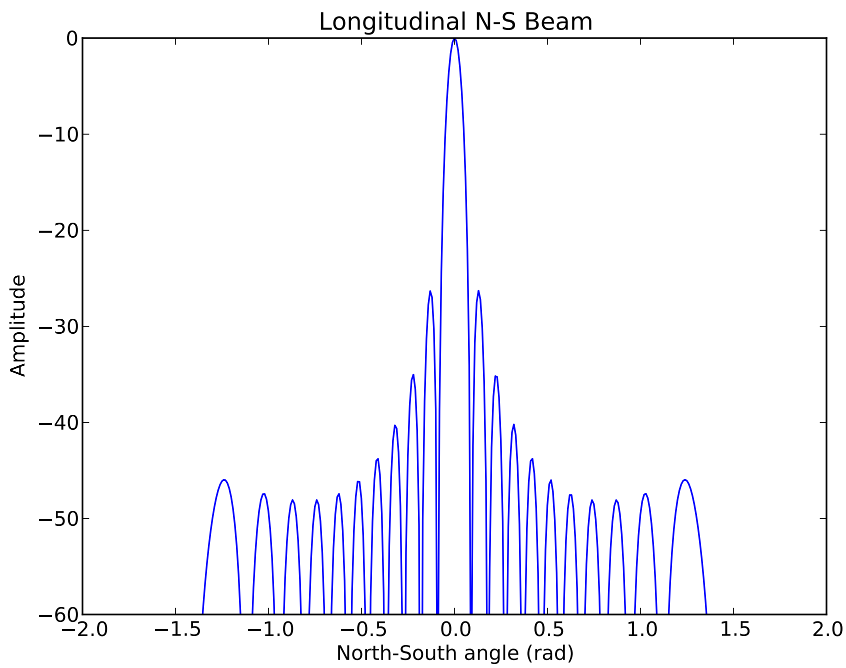

Figure 3.7: North-south dirty beam model, assuming equal weighting for all visibilities. This is the closest model to the weightings used for imaging.

3.2 Continuum Map

The imaging procedure and calibration of the previous section was applied to data taken drift scanning the telescope for ∼28 contiguous hours. The band from

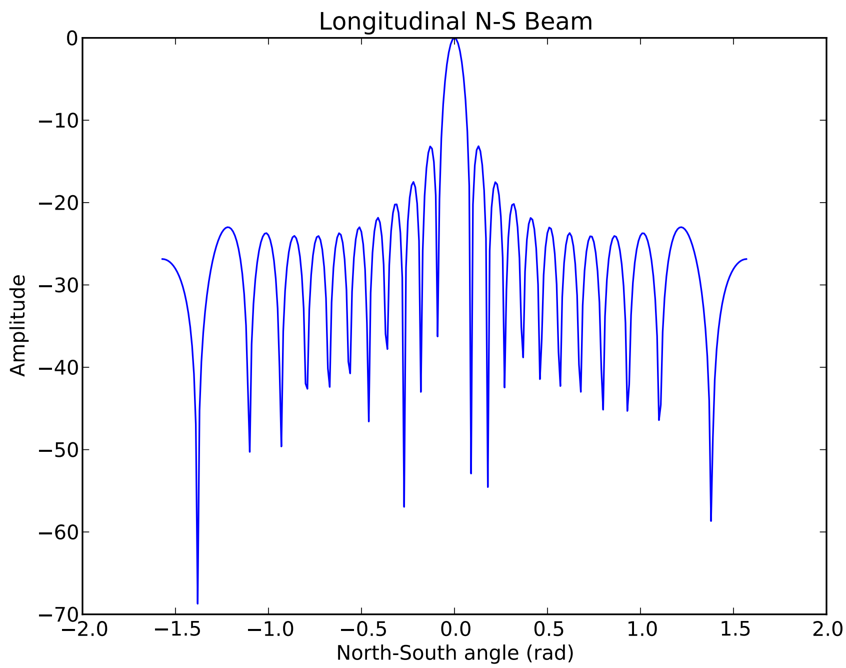

Figure 3.8: North-south dirty beam model using natural weighting. Each possible visibility is weighted equally, regardless of how well the baselines are measured. This weighting makes the side-lobes higher, but provides the highest signal to noise if the baselines have similar noise.

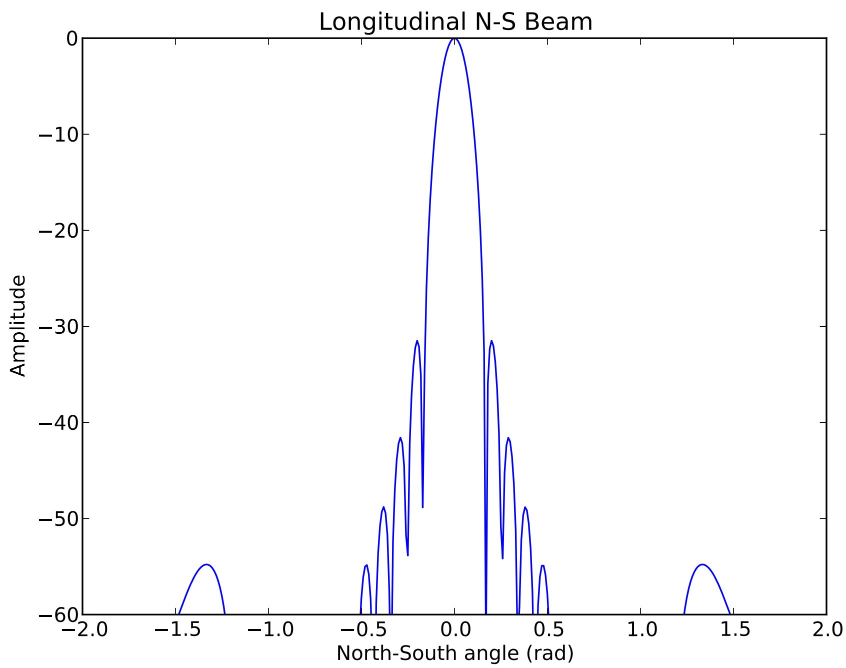

Figure 3.9: North-south dirty beam model with Hanning weighting. The visibilities are weighted as $cos^2(v)$, giving very low side response, but widening the primary beam.

1395MHz to 1425MHz is averaged together. Only the longitudinal dipoles were used. The visibilities were weighted (w_{ij}) using the calculated gain divided by the standard deviation of the first ~ 3 minutes of data. The map is shown in figure 3.10. The map was normalized to Cygnus A at a amplitude of 1600Jy. The bandwidth used was 30MHz. This is an image of the entire visible sky completed in just one day.

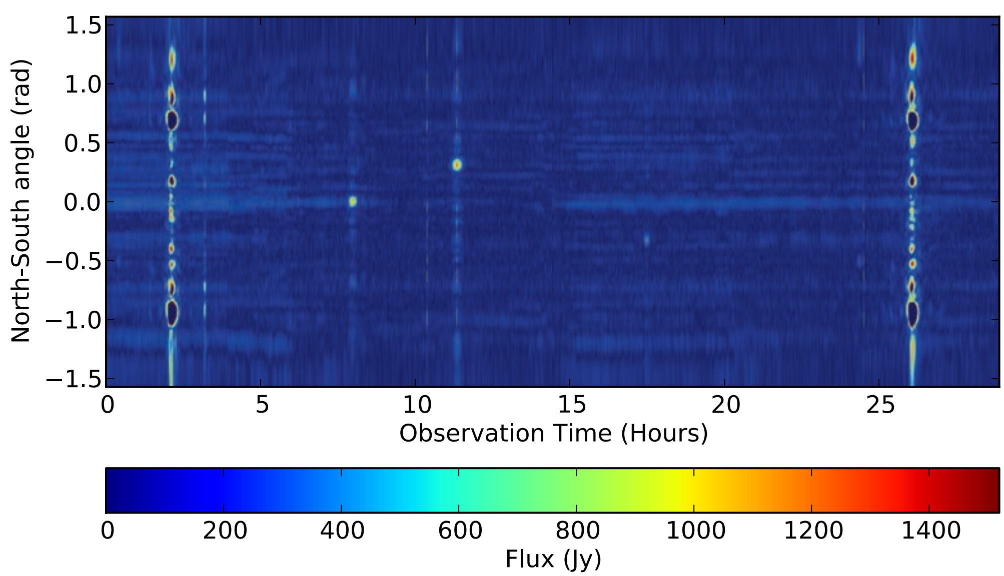

Figure 3.10: Continuum image averaged from 1395-1425 MHz. All-sky map with 28 hours of continuous data. The very bright source that is cut is the Sun, which crossed the beam twice during the observation.

Another interesting aspect to look at is the differences between the images made with the transverse and longitudinal antennas, as well as the within cylinder and between cylinder correlations. Using only cross-cylinder correlations, the longitudinal map is much cleaner and has a higher dynamic range by a factor of ~ 3

when compared to the transverse map, shown in figure 3.11. The only thing visible in the map are the brightest point sources. Two possible reasons for the transverse map having higher noise than the longitudinal map:

- The transverse dipoles are more sensitive to RFI radiation from the horizon in the north-south direction, raising the contribution from RFI
- The transverse dipoles are broadside and couple to each other more strongly. In simulations of the feeds this effect is quite small, and may well not be an actual cause for concern.

Using the within cylinder correlations, the images show more larger scale structures. The longitudinal map remains cleaner than the transverse map here as well. The extended structure of the continuum Milky Way Galaxy is apparent. The images are in figure 3.12

Looking closer at the image beam around Cygnus A and Cassiopeia A, the measured beams come close to ideal. See figure 3.15 and 3.18 for zoomed images around the point sources. Figures 3.13 and 3.14 have the cuts through Cygnus A in the east-west and north south direction. Figures 3.16 and 3.17 have the cuts through Cassiopeia A in the east-west and north south direction. Without applying any sort of clean algorithm the image is already showing few artifacts. Since the u-v plane is sampled well in the region of interest, the resulting image does not have the huge sidelobes of a standard interferometer which need to be subtracted out of the image.

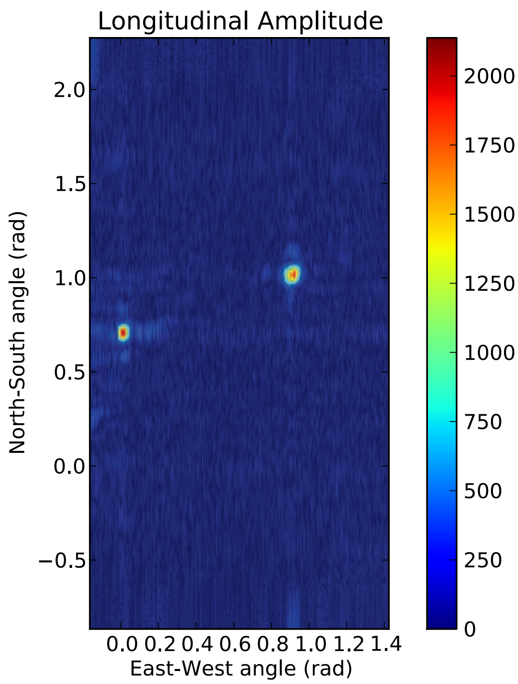

(a) Longitudinal

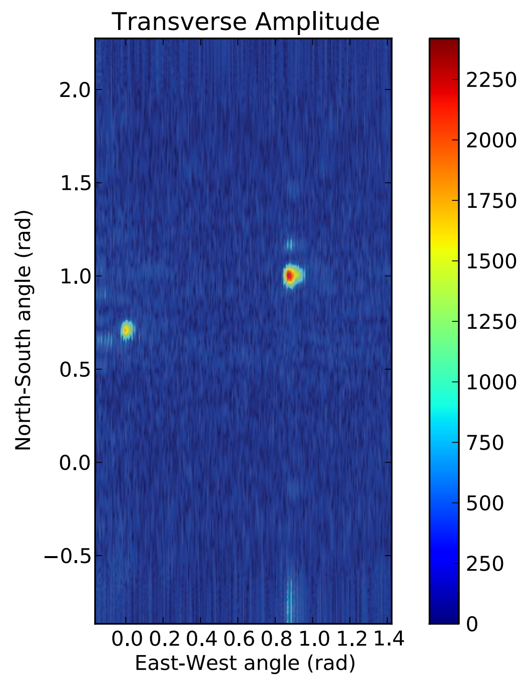

(b) Transverse

Figure 3.11: Continuum image of Cygnus A and Cassiopeia A made using only the correlation pairs between the cylinders. The longitudinal dipoles show a better dynamic range than the transverse polarization.

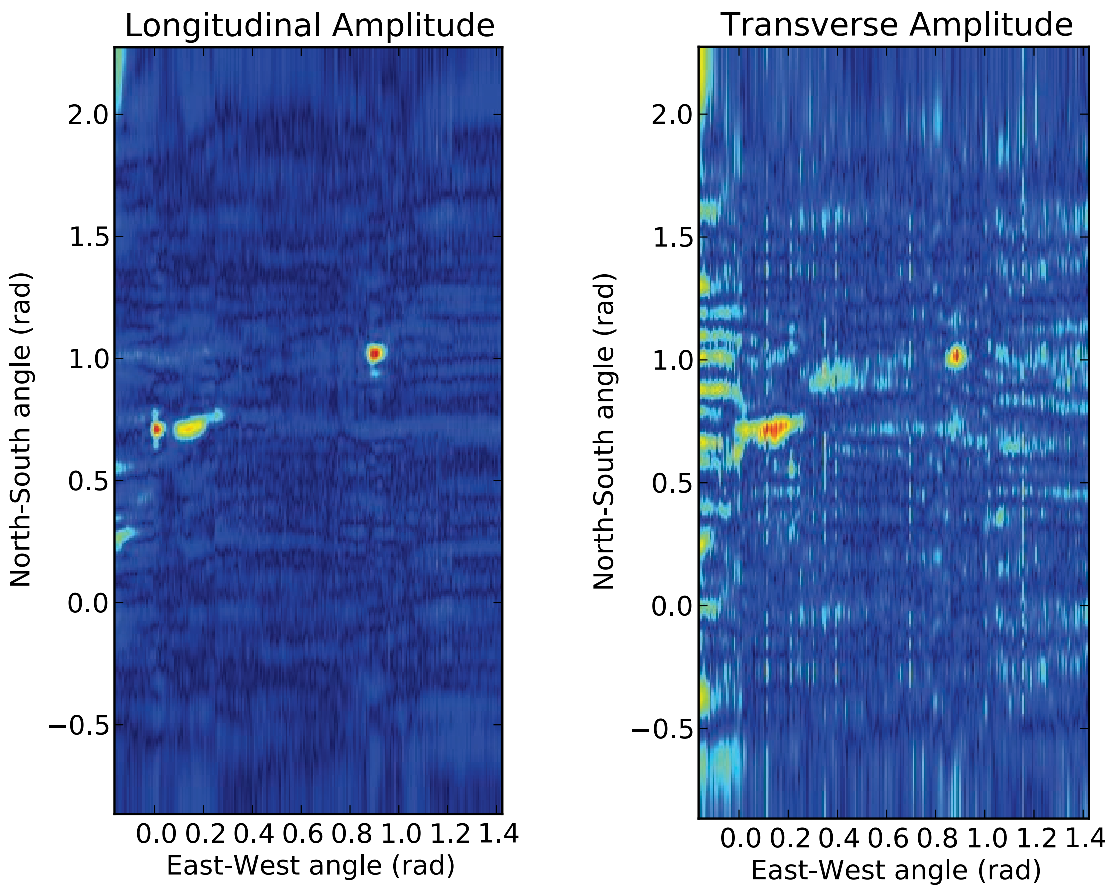

(a) Longitudinal

(b) Transverse

Figure 3.12: Continuum image of Cygnus A and Cassiopeia A using only the correlation pairs within a cylinder. The transverse map has much higher noise than the longitudinal map. Extended structure of the Milky Way becomes apparent using the within-cylinder correlation pairs.

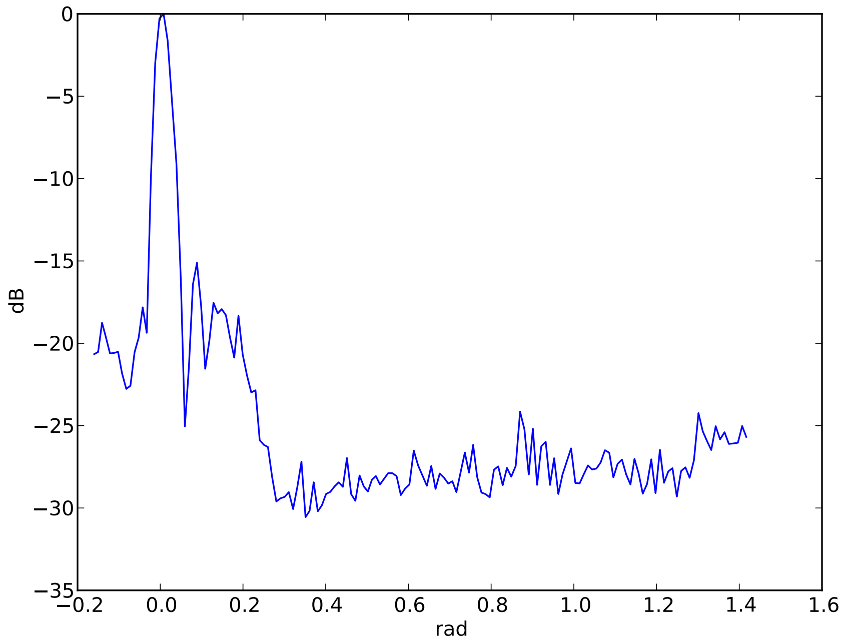

Figure 3.13: East-west beam measured on Cygnus A. Shows -20dB sidelobes and -30dB noise floor.

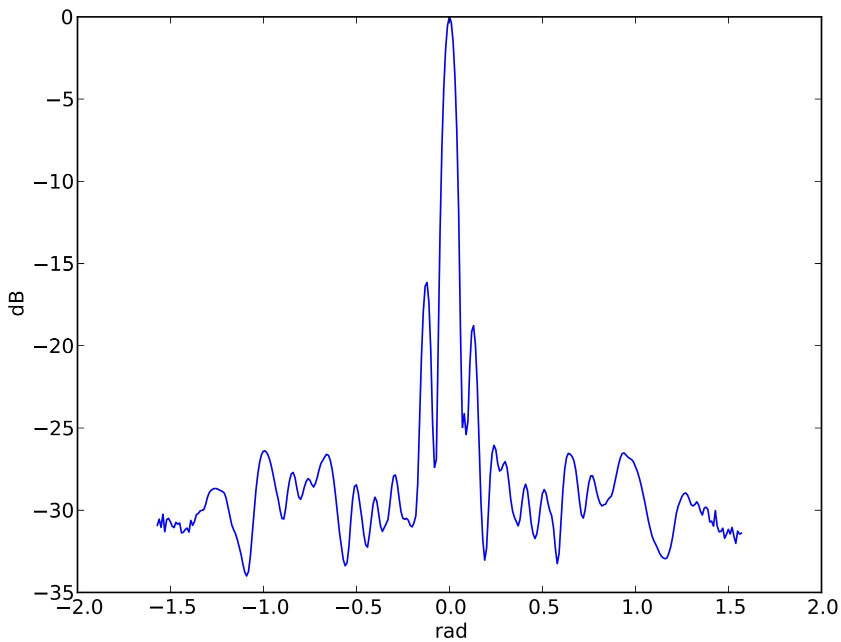

Figure 3.14: North-south beam on Cygnus A. Synthesized beam direction with 16 dipoles. Shows -20dB sidelobes and -30dB noise floor.

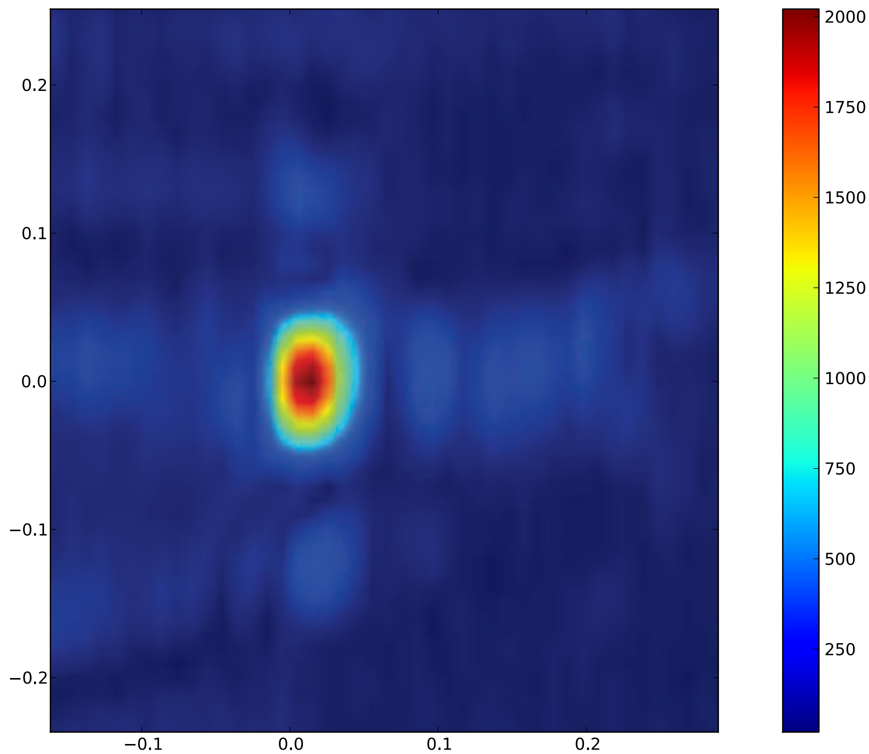

Figure 3.15: Continuum image of Cygnus A. Units of Janskys.

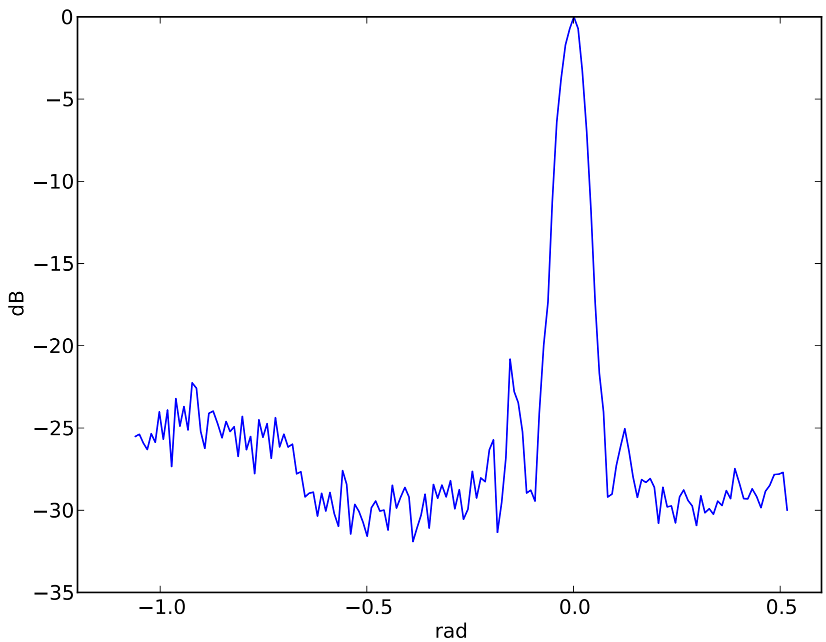

Figure 3.16: East-West beam on Cassiopeia A. Has -20dB side-lobes and -25 to -30dB noise floor.

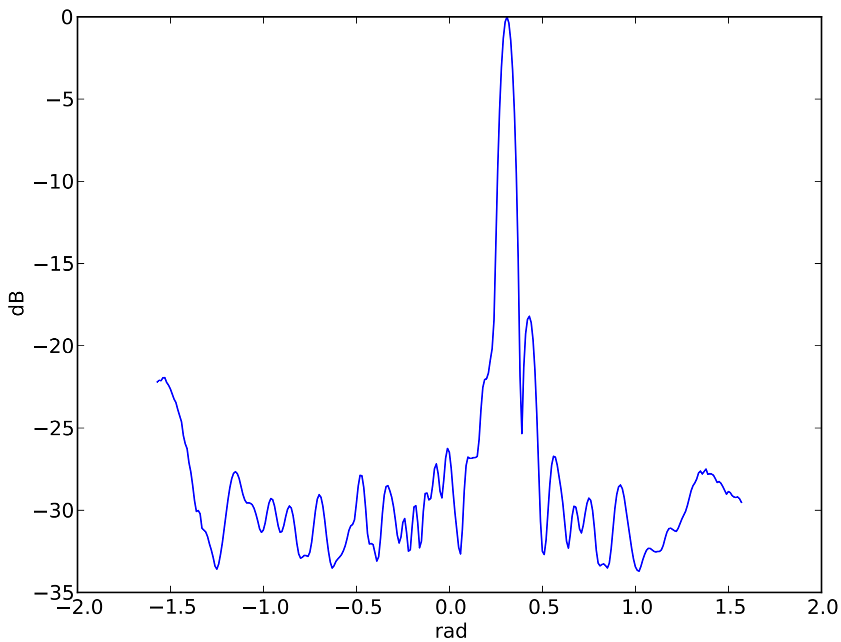

Figure 3.17: North-South beam on Cassiopeia A. Asymmetric side-lobes since not centered on overhead. Larger side-lobe alias visible at the horizon.

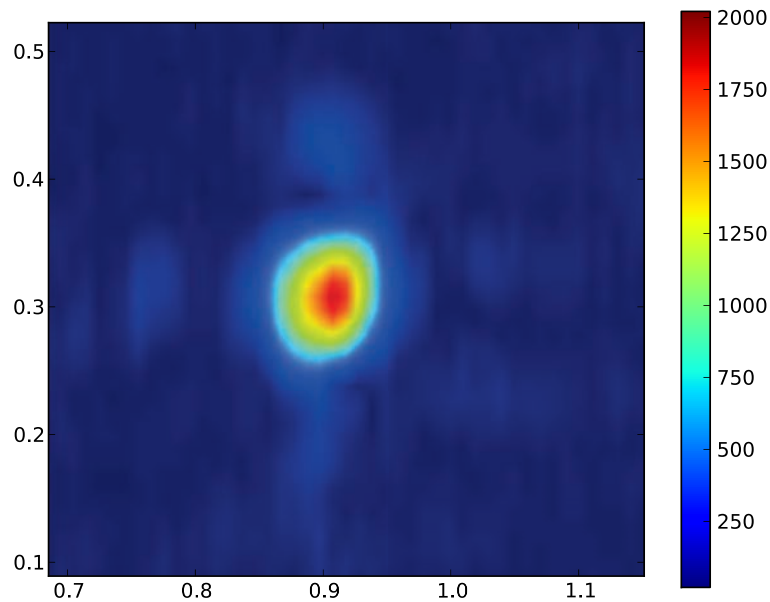

Figure 3.18: Continuum image of Cassiopeia A. Units of Janskys. Shows very little structure along the diagonal.

3.3 Image noise level

For a continuum map the signal to noise ratio $R_{SN} = S_r/\sigma$ where σ is the noise level in a empty piece of the map is defined as:

$$R_{SN} = \frac{AI\eta\sqrt{2N\Delta\nu\tau}}{2k_B T_{sys}} \tag{3.18}$$

Where R_{SN} is the signal to noise, A is the effective area of a single element, I is the flux density of the source, N is the number of correlation pairs used, $\Delta\nu$ is the bandwidth, τ is the integration time, k_B is boltzmann's constant, and T_{sys} is the effective system temperature for producing the image.

For each individual correlation pair, $N = 1$. Calculating $\frac{T_{sys}}{\eta A}$ is then:

$$\frac{T_{sys}}{\eta A} = \frac{S\sqrt{\Delta\nu\tau 2N}}{2R_{SN}k_B} \tag{3.19}$$

In our continuum image made, $\tau = 1.28$s, $\Delta\nu = 30$MHz, $N = 248$, $S = 1600$Jy for Cygnus A, and $R_{SN} = 80$ for the less noisy parts of the map. This gives a $\frac{T_{sys}}{\eta A} = 1000$. Our dipoles all have slightly different effective areas, but each has an approximate collecting area of 1.4 m^2 giving an effective T_{sys} for the map of 1400K. This high T_{sys} is driven by the RFI environment in Pittsburgh as well as not fully understanding and correcting for the instrument.

3.4 Milky Way Map

The Milky Way does not have much power in the scale corresponding to the visibilities between cylinders, and maps made with just visibilities between cylinders do not show an image. Instead, the within cylinder visibilities are required. Calibration for the within cylinder baselines were solved for using the continuum map and cross-cylinder baselines. This is an important point about the cylinder calibration to understand. Without the cross-cylinder visibilities, an individual cylinder is not calibrated to nearly the same level. The images have the continuum subtracted by just taking the average image in the 1419.57MHz, 1419.66MHz, 1421.35MHz,and 1421.47MHz 100kHz wide bins, and subtracting that from all the images. The stripes around the sun are set to zero to remove the residual.

The map is shown in figure 3.19 through figure 3.26. The aliases of the galaxy at the north and south ends are due to the 0.7λ spacing of the dipoles. The images were made using only the within-cylinder visibilities.

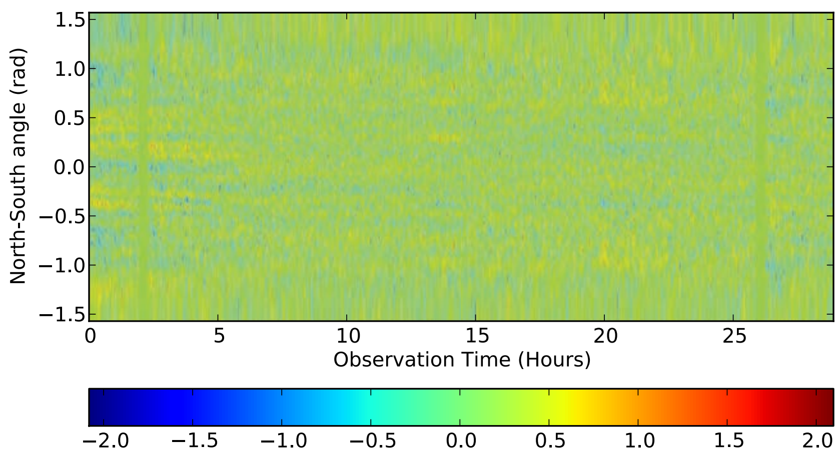

(a)

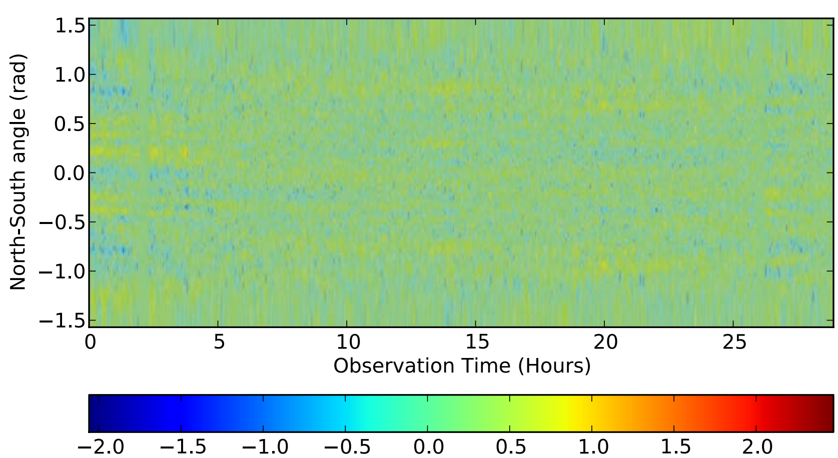

(b)

Figure 3.19: Milky Way galaxy 21cm emission. Frequency bins 100KHz each. 1419.57MHz and 1419.66MHz. These bins were averaged with the 1421.35MHz and 1421.47MHz bins and subtracted from all as the continuum subtraction. Shows the noise level after subtraction.

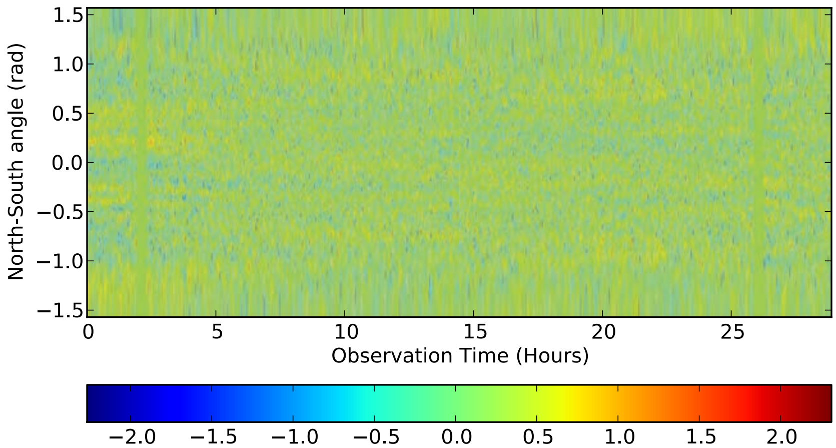

(a)

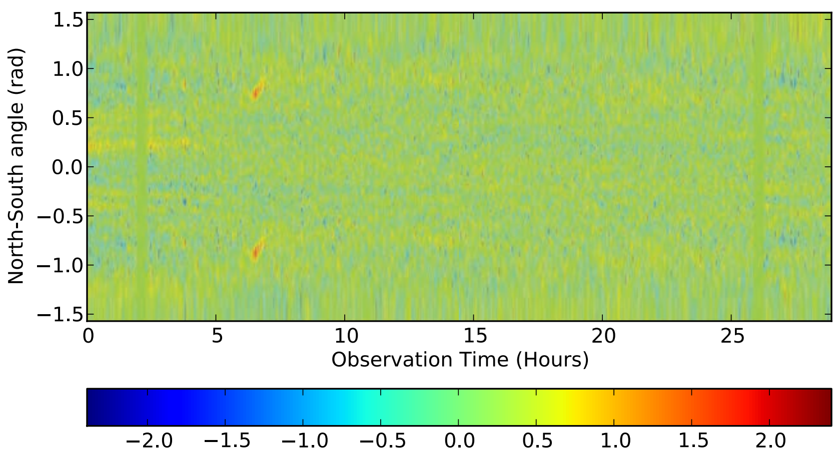

(b)

Figure 3.20: Milky Way galaxy 21cm emission. Frequency bins 100 KHz each. 1419.76 MHz and 1419.86 MHz. Neighboring bins to those used for continuum subtraction. Also shows the noise level of the images.

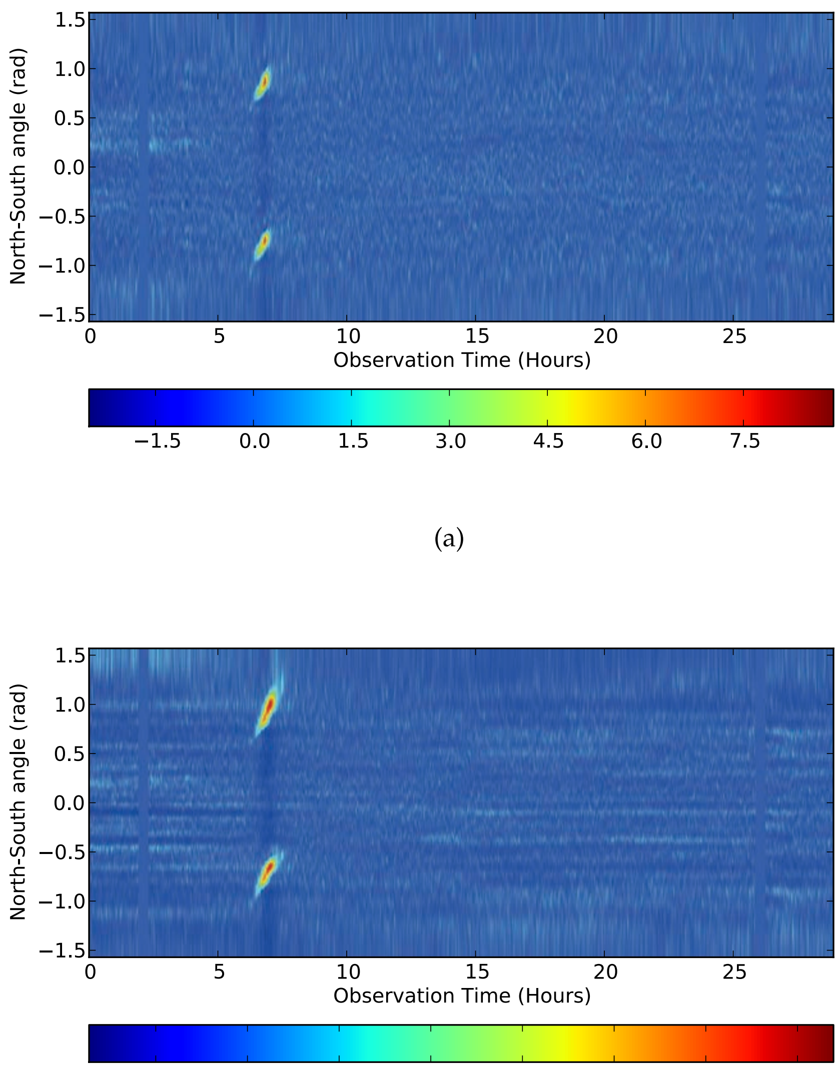

(a)

(b)

Figure 3.21: Milky Way galaxy 21cm emission. Frequency bins 100KHz each. 1419.96MHz and 1420.05MHz. The Milky Way galaxy is becoming apparent.

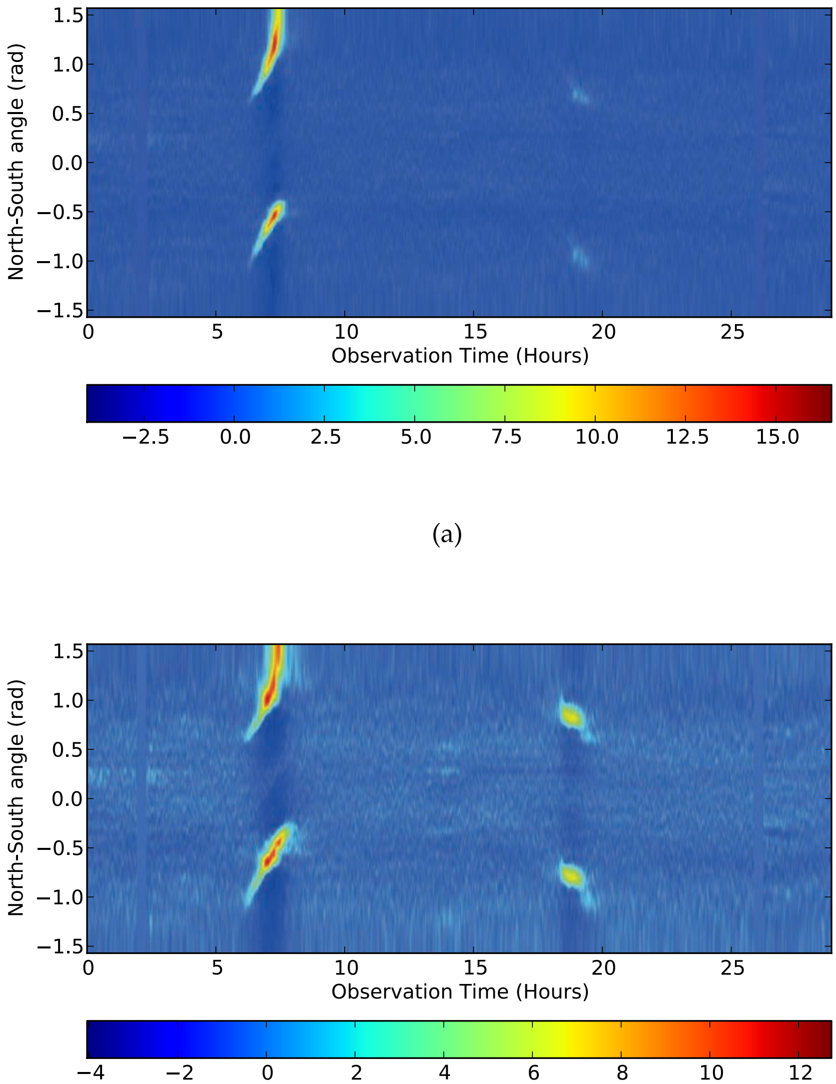

(a)

(b)

Figure 3.22: Milky Way galaxy 21cm emission. Frequency bins 100KHz each. 1420.15MHz and 1420.25MHz. The Milky Way is now visible in two regions.

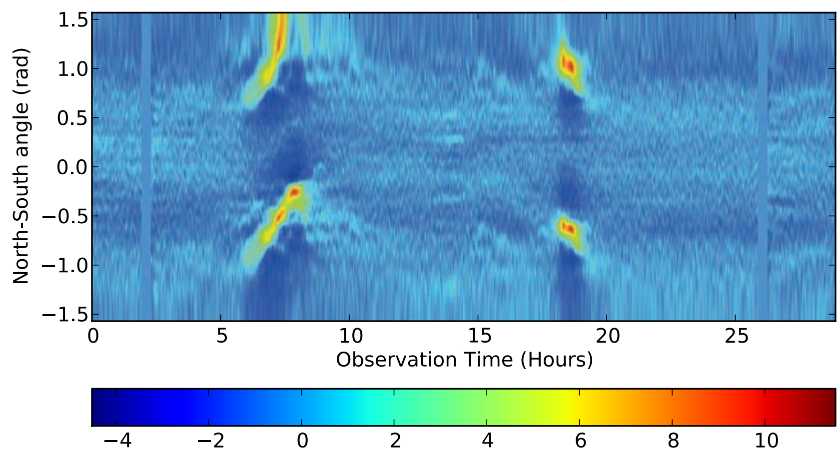

(a)

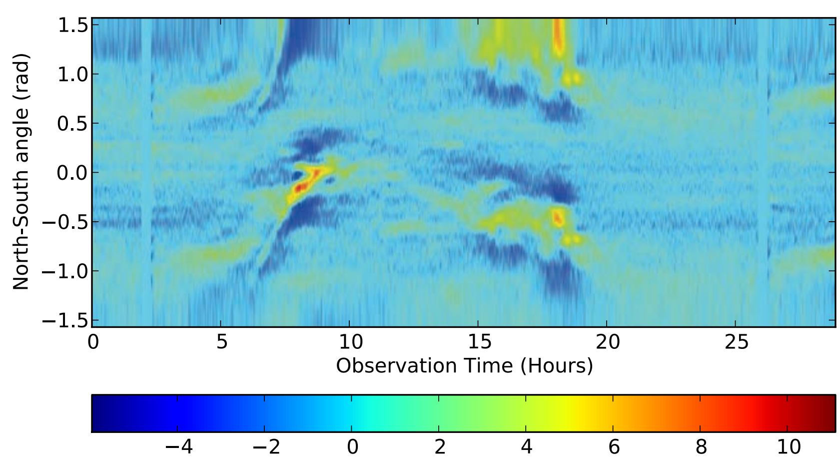

(b)

Figure 3.23: Milky Way galaxy 21cm emission. Frequency bins 100KHz each. 1420.35MHz and 1420.44MHz. More extended structure of the Milky Way visible.

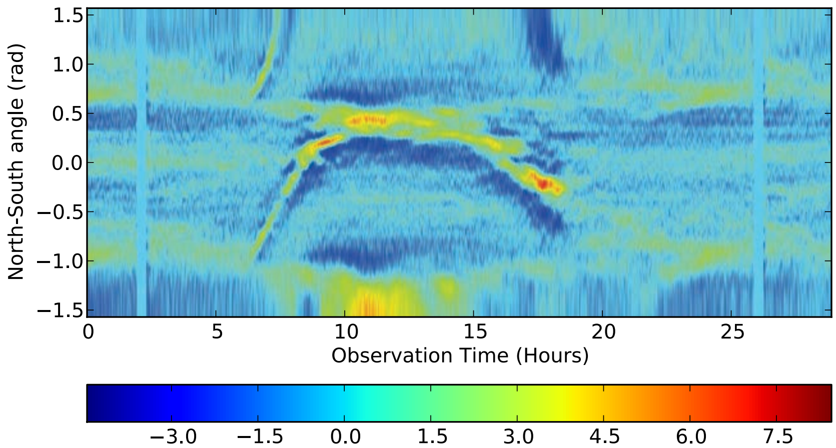

(a)

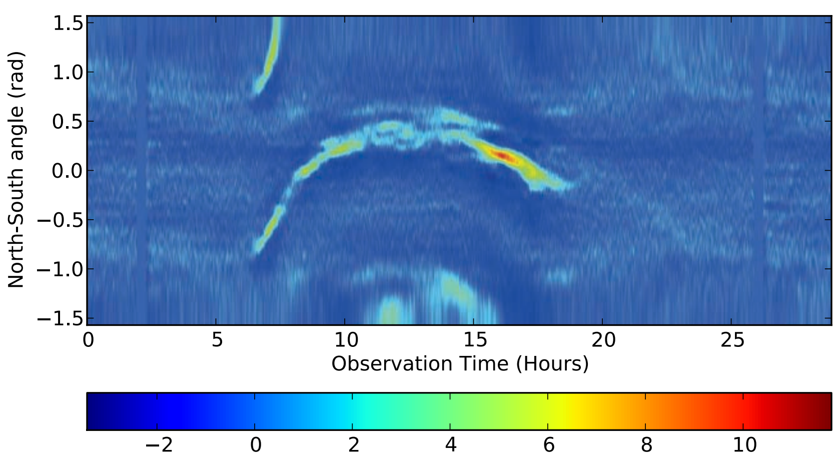

(b)

Figure 3.24: Milky Way galaxy 21cm emission. Frequency bins 100KHz each. 1420.54MHz and 1420.64MHz. Continuous slices of the Milky Way are visible.

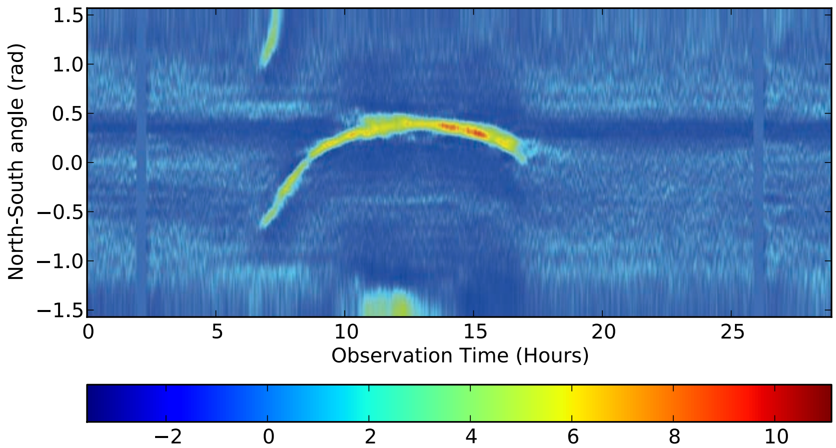

(a)

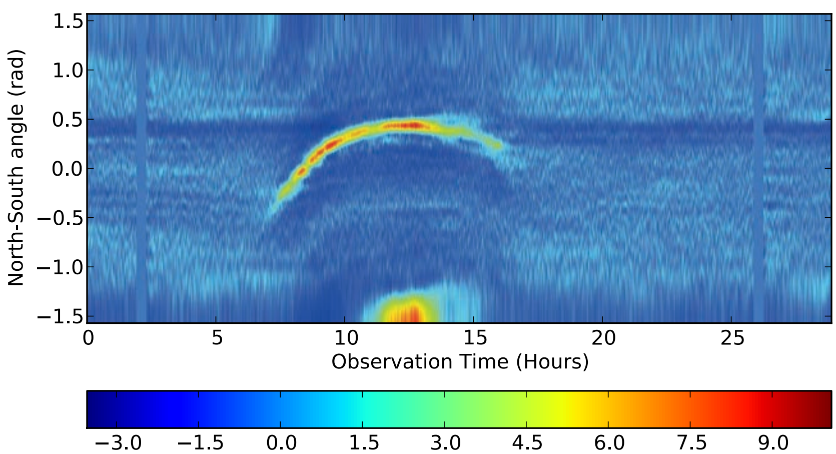

(b)

Figure 3.25: Milky Way galaxy 21cm emission. Frequency bins 100KHz each. 1420.74MHz and 1420.84MHz. Large regions of the Milky Way are visible.

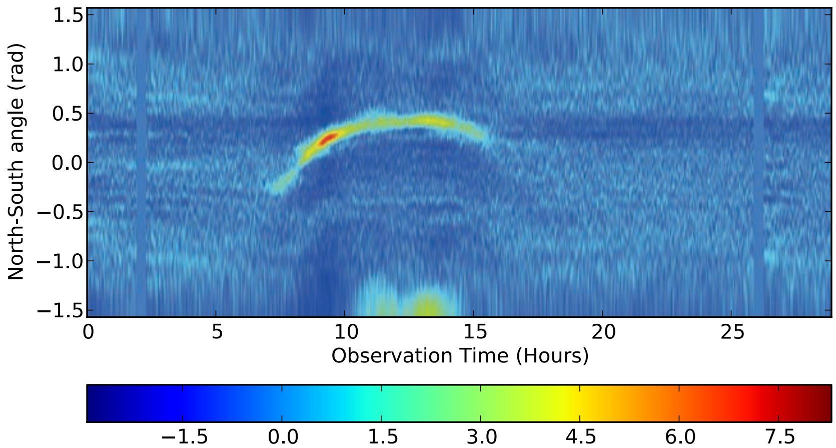

(a)

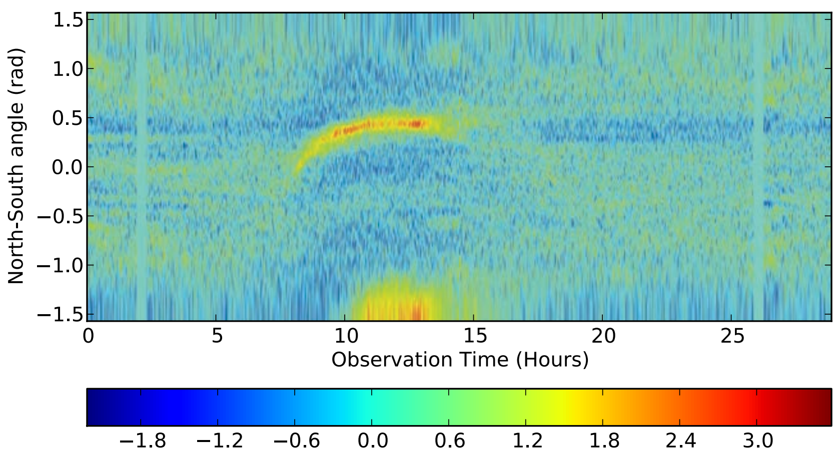

(b)

Figure 3.26: Milky Way galaxy 21cm emission. Frequency bins 100KHz each. 1420.93MHz and 1421.03MHz. Beginning to get out of the region of neutral hydrogen emission from the Milky Way.

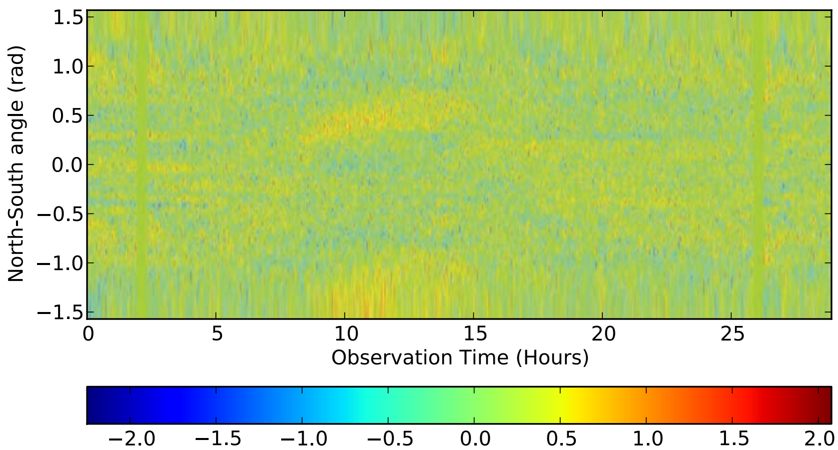

(a)

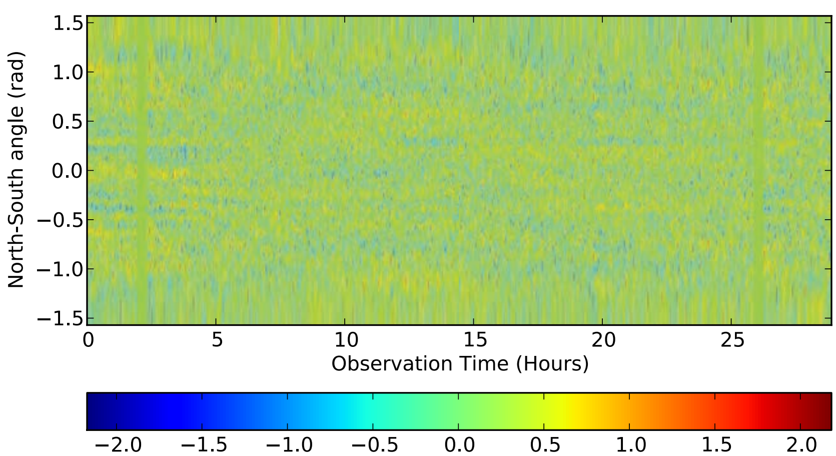

(b)

Figure 3.27: Milky Way galaxy 21cm emission. Frequency bins 100KHz each. 1421.13MHz and 1421.23MHz. Mostly just noise left visible.

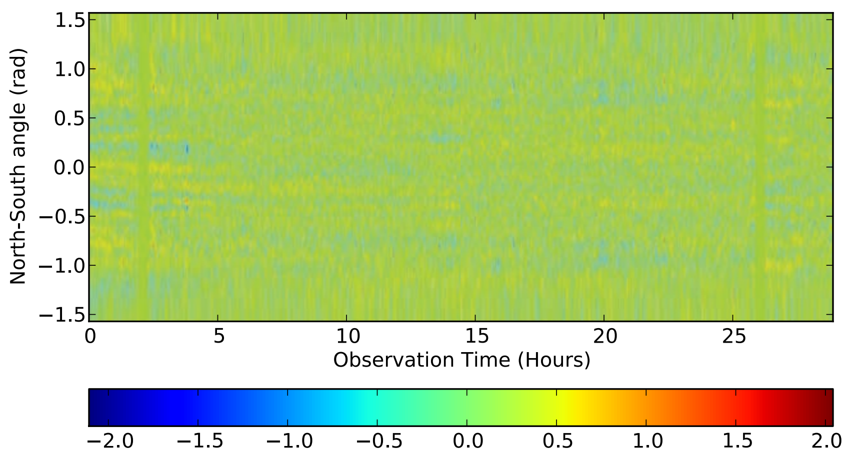

(a)

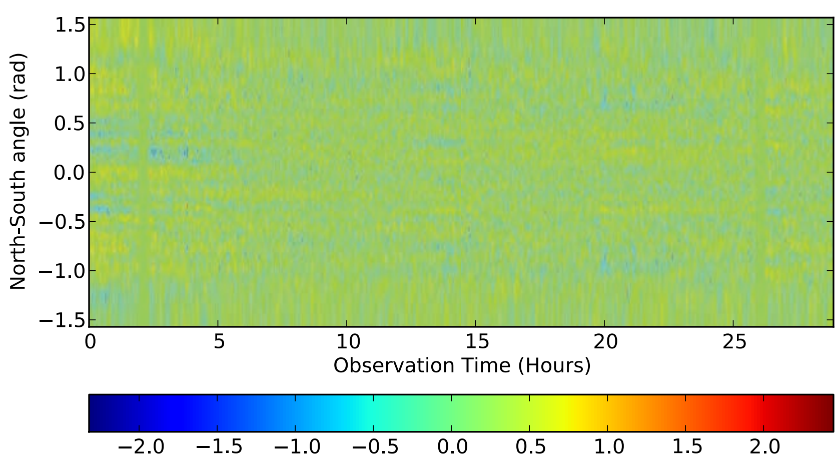

(b)

Figure 3.28: Milky Way galaxy 21cm emission. 100KHz wide frequency bins. 1421.35MHz and 1421.47MHz. Both used in average with 3.19a and 3.19b as a continuum subtraction.

4

Winter Storm Cylinder Collapse and Rebuild

4.1 Collapse

On February 5th-6th 2010 Pittsburgh was covered in 21 inches of snow falling within a 24hr period. This amount of snowfall happens only once every 30 year in Pittsburgh. It was a heavy snow with no wind. The cylinders are made with the surface mesh as the major structural element. The mesh has a half inch hole spacing. It was designed so that snow and weather would fall through the mesh, with only some collecting on the metal battens. In all previous storms the system functioned as planned. However during this storm the snow collected in the dish. The snow was compressed enough to form pieces hanging below as well as that collected above, see figure 4.1. The total collected snow was nearly 2 feet over the entire surface, see figure 4.2. This brought the structure to its limit and the surface partially collapsed (half of the east side) on the East cylinder and fully collapsed on the west side of the West cylinder. See figure 4.3a and 4.3b. The next few days brought another six inches of snow, and the East cylinder fully collapsed on the east side, see figure 4.4.

Figure 4.1: The snow collected and created square icicles which hung below the mesh adding weight to what was already collecting above.

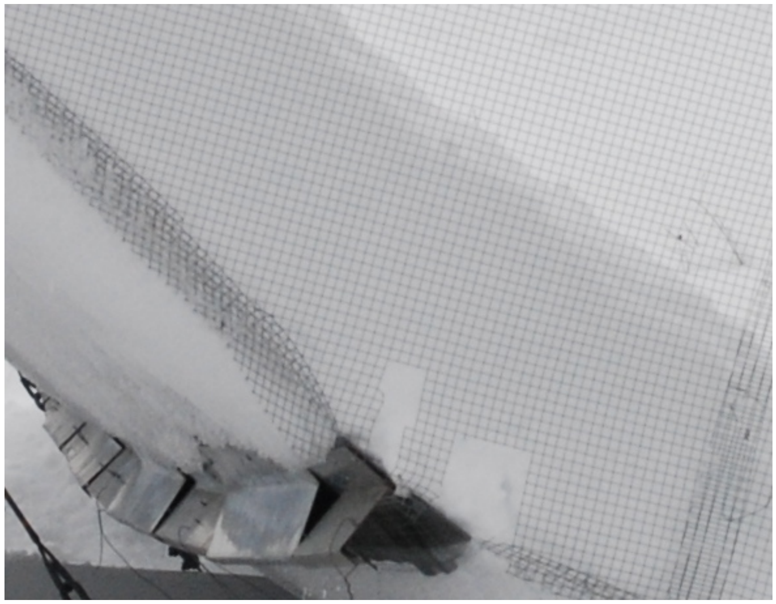

Figure 4.2: Depth of the snow collected on the cylinder. Approximately 14-16 inches above and 4 inches below the mesh surface.

(a) Partial collapse of the east cylinder.

(b) Collapse of the west cylinder

Figure 4.3: The snow storm on Febuary 5th and 6th built up too much weight on the surface of the cylinder mesh causing collapse.

Figure 4.4: After more snowfall and a few days, the East cylinder collapsed fully on the east side.

4.2 Failure analysis

The system was designed to fail by the steel wires breaking first. On the East cylinder the failure modes were close to what was expected. We found that the steel wire broke where it was bent to a small radius to attach to a punched hole, see figure 4.5. There were instances where the wire broke along its length as expected, see figure 4.6. The fence wires connect to a ”finger plate” which is used to connect the high strength wires to the mesh. The finger plate also was a point of failure, where the plate bent and then tore through the mesh. See figure 4.7 for an example.

On the West cylinder the failure mode seemed to be different. On the north-west side the fence wire cables did break, and are believed to be the first to fail. The rest of the length broke at the mesh right at the top batten point, see figure 4.8. The theory is that the north-west corner failed first, but the mesh was frozen enough to the tops of the trusses for the rest of the cylinder that the mesh tore, and then a zipper effect brought the rest of the cylinder down.

Both the West and East cylinders also had failures of the steel trusses. The worst failure was the north-east truss of the East cylinder, which is the section that collapsed a few days after the others. The trusses were only designed for a vertical load, no side loading. In the collapse (due to freezing of the mesh?) the trusses were twisted towards the center of the cylinder, with some breaking welds to the plate that hold the trusses in place, see figure 4.9. The north-east truss in particular came very close to failure, with all but one weld broken, see figure 4.10.

The feedline made it through the snow completely undamaged, see figure 4.11.

Figure 4.5: The wires were designed to be the failure point. Most wires that broke failed where they were bent to a small radius.

4.3 Tests

Heavy snow weighs about 20 lbs/ cu ft.[1]. The exact weight of the snow from that storm was not recorded and is unknown. Each cylinder has 65 ft long mesh by about 40ft arc length between the columns, and had about 20 inches (1.67 ft) of snow built up, which is a volume of 4333.33 cu ft. 20lbs/ cu ft gives 86,666 lbs of

[1]http://www.flagstaff.az.gov/DocumentView.aspx?DID=12809

Figure 4.6: The wire was designed to be the failure point. This is an example of a wire that failed as expected.

Figure 4.7: The finger plates also ended up being a point of failure. They bent and tore through the mesh.

Figure 4.8: The West cylinder seemed to fail differently. The northwest end had fence wire failures. The rest of the cylinder failed at the mesh right above the top batten.

Figure 4.9: The truss twisted and was torqued when the mesh fell instead of being under pure compression.

(a) north end

(b) south end

Figure 4.10: This truss was twisted so strongly that welds to the plate, which bolted the truss in place, were broken. This was an unforeseen failure mode. (a) shows the northern end of the truss where all the welds were broken, and the truss was just resting on the column plate. (b) shows the south end of the truss where one weld point was still attached.

Figure 4.11: Image of the feedline covered with snow. The feedline did not get damaged from the snow.

snow per cylinder! The 5 ft sections of mesh are held up by two 2000 lb tension strength wires pulling off at 45° in the north south direction, giving a tension strength about 2800 per 5 linear feet, or 36,400 per side of the cylinder, or 72,800 lbs total weight on the cylinder. None of these numbers are known exactly, but the fact that the east cylinder partially failed before totally failing after more snow means that the snow weight was almost exactly at the breaking point of the cylinders.

4.3.1 Mesh Stress Tests

We set up a stress test to determine how the current system failed. We attached mesh on one side strongly. We used a 2in diameter iron pipe, wrapped the mesh around it and clamped it together with a strip of sheet metal and fender washers. We then used the same fence wire, wrapping around the pipe approximately 1/4 of the way from the end of the mesh. The first round of testing just had the wire looped around the ends which made the pipe bend a bit. This was considered our "fixed end" of the mesh, and throughout the testing it never failed, see figure 4.12. The other side was the tested side.

The tested side was terminated to a winch with a 0.5 inch radius. The tension was measured using a torque wrench as shown , see figure 4.12.

First we tested a finger attach point as used, with a finger plate connected with two fence wires through the punched hole. We found that the bend in the finger plate was pulled out at 1800lbs of tension. At 2600lbs tension the finger plate buckled perpendicular to the mesh, and fence wires were pulling through the punched hole, see figure 4.13. This shows the finger plate as a point of failure.

The second test was again with a finger plate, but wire wrapped around bolt with washers, going through hole in fingers, see figure 4.14a. This was to alleviate the high stress point of failure in the previous test. We found deformation of the finger plate at 1200lbs of tension, see figure 4.14b, but the failure was actually the fence wire at the winch at 2900lbs.

The third test was a standard batten attachment, attaching to the center carriage bolt and wrapping around the washer on then bottom, see figure 4.15a. This scheme would be the easiest to use to raise the downed cylinders, if it was strong enough. In this test, the mesh ended up being the failure point, and it tore near the bolts at 2000lbs. The mesh seemed to rip out at one end first. It then just zippered across from each bolt to complete failure, see figure 4.15b.

The fourth test involved taking a finger plate and flatten out its bend. The finger plate was then attached to the mesh, tightened up, and screwed into a standard batten attachement with five self tapping screws, see figure 4.16b. The fence wire was then attached by wrapping around washers attached with a carriage bolt to the finger plate, see figure 4.16a. Using this setup the fence wire broke at 3200lbs of tension. The fingerplate and mesh showed no signs of problems before the fence wire broke.

Figure 4.12: The fixed end of the mesh pulling test setup.

Figure 4.13: Test of mesh connection similar to the as-configured termination. Both wires were pulled straight instead of at an angle. The bend in the finger plate straightened out at 1800 lbs of tension. At 2600 lbs the plate buckled in the perpendicular direction and the wires sheared through the punched hole.

(a) new wire attachment method (b) finger plate starting to bend

Figure 4.14: Wire attachment to finger plate was changed to use a bolt through the finger plate, with the fence wire wrapped around smaller washers, and a larger washer to hold it in place. With this connection method the finger plate started to bend at 1200 lbs of torque, but the catastrophic failure mode was, in fact, the fence wire at 2900 lbs.

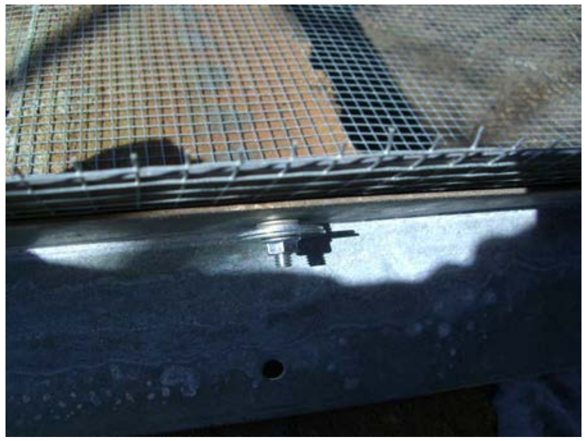

(a) wire attachment method

(b) mesh beginning to tear

(c) all tearing

Figure 4.15: Wire attachment to mesh changed to use standard batten scheme. Flat sheet metal on top of a bent sheet with 5 carriage bolts sandwiching the mesh. The attachment was to use the washer on the middle carriage bolt, shown in (a). At 2000 lbs of tension the mesh tore, shown in (b). Full failure is shown in (c).

(a) wire attachment method

(b) mesh setup

(c) under tension

Figure 4.16: Wire attachment to mesh changed to use finger plate attached to a standard batten scheme. The finger plate is flattened and then screwed to a flat sheet metal on top of a bent sheet with 5 carriage bolts sandwiching the mesh. The attachment was to use the washers through the hole in the finger plate. All shown in (a). The fence wire broke at 3200 lbs of tension. Shown in (c) is the mesh under approximately 2900 lbs.

4.4 Changes Made

On the fallen side, the mesh attaches to the wire inside the cylinder. This creates less friction going over the truss tube making adjustment easier (before the mesh would have to settle for a day or two to reach a static shape), and lessening the possibility of twisting the truss. The attachment of the mesh to the steel cable is now the same as testing method 4, figure 4.18 for most of the East cylinder. Concrete coffin blocks were added along the outside of each cylinder to enable attachment of the steel wire with no north-south component, such that adjustment is easier and the load per wire is reduced. Where straight pulls were not possible we switched to using a pulley attach point on the finger plate. One side of the fence wire terminated to a concrete block and the other using a winch. The West cylinder was changed to use pulleys to attach all, even the straight pulls, see figure 4.19. Attachment of the steel wire to the coffin blocks was done using DOT winches (see figure 4.17) instead of hayes, see figure 4.20 or wheel style, see figure 4.21 winches as they were not easy to adjust, did not loosen very well.

4.4.1 Truss Repair

The trusses were twisted and pulled back into place, but the $\sim$5mm precision of the location was lost. The positions of the end of each truss were remeasured using steel tape relative to each other, and the positions were made accurate to about 3cm. The heights were not remeasured or readjusted. The trusses were repaired

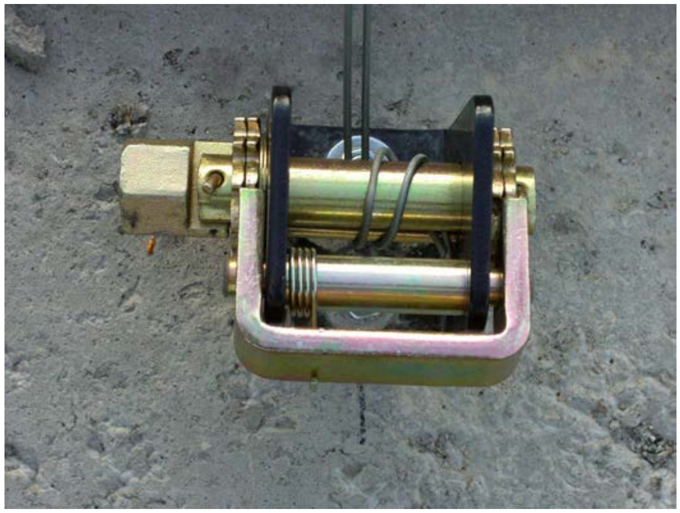

Figure 4.17: The DOT winch, standard for flat bed trucks.

Figure 4.18: East cylinder new standard attachment of the mesh to the steel wire.

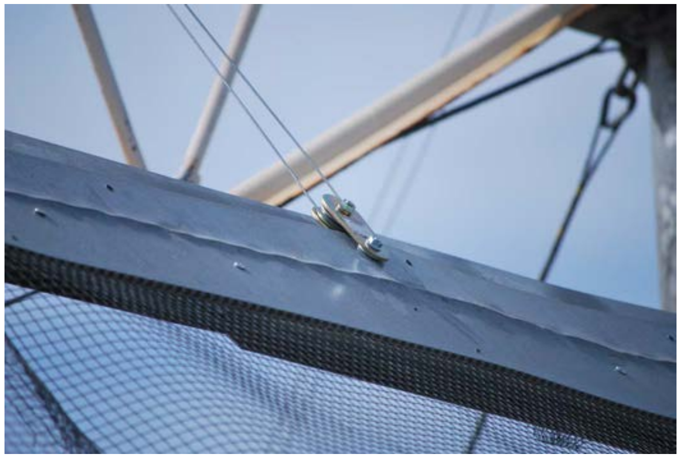

Figure 4.19: West cylinder new standard attachment of the mesh to the steel wire.

Figure 4.20: Hayes style wire tightener.

Figure 4.21: Wheel style wire tightener

by not just redoing the spot welds, but by welding all along the sides of the plate, see figures 4.22 and 4.23. This was to reduce the possibility of the truss breaking off from the attachment to the top of the columns and falling during a major failure. Under normal load stresses it should not be a problem.

Figure 4.22: Welding the truss back together.

Figure 4.23: Finished weld

4.4.2 Mesh Raising

The mesh was cut back to the highest batten on the side that fell down. The mesh was then pulled over to a working height using standard tiedown straps, see figure 4.24. Then finger plates, figure 4.25, were flattened and attached to the mesh below the batten, and then screwed into the batten. The steel wire was attached and then made slightly tight. See figure 4.24 for the first connection. Once all the unbent sections were connected the mesh was raised enough such that the bent battens were no longer touching the steel column cable supports. These battens were then repaired or replaced, and a fingerplate was attached. The entire row was reattached and then ready to be raised, see figure 4.26. The winches were tightened one or two at a time raising each by 10-20cm before moving to the next, see figure 4.27, until the mesh was completely back off the ground, see figure 4.28. The same procedure was done on the West cylinder until it was raised again as well, see figure 4.29. The missing top sections of mesh were then again filled with mesh, which was attached to the trusses and overlaps with the rest of the cylinder, it does not actually attach to it. The cylinder was then readjusted to a parabolic shape using physical and optical methods described in section 2.2. The final states are shown in figures 4.30 and 4.31

Figure 4.24: East cylinder at the start of the raising process. The top batten on the fallen side is brought to a working height with standard straps. Finger plates are attached to the mesh and steel wire, which then runs over the truss.

Figure 4.25: Example of a finger plate.

Figure 4.26: East cylinder re-attached and ready to raise.

Figure 4.27: Raising the East cylinder. Each winch was tightened 10-20cm before moving to the next, going north-south along the cylinder.

Figure 4.28: East cylinder again off the ground.

Figure 4.29: West cylinder again off the ground.

Figure 4.30: West cylinder raised and adjusted, mesh added back along the top side.

Figure 4.31: East cylinder raised and adjusted, mesh added back along the top side.

5

Brightness Mapping with the Green Bank Telescope

5.1 The Green Bank Telescope

5.1.1 GBT Design

The Green Bank Telescope is a 100m diameter fully-steerable radio telescope designed for use from 290 MHz to 100 GHz. It is off axis design, meaning that the aperture is not blocked by the feed structure, see the image of the telescope in figure 5.1. The offset makes the primary 100m by 110m. In order to have good efficiency up to 100 GHz the surface is made of panels which are actively moved to counter the effects of gravity, temperature and wind to keep their shape.

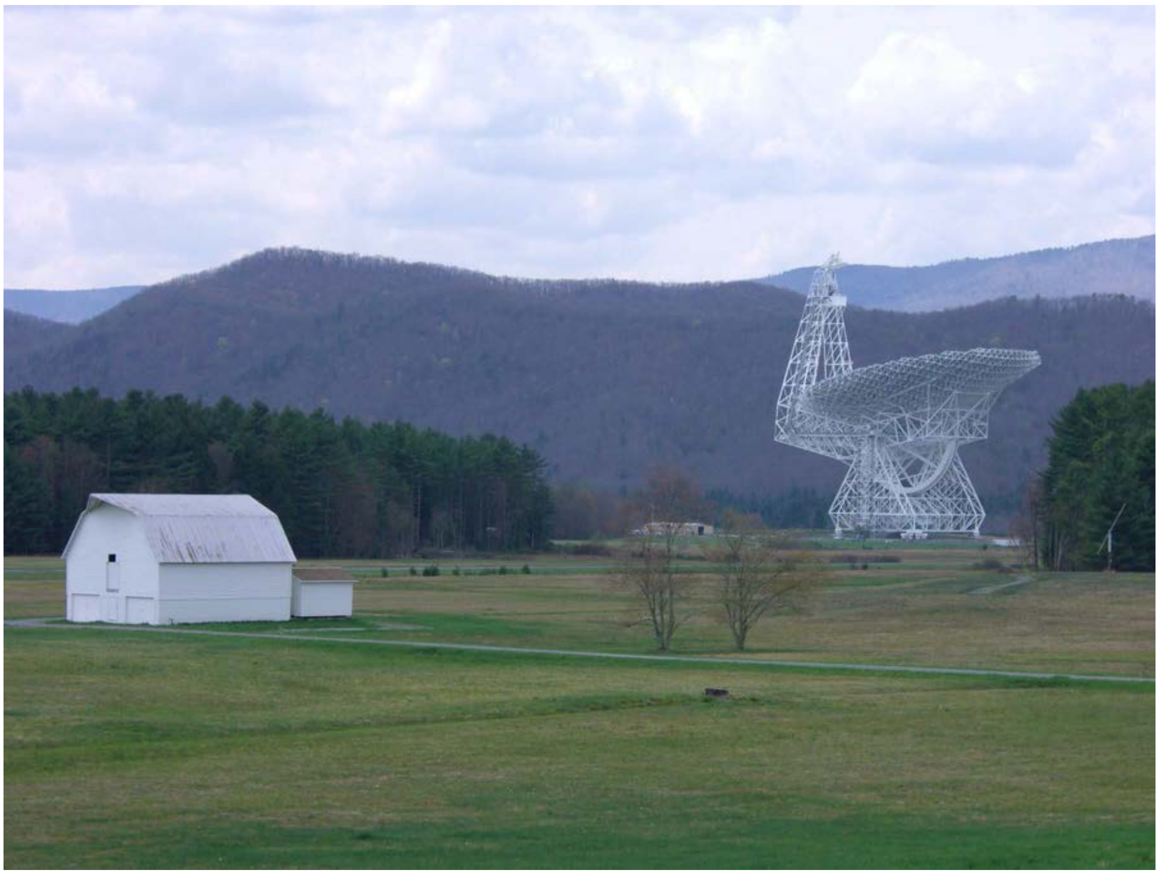

Figure 5.1: Image of the Green Bank Telescope

5.1.2 Single Dish Astronomy

Intensity mapping requires good brightness sensitivity, and single dishes generally have higher sensitivity than aperture synthesis telescopes.

In aperture synthesis astronomy, the RMS brightness-temperature error is given by:

$$\Delta T_b = \frac{M\, \lambda^2\, T_{sys}}{A_e \Omega_b \sqrt{2N\ t\ \Delta\nu}} \tag{5.1}$$

where ΔT_b is the RMS brightness temperature, M is a correlator efficiency factor of order 1, k is boltzmanns constant, λ is the wavelength, T_{sys} is the system temperature, A_e is the effective collecting area of a single telescope, Ω_b is the synthesized beam solid angle,N is the number of pairwise correlations, t is integration time and $\Delta\nu$ is the bandwidth. This equation can be simplified to approximately:

$$\Delta T_b \approx \frac{T_{sys}\, B^2}{d^2\, n \sqrt{t\ \Delta\nu}} \tag{5.2}$$

where B is the longest baseline, d is a single dish diameter, and n is the number of dishes and M has been set to 1.

This is easily compared to the single dish radiometer equation where:

$$\Delta T_b = \frac{T_{sys}}{\sqrt{t\ \Delta\nu}} \tag{5.3}$$

and the area of the telescope does not effect the final Brightness Sensitivity

Temperature. If the required signal level ΔT_b is held constant, a single dish sensitivity is determined by its system temperature, integration time and the bandwidth of the spectrum elements. An interferometer's sensitivity is reduced by the 'filling factor' ($\frac{d^2}{B^2}$), where the brightness sensitivity falls with the area covered out of the total area expected from the longest baseline. However if $\frac{d^2}{B^2} = n$, then the interferometer will be just as good as the single dish, and if $\frac{d^2}{B^2} < n$ the interferometer would appear to be more sensitive than a single filled dish, but this is not possible since dishes touch when $d^2 = B^2 n$

5.1.3 Why Green Bank

A filled, or nearly filled aperture telescope is necessary in order to get the best brightness sensitivity. Since we have not yet built CRT, there are no close packed interferometers in existence, making a single dish telescope the only way to proceed. With a single dish, the brightness sensitivity is independent of the size of the dish, but the beam size scales with the size of the telescope. We would like to resolve the non-linear scale, $\sim$ 10h^{-1} Mpc. At redshift one, 10 h^{-1} Mpc is approximately 15′ on the sky assuming WMAP5 cosmology [38]. This angular resolution at 700MHz corresponds to a telescope diameter of 100m. In order to study large scale structures down to the non-linear scale at redshift one, a 100m class telescope is needed.

5.2 Observation

Observations of the DEEP2 fields were conducted in the spring (April 25th and 28th, May 1st) and summer (August 28th and 29th, September 6th, 7th, and 17th) of 2008. Observations of the zCOSMOS field were conducted in the fall/winter of 2009 (October 17th and 18th, November 23rd, and December 22nd) and the winter of 2010 (January 13th).

5.2.1 Scan Strategy

We tried multiple scan strategies. We want to optimize useful on sky time while also getting data that could be calibrated extremely well with the fewest systematics. On the DEEP2 fields we tried three different scan modes:

- Standard mapping mode. In this mapping mode data was taken by actively scanning the telescope at 1.75°/minute at constant Right Ascension across the DEEP2 fields. There were 6 such scans, half increasing in RA, half decreasing in RA, at different declination separated by 0.05° creating overlapping beams. The GBT beam size is approximately 0.25° at this frequency range. Data was saved every 0.5 seconds with full stokes information.

- Drift Scan. In this mode data was taken by parking the telescope and letting the sky drift by at constant Right Ascension, covering the DEEP2 fields. There were 6 such scans across a field at different declination separated by

0.05° creating overlapping beams. The GBT beam size is approximately 0.25° at this frequency range. Data was saved every 0.5 seconds full stokes information.

- Daisy Scan. This mode had the telescope actively moving in Azimuth at constant elevation while letting the DEEP2 field drift through the beam. The telescope pointed within the field being observed the entire time, so the turn around points dominated the observing time.

Of these three observing modes, the drift scans and standard maps seemed to work best. The Daisy scan method was a custom modification of a higher frequency observing mode which only moved the telescope arc minutes. We were using the mode to move the telescope by about a degree. Therefore, the saved pointing information may not have been accurate enough during the turning of the telescope, which is when the majority of the data is recorded.

The coverage of the DEEP2 field3 are plotted in figures 5.3, 5.2, and 5.4.

5.2.2 RFI Mitigation

Green Bank is an official national radio quiet: approximately 13,000 square miles where cell phone and tv towers are prohibited. The telescope is also surrounded by mountains, so there is no direct path to most interfering signals. Even so, RFI is a major problem at Green Bank, because the receiver is typically 400 feet above the ground and also very sensitive.

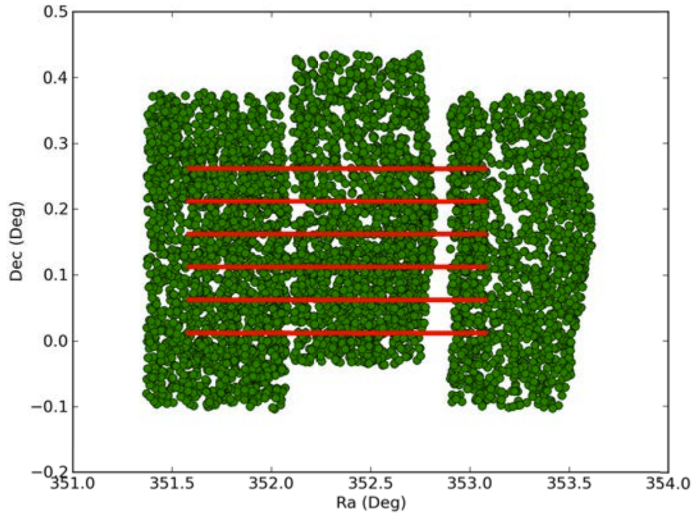

Figure 5.2: Coverage of the DEEP2 field3 in right ascension and declination. The green circles are the locations of the optically identified DEEP2 galaxies, giving an idea of the optical survey angular coverage. The red lines are the pointing centers of the radio observations.

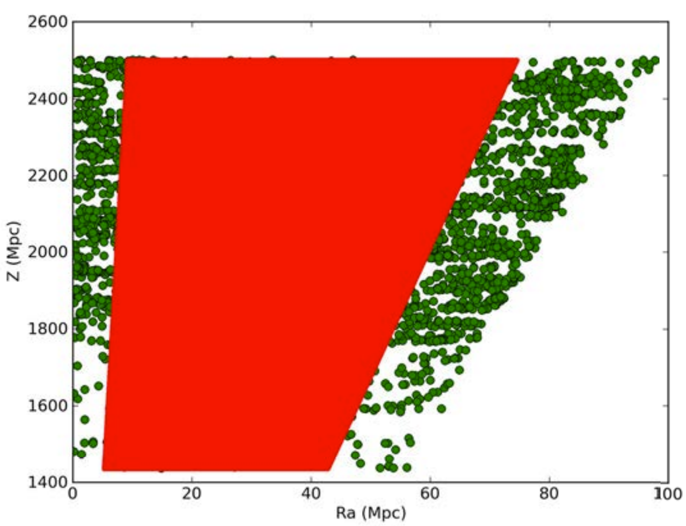

Figure 5.3: Coverage of the DEEP2 field3 in right ascension and Redshift. The green circles are the locations of the optically identified DEEP2 galaxies. The red lines are the pointing centers of the radio observations.

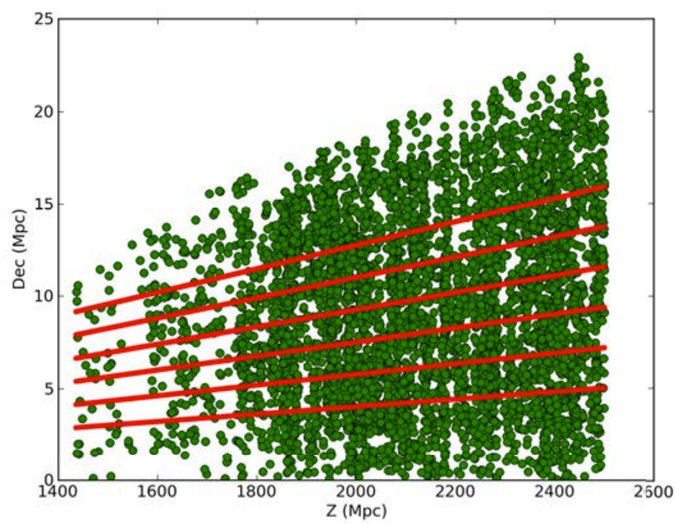

Figure 5.4: Coverage of the DEEP2 field 3 in declination and redshift. The green circles are the locations of the optically identified DEEP2 galaxies. The red lines are the pointing centers of the radio observations.

In general the strong line-spectrum RFI is flagged. To accomplish this the cross-polarization information was used. Since RFI is in general highly polarized, any strong signals in the cross-polarizations should be RFI. In order to determine the RFI cut, the cross-correlation coefficient of the signal from the X and Y polarized feeds is calculated as:

$$r = \frac{\sqrt{XY^2 + YX^2}}{\sqrt{XX\,YY}} \tag{5.4}$$

where XX is the X polarization power, YY is the Y polarization power, XY is the real part of the cross-power, and YX is the imaginary part of the cross power.

To flag RFI, first, anywhere in the time-frequency data stream that $r > 0.05$ is considered RFI and flagged. For each 60 second sweep of the field, the median is calculated and the frequency structure is fit to a 20th order polynomial and then subtracted from each spectrum. The RMS of the sweep is then calculated and anything above 4σ is cut as RFI as well. This results in approximately 5-10% of the data being cut.

Further RFI excision is done after the data is averaged together from all the different days. Each 2d frequency-right ascension slice is arranged as a matrix. A singular value decomposition (SVD) is then performed on the matrix.

Any real mxn matrix can be written as:

$$M = UsV^* \tag{5.5}$$

Where U is an mxm unitary matrix ($UU^* = 1$), s is an mxn diagonal matrix of non-negative real numbers, and V^* is an nxn unitary matrix which is the conjugate transpose of V. By convention the elements of s are listed in descending order, and are the singular values of the matrix. The singular values are unique to the matrix, but the matrices U and V do not necessarily have only one solution. U and V form an orthonormal basis. The original matrix can be written as:

$$M = \sum_i s_i U_i \otimes V_i^* \tag{5.6}$$

where U_i and V_i are the ith column of the matrices, and s_i is the i^{th} singular value. In this way U can be thought of as containing the vertical structure of the matrix, V contains the horizontal structure, and s is the weighting for each. The structure we are looking for should not have any broad structure in the horizontal or vertical component (right ascension and frequency). Any structure constant in right ascension will be some sort of noise, and any structure constant in frequency will be either a continuum source on the sky or broadband RFI on the ground. The 21cm wideband signal should be very small.

5.2.3 GBT Measured Beam

In order to do a flux calibration with frequency both the point source fluxes and antenna gain (in Kelvin per Jansky) must be known. The flux calibrators used were the sources 3c218 (Hydra A), 3c48, and 3c286 which are all active galaxies. To get a spectral index, all the data on NED[1] between 150MHz and 8GHz was fit to a power law. For 3c286, it deviated from a power law below 350MHz, so it was fit from 365MHz to 2.7GHz. See the plots below in Figures 5.5,5.6, 5.7, 5.8

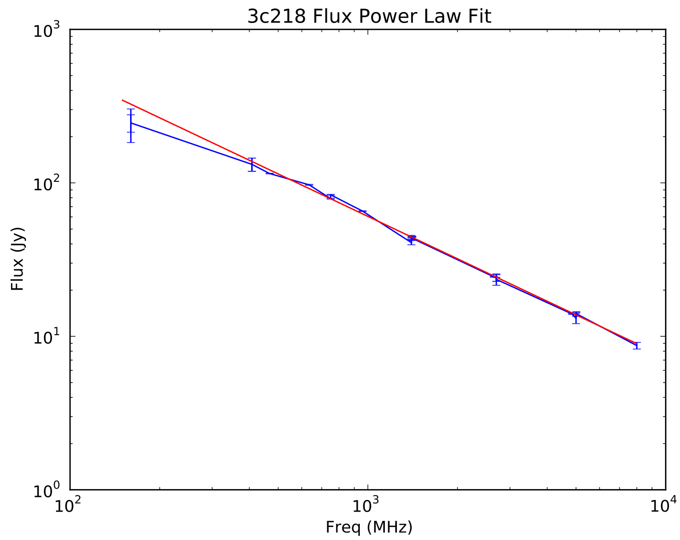

Figure 5.5: Fit to measured catalog flux for 3c218

Green Bank documentation claims the gain of the telescope at low frequencies is a flat ~1.99 K/Jy. In order to measure the gain, the beamwidth was measured. Given a measured gaussian fit round Half-Power beam width(HPBW) on the sky, θ_{HPBW}, and an assumed gaussian illuminated dish, the effective area of a telescope, A_e is then given by:

$$A_e = \frac{4\ln(2)}{\pi}\frac{\lambda^2}{\theta_{HPBW}^2} \tag{5.7}$$

[1] http://nedwww.ipac.caltech.edu/

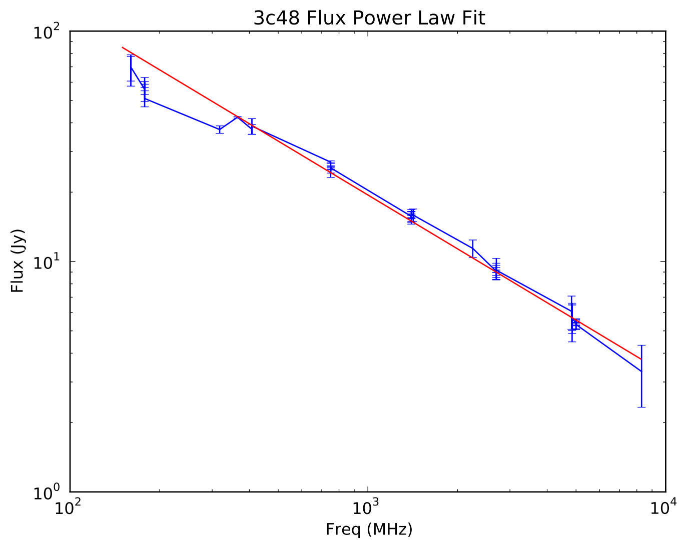

Figure 5.6: Fit to measured catalog flux for 3c48

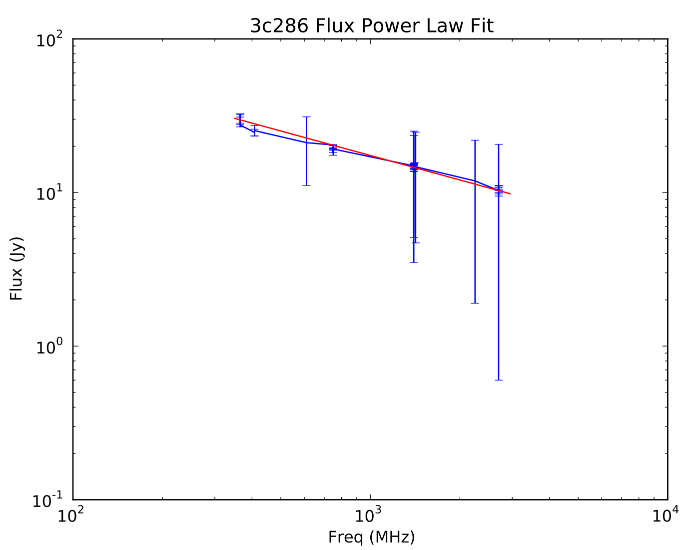

Figure 5.7: Fit to measured catalog flux for 3c286

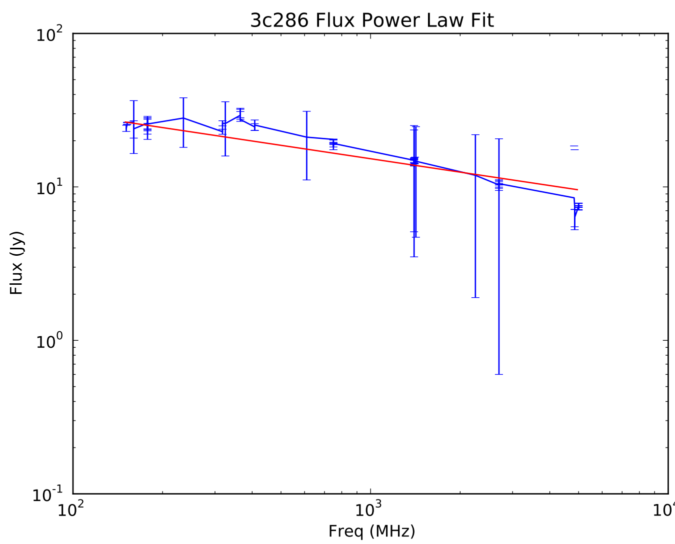

Figure 5.8: Fit to measured catalog flux for 3c286 over the wider range from 150 MHz to 8 GHz. Can see the tail off from a linear fit at about 300 MHz

where λ is the wavelength. The gain of a telescope in K/Jy is given by:

$$G = \frac{A_e}{2k_B} \tag{5.8}$$

where k_B is Boltzmann's constant, so the gain can be directly calculated from a measured beamwidth.

Using spider scans, where we scan across the source in 4 directions (see figure 5.9), on 3c286, we measured the GBT beam. The beam was then fit to a 2d gaussian, see figure 5.9, and the resultant was used to calculate a gain, which is plotted in figure 5.10. There is quite a scatter in the measurement, but there is a good bit of slope to the measured curve. 3c286 is a polarized source, which could cause an error in the measurement.

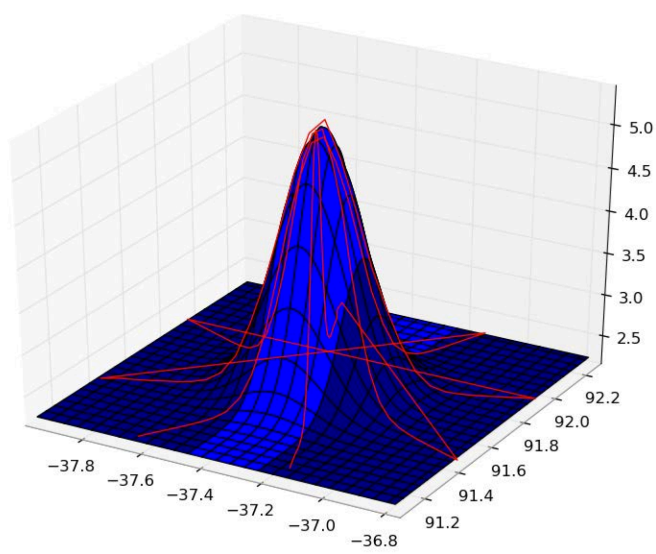

Figure 5.9: Measured GBT beam pattern example. Plotted is the actual scan data in red, and the 2-D Gaussian fit surface below.

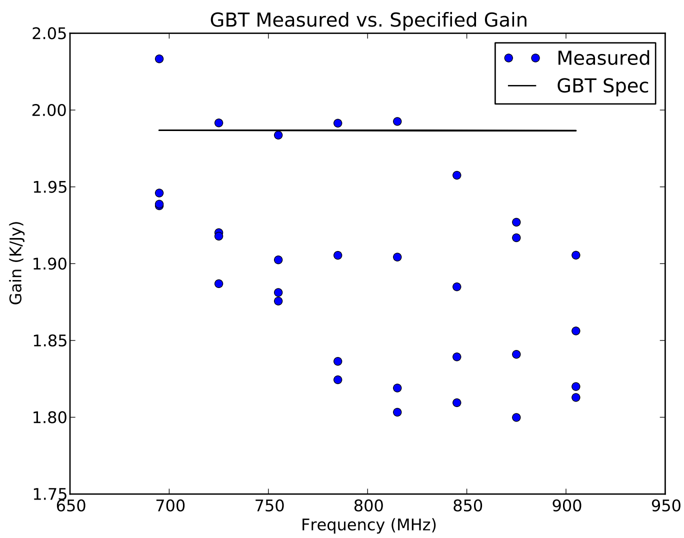

Figure 5.10: Measured GBT gain vs. expected gain. Units in Kelvin per Jansky.

5.3 Results

5.3.1 Cross-Correlation with zCOSMOS

In order to continue detection of neutral hydrogen at redshift of one, another redshift optical survey was targeted, the zCOSMOS survey [41]. We used a drift scanning technique and daisy scanning for these observations, see section 5.2 for a review of the scanning strategies. However, for the actual data analysis only the drift scans were used. It has thus far been found that the daisy scans were not stable enough to actually use. Plots of the field coverage and scans are shown in figure 5.19.

The data was calibrated using a combination of astronomical observation and the noise diode switched in and out every 0.5 seconds. An astronomical flux calibration source was observed multiple times throughout an observing session. See figure 5.6 and others in section 5.2.3. These observations were used to calculated the temperature of the noise diode with frequency. This frequency structure was then fit to a 20th order polynomial. An example of the fit is shown in figure 5.11

The noise diode calibration temperature with frequency was found to be very stable. We did however calculate the T_{cal} value to use for every session from a source on the the sky.

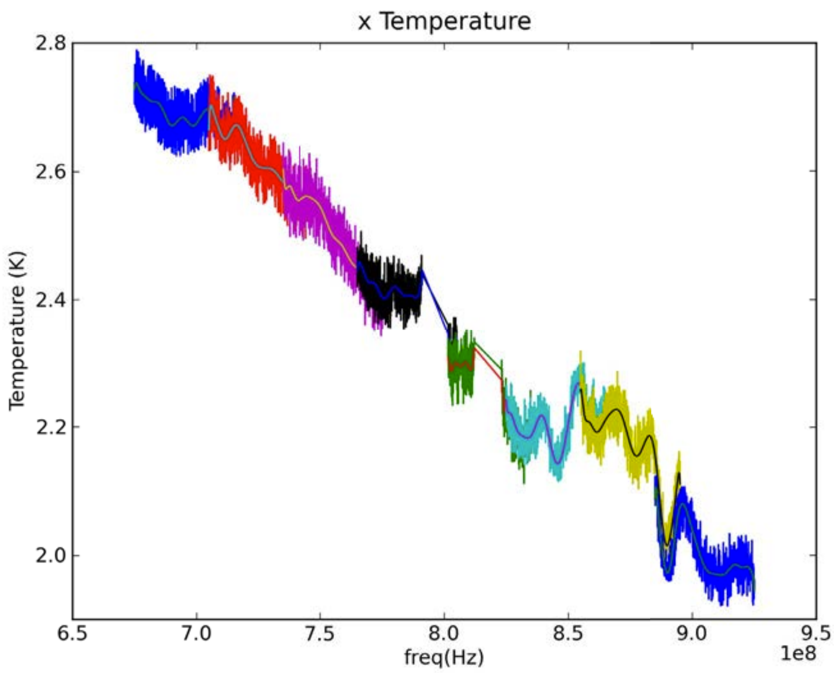

Figure 5.11: Fit of the noise cal with frequency using 3c218 as the flux calibration source. Each 50MHz overlapping frequency window was fit to a 20th order polynomial. This fit was used then for the session to calibrate the system temperature.

We found that the calculated T_{sys} using

$$T_{sys} = \frac{CAL_{off}}{CAL_{on} - CAL_{off}} \tag{5.9}$$

where CAL_{on} and CAL_{off} are frequency averaged raw data counts divided by exposure time per bin. This calculated T_{sys} had major spikes high or low approximately every 3 seconds, see figure 5.12. In order to use the data, for each drift scan T_{sys} is calculated, and if it varies from the median by more than 5% then that particular time bin is cut.

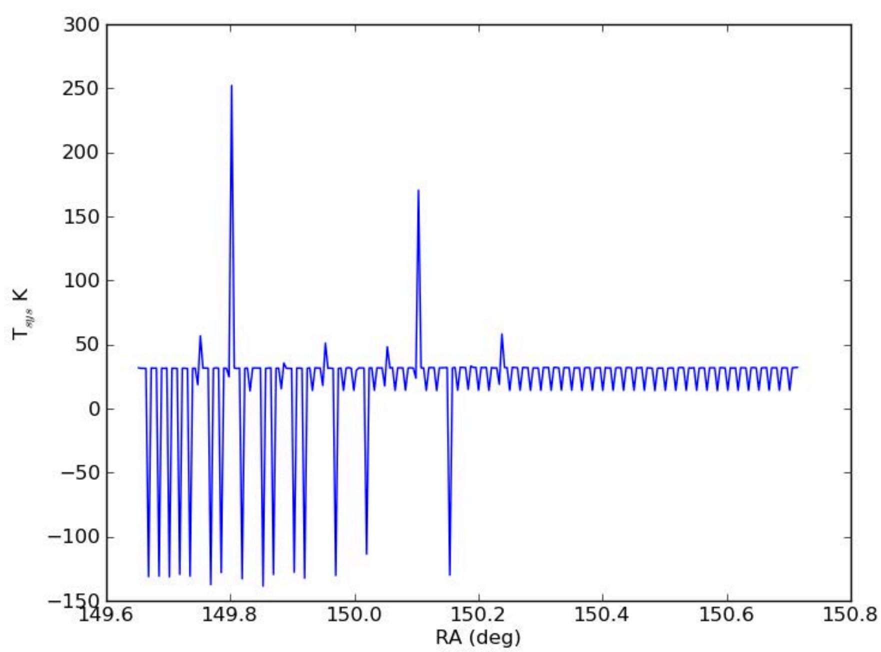

Figure 5.12: The T_{sys} calculated for one particular scan of the zCOSMOS field, averaged over the 755 MHz 50 MHz window. There was a major problem with the data approximately every 3 seconds. The data was flagged here for a T_{sys} that varied more than 5% from the median for that particular scan. This problem has been identified as a problem with the doppler tracking of the GBT system.

Then RFI is flagged using the method described in section 5.2.2.

For the data set used, 15 drift scan maps were made, each with 9 strips 255 seconds long. This gives a total on sky integration time of ∼9.6 hours. The data from the 15 scans were averaged together, and the standard deviation and number of points going into the average were also recorded. The full radio map is shown in the appendix in figure A.1. This map had a total of about 5 hours of actual integration time after flagging of RFI and bad data. Using a 500kHz frequency bin (approximately 2 h^{-1}Mpc), an integration time per angular pixel of 40 seconds (after some smoothing) and a T_{sys} of 30K, this should give a map RMS of 670 μK. After the SVD and binning to the same resolution, the map RMS is approximately 980μK, see figure 5.13a. The remaining signal is only a factor of 2 higher than the expected thermal noise.

The full radio maps are shown in the appendix. Figure A.1 is the mean value of the multiple days of data. The statistical variance is shown in figure A.2. This variance is calculated as the standard error on the mean. Single examples are shown in figure 5.14

I found that the SVD was dependent on the mask value used in the matrix, and did not clean up the better regions of data as well when the strong RFI regions were included. The SVD would leave a visible offset from zero of a smooth function in the clean regions. Therefore I restricted the frequency range from 720MHz to 790MHz. This was done by performing an SVD on the data, and looking for

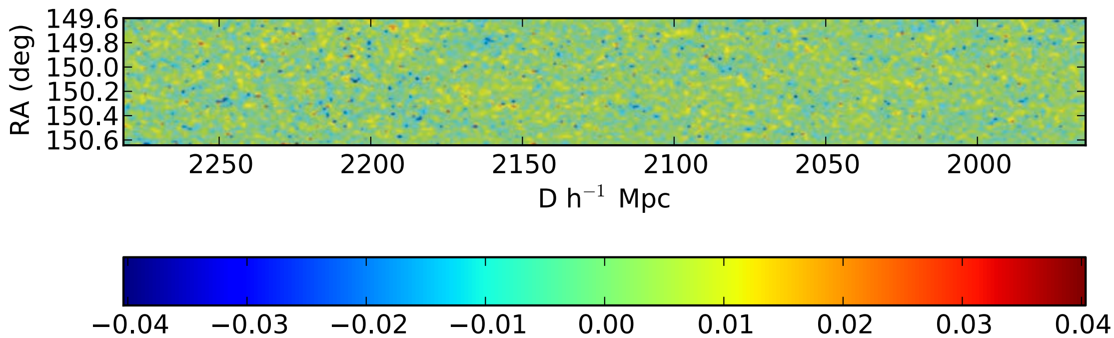

(a) Temperature

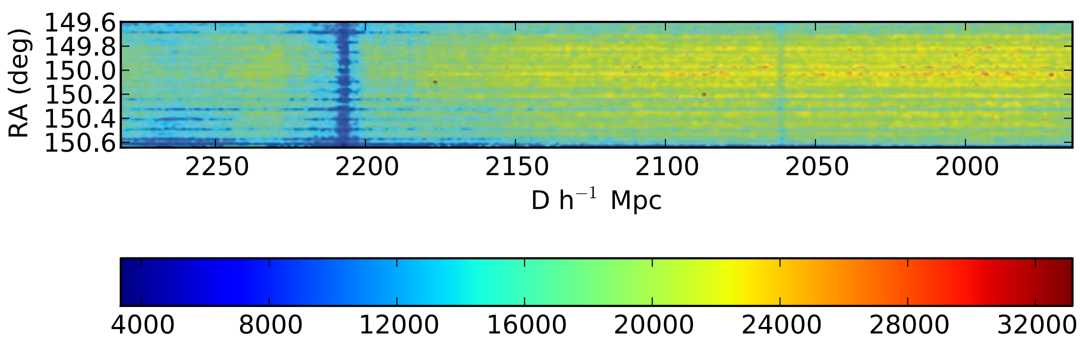

(b) 1/Variance

Figure 5.13: Radio and Variance maps of zCOSMOS data. This is one declination of the map that was stacked to calculate the cross-correlation. The second map is the weighting for each pixel used. Higher frequencies are weighted more.

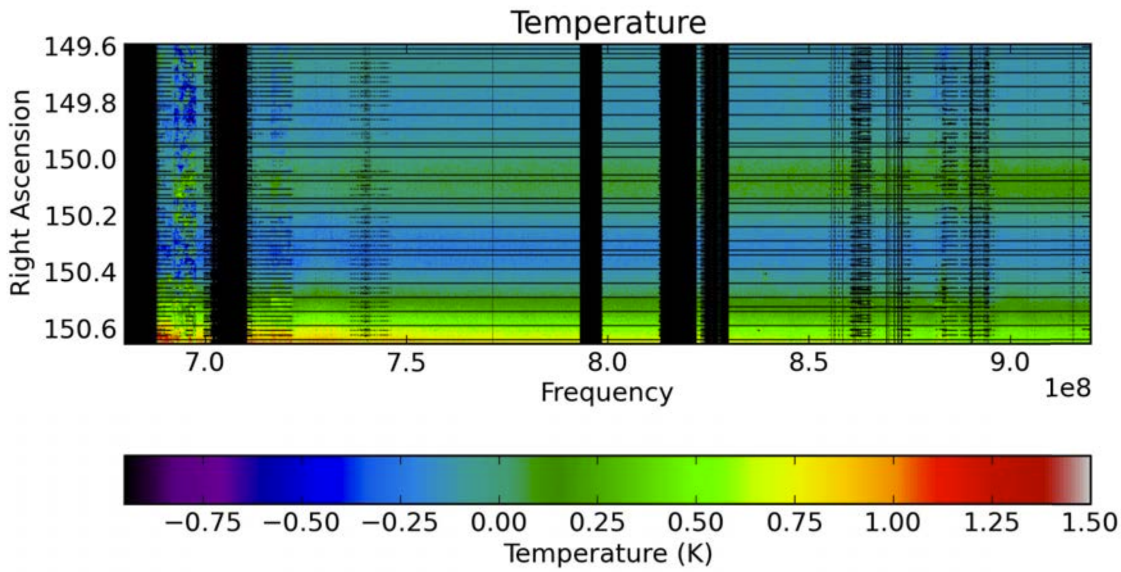

(a) Temperature

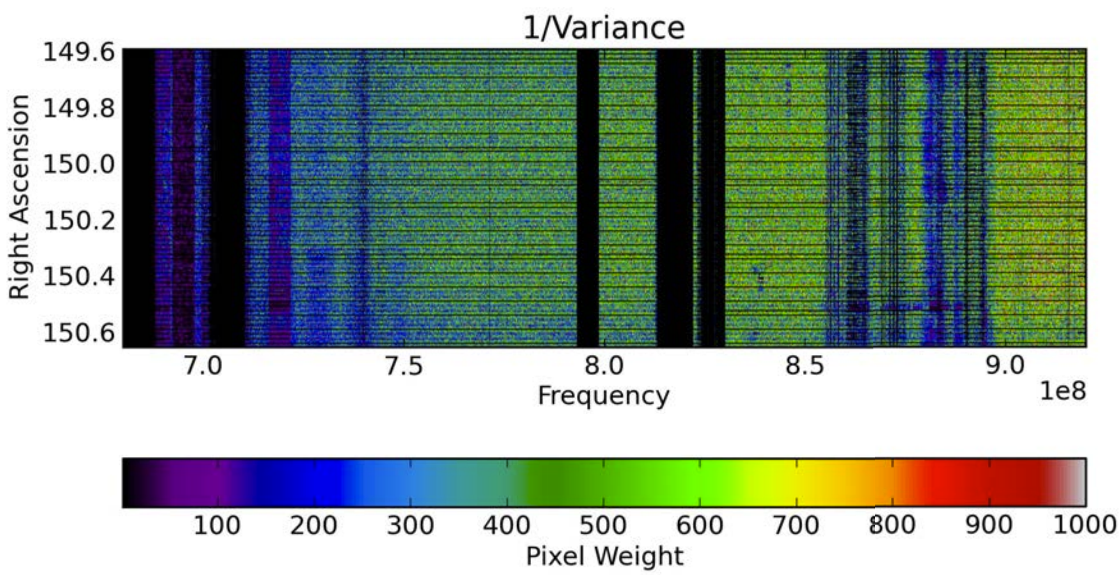

(b) 1/Variance

Figure 5.14: Example Radio and Variance maps of zCOSMOS data. These maps are at full resolution, as data was taken. 15 observations are averaged together. The temperature map shows the continuum structure, and how much data is cut due to RFI and flagging due to system issues. The 1/Variance map shows how each pixel was weighted for use in the data analysis. Higher frequencies were consistently weighted higher.

the largest clean contiguous region. Then the other regions of data were removed, and the SVD performed only on the clean region. The selected region then did not have any visible broad frequency structure.

The SVD was performed in two stages. First an SVD was performed on the raw data matrix of frequency vs. RA, and the first 6 SVD modes were removed. The average and standard deviation were calculated and any pixel over 2 sigma was cut. This data was then binned dividing the resolution by 10 in the frequency direction and 5 in the RA direction taking the inverse variance weighted mean of all uncut data, and this resultant map had a second SVD performed, with the first 2 SVD modes removed.

The resultant map is then cross-correlated with the zCOSMOS data set. There are approximately 1000 zCOSMOS galaxies within our observed field and redshift range restricted from 720MHz to 790MHz. The cross-correlation is done with a stacking method. For each galaxy in the zCOSMOS catalog that is within the observed radio region, the radio data pixel that is nearest to the point in right ascension and declination is chosen, and the surrounding spectra are averaged together. The resultant spectrum is then centered on the galaxy redshift, and the surrounding +/- 100 h^{-1} Mpc is saved. The radio spectra for all the galaxies are thus averaged together, using the variance of each pixel as a weighting. The positive and negative parts of the spectrum are averaged together, and the resultant gives the cross-correlation.

In order to calculate an estimate for the error as well as test if the signal is real, a null test was performed. The optical zCOSMOS data redshift information was randomized, and the cross-correlation was again performed. The randomization was done both by shuffling, which keeps the histogram of the zCOSMOS catalog the same but still randomizes the data, and with a flat ra,dec and redshift distribution with the same number of galaxies within the observed region. The randomizations were repeated 256 times, and the average and standard deviation of the resultant cross-correlations calculated. The the cross-correlated data is then plotted vs. lag, using the standard deviation of the null test as the error bars. The plot is shown in figure 5.15. The excess shown is about 0.15 mK. The two randomizations are show in figures 5.18 and 5.17. The random optical map that preserved the redshift/angular distribution showed a bit more structure in the resultant cross-correlation. Both would have shown expected structure if the errorbars were the error on the mean (factor of 16 smaller) which are the more appropriate errorbars to display for the null test.

Also plotted in figure 5.15 is a theoretical $\xi = (r/3.5)^{-1.66}$ correlation taken from [16] which is convolved with a velocity dispersion term, a gaussian with width 300km/s at z=0.8, and set to 1.5×10^{-4}K at zero lag.

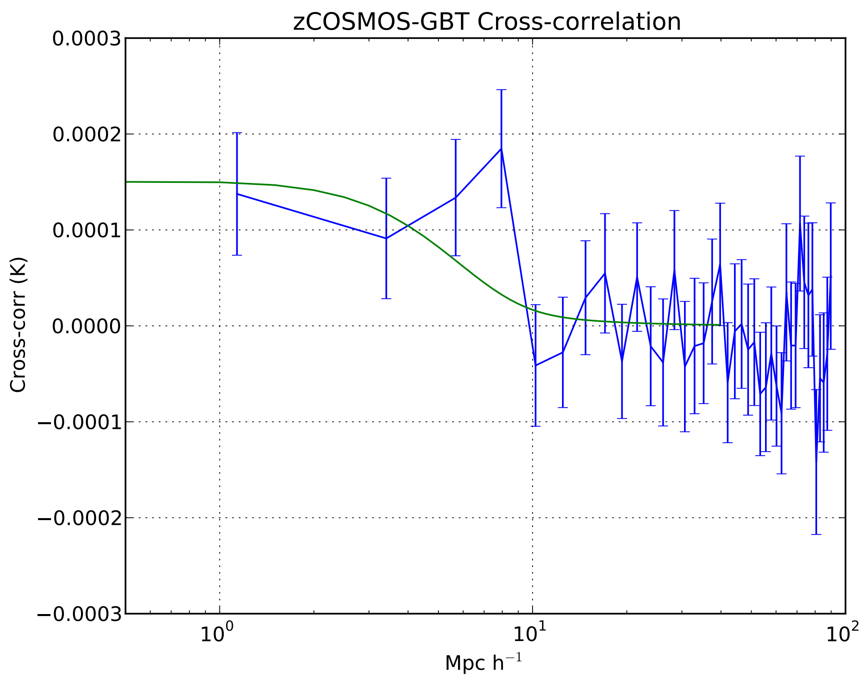

Figure 5.15: Cross-correlation by stacking of the radio and optical maps shown in figure 5.13a on the optical zCOSMOS data catalog. Consistent with a 150μK cross-correlation.

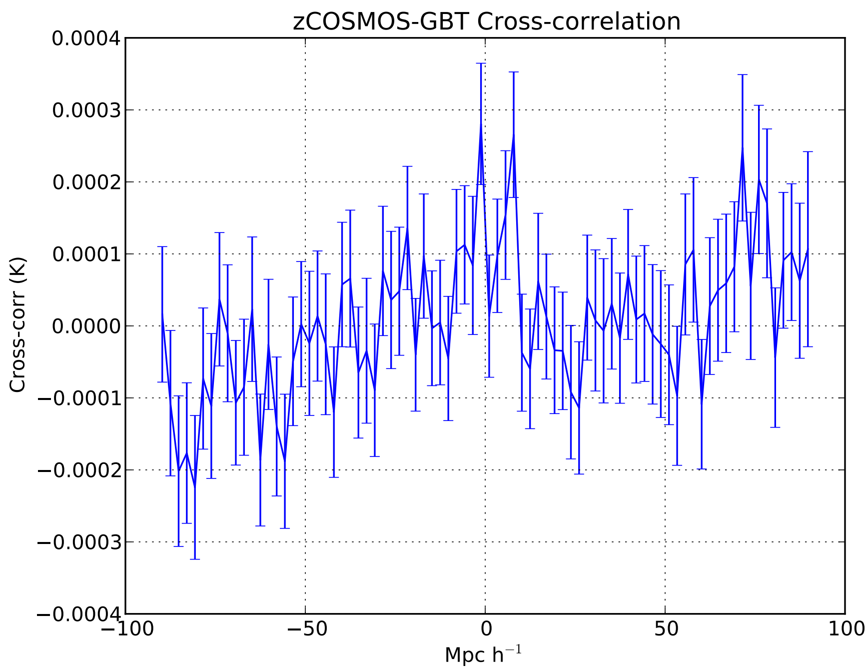

Figure 5.16: Cross-correlation of the radio and optical maps shown in figure5.13a with the zCOSMOS optical data. Shown in both the positive and negative frequency directions on a linear scale. At greater than 50 h^{-1} Mpc the noise looks higher.

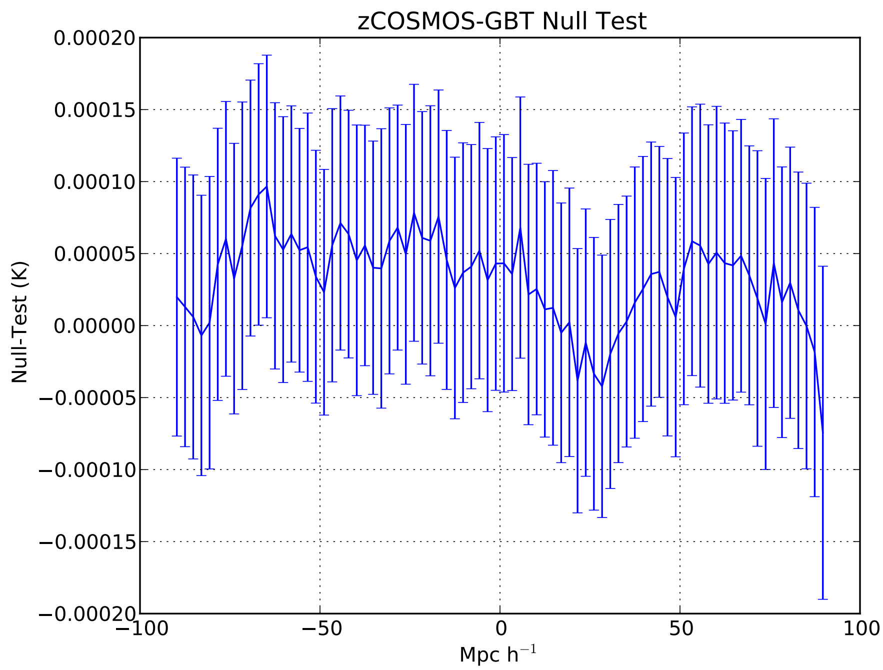

Figure 5.17: Null test of the cross-correlation. The optical data redshifts were shuffled randomly and the correlated with the radio. 256 realizations were computed, and the average and standard deviation are plotted. This standard deviation is what was used as the error on the cross-correlation shown in figure 5.16. The error on the mean is 16 times smaller.

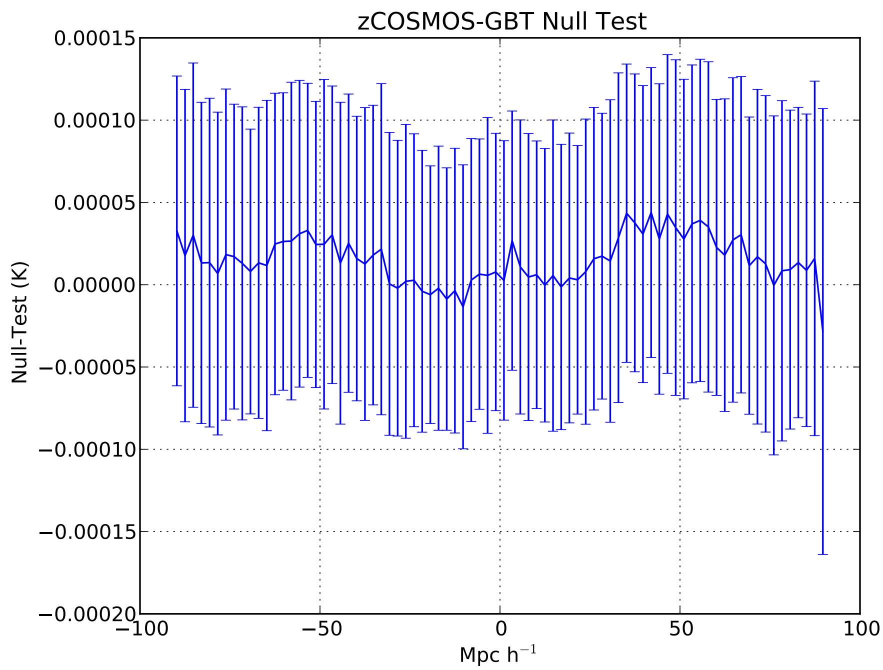

Figure 5.18: Null test of the cross-correlation. A randomly generated optical catalog evenly distributed in redshift, right ascension, and declination was correlated with the radio. 256 realizations were computed, and the average and standard deviation were plotted.

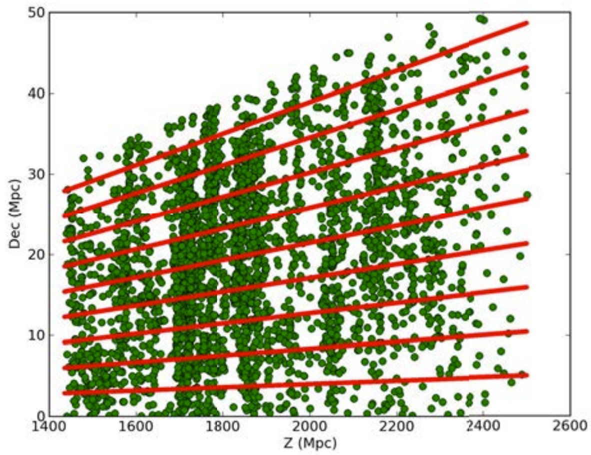

(a) Dec - Redshift (Mpc)

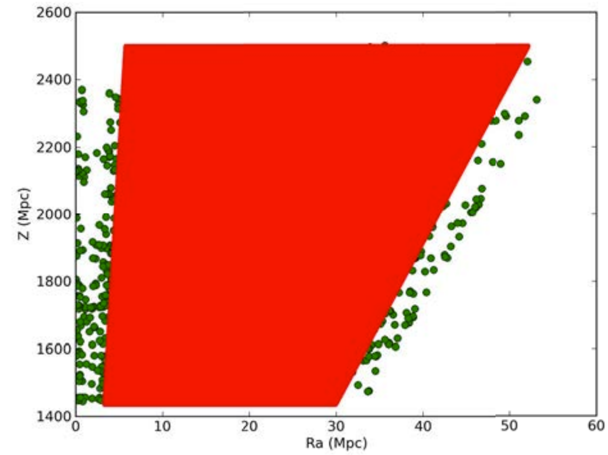

(b) Ra - Redshift (Mpc)

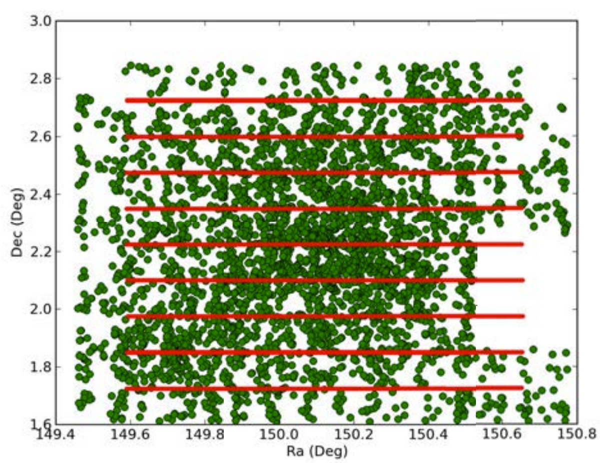

(c) Ra - Dec (deg)

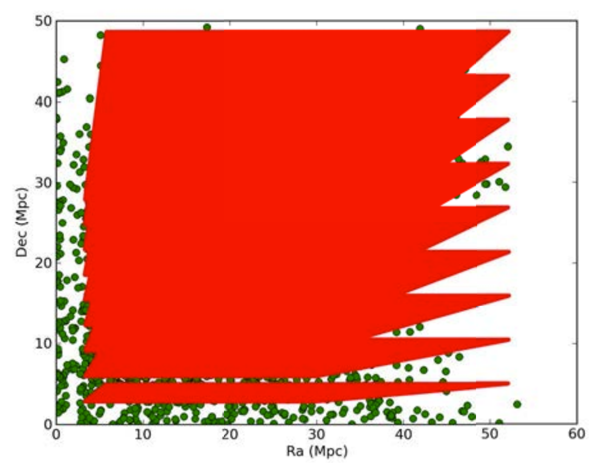

(d) Ra - Dec (deg)

Figure 5.19: Coverage of the zCOSMOS filed. Red is the radio data. Green circles are the locations of galaxies identified in the zCOSMOS survey.

5.3.2 Cross-Correlation with DEEP2

We used the Green Bank Telescope to make the first detection of 21 cm Hydrogen at a redshift of ~ 0.8. This data was taken before the zCOSMOS data. The first optical survey region we observed were the DEEP2 [16] fields 3 and 4. Field 3 is a roughly 2° by 0.5° field at about 23.4 hours right ascension and 0° declination. See figure 5.2 for a plot of the optical and radio coverage. Field 4 is at about 2.5 hours right ascension, 0.6° declination, and is roughly 1.5° by 0.5° in size. See figure 5.20 for a plot of the optical field and the radio coverage.

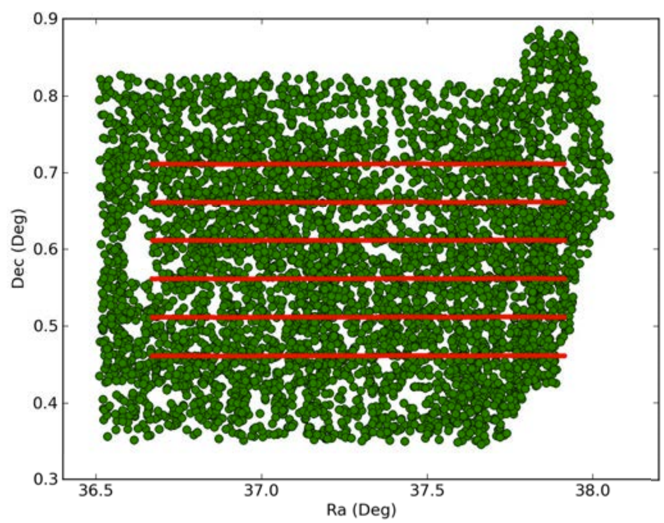

Figure 5.20: Coverage of the DEEP2 field 4 in right ascension and declination. The green circles are the locations of the optically identified DEEP2 galaxies, giving an idea of the optical survey angular coverage. The red lines are the pointing centers of the radio observations.

First, anything with greater than 5% polarization was flagged and cut. The data was then calibrated into units of temperature and averaged together. This results in a map like the top of figure 5.21. Then an SVD continuum and RFI removal was performed. The resultant radio map is then weighted with the inverse variance of each pixel to down-weight the regions with RFI still remaining. This results in the map shown in the middle panel of figure 5.21. This figure uses $\Omega_m = 0.24$ and $\Omega_\Lambda = 0.76$. The 3d radio map is then correlated with the 3d optical map, which results in the correlation function shown in figure 5.22. This technique was primarily done by Tzu-Ching Chang and published in Nature[14].

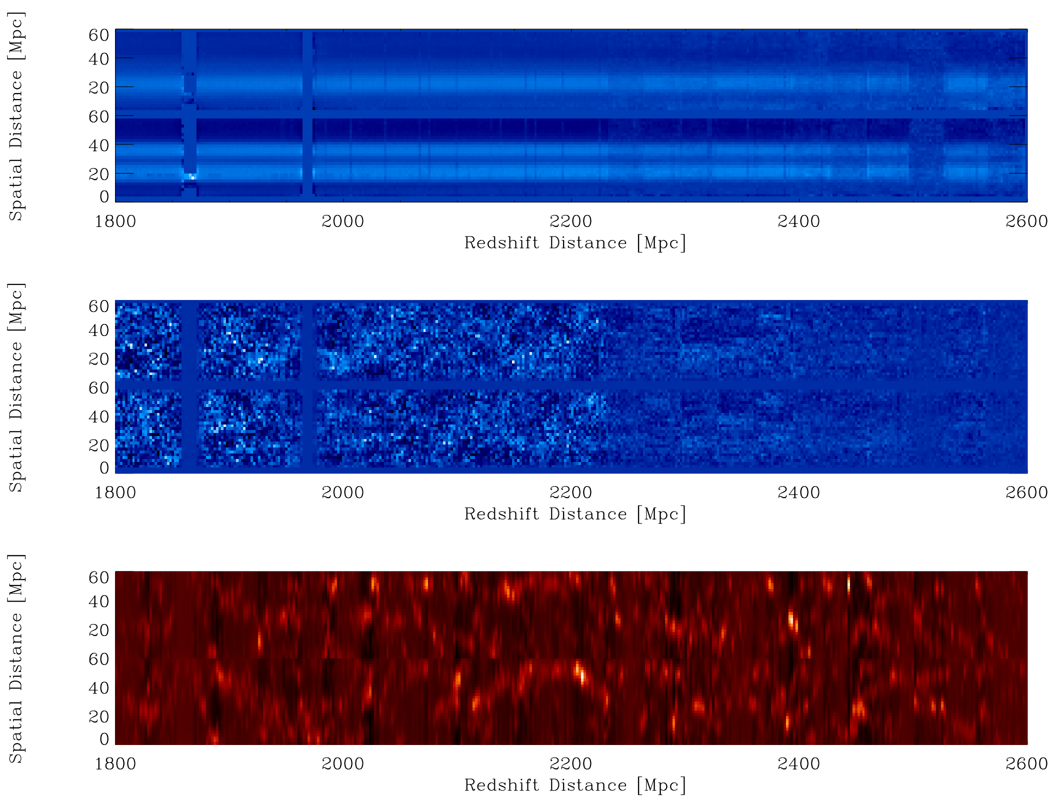

Figure 5.21: Deep2 field 4 maps. Top is a 2-D plot of the radio map before SVD continuum source removal. Middle plot is the radio map after SVD removal, used to cross-correlate. Bottom is the optical map binned to 2 h^{-1} pixels.

I conducted another method of cross-correlation. Instead of smearing out

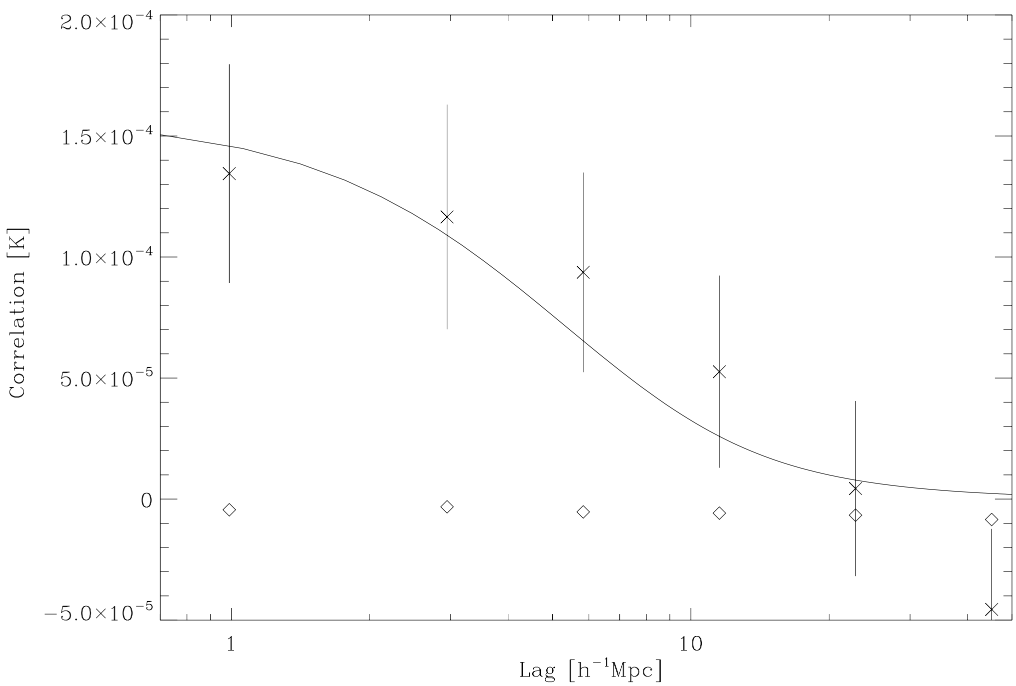

Figure 5.22: Cross-Correlation of the radio and optical maps shown in figure 5.21. The diamonds across the bottom are the average of the Null test. The line is a model of the expected signal, with the zero lag signal fit to the data.

the optical field to the radio resolution, I carried out a stacking sum. The optical field was not treated as a density field, but instead a catalog of points. For each point the nearest radio data point was found in angle and redshift. In the angular direction the data within the GBT beam around that point was averaged together, and the spectra +/-100 h^{-1}Mpc from that point was recorded. Then each of these spectra centered on galaxy points were averaged together. This technique of stacking is less sensitive to the exact nature of the optical field and weighting functions.

The radio maps were made in a similar way to the previous analysis. Discussion of the exact radio map data reduction process is in section 5.3.1. An example of the raw data radio map and the variance weighting map is shown in figure 5.23. Almost 50% of the data is cut due to RFI removal or systematic problems with the data taking.

All of the raw maps in Right Ascension and Frequency for each of the six declinations are shown in the appendix A in figure A.3 for field 4 and in figure A.5 for field 3. The inverse variance maps, used to weight each pixel, are shown in figures A.4 and A.6 respectively. My temperature maps binned in the same was as for the nature paper are shown in figures 5.24a and 5.24b. I used $\Omega_m = 0.275$ and $\Omega_\Lambda = 0.725$ from [38] as my reference cosmology.

My RFI cleaned and SVD removed radio map for field 3 and 4 are shown in figures 5.25 and 5.26. The data was cut to the largest contiguous frequency range with minimal RFI. The piece of used spectrum was 725MHz-790MHz for field 4, and 740MHz-790MHz for field 3.

My stacking does not cleanly show the cross-correlation, and is dominated by residual RFI and noise not removed by the cleaning. I was also using a smaller range of frequencies. Field 3 and field 4 are plotted independently. The field 4 cross-correlation is shown in figure 5.27 and the null test is shown in figure 5.28. The fact that the null-test still has structure means that there is still a residual frequency structure in the data which hasn't been eliminated by the RFI and foreground removal techniques. The cross-correlation for field 3 is plotted in figure 5.29, and the corresponding null test in figure 5.30. Field 3 showed slightly better results, however there is significant structure at high lags such that no real conclusions can be drawn thus far from this data set. Plots on a linear scale showing the positive and negative sides are shown in figures 5.31 and 5.32 for field 4 and field 3 respectively. The null test shown on the +/- scale are shown in figures 5.33 and 5.34. The residual structure is still larger than the expected signal.

The lack of a detection reported here is not meant to deminish what was previously reported in Nature. The data reduction was completely independent, and here has proven to be insufficient to reduce the noise level to the signal.

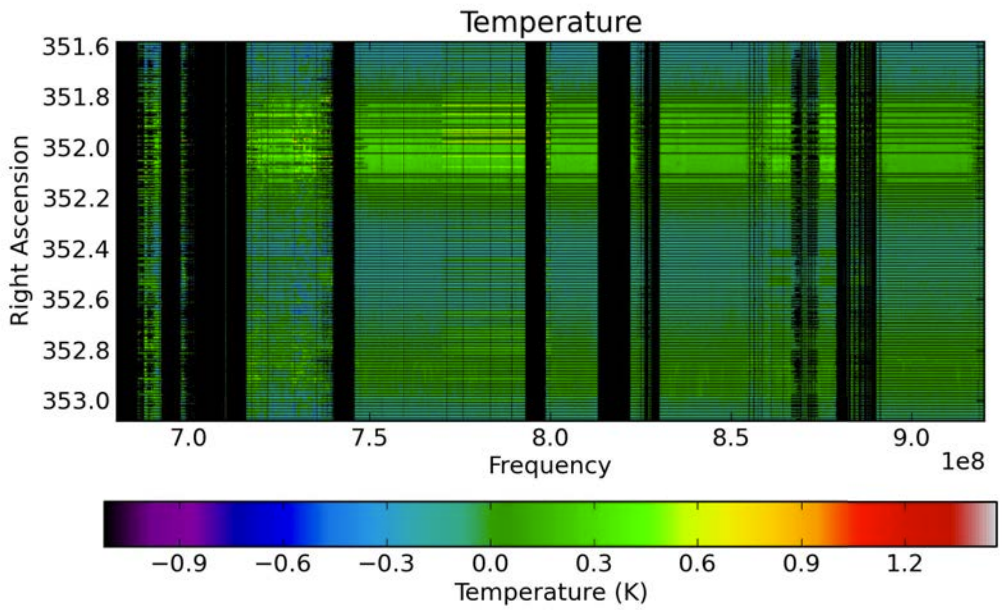

(a) Temperature

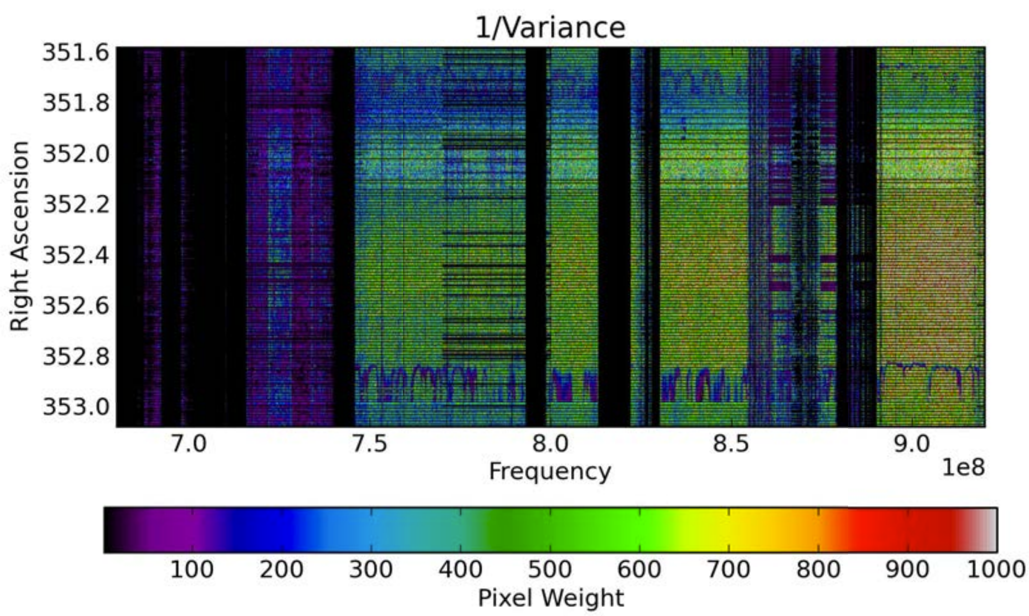

(b) 1/Variance

Figure 5.23: Example of full resolution Temperature and 1/Variance maps of the DEEP2 field3 radio data. Large portions of the data (shown in black) are cut due to RFI and systematic problems. The variance map shows the higher frequencies were given higher weight, and the systematic problems with the spectrometer still visible.

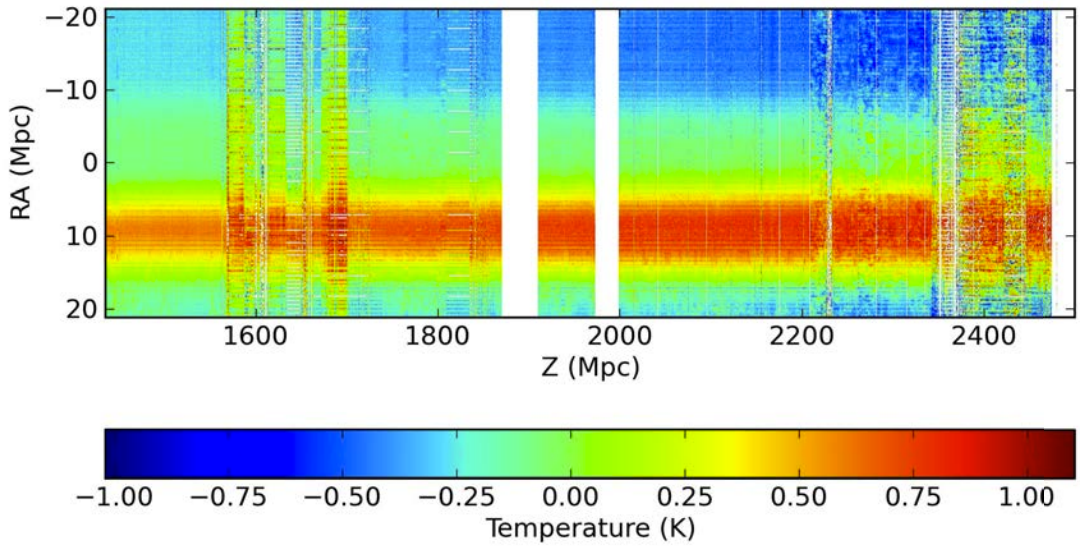

(a) First declination

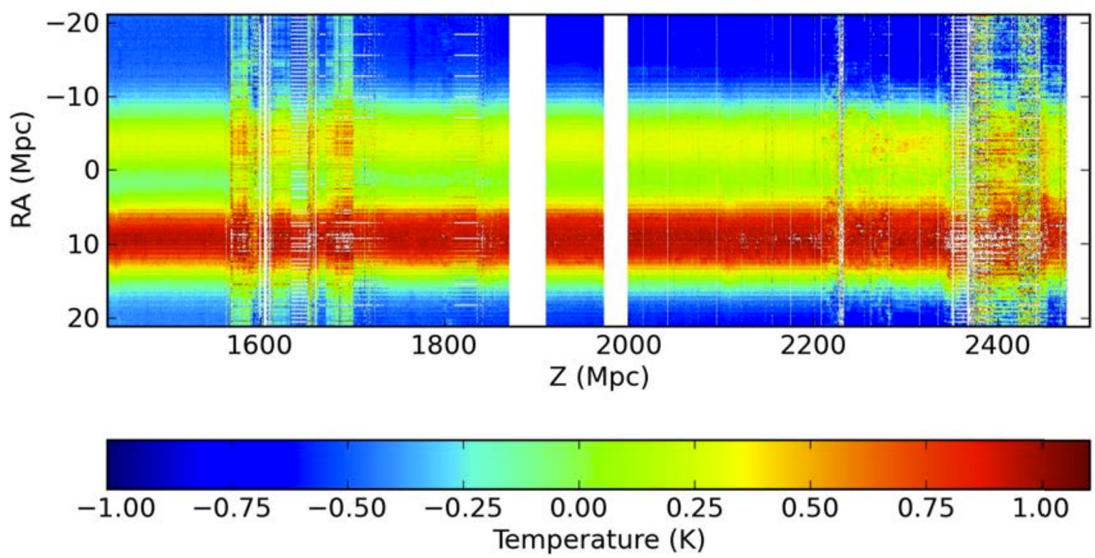

(b) Second declination

Figure 5.24: Radio map of DEEP2 field 4, Top and bottom half of the field. Comparable to the maps in figure 5.21.

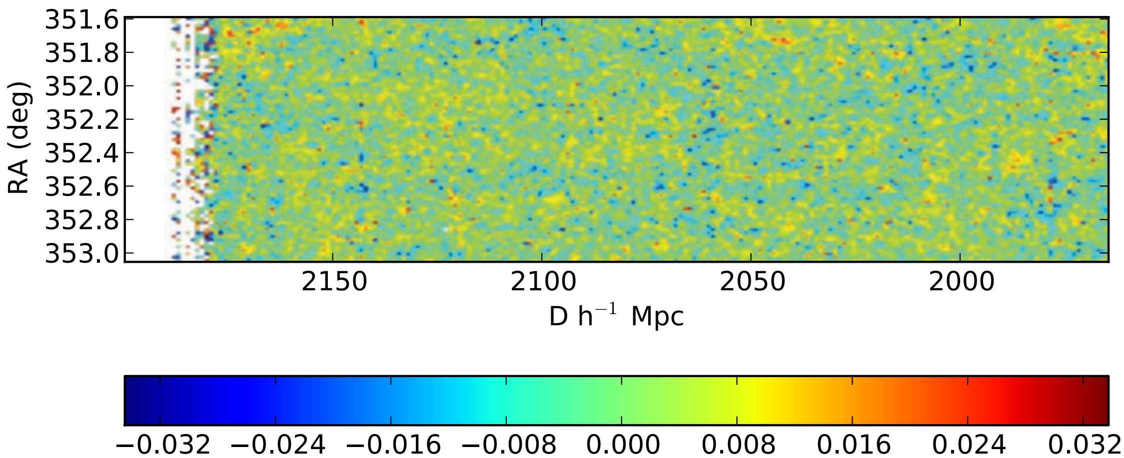

(a) Temperature

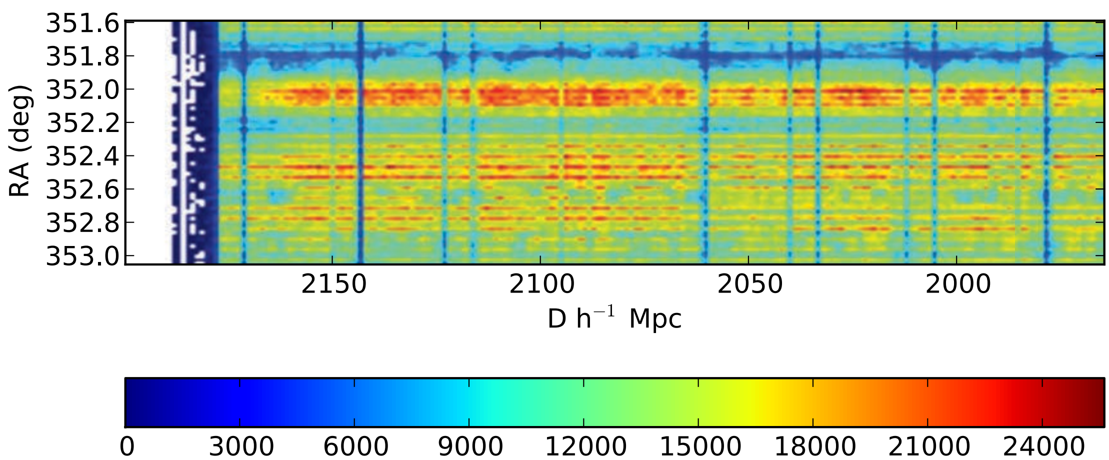

(b) 1/Variance

Figure 5.25: Radio and Variance maps of DEEP2 field3 data. This is one declination of the map that was stacked to calculate the cross-correlation. The second map is the weighting for each pixel used. Higher frequencies are weighted more.

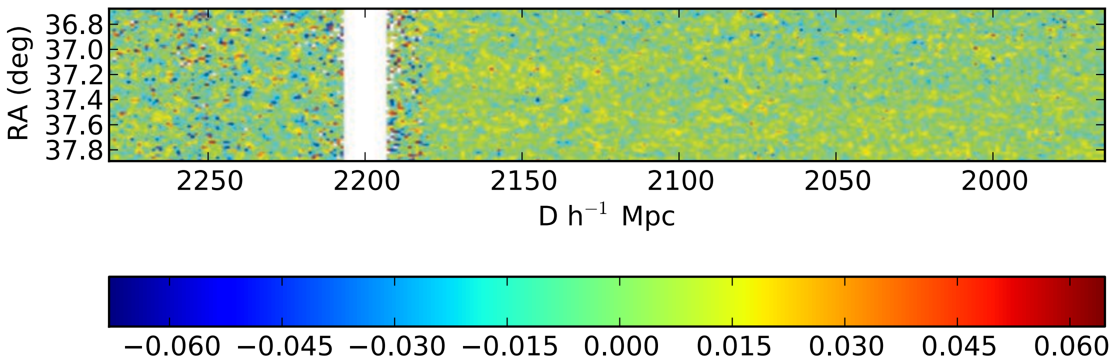

(a) Temperature

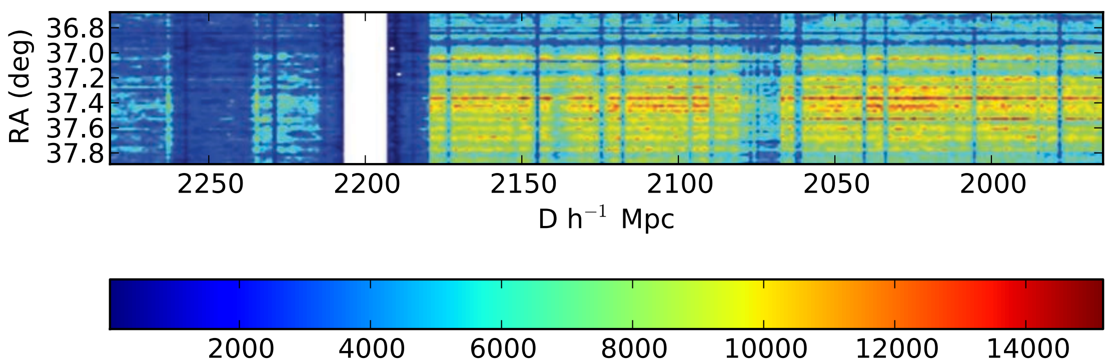

(b) 1/Variance

Figure 5.26: Radio and Variance maps of the DEEP2 field4 data. This is one declination of the map that was stacked to calculate the cross-correlation. The second map is the weighting for each pixel used. Higher frequencies are weighted more.

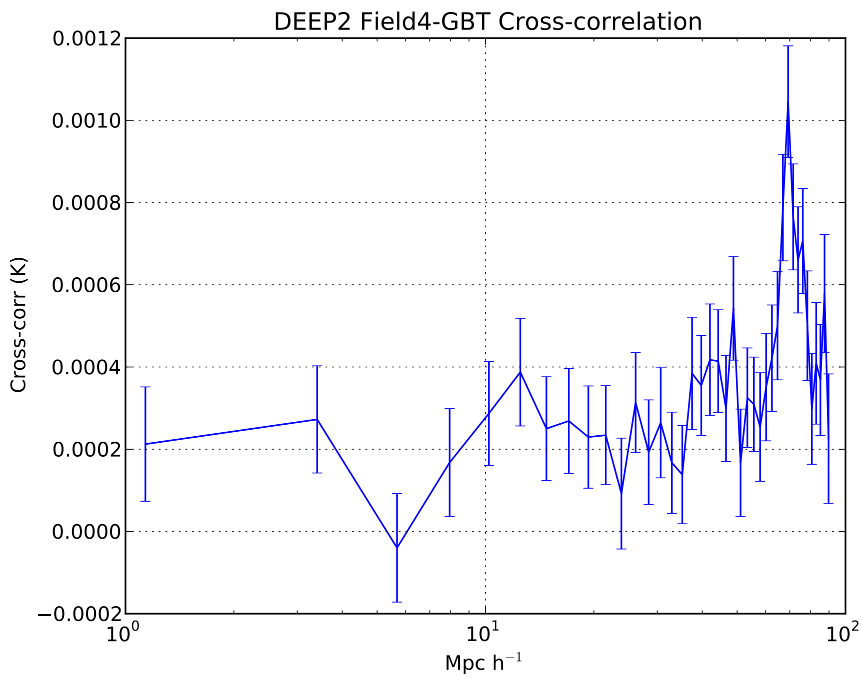

Figure 5.27: Cross-correlation by stacking of the radio data shown in figure 5.26 on the DEEP2 field 4 optical catalog. Error bars do not seem to account for all the structure seen.

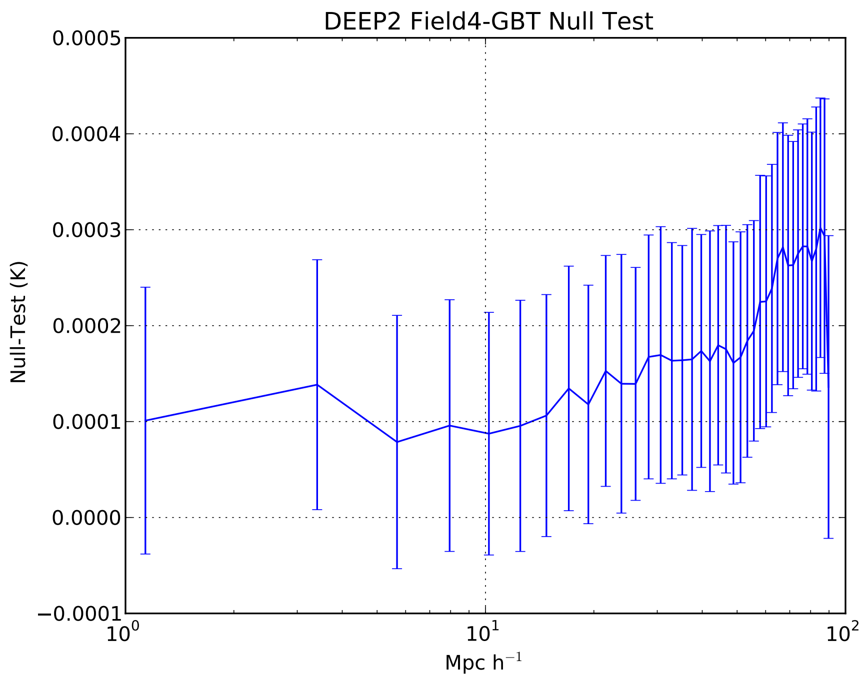

Figure 5.28: Null test cross-correlation of the radio data shown in figure 5.26 with 256 redshift shuffled optical catalogs. The mean here shows residual structure significantly deviating from zero. The standard deviation of this is used in figure 5.27.

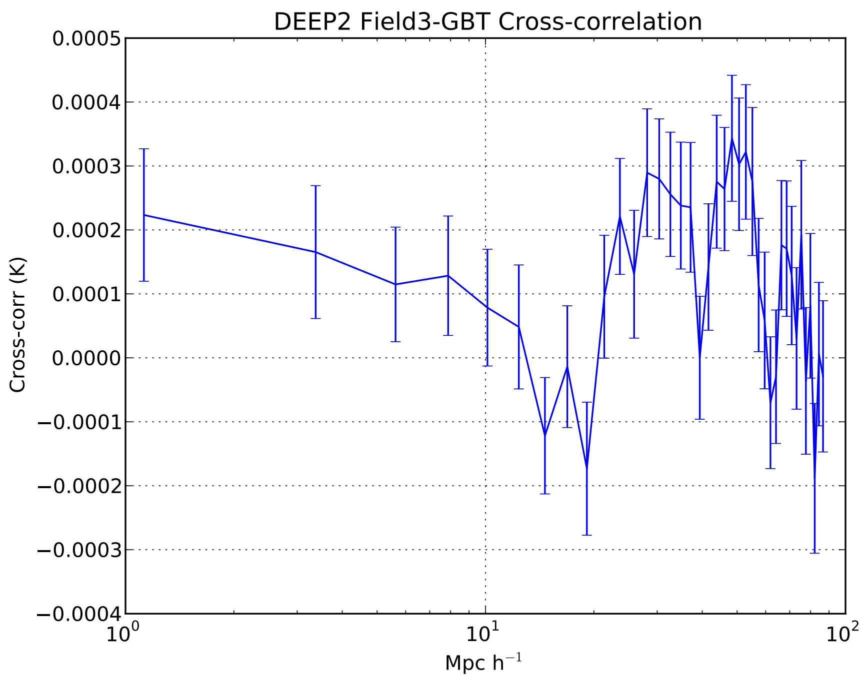

Figure 5.29: Cross-correlation by stacking of the radio data shown in figure 5.25 with the DEEP2 field 3 optical catalog. Shows residual structure at scales larger than 20 h^{-1} Mpc.

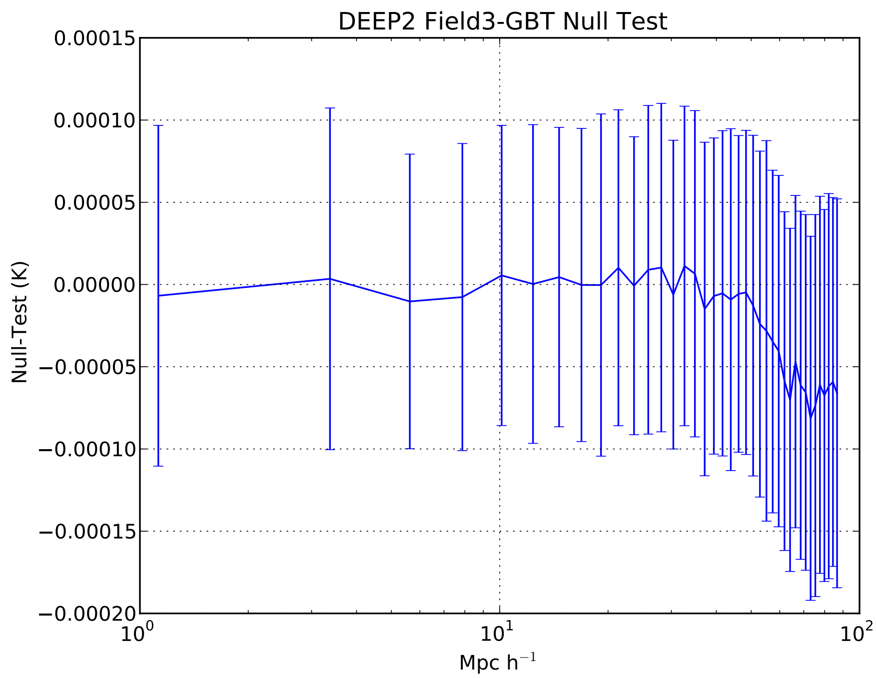

Figure 5.30: Null test by stacking of the radio map shown in figure 5.25a with 256 redshift shuffled optical maps. The mean and standard deviation are plotted. The standard deviation is used as the error estimator in figure 5.29. Deviates from zero at lag larger than 50 h^{-1} Mpc.

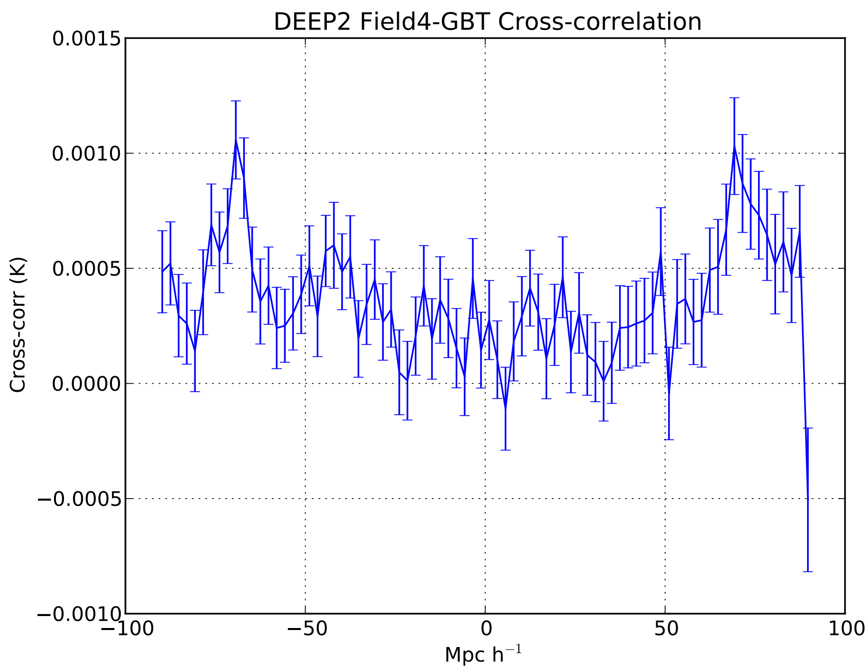

Figure 5.31: Cross-correlation by stacking of the radio shown in figure 5.26 with the DEEP2 field 4 optical catalog. Shown in both the positive and negative frequency directions. Shows residual structure much larger than the expected signal.

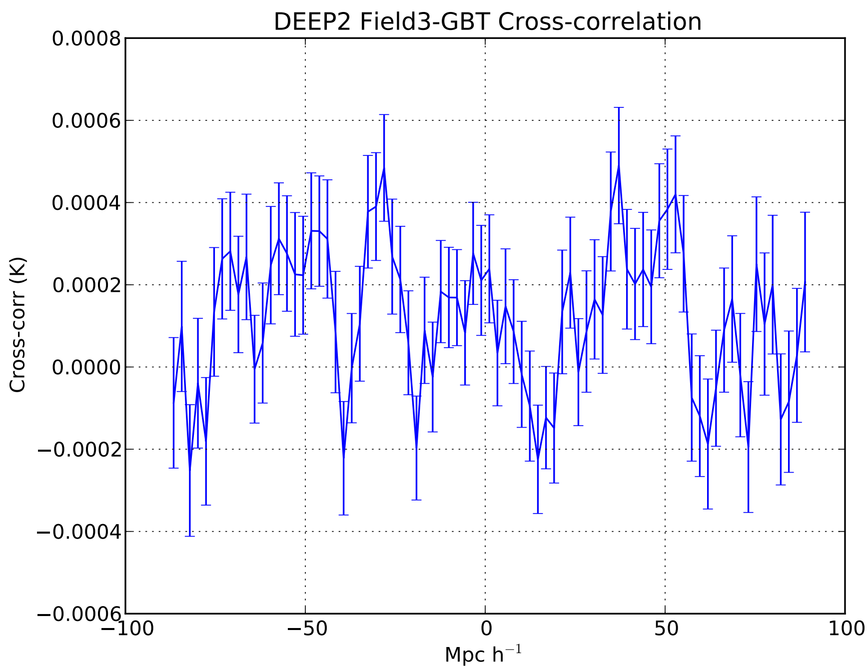

Figure 5.32: Cross-correlation by stacking of the radio shown in figure 5.25 with the DEEP2 field 3 optical catalog. Shown in both the positive and negative frequency directions. Again the structure is larger than the expected signal.

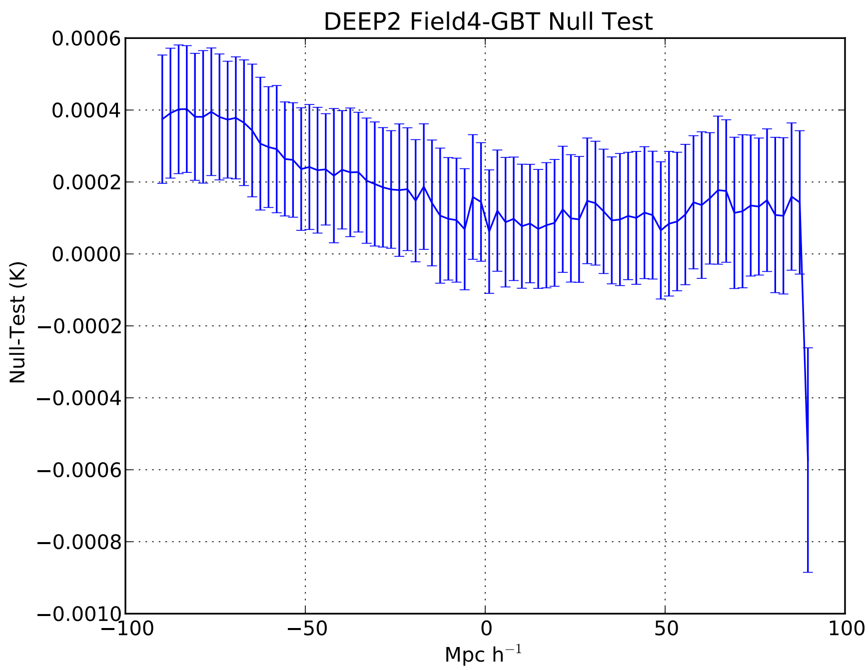

Figure 5.33: Cross-correlation of the radio shown in figure 5.26 with 256 random optical catalogs. Shown in both the positive and negative frequency directions. Systematically higher at negative lag.

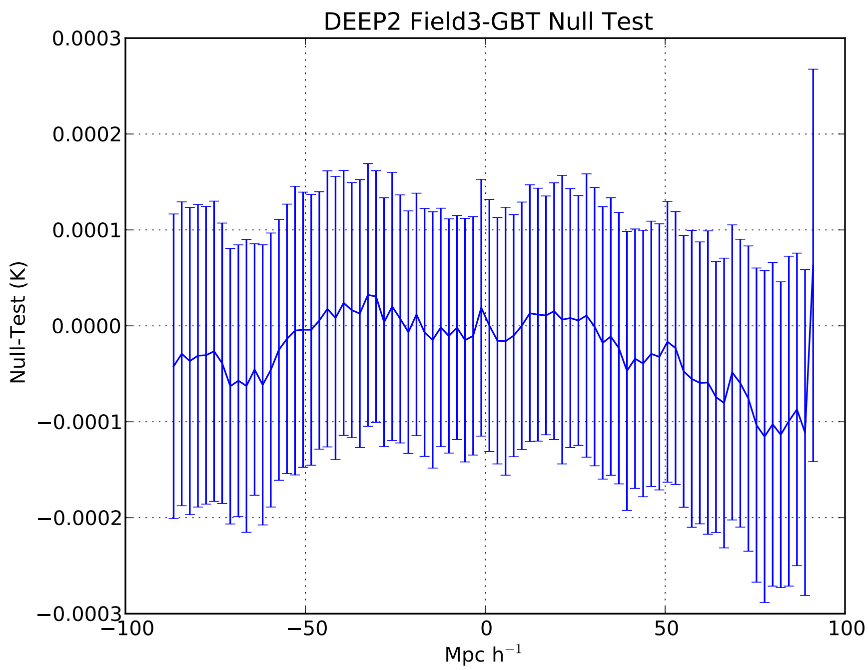

Figure 5.34: Cross-correlation of the radio shown in figure 5.25 256 random optical catalogs. Shown in both the positive and negative frequency directions. Systematically low at both positive and negative lag.

6

Next Steps with Existing Telescopes

6.1 Green Bank

At Green Bank we continue to observe with the single pixel system. We will continue to collect more data to attempt a preliminary BAO detection. As worked out in Masui et al. [47], 2000 hours of integration time may be enough to detect a BAO signal. We will continue to collect data and find the real world problems to integrate time and remove foregrounds well enough to detect the BAO signal.

6.2 Arecibo

To continue to pursue 21-cm intensity mapping, a program at Arecibo is being established. More sophisticated arguments are presented in Masui et al. [47]. With approximately 2000-10000 hours of sky time depending on actual RFI and system temperature, a marginal detection of BAO is possible.

Arecibo is a spherical reflector. It has a gregorian dome feed system which corrects the spherical aberration and allows for standard point feeds to be used instead of a line feed. We will also use a point feed, but placed at the parafocus and not at the gregorian focus. This feed can then be observing the sky concurrent with other observations using the gregorian feed system, but sacrifices total gain. This will enable the project to collect thousands of hours of data within a year.

6.2.1 Feed Design Starting Parameters

The feed was designed for the band from 700Mhz to 800MHz. It is designed to be dual polarization, and as symmetric as possible in the E and H planes. The design of the system is to match 50 ohms. The desired 3db beam-width is$\pm 20^\circ$

6.2.2 Feed Design

The feed was simulated in cocoaNEC using the NEC2c engine. The design reference frequency was 750MHz, and distances were referenced to that wavelength. The dipoles are 0.464λ long and 0.2475λ above the groundplane. The dipoles have a 5mm radius and each pair are separated by 0.5λ. The dipoles are fed with 100Ω transmission line made from #6 wire with a center to center separation of 4.7385mm. The groundplane is a circle with a radius of 0.75λ.

The results are plotted in the following figures. Figure 6.1 shows the physical design of the simulated feed. Figure 6.2 shows the corresponding far field pattern elevation plots, and figure 6.3 shows the azimuth plots. Figure 6.4 shows the overall pattern. The actual 3db beam-width is $\pm 27^{\circ}$ which is wider than optimal. However the design is not very sensitive to beam-width.

Figure 6.5 shows the impedance of the design at 750MHz. Figure 6.6 shows the VSWR over the frequency range from 700MHz to 800MHz. The antenna has a VSWR of less than 1.5 from 700MHz to 790Mhz.

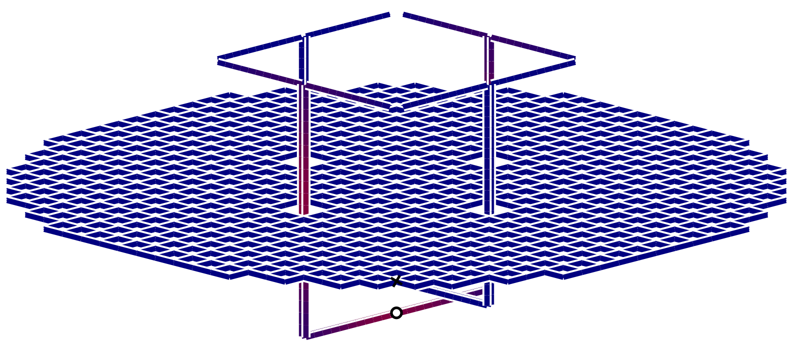

Figure 6.1: Feed physical design

6.2.3 Beam Pattern Simulation

The beam on the sky was simulated using a ray tracing technique. Using the amplitude and direction of the feed, Each ray is traced to the aperture plane with a

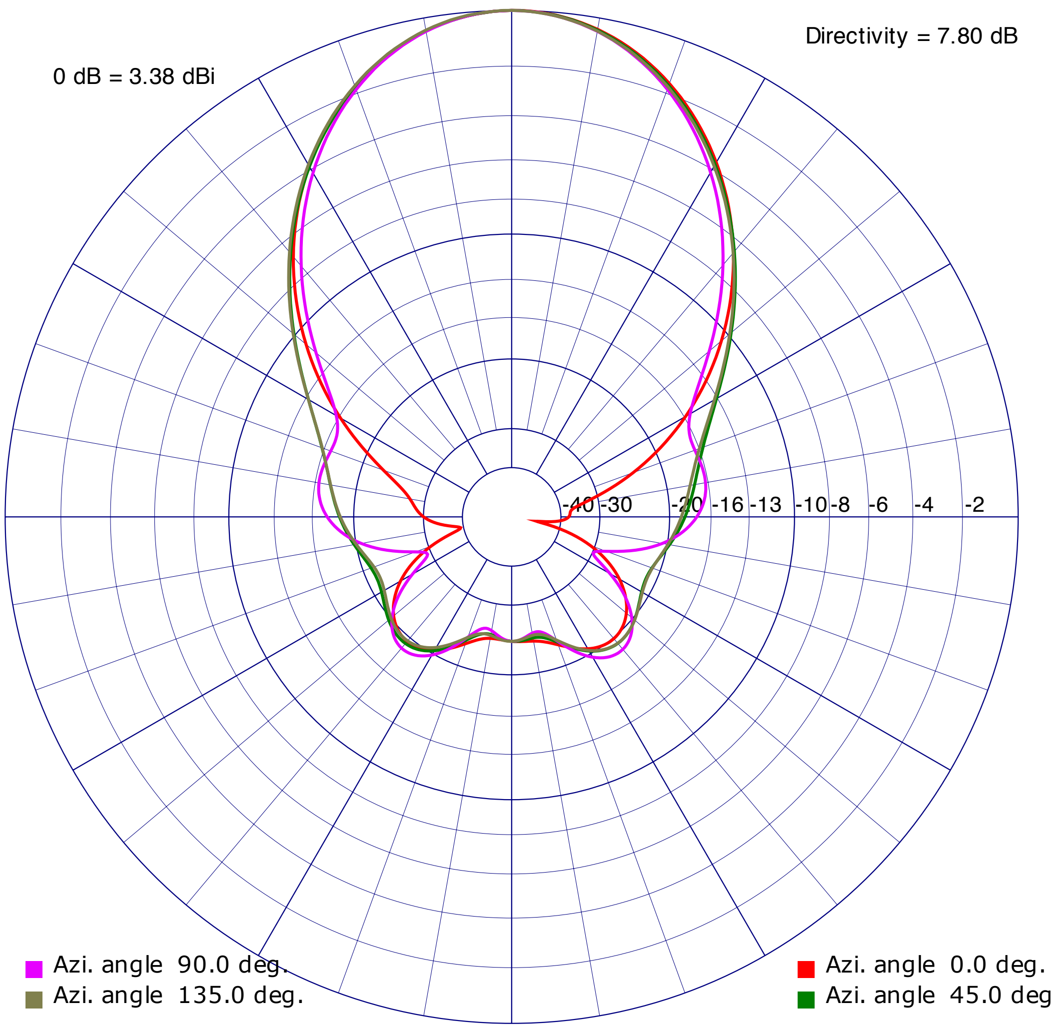

Figure 6.2: Feed elevation plots

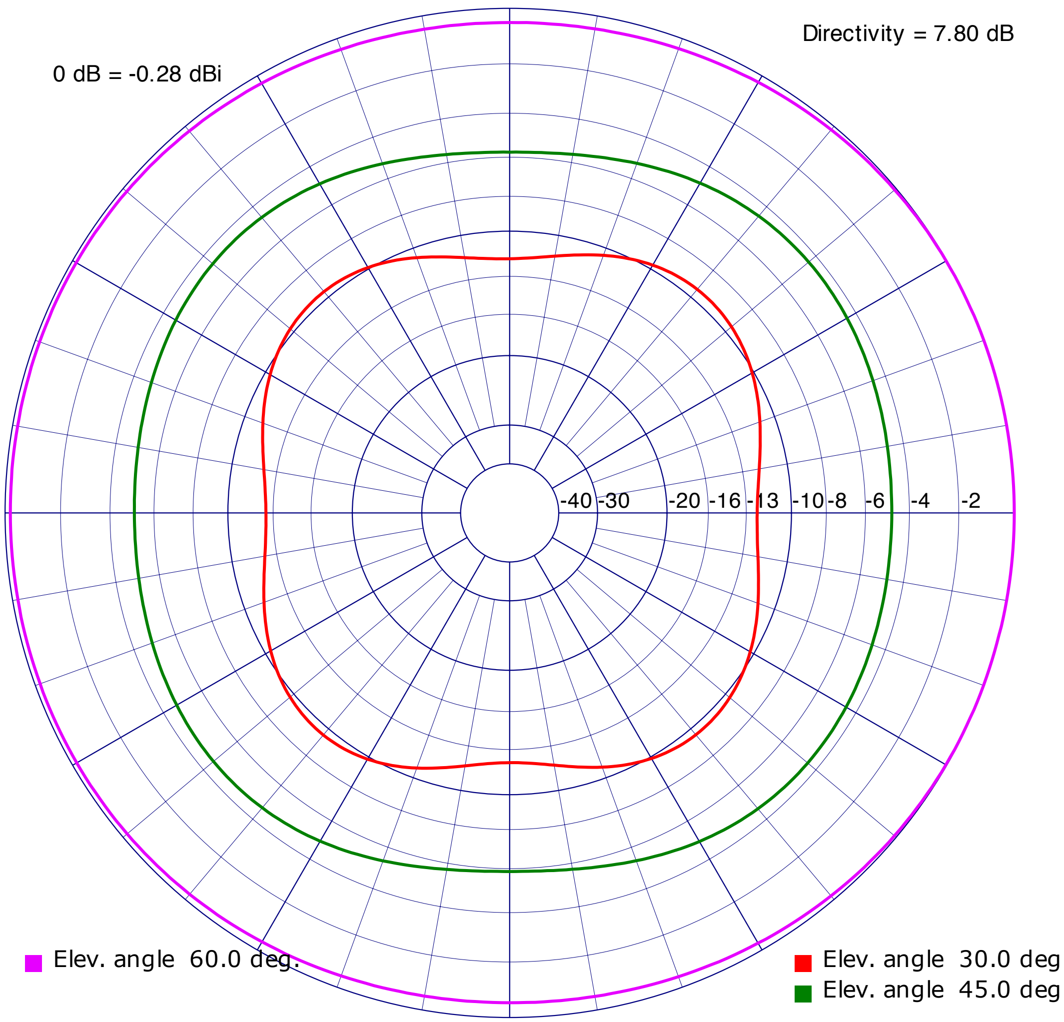

Figure 6.3: Feed azimuth plots

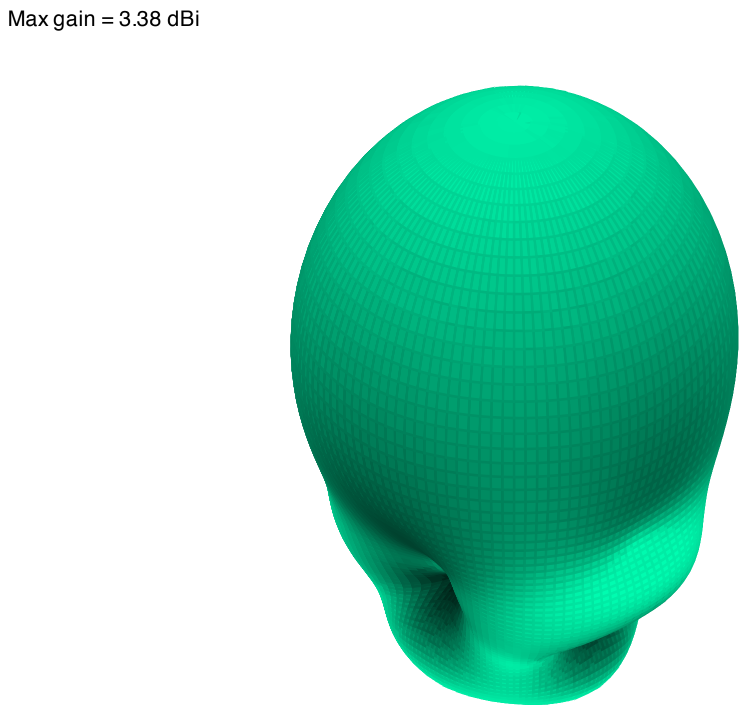

Figure 6.4: Feed 3-D pattern

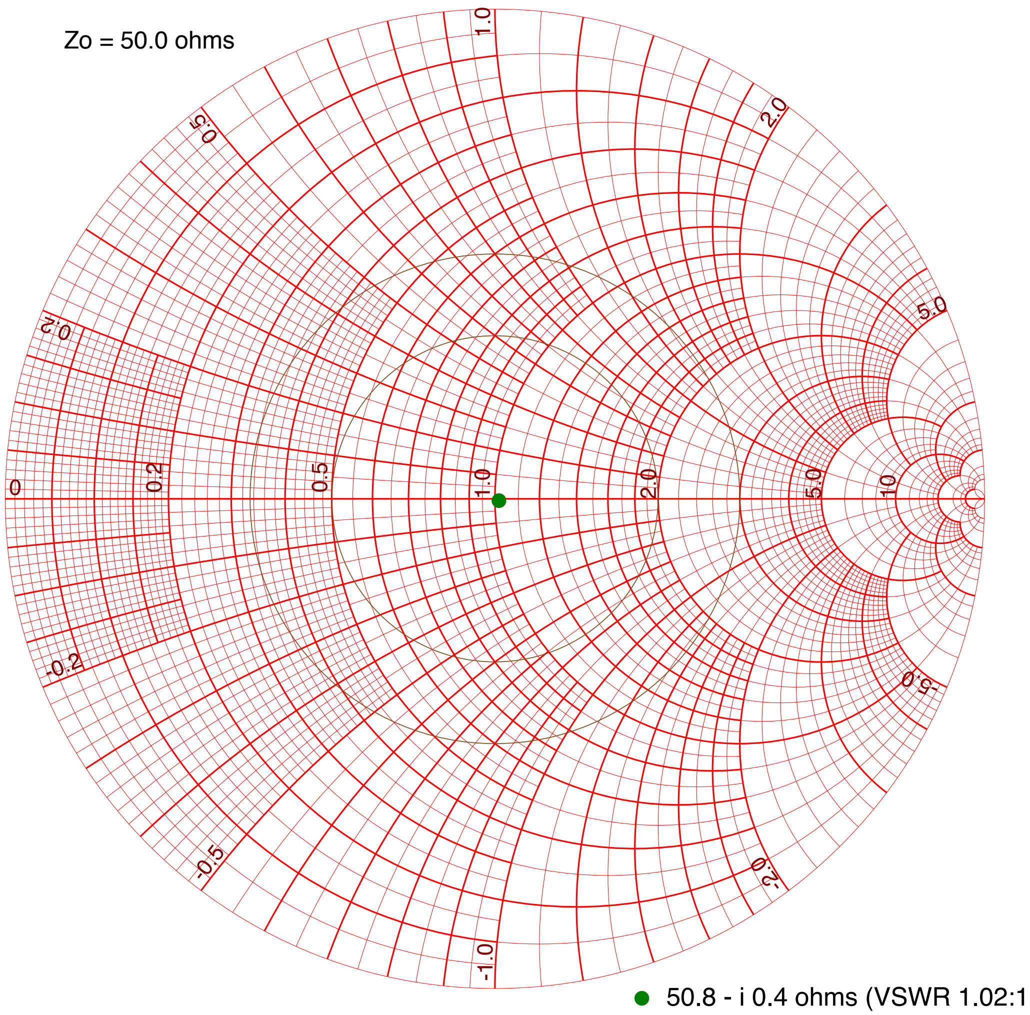

Figure 6.5: Feed 750 MHz impedance

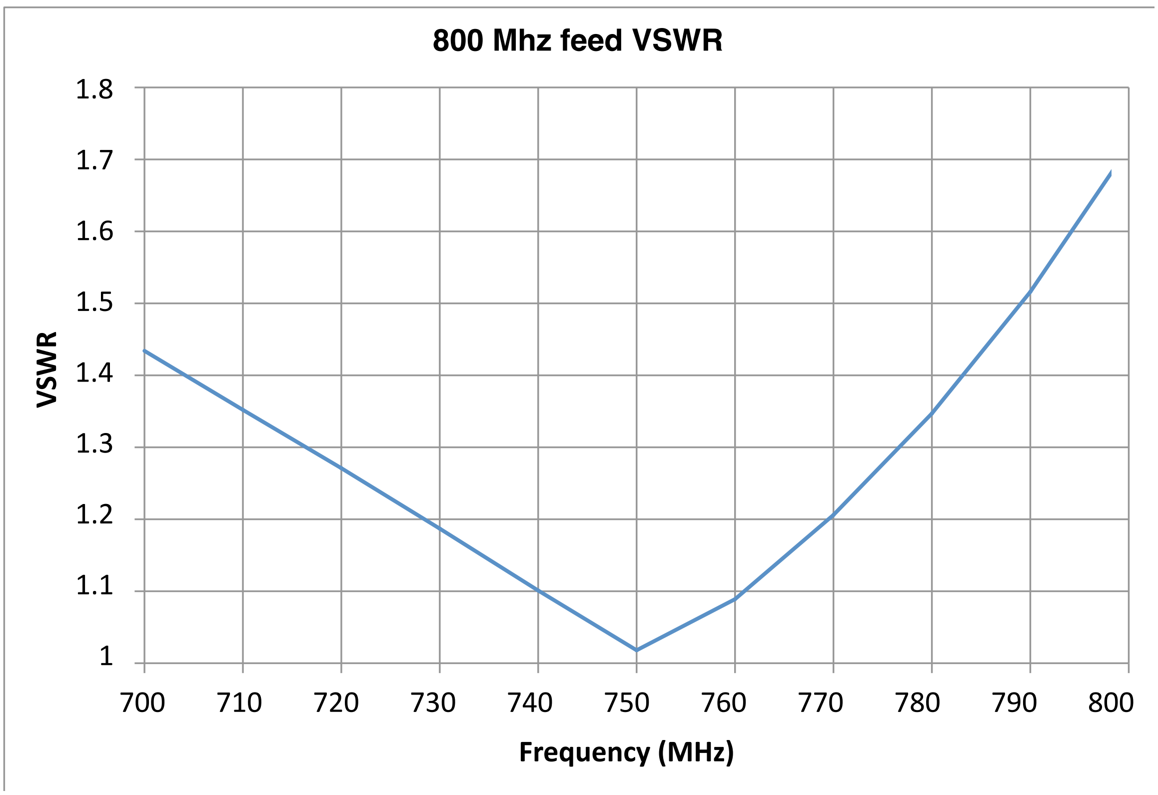

Figure 6.6: Feed VSWR

new phase based on geometric delay. The overall beam was simulated using a spherical reflector with radius 265m, with an aperture diameter of 304m. First a simulation is done using a perfect $\cos^2(2.578\theta)$ power pattern with the feed placed at -2.213m from the ideal parafocus of r/2. These parameters are the ideal solution calculated by Condon to optimize point feeds for Arecibo. The simulation results are plotted in figures 6.7, 6.8 and 6.9. The 3db beam-width of this $\cos^2$ feed would be $\pm 17.5^{\circ}$, and corresponds to a FWHM of 10 arcminutes on the sky. Figures 6.10 and 6.11 show the FWHM plotted vs. z, where z is the distance of the feed placement from the parafocus. This sweeps shows that the minimum occurs with the feed placed at -2.3m, coinciding well with that predicted by Condon.

The overall beam was then simulated with the actual feed designed in the previous section. The results are plotted in figures 6.12, 6.13, 6.14, 6.15. Simulations were done with both a perfect spherical reflector and a more realistic 2.2mm RMS surface with a 10m circular feed blockage which attempts to more closely simulate the actual dish. Figure 6.16 and figure 6.17 show the FWHM again plotted vs. z, where z is the distance of the feed placement from the parafocus. The narrowest FWHM occurs need a z of -3m. However, the minimum of the first sidelobe happens somewhere between a z of -1.5m and -2m.

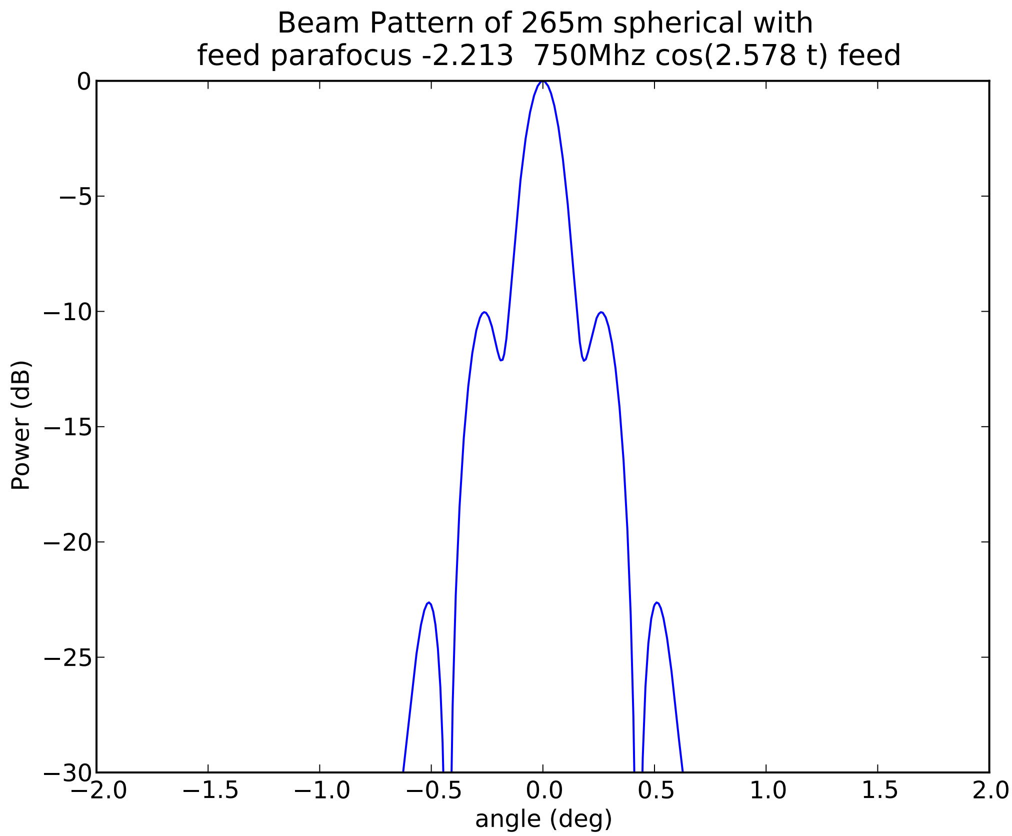

Figure 6.7: Feed with $\cos^2(2.587\theta)$ pattern placed at -2.213m from parafocus. Ideal spherical reflector.

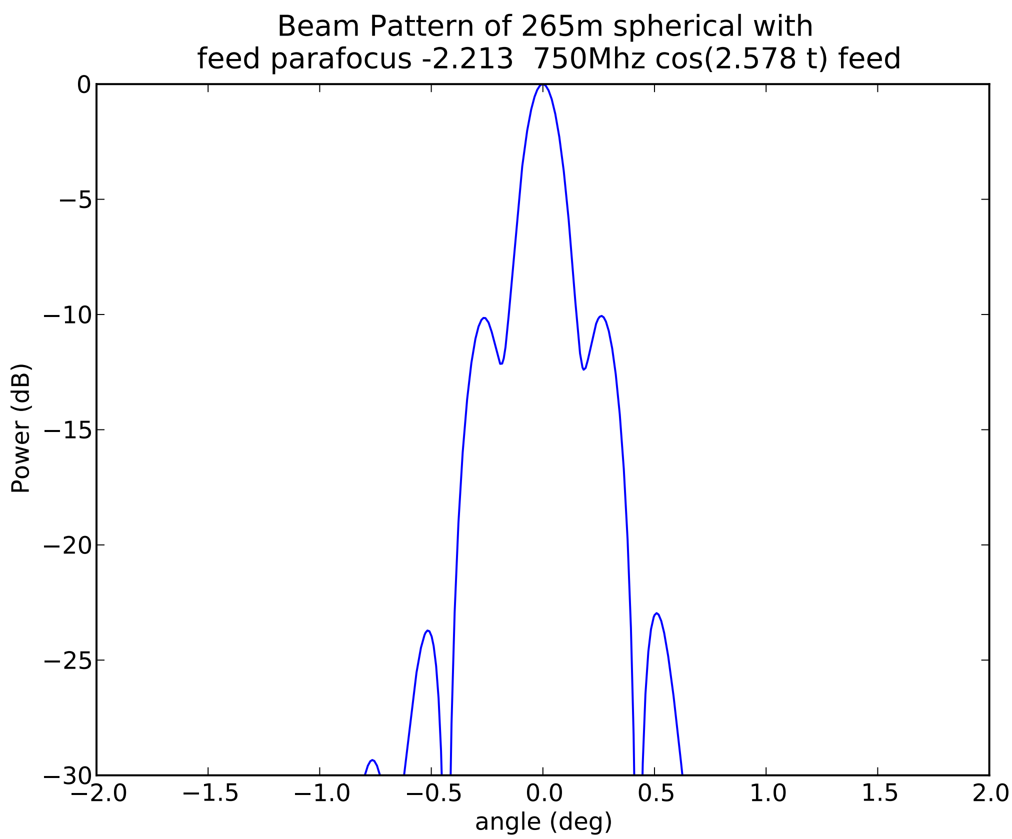

Figure 6.8: Feed with $\cos^2(2.587\theta)$ pattern placed at -2.213m from parafocus. Spherical reflector with 2.2mm RMS.

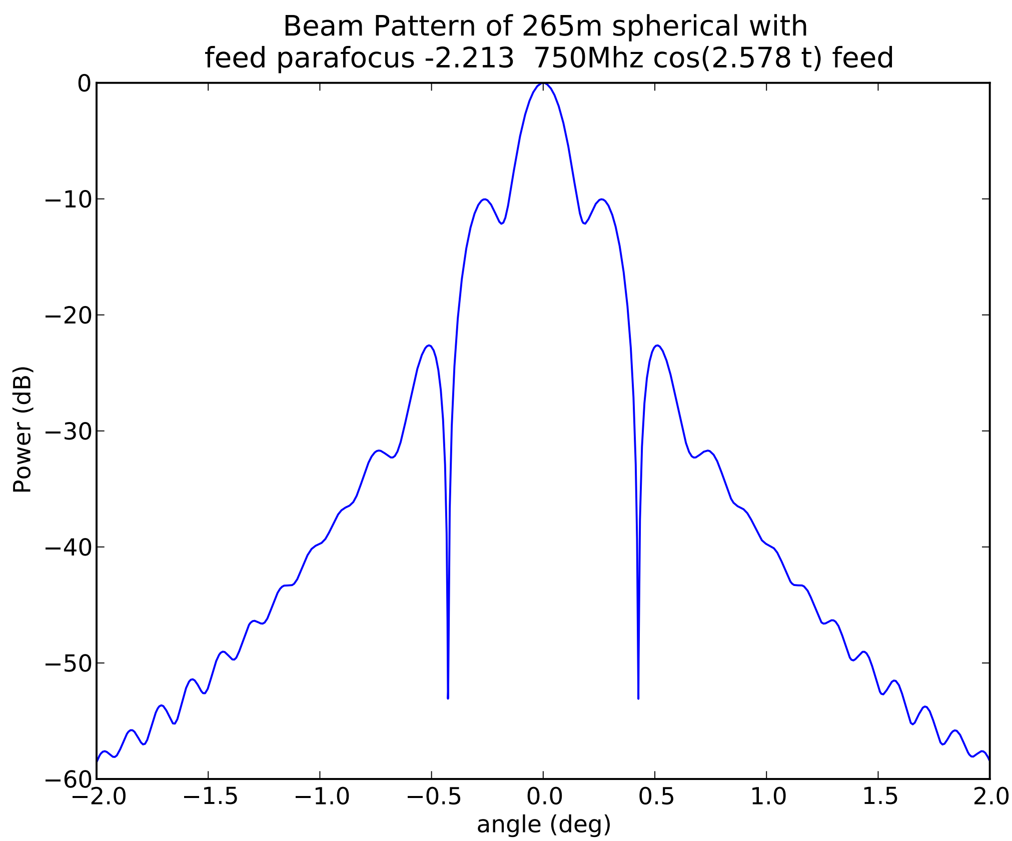

Figure 6.9: $\cos^2(2.587\theta)$ feed placed at -2.213m from parafocus. Ideal spherical reflector, showing more of the side-lobes.

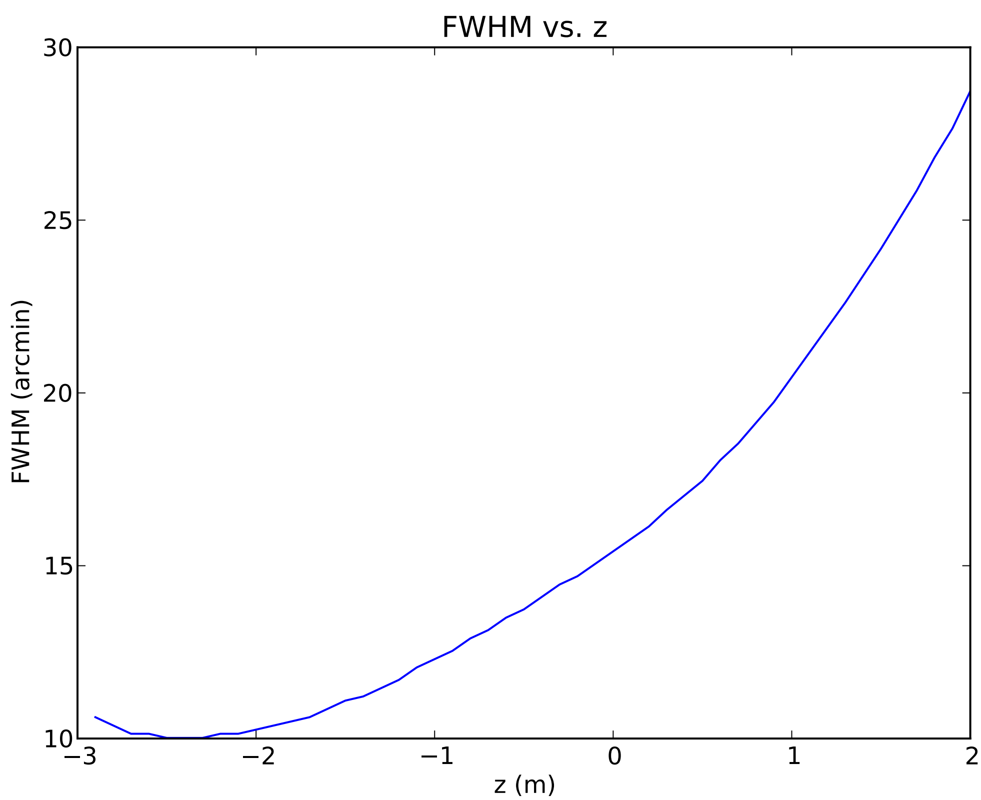

Figure 6.10: An assumed $\cos^2(2.587\theta)$ feed. The resultant FWHM is plotted agains z, where z is the distance from the parafocus. Ideal spherical reflector.

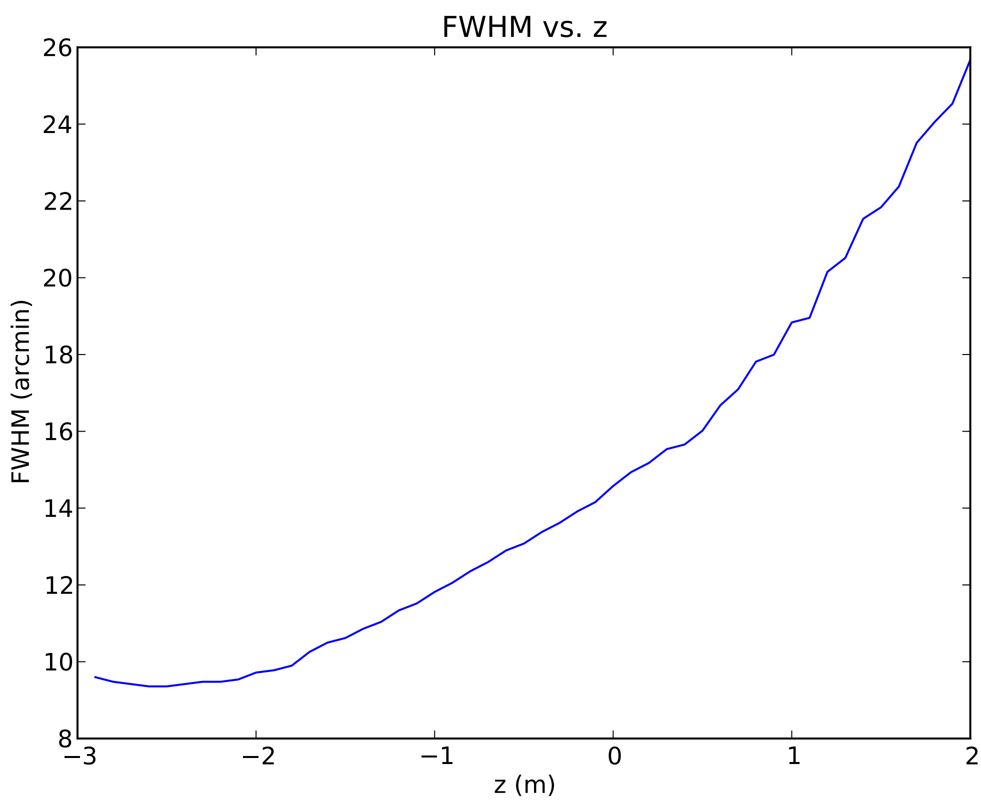

Figure 6.11: An assumed $\cos^2(2.587\theta)$ feed. The resultant FWHM is plotted agains z, where z is the distance from the parafocus. Spherical reflector with 2.2mm RMS.

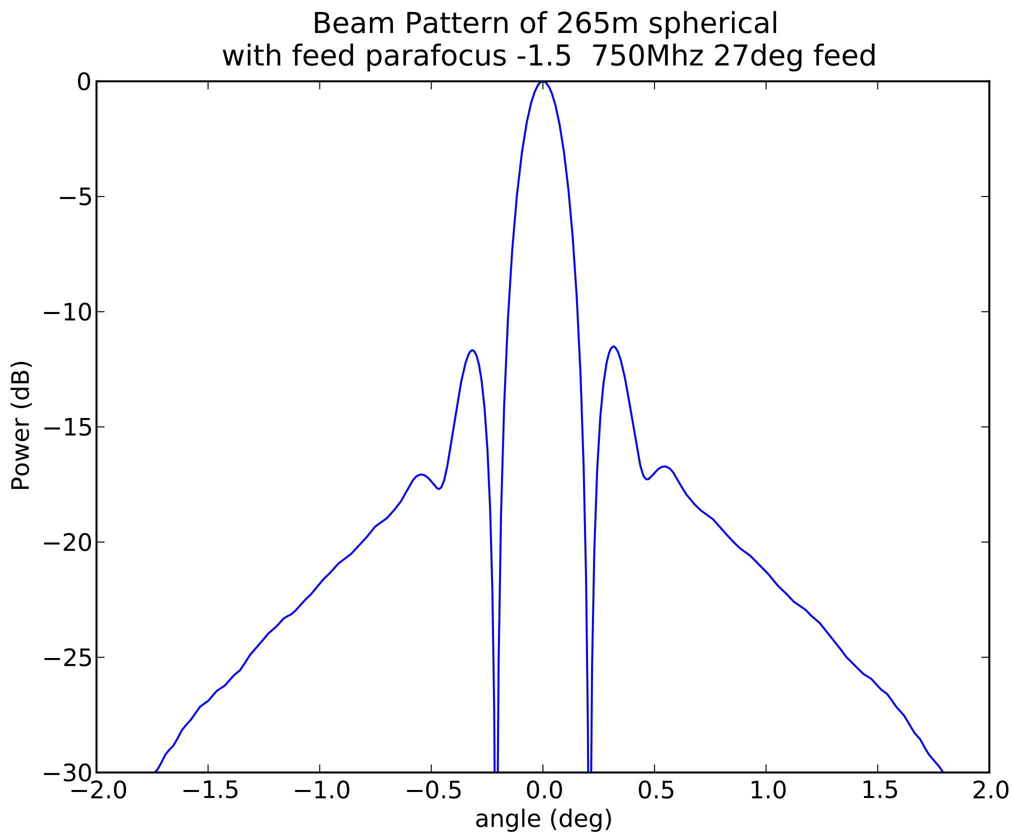

Figure 6.12: Beam pattern with current feed design. Perfect spherical reflector. Feed placed -1.5m from the parafocus.

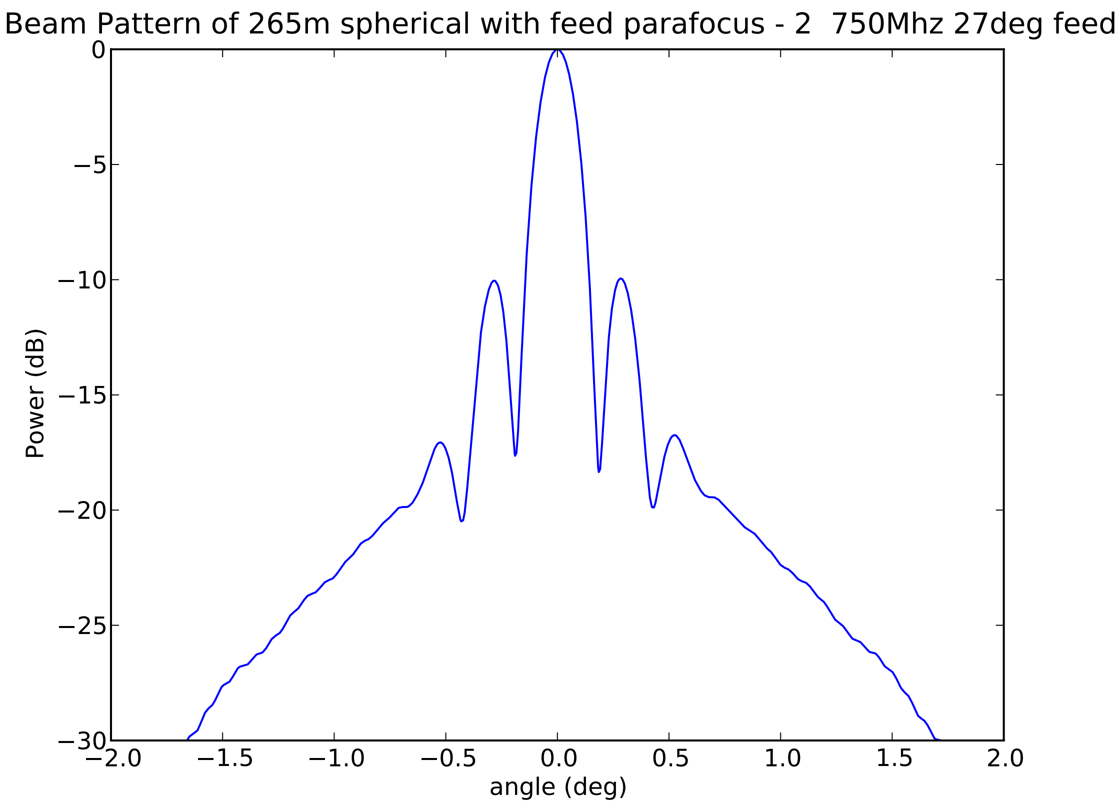

Figure 6.13: Beam pattern with current feed design. Perfect spherical reflector. Feed placed -2m from the parafocus.

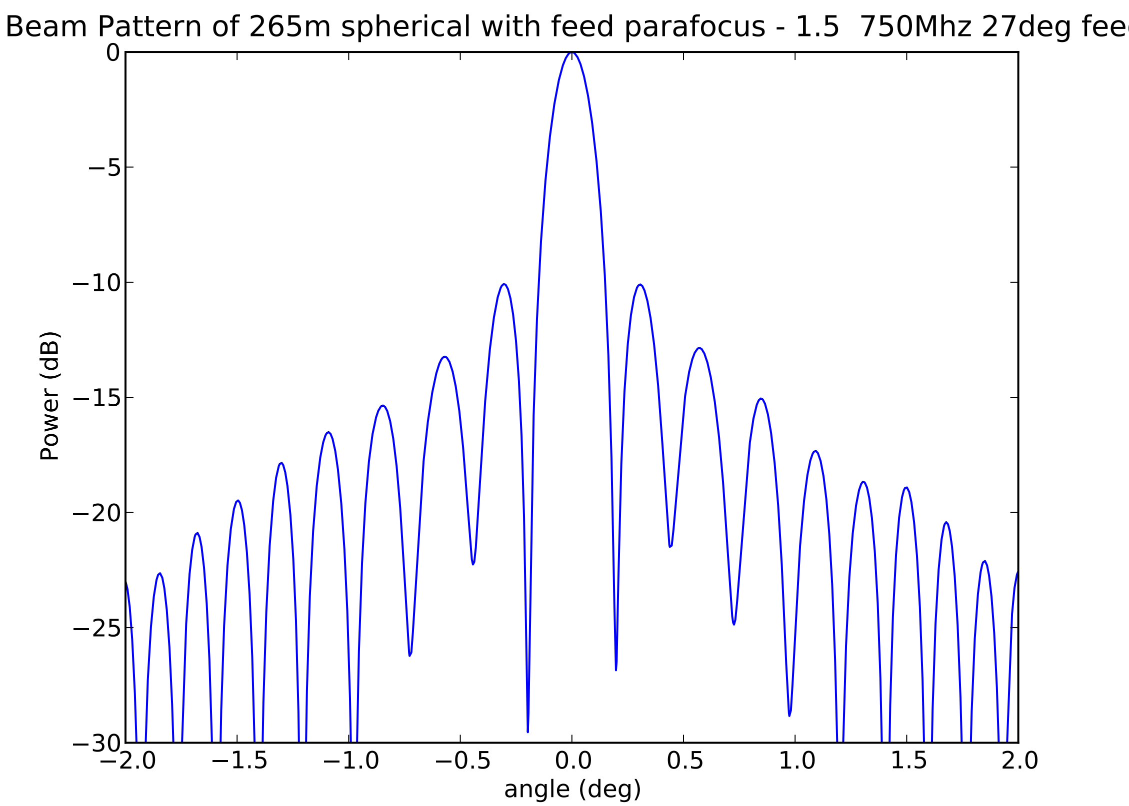

Figure 6.14: Beam pattern with current feed design. Feed placed -1.5m from the parafocus. Spherical reflector with 2.2mm RMS. 10m centered circular feed blockage assumed.

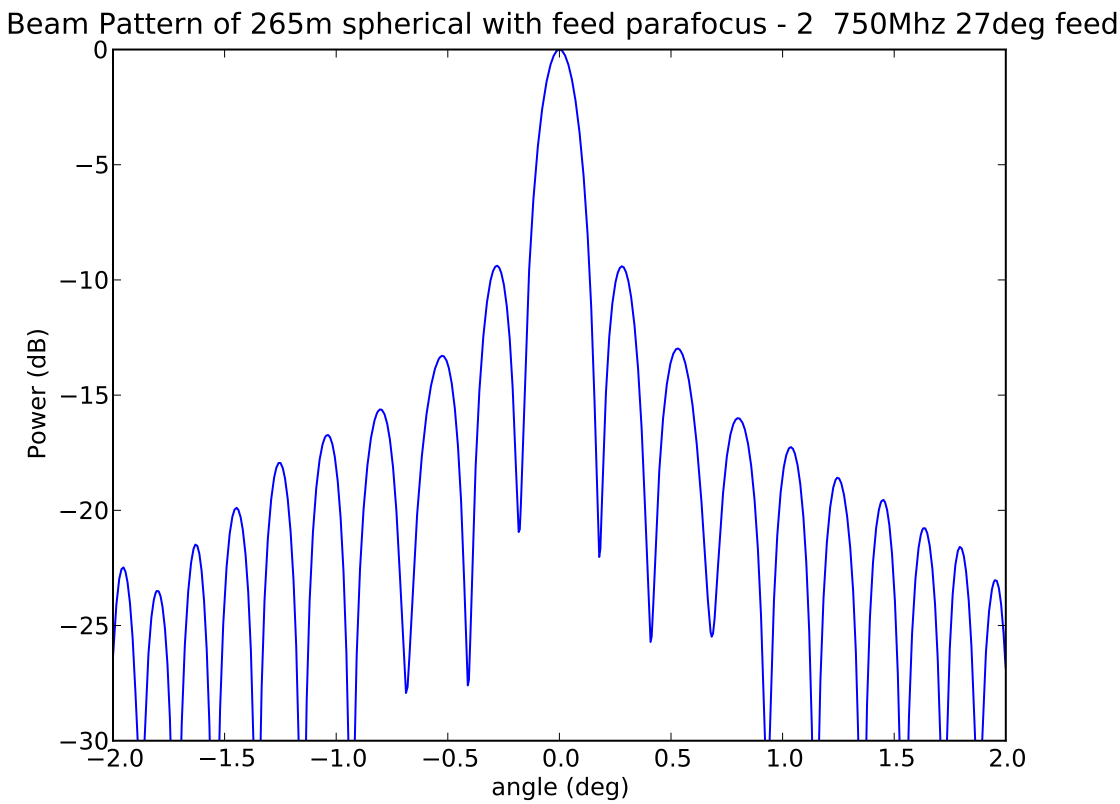

Figure 6.15: Beam pattern with current feed design. Feed placed -2m from the parafocus. Spherical reflector with 2.2mm RMS. 10m centered circular feed blockage assumed.

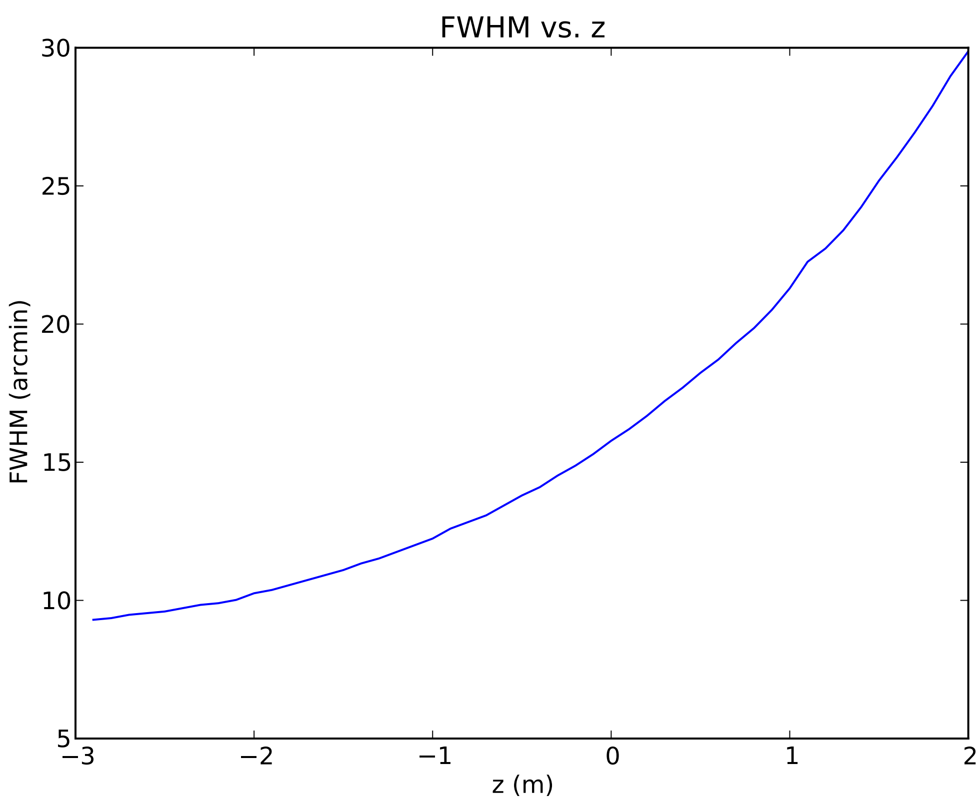

Figure 6.16: Beam pattern with current feed design. The FWHM is plotted against z, where z is the distance from the parafocus. Perfect spherical reflector.

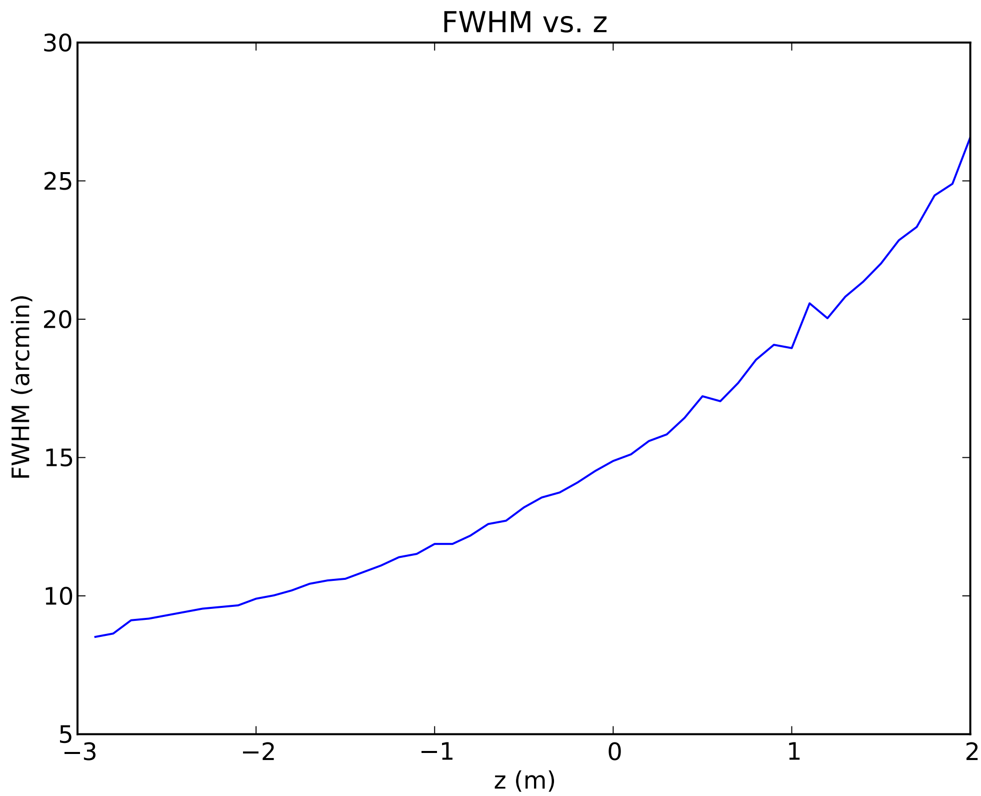

Figure 6.17: Beam pattern with current feed. The FWHM is plotted agains z, where z is the distance from the parafocus. Spherical reflector with 2.2mm RMS. Central circle of 10m blocked out.

6.2.4 Measured Prototype Feed

The prototype feed is shown in figure 6.18 and 6.18. The main changes from the simulation was the use of 100Ω coaxial cable instead of twin-lead transmission line, and an octagon ground-plane instead of circular. Measurements of the prototype were conducted in an anechoic chamber. The measurements of the H-plane pattern are shown in figure 6.20, the E-plane measurement is shown in figure 6.21, and the match is shown in figure 6.22. The measurements agree well with the simulated pattern.

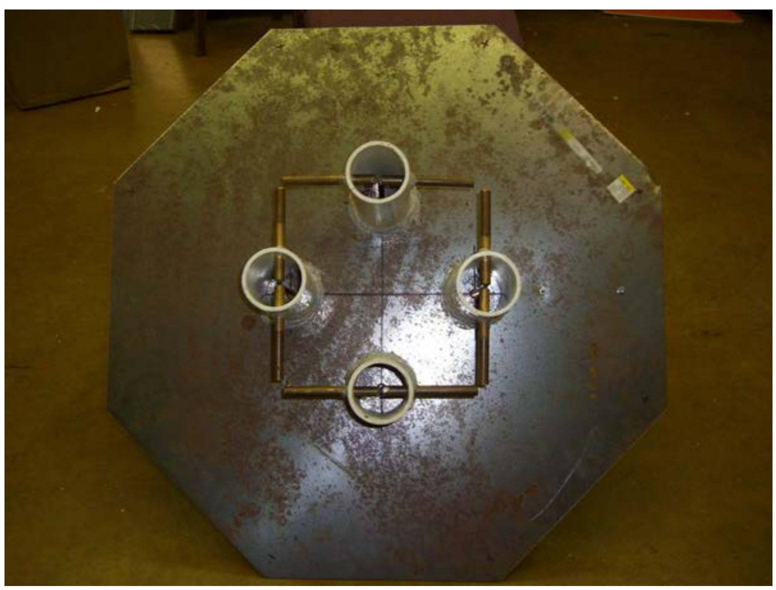

Figure 6.18: Image of prototype feed. Opposite dipoles are summed.

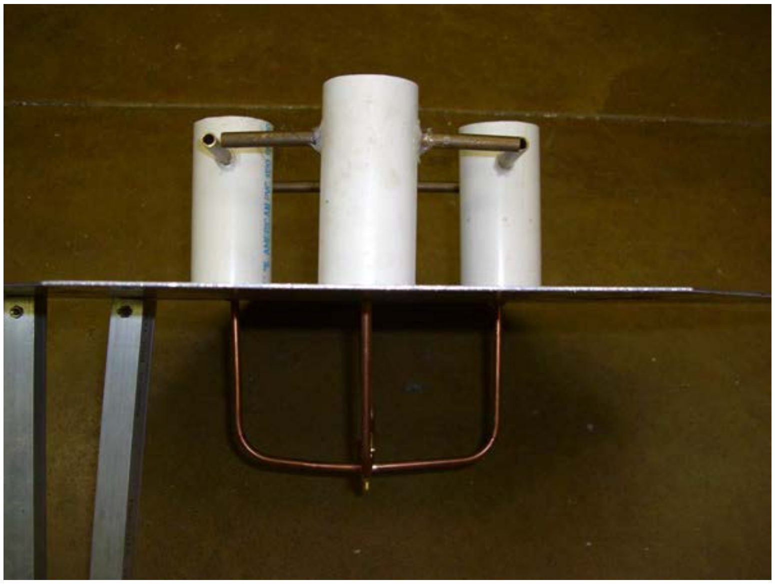

Figure 6.19: Image of prototype feed, end on. 100Ω custom hard-line coaxial cable visible. Cable feeds an SMA connector.

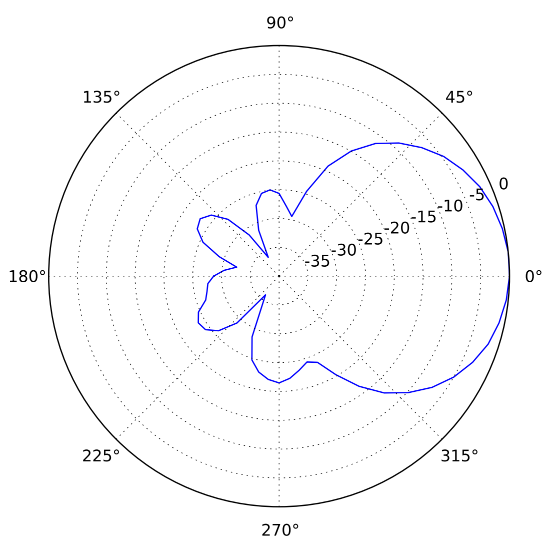

Figure 6.20: H-Plane measurement of prototype feed.

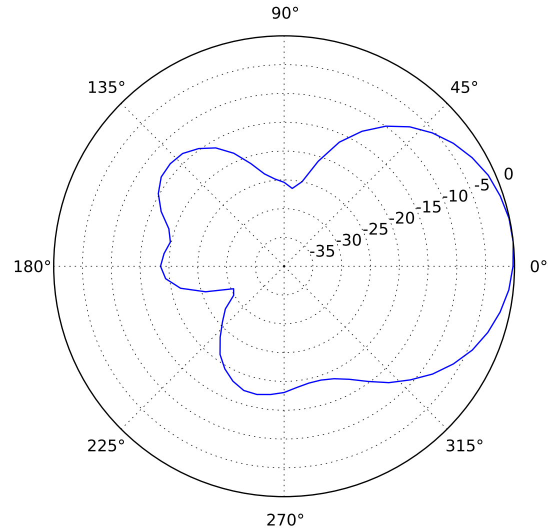

Figure 6.21: E-Plane measurement of prototype feed.

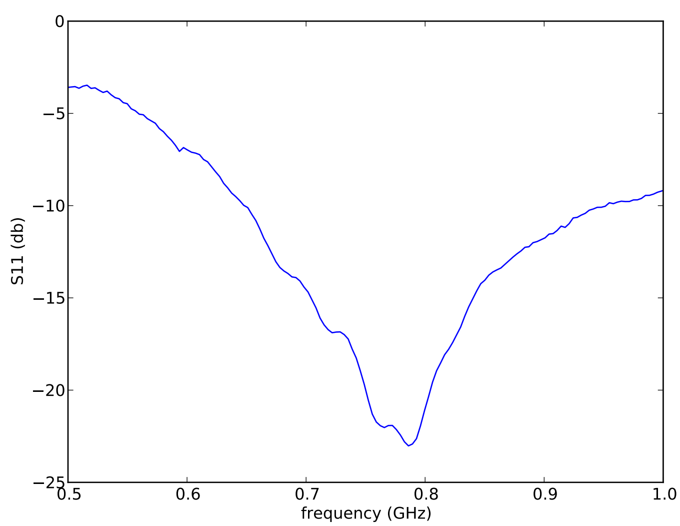

Figure 6.22: Antenna reflection coefficient measurement(S11). Good match to 50Ω from 700 MHz to 830 MHz. The center of the prototype match was closer to 775 MHz than the designed for 750 MHz.

6.3 21cm BAO Redshift Survey Prospects

The neutral hydrogen at redshift one associated with optical galaxies has been measured to be emitting at the 0.15 mK level. Assuming a system temperature of 30K, a scale of 10 h^{-1}Mpc at redshift one (2MHz), and using the single dish radiometer equation, as 5.3, the integration time to get a noise level of 0.1 mK is 4.5×10^4seconds, or 12.5 hours on each 0.25° pixel. To get a large enough volume to well constrain BAO, 10,000 sq. deg. (π sr) is necessary to get a large survey volume, or 1.6×10^5 angular pixels. This is 2 million pixel observing hours. This would be over 200 years on a single pixel instrument. However, with a 228 receiver instrument (456 with dual polarization) it would be possible to get the necessary observing time with one year of on sky time. It will take a 500 receiver class instrument to be able to well constrain the BAO, assuming excellent system parameters, calibration, and perfect foreground removal. See Seo et al. [63] for recently calculated parameters.

The largest scale of interest (120 h^{-1}Mpc) is about 3° at redshift one. This corresponds to an 8m telescope.

In this case the cosmological goal sets the parameters. What is needed is a filled aperture with angular information on scales from 0.25° to 3° at redshift one. A moving dish will require a 100m aperture and a scan strategy which includes information on such angular scales. A stationary interferometer would need to be comprised of elements that are spaced by 8m and fill 10,000 sq. meters.

A packed array of 8 meter dishes each with a focal plane array of at least 2 dual-polarization elements should be able to do the experiment well, and may well be an excellent choice for the experiment.

A 100m long cylinder sampled $\lambda/2$ requires 500 feeds per polarization. Assuming a feed design with summing of feeds in sets of 16, with eight 12m diameter cylinders, this would also exactly cover the necessary scales well.

Reaching a low enough noise level and covering the necessary scales gives needed constraints, but not sufficient constraints on whether a BAO detection is possible. There are foreground signals which are $> 10^4$ times the expected signal. This is a known problem with many presented solutions[20][70][45][46][43][44]. A survey instrument will need to be constructed with foreground removal in mind.

7

Conclusions

Twenty-one centimeter cosmology is a wide open, rapidly developing field. The idea of using neutral hydrogen to map out the Universe, measure the baryon acoustic oscillation scale, and constrain dark energy have been well thought out. However there has been little previous experimental work done at redshifts of 0.5-3.

We have made statistical detection of the 21cm neutral hydrogen emission with the Green Bank telescope at redshifts from 0.6-1 in cross-correlation. We found that the neutral hydrogen does correlate with the optically detected galaxies of the DEEP2 and zCOSMOS surveys. The SVD data reduction technique was shown to reduce foregrounds to the level where the statistical detection is possible. The noise level is approaching that necessary to detect the hydrogen without cross-correlation, and further observations must be made to get to the detection level.

We have constructed a cylindrical prototype survey telescope. Some performance parameters, particularly the system temperature, measured on the sky higher than on the bench. The cylinder is, I believe, the first cylinder telescope to image the entire visible sky in one day with continuous data. I have made images of our own Milky Way galaxy in 21cm emission. The telescope has been calibrated to the best level possible in Pittsburgh, and has shown a beam pattern well suited to such experiments. The primary calibration comes from the correlation between cylinders and the sampling of every single feed. The instrument is stable enough that the calibration using just one point source is enough to image the sky over 24 hours. Over multiple days the instrument is quite stable in its calibration.

The combination of these results further buttress the case for a large scale 21cm dark energy survey.

Appendix A

Radio and Variance Maps

A.1 zCOSMOS

A.2 DEEP2

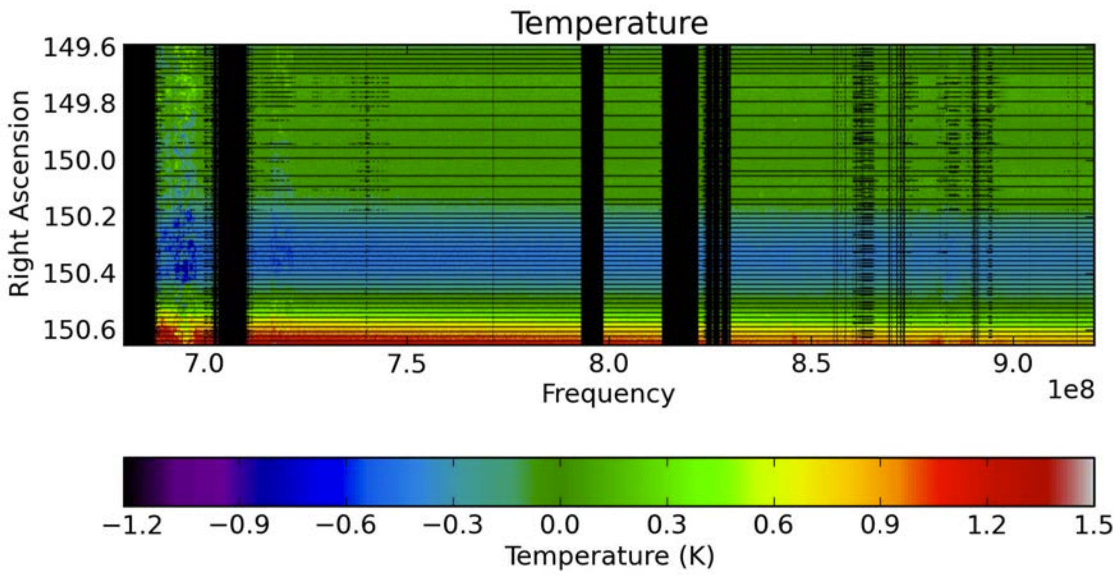

(a) dec 1

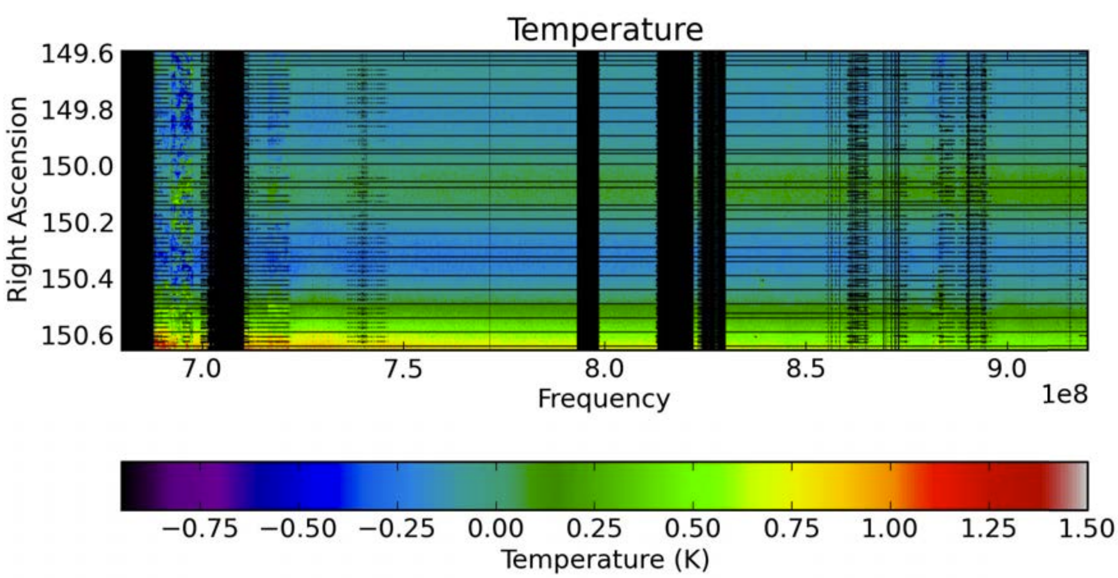

(b) dec 2

Figure A.1

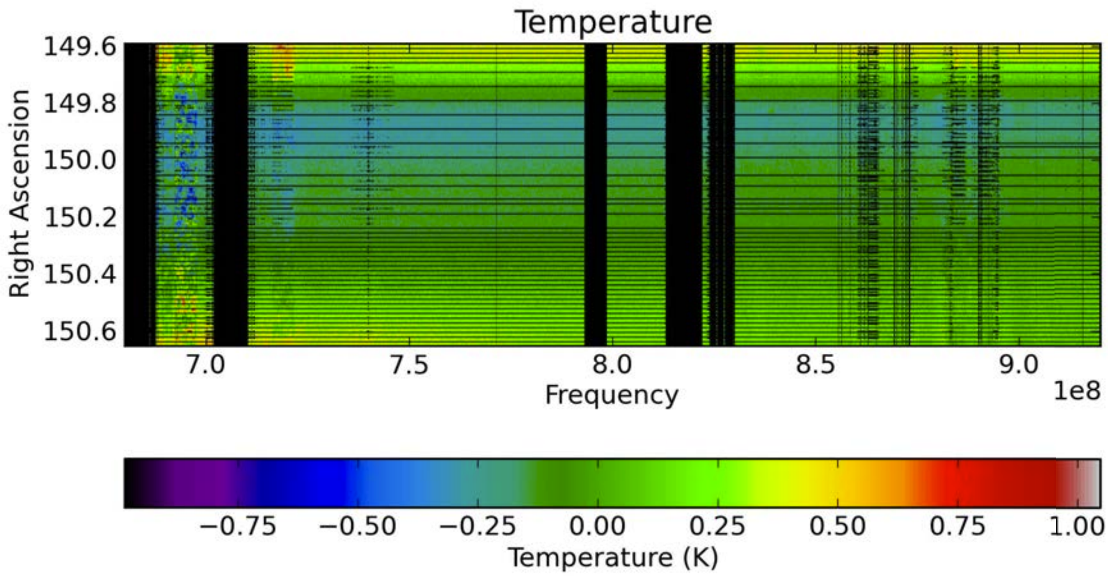

(c) dec 3

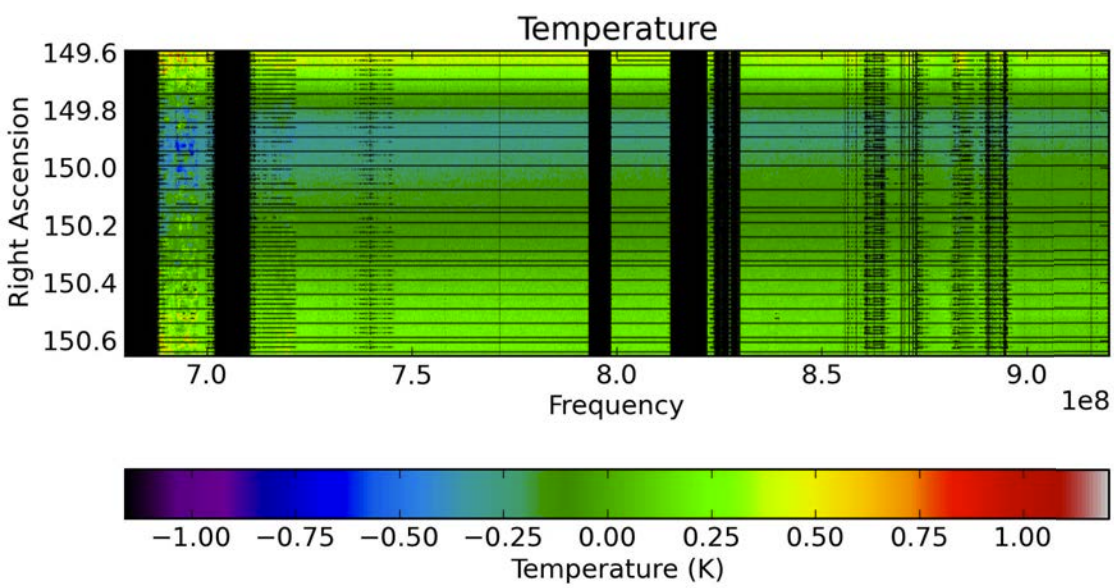

(d) dec 4

Figure A.1

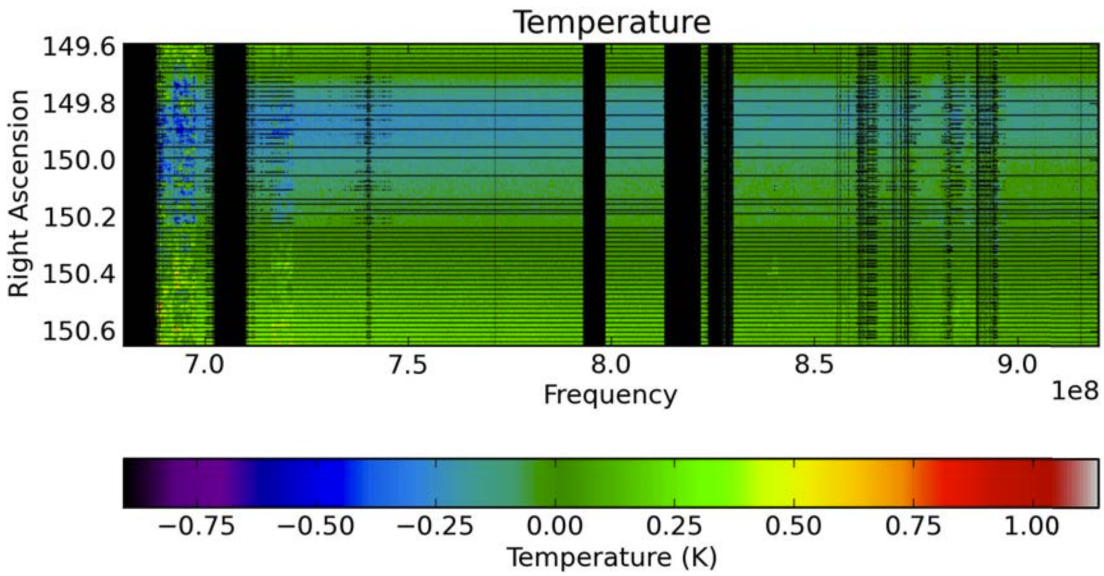

(e) dec 5

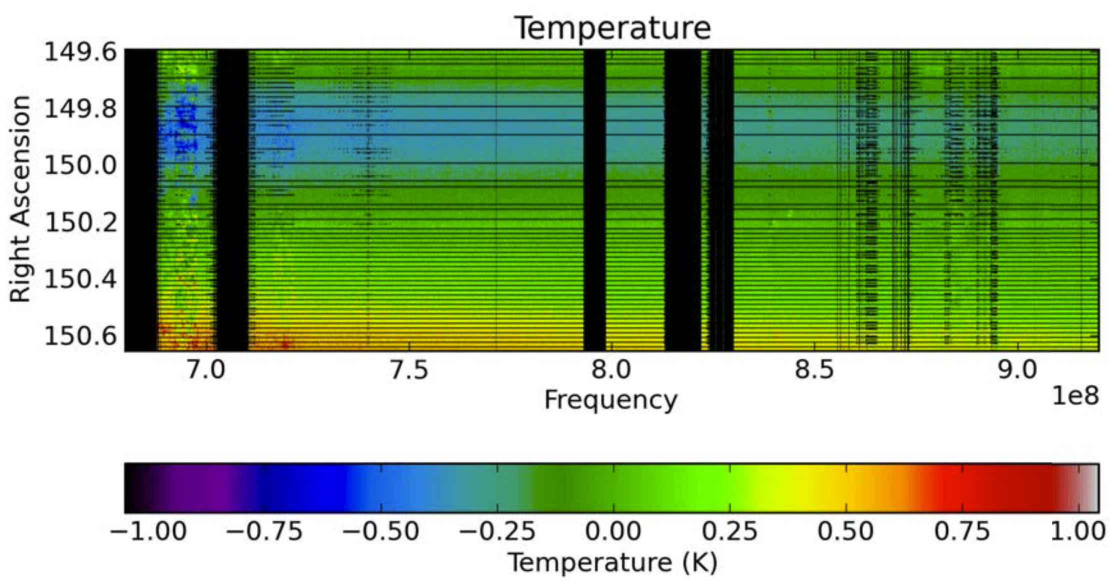

(f) dec 6

Figure A.1

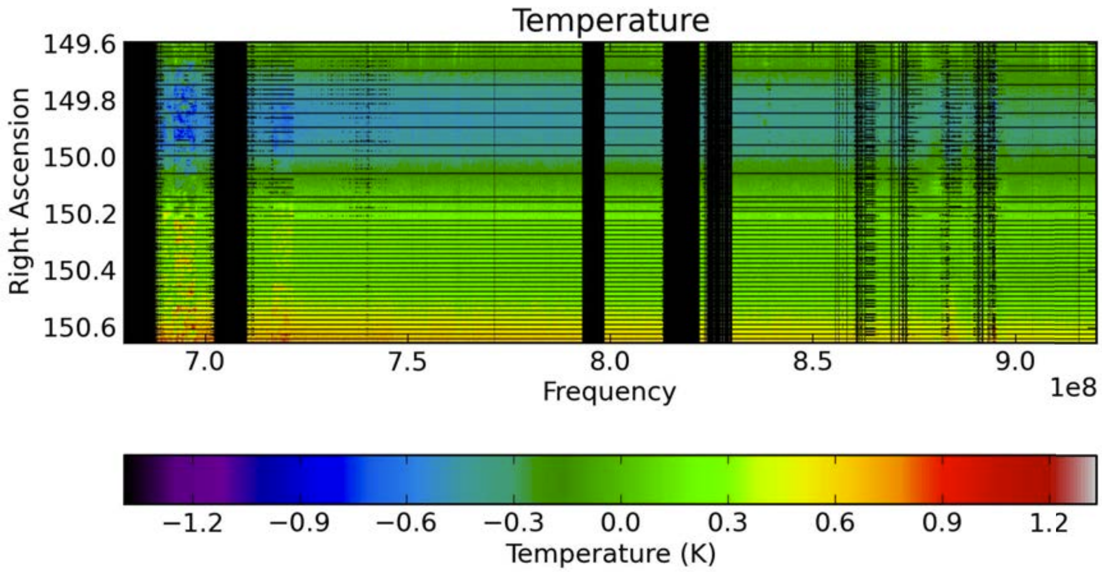

(g) dec 7

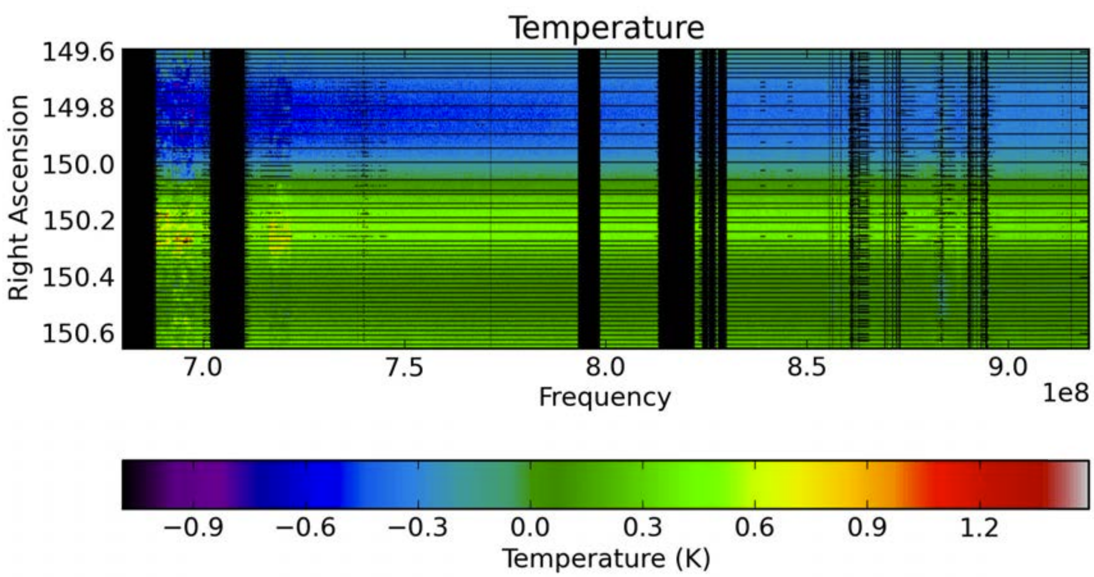

(h) dec 8

Figure A.1

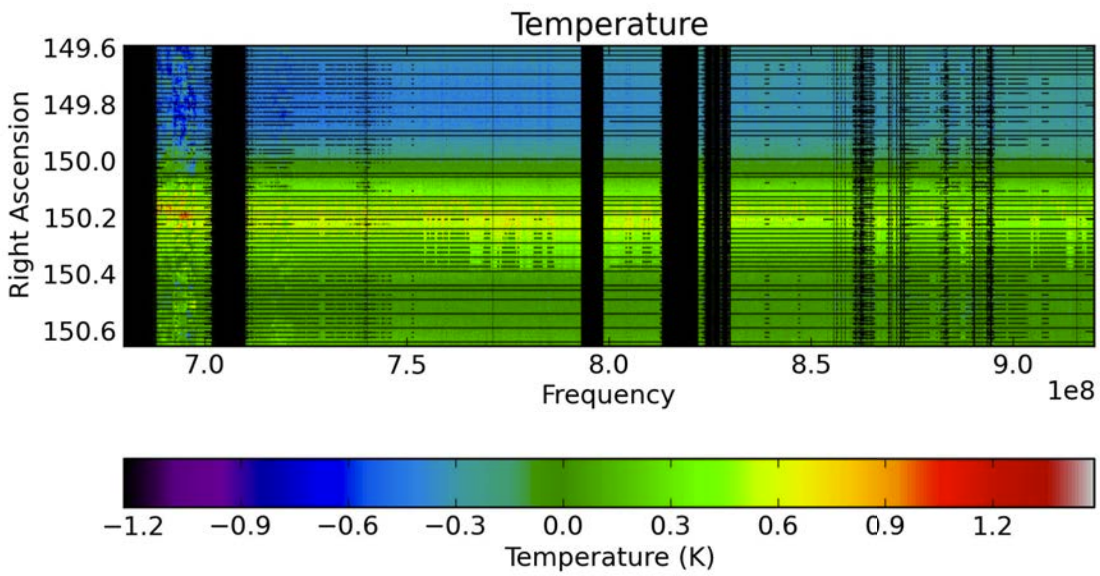

(i) dec 9

Figure A.1: Radio map of zCOSMOS. Unreduced resolution, as data was taken. Averaged all observations together.

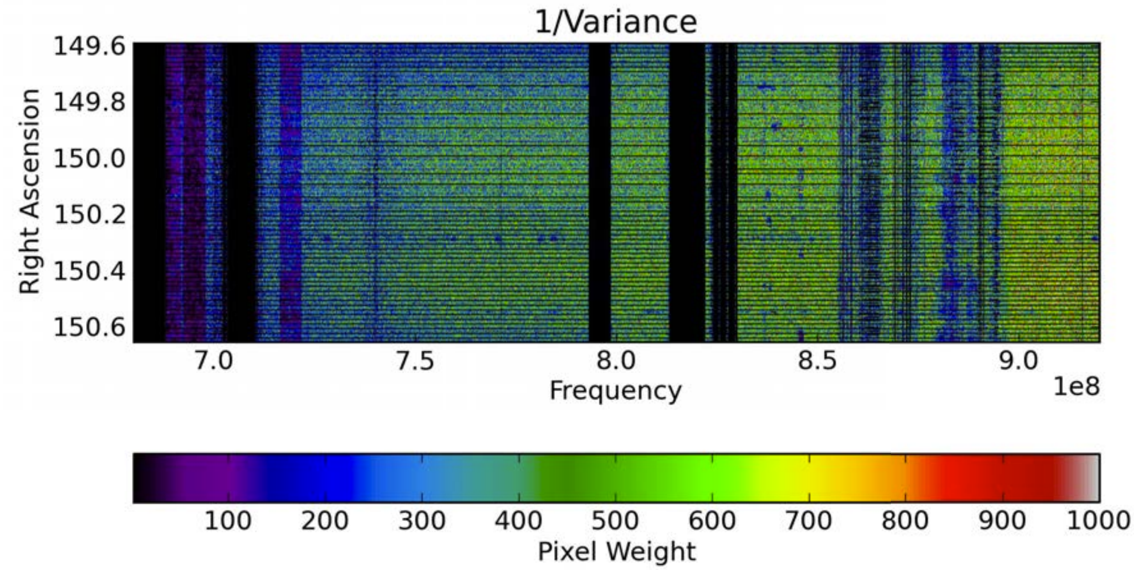

(a) dec 1

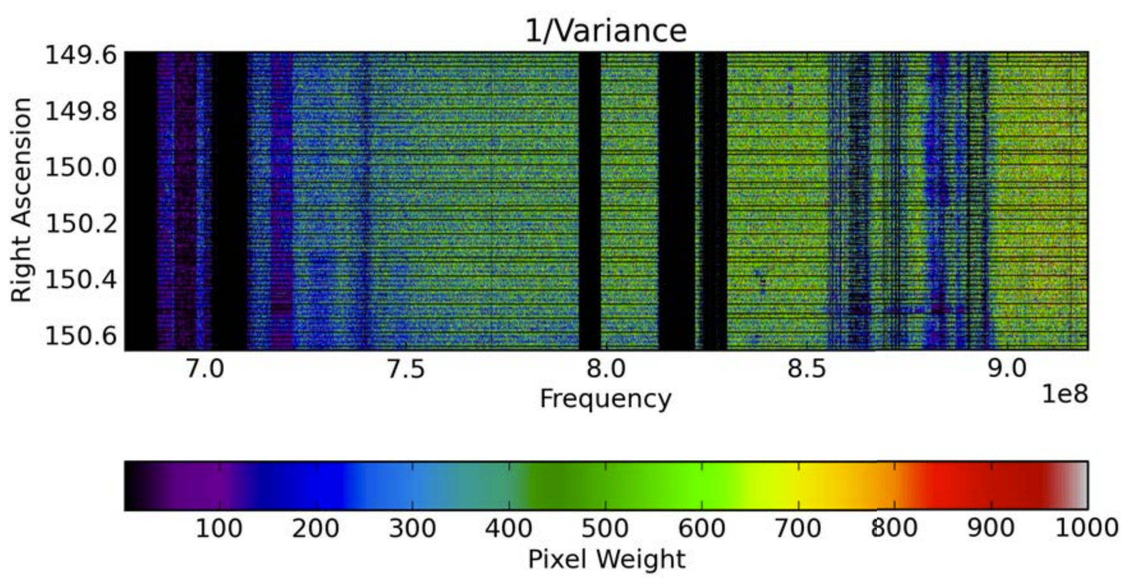

(b) dec 2

Figure A.2

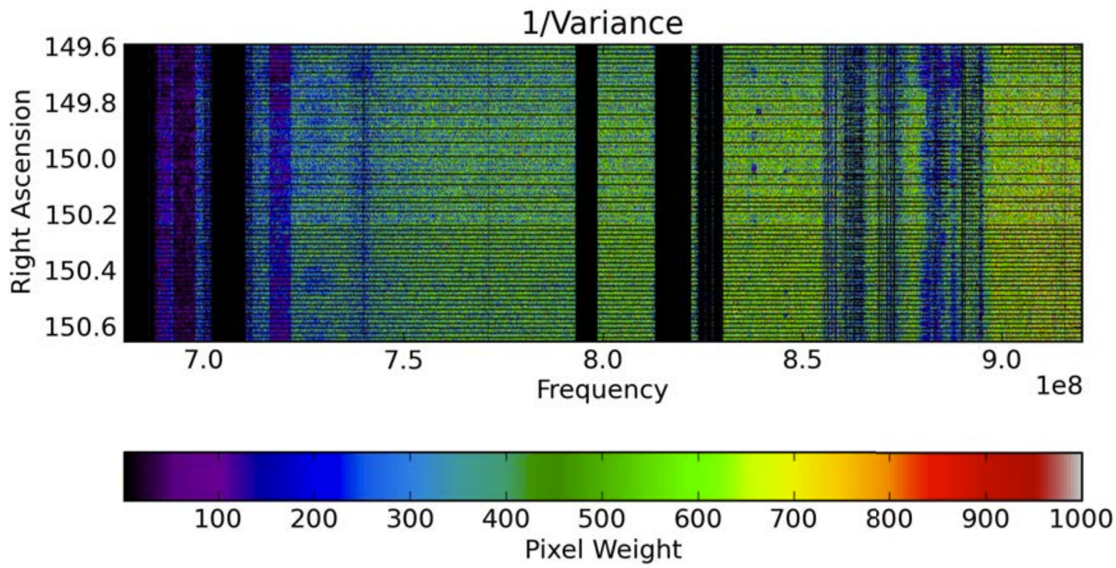

(c) dec 3

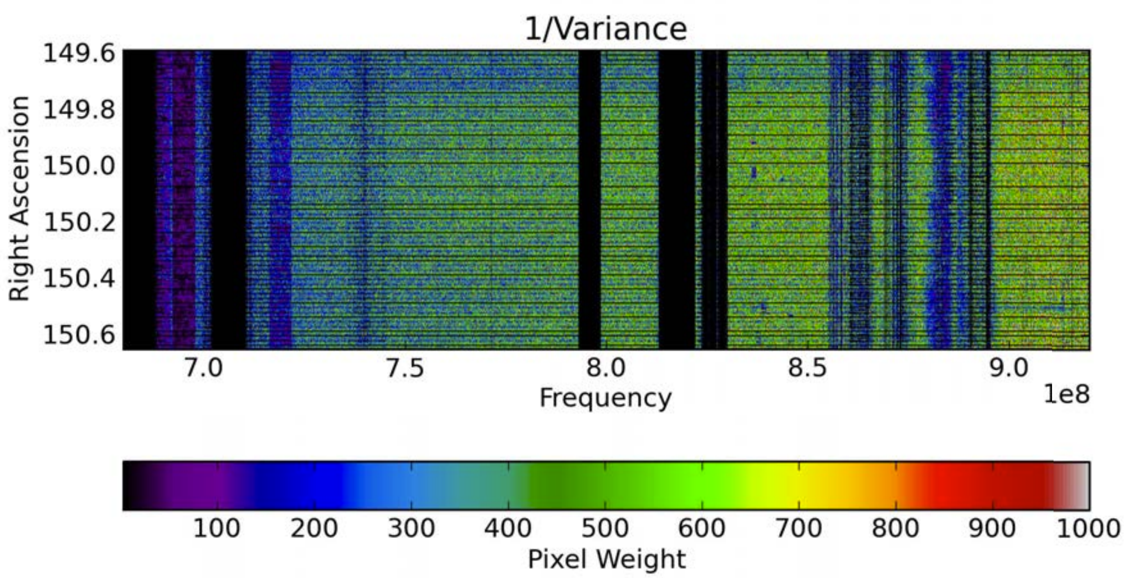

(d) dec 4

Figure A.2

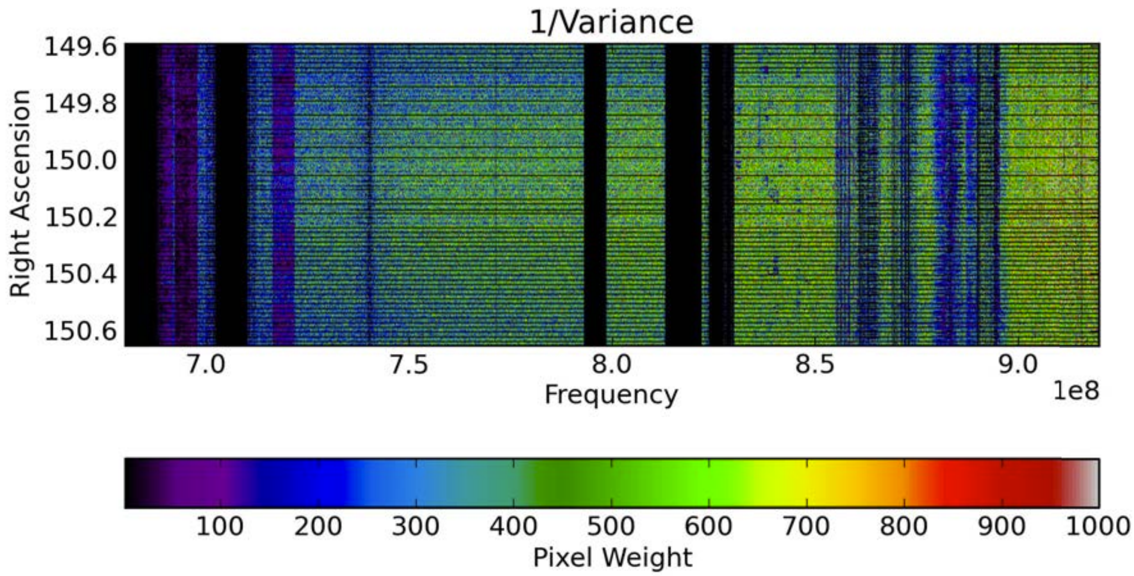

(e) dec 5

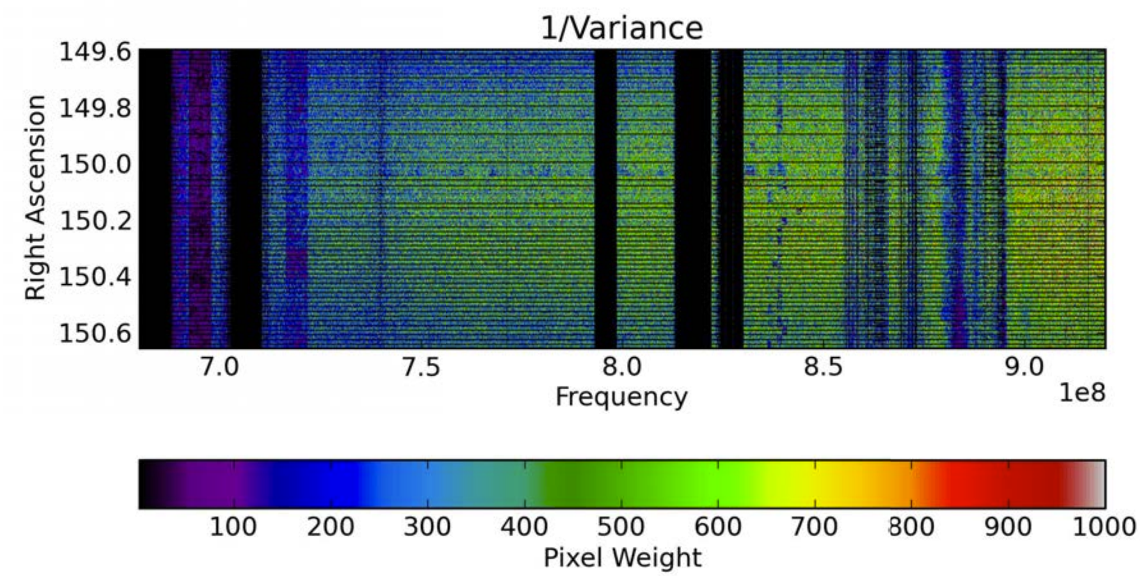

(f) dec 6

Figure A.2

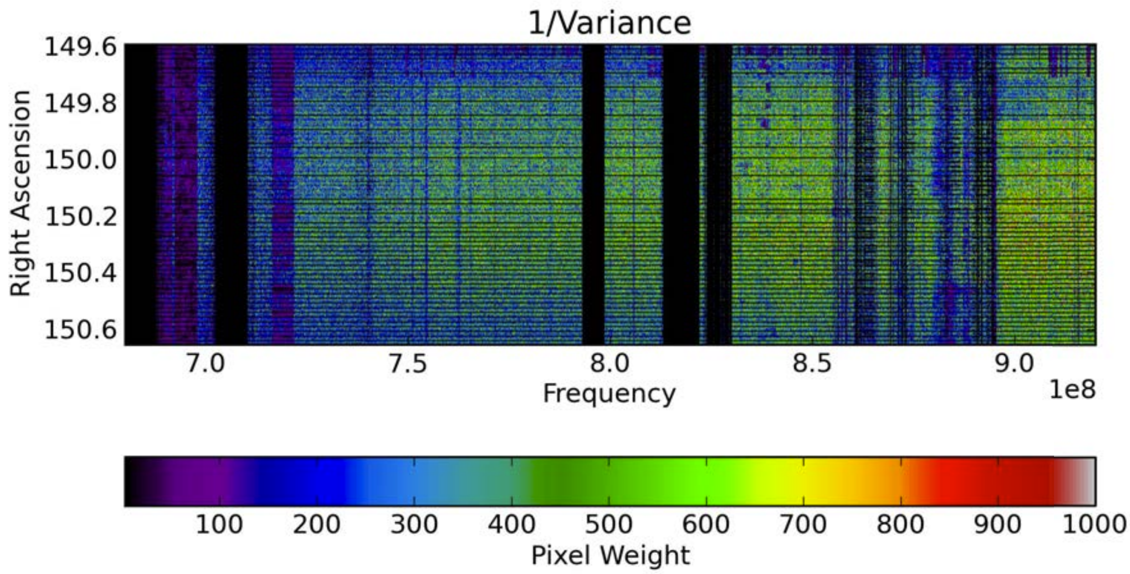

(g) dec 7

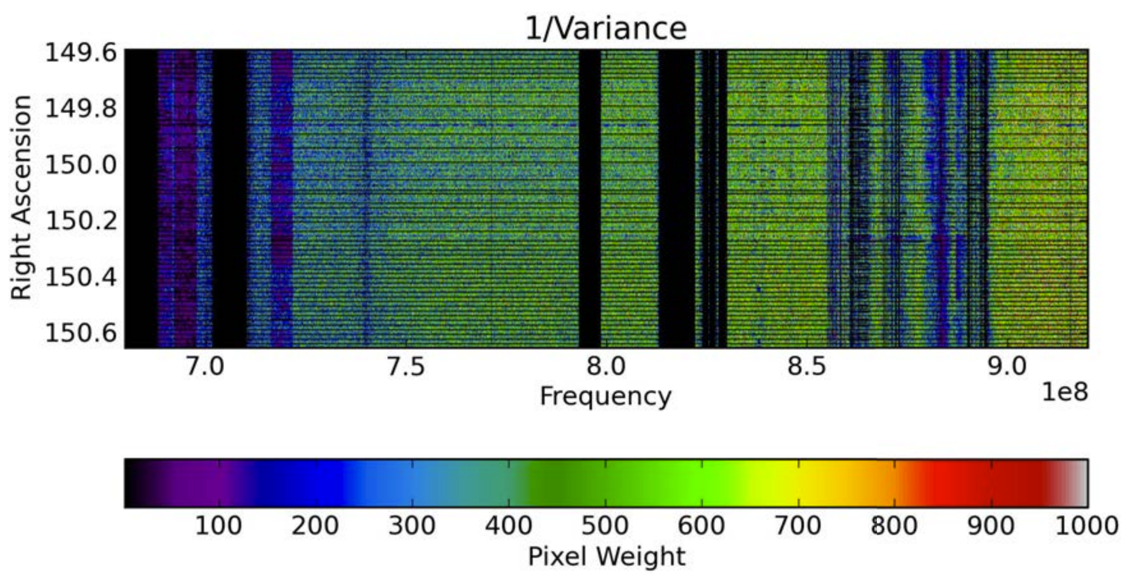

(h) dec 8

Figure A.2

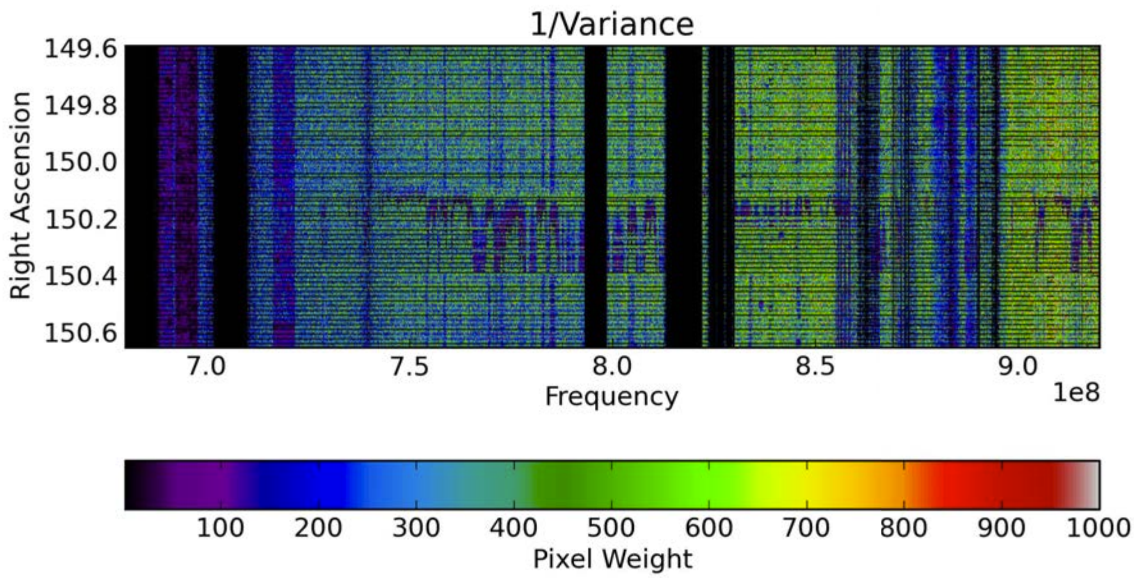

(i) dec 9

Figure A.2: Variance map of zCOSMOS data. Unreduced resolution, as data was taken. Averaged all observations together.

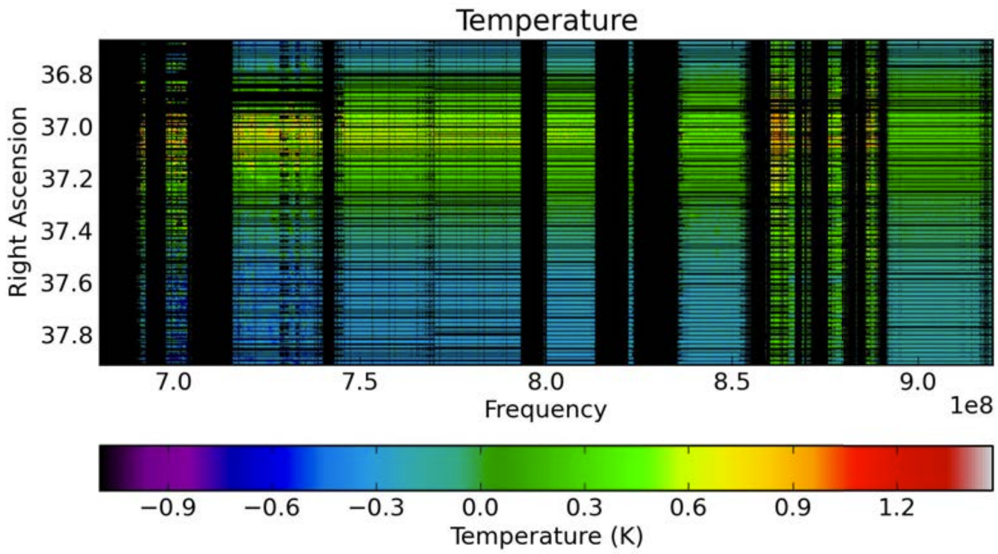

(a) dec 1

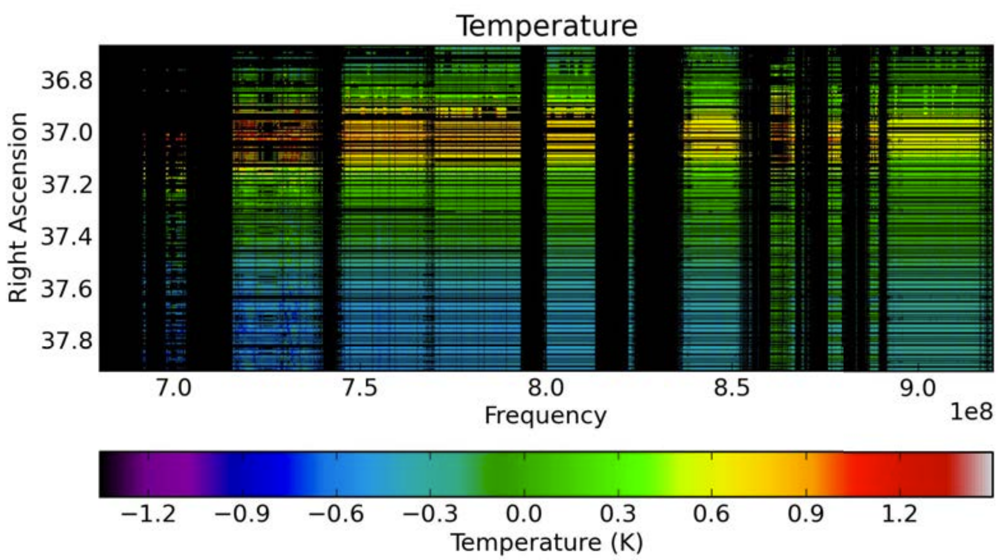

(b) dec 2

Figure A.3

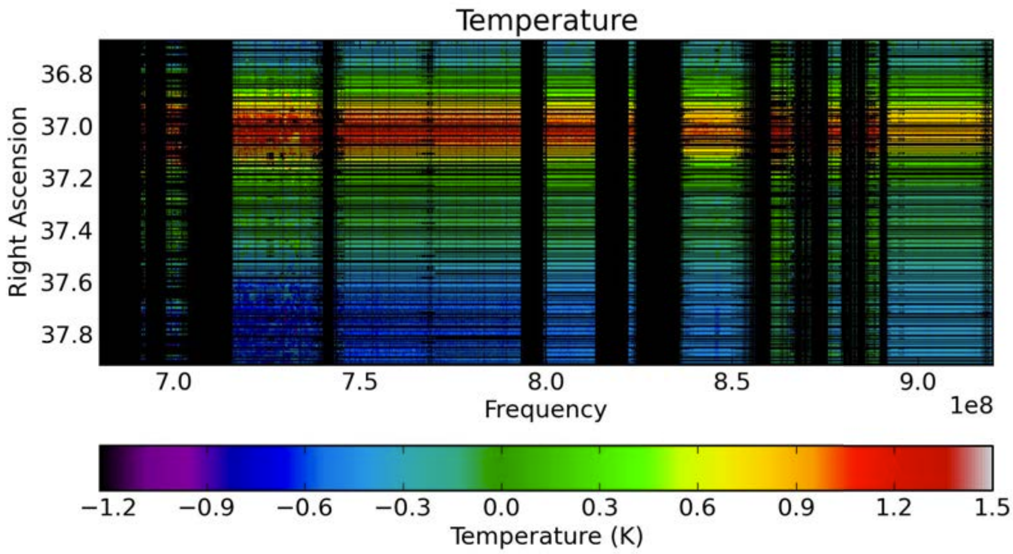

(c) dec 3

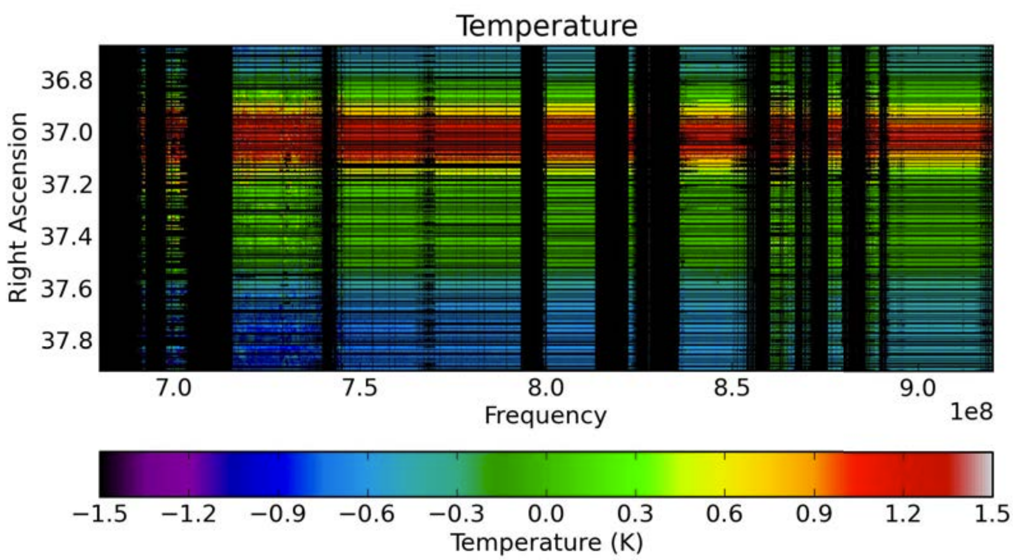

(d) dec 4

Figure A.3

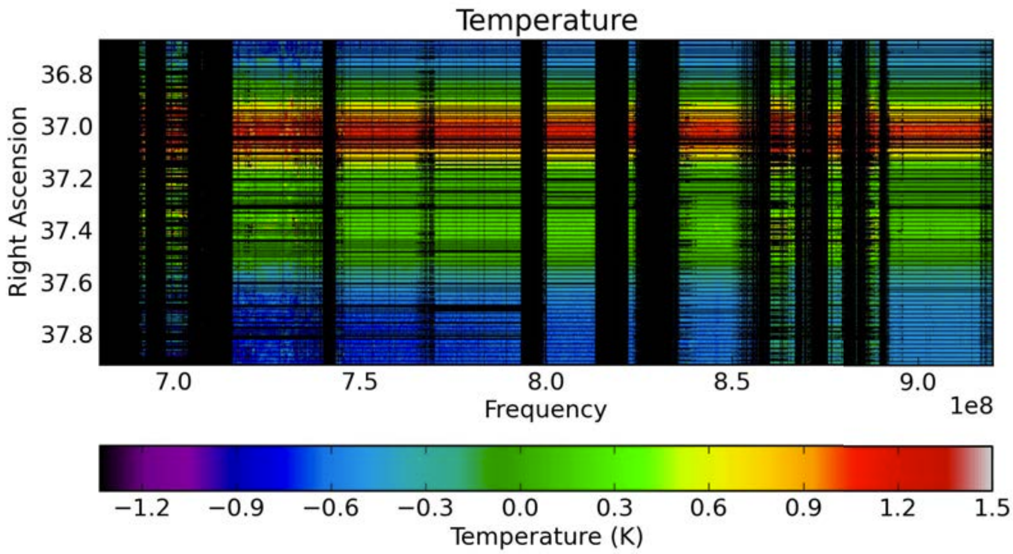

(e) dec 5

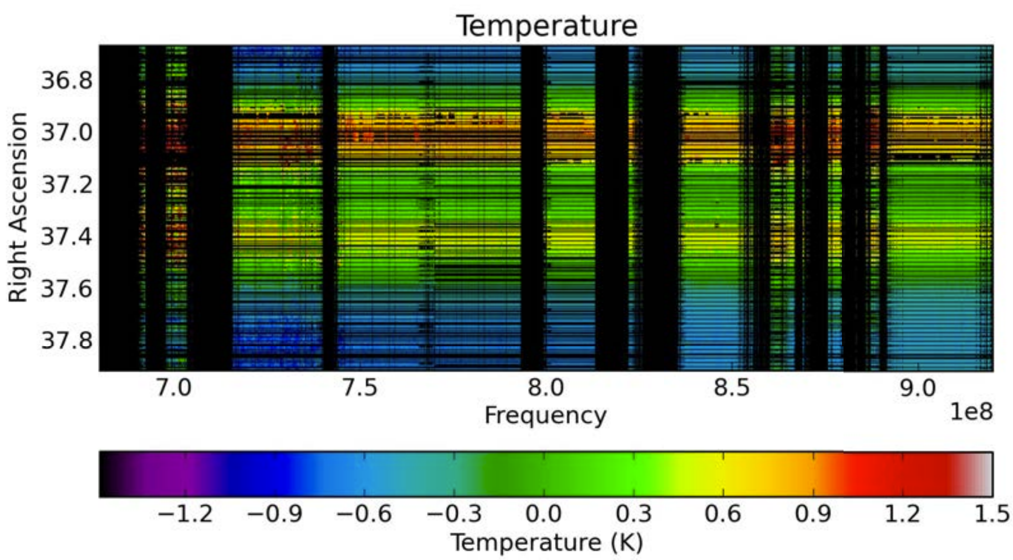

(f) dec 6

Figure A.3: Radio map of DEEP2 field4. Unreduced resolution, as data was taken. Averaged all observations together.

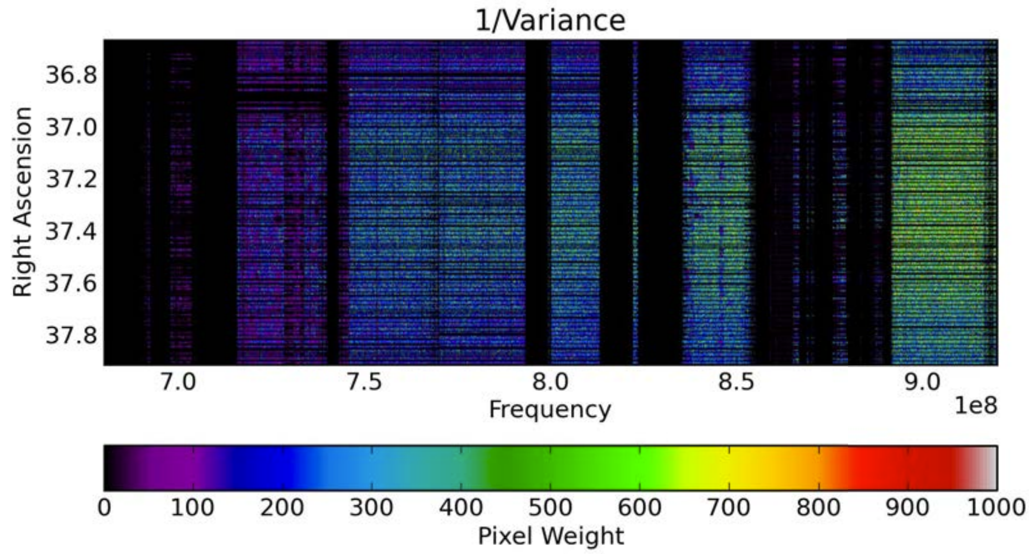

(a) dec 1

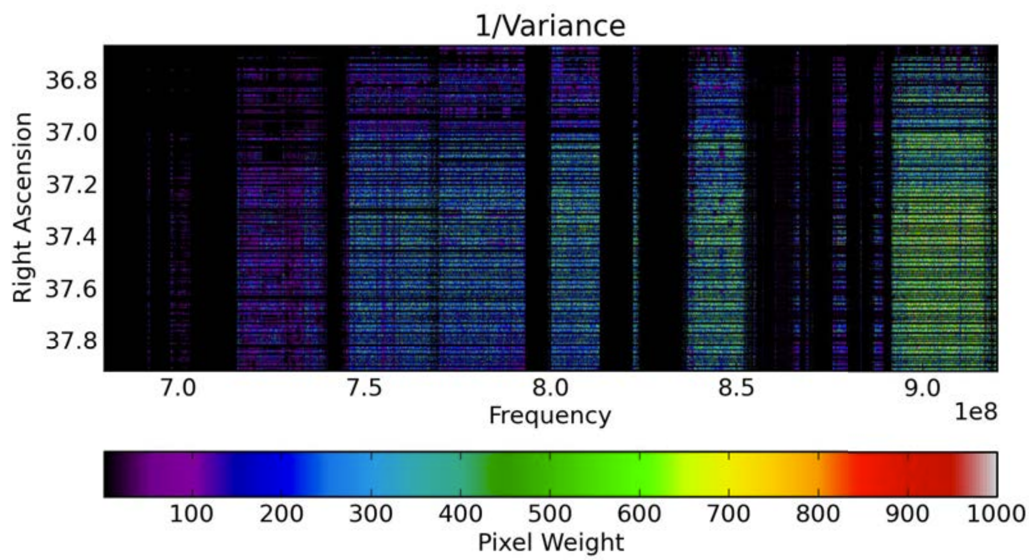

(b) dec 2

Figure A.4

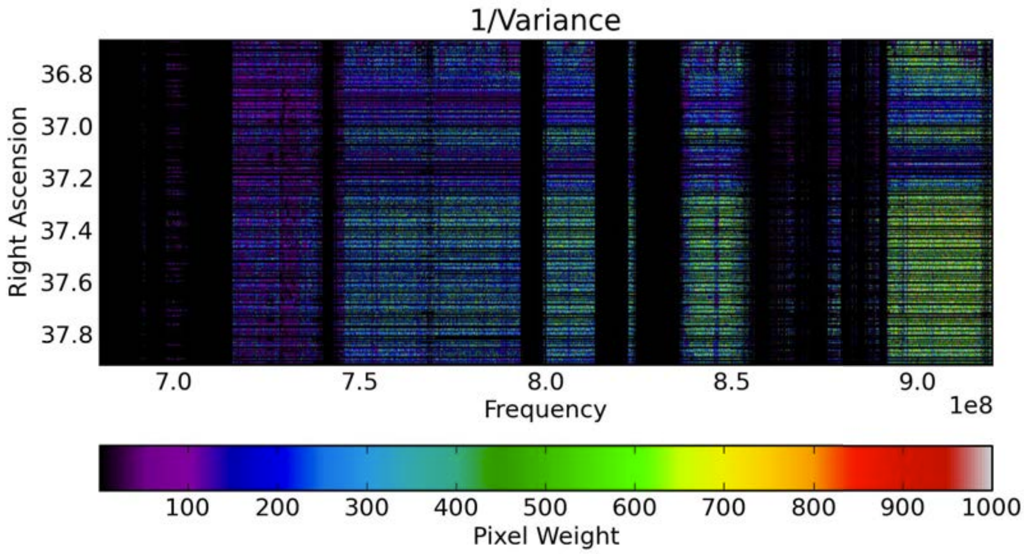

(c) dec 3

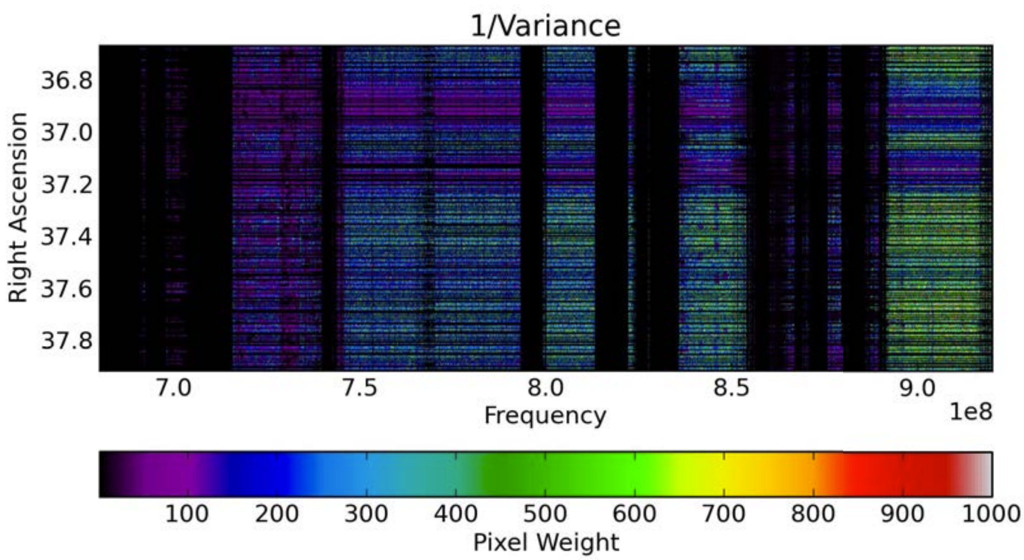

(d) dec 4

Figure A.4

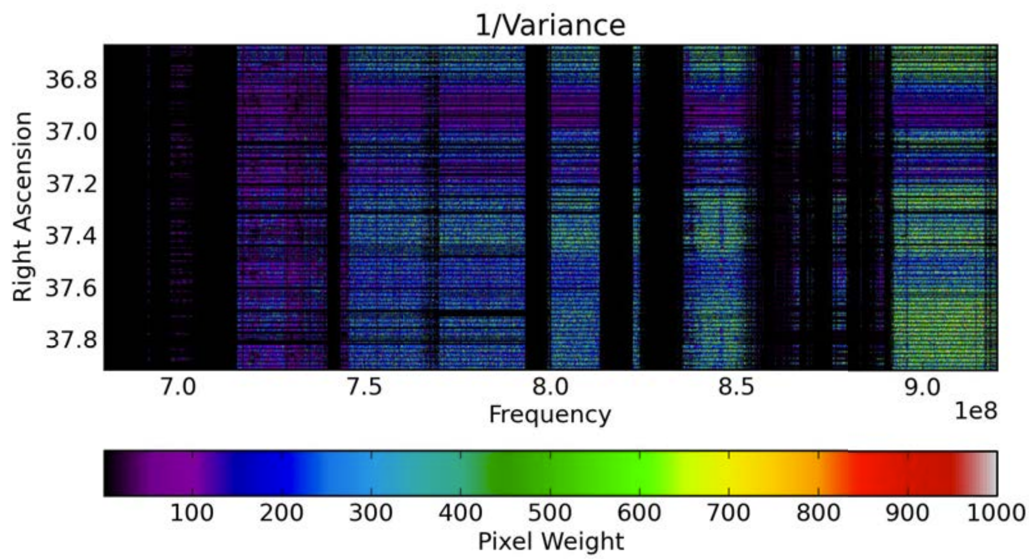

(e) dec 5

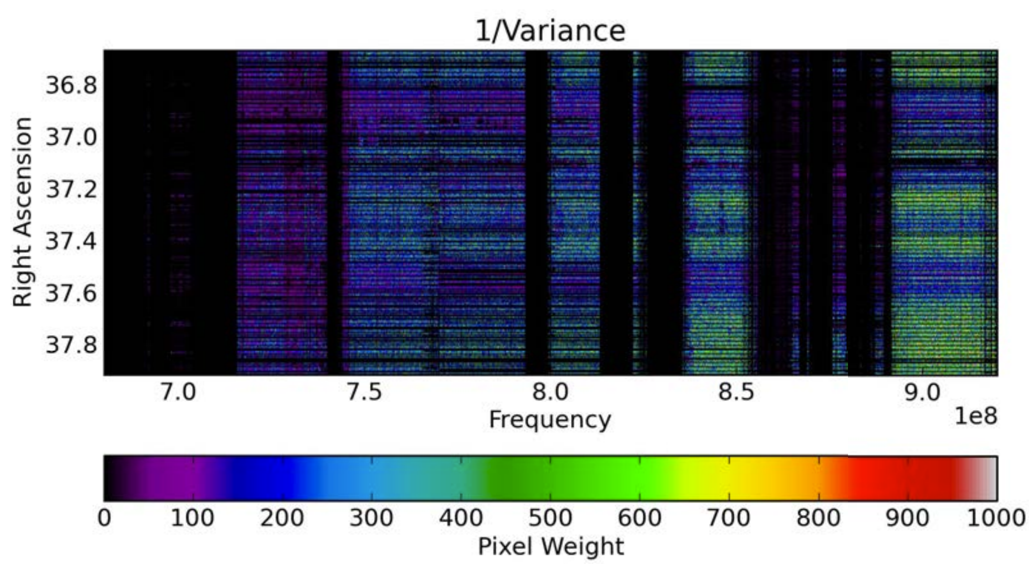

(f) dec 6

Figure A.4: Variance map of DEEP2 field4 radio data. Unreduced resolution, as data was taken. Averaged all observations together.

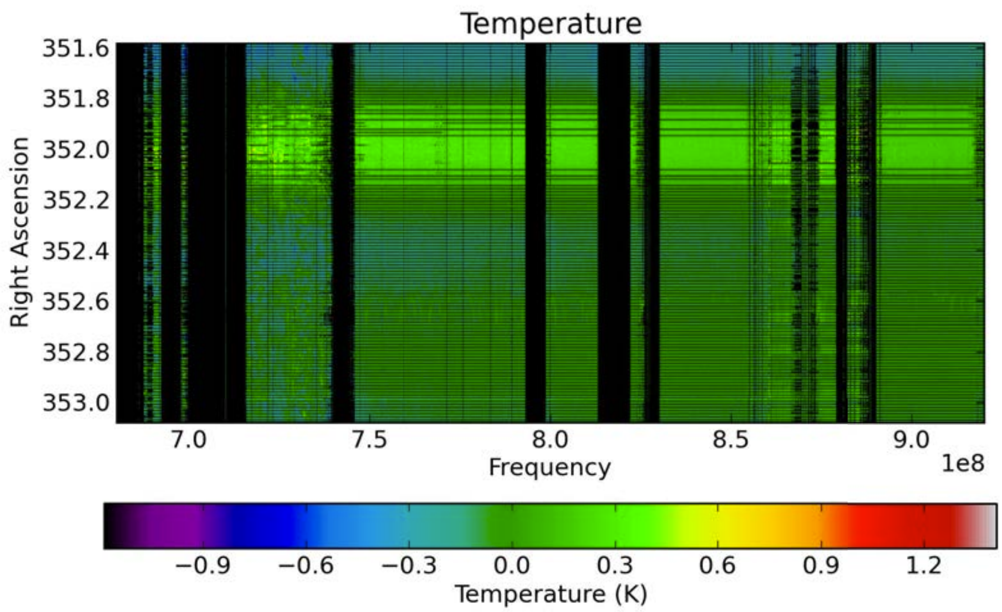

(a) dec 1

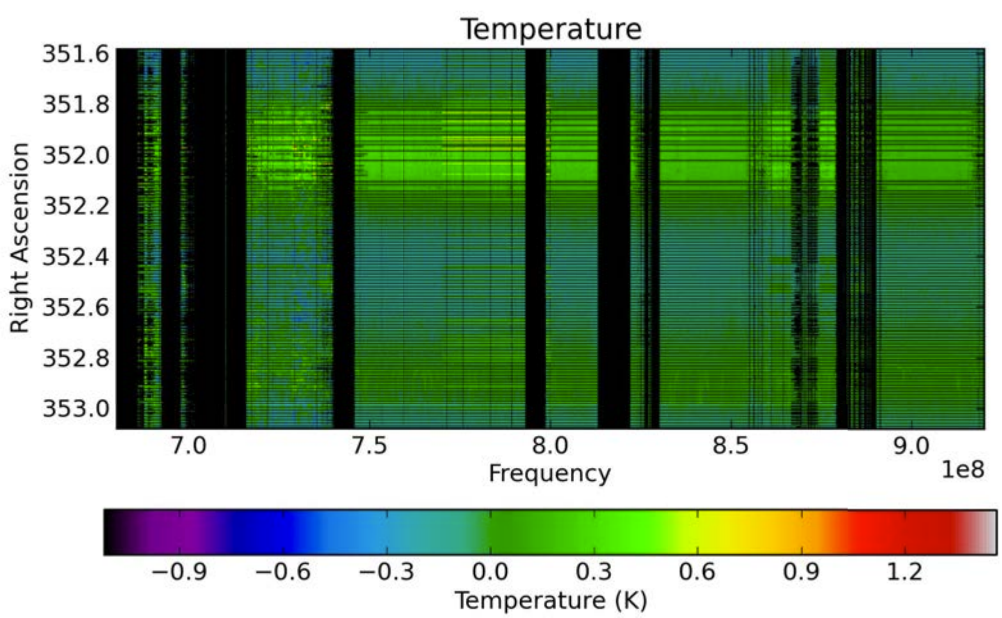

(b) dec 2

Figure A.5

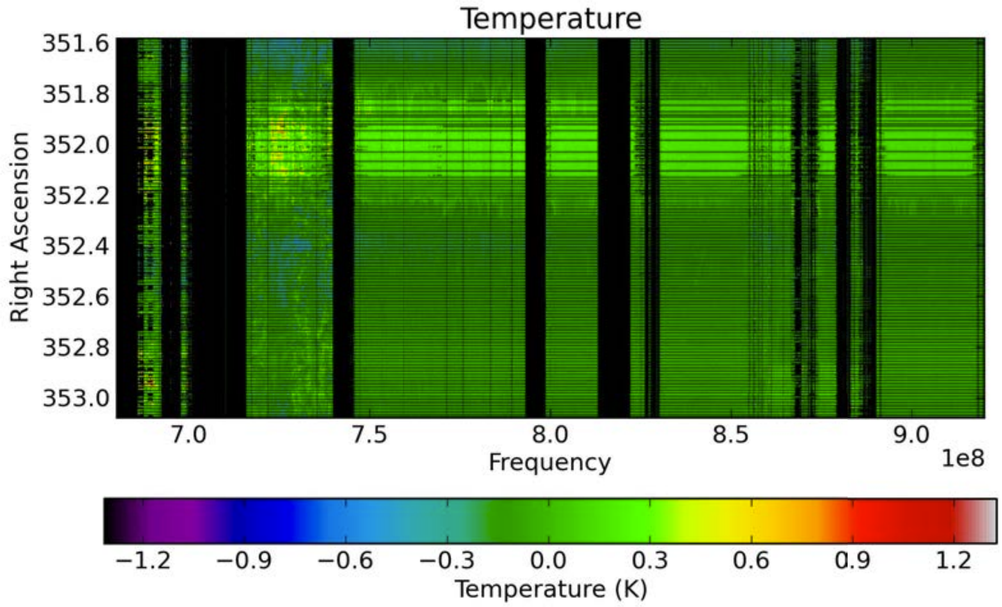

(c) dec 3

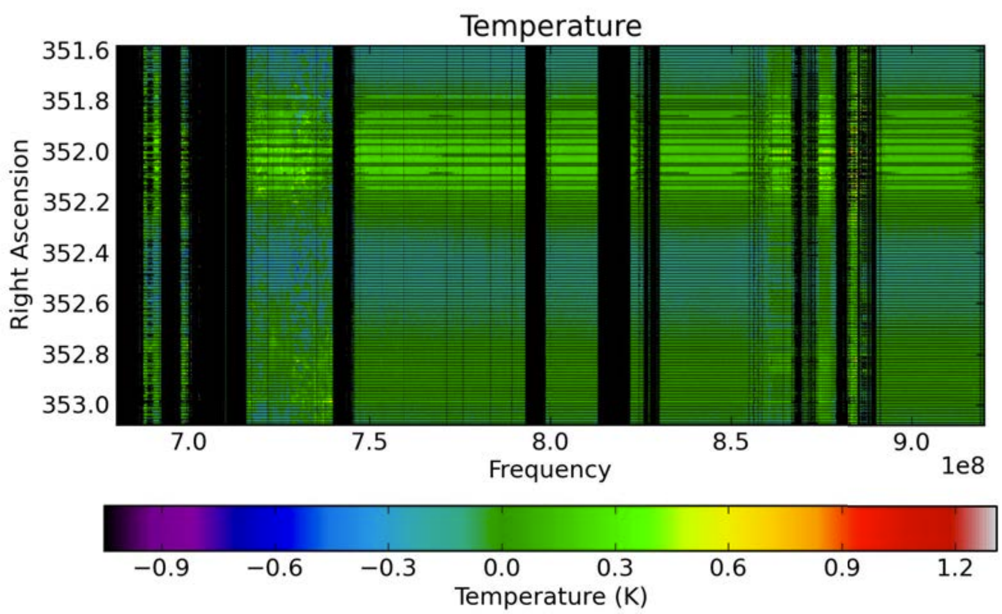

(d) dec 4

Figure A.5

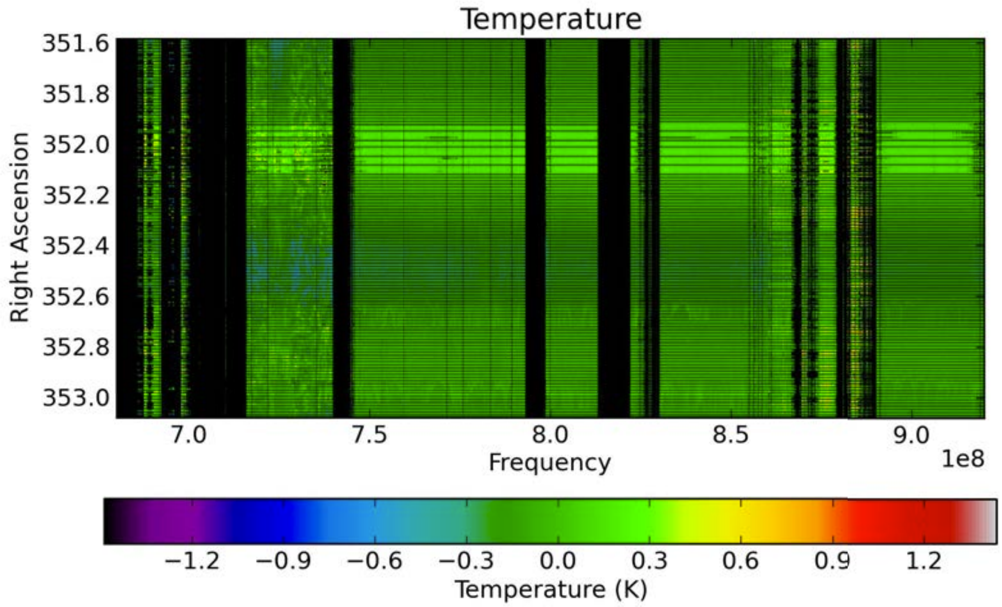

(e) dec 5

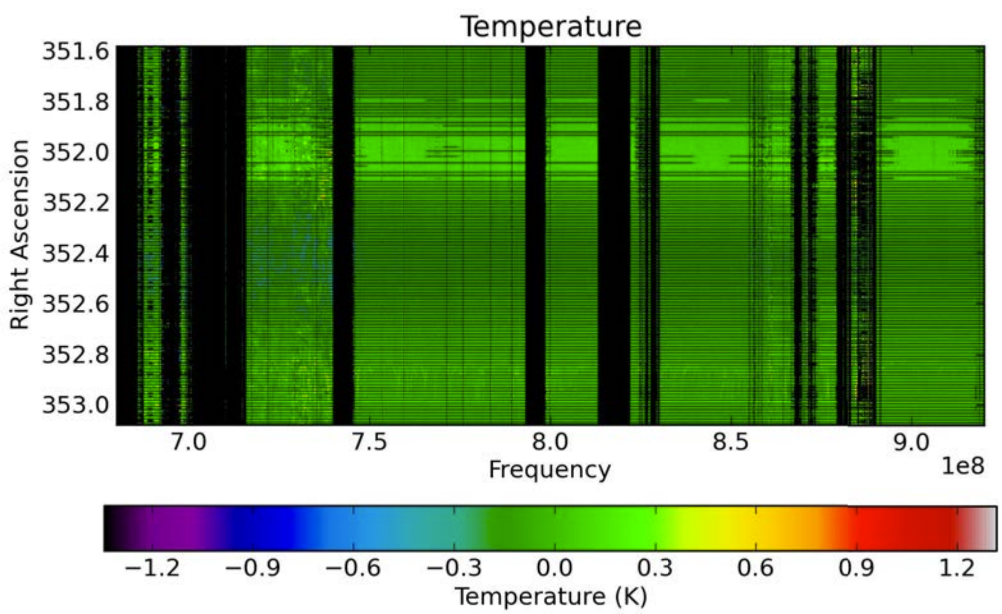

(f) dec 6

Figure A.5: Radio map of DEEP2 field3. Unreduced resolution, as data was taken. Averaged all observations together.

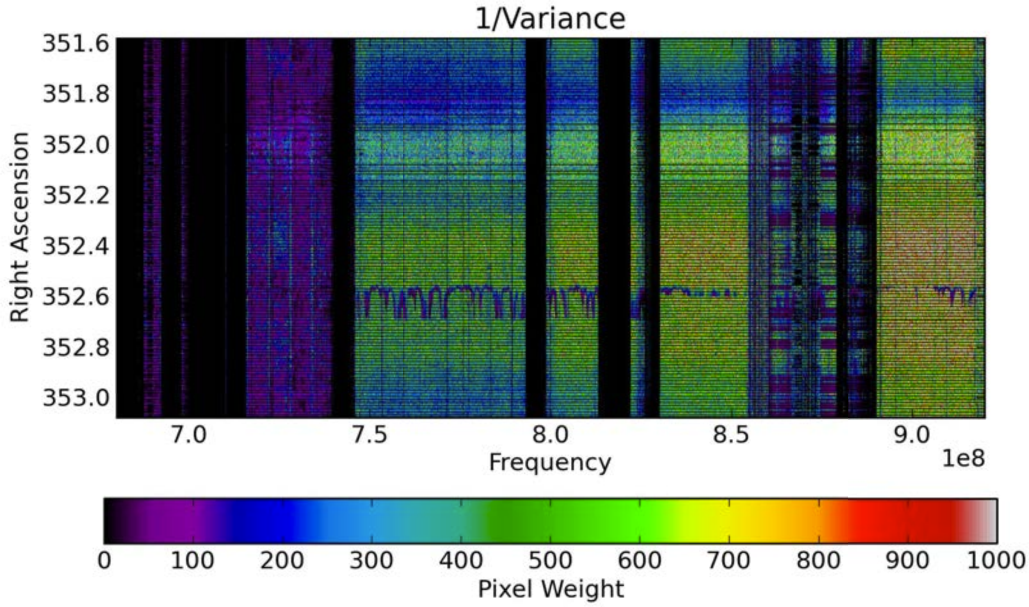

(a) dec 1

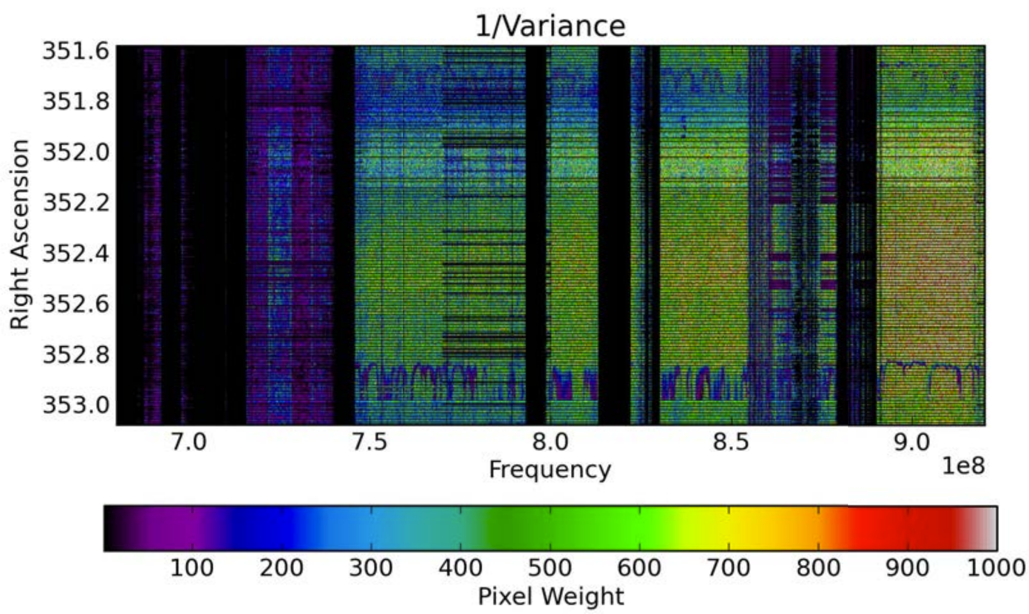

(b) dec 2

Figure A.6

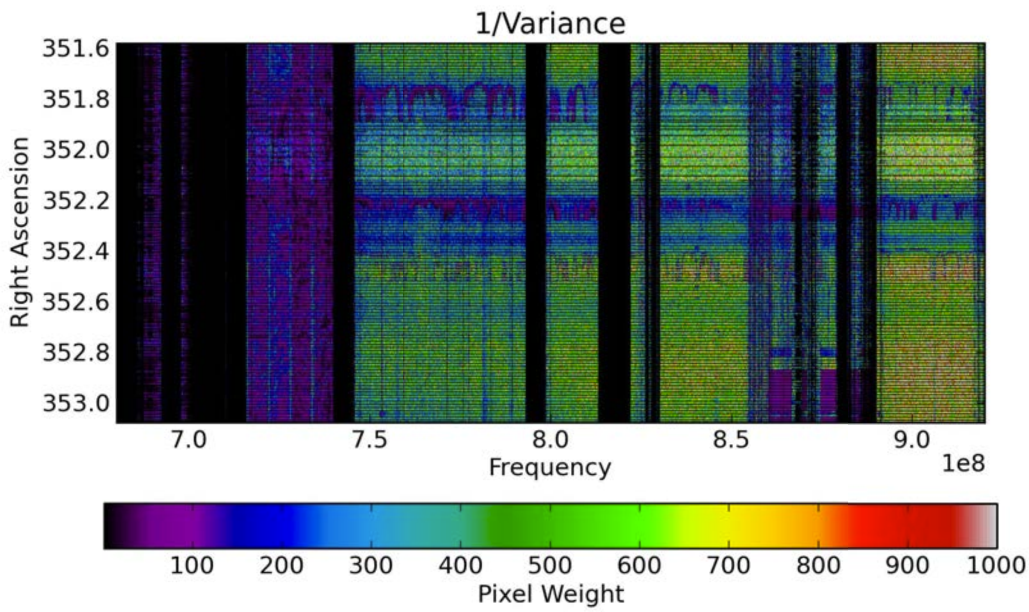

(c) dec 3

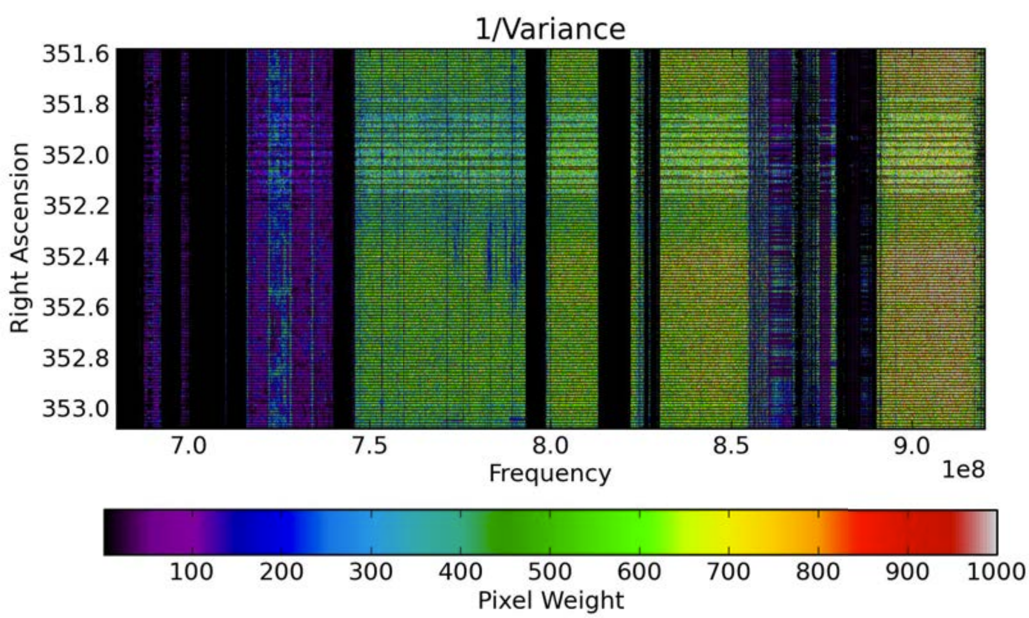

(d) dec 4

Figure A.6

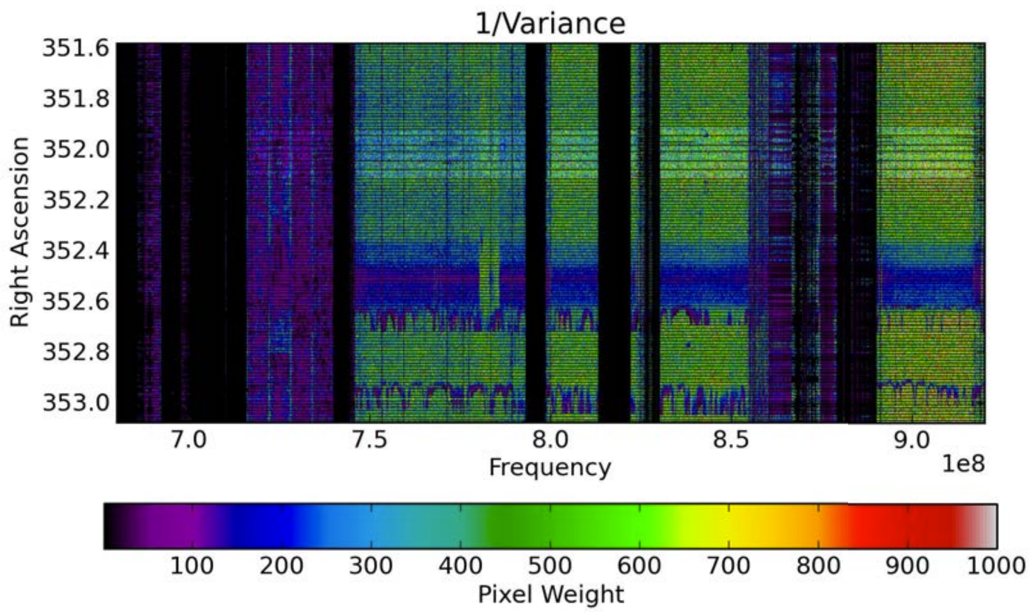

(e) dec 5

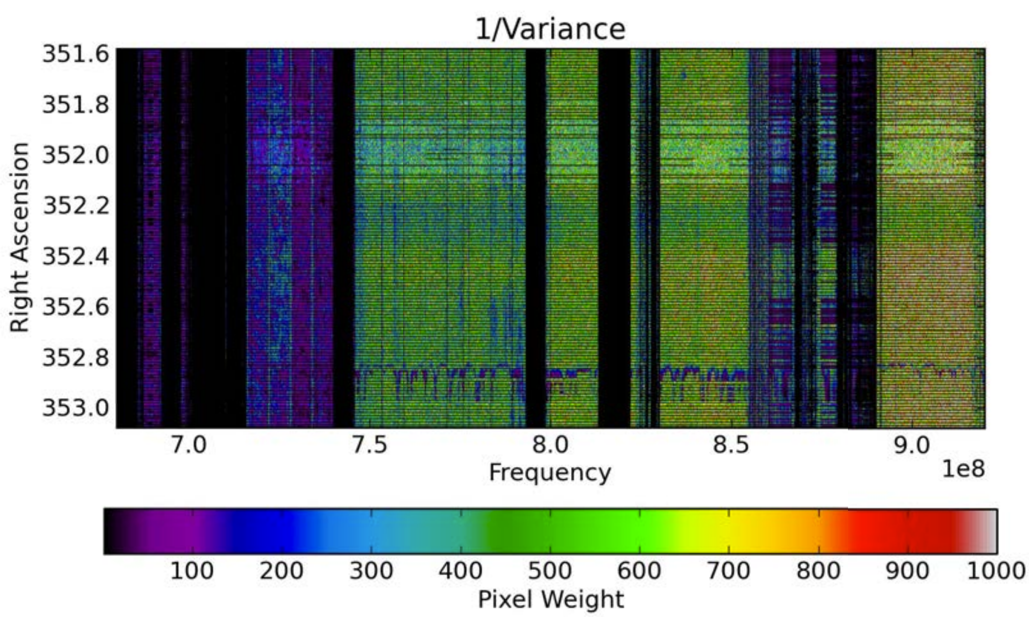

(f) dec 6

Figure A.6: Variance map of DEEP2 field3 radio data. Unreduced resolution, as data was taken. Averaged all observations together.

Bibliography

[1] F. B. Abdalla and S. Rawlings. Probing dark energy with baryonic oscillations and future radio surveys of neutral hydrogen. *Monthly Notices of the Royal Astronomical Society*, 360(1):27–40, June 2005.

[2] F. B. Abdalla, C. Blake, and S. Rawlings. Forecasts for dark energy measurements with future HI surveys. *Monthly Notices of the Royal Astronomical Society*, 401(2):743–758, Jan. 2010.

[3] L. Amendola, C. Quercellini, and E. Giallongo. Constraints on perfect fluid and scalar field dark energy models from future redshift surveys. *Monthly Notices of the Royal Astronomical Society*, 357(2):429–439, Feb. 2005.

[4] R. Ansari, J. M. Le Goff, C. Magneville, M. Moniez, N. Palanque-Delabrouille, J. Rich, V. Ruhlmann-Kleider, and C. Yèche. Reconstruction of HI power spectra with radio-interferometers to study dark energy. *arXiv.org*, 0807:3614, July 2008.

[5] R. Ansari, J. M. Le Goff, C. Magneville, M. Moniez, N. Palanque-Delabrouille, J. Rich, and von Ruhlmann-Kleider. Reconstruction of HI power spectra with radio-interferometers to study dark energy. *arXiv*, astro-ph, July 2008.

[6] J. S. Bagla, N. Khandai, and K. K. Datta. HI as a probe of the large-scale structure in the post-reionization universe. *Monthly Notices of the Royal Astronomical Society*, 407(1):567–580, Sept. 2010.

[7] R. Barkana and A. Loeb. In the beginning: the first sources of light and the reionization of the universe. *Physics Reports*, 349(2):125–238, July 2001.

[8] T. Bird and G. Cortes-Medellin. Multibeam feed array design for the Arecibo radio telescope. *Antennas and Propagation Society International Symposium, 2003. IEEE*, 1:116–119 vol.1, June 2003.

[9] C. Blake and K. Glazebrook. Probing Dark Energy Using Baryonic Oscillations in the Galaxy Power Spectrum as a Cosmological Ruler. *The Astrophysical Journal*, 594(2):665–673, Sept. 2003.

[10] J. R. Bond and G. Efstathiou. Cosmic background radiation anisotropies in universes dominated by nonbaryonic dark matter. *Astrophysical Journal*, 285: L45–L48, Oct. 1984.

[11] J. R. Bond and G. Efstathiou. The statistics of cosmic background radiation fluctuations. *Royal Astronomical Society*, 226:655–687, June 1987.

[12] B. F. Burke. Mills Cross telescopes. *The Astronomical Journal*, 61:167, May 1956.

[13] T.-C. Chang, U.-L. Pen, J. B. Peterson, and P. McDonald. Baryon Acoustic Oscillation Intensity Mapping of Dark Energy. *Physical Review Letters*, 100(9): 91303, Mar. 2008.

[14] T.-C. Chang, U.-L. Pen, K. Bandura, and J. B. Peterson. An intensity map of hydrogen 21-cm emission at redshift z 0.8. *Nature*, 466(7305):463–465, July 2010. (c) 2010: Nature.

[15] B. G. Clark. An efficient implementation of the algorithm 'CLEAN'. *Astronomy and Astrophysics*, 89:377, Sept. 1980. A&AA ID. AAA028.021.016.

[16] A. L. Coil, M. Davis, D. S. Madgwick, J. A. Newman, C. J. Conselice, M. Cooper, R. S. Ellis, S. M. Faber, D. P. Finkbeiner, P. Guhathakurta, N. Kaiser, D. C. Koo, A. C. Phillips, C. C. Steidel, B. J. Weiner, C. N. A. Willmer, and R. Yan. The DEEP2 Galaxy Redshift Survey: Clustering of Galaxies in Early Data. *The Astrophysical Journal*, 609:525, July 2004.

[17] S. Cole, W. J. Percival, J. A. Peacock, P. Norberg, C. M. Baugh, C. S. Frenk, I. Baldry, J. Bland-Hawthorn, T. Bridges, R. Cannon, M. Colless, C. Collins, W. Couch, N. J. G. Cross, G. Dalton, V. R. Eke, R. de Propris, S. P. Driver, G. Efstathiou, R. S. Ellis, K. Glazebrook, C. Jackson, A. Jenkins, O. Lahav, I. Lewis, S. Lumsden, S. Maddox, D. Madgwick, B. A. Peterson, W. Sutherland, and K. Taylor. The 2dF Galaxy Redshift Survey: power-spectrum analysis of the final data set and cosmological implications. *Monthly Notices of the Royal Astronomical Society*, 362(2):505–534, Sept. 2005.

[18] T. J. Cornwell. Multiscale CLEAN Deconvolution of Radio Synthesis Images. *IEEE Journal of Selected Topics in Signal Processing*, 2(5):793–801, Oct. 2008.

[19] W. D. Cotton. Special Problems in Imaging. *Synthesis Imaging in Radio Astronomy II*, 180:357, Jan. 1999.

[20] T. Di Matteo, R. Perna, T. Abel, and M. J. Rees. Radio Foregrounds for the 21 Centimeter Tomography of the Neutral Intergalactic Medium at High Redshifts. *The Astrophysical Journal*, 564(2):576–580, Jan. 2002.

[21] S. Dodelson. *Modern Cosmology*. Academic Press, 2 edition, Jan. 2003.

[22] D. J. Eisenstein and W. Hu. Baryonic Features in the Matter Transfer Function. *Astrophysical Journal v.496*, 496:605, Mar. 1998.

[23] D. J. Eisenstein, W. Hu, and M. Tegmark. Cosmic Complementarity: H 0 and Omega M from Combining Cosmic Microwave Background Experiments and Redshift Surveys. *Astrophysical Journal Letters v.504*, 504:L57, Sept. 1998.

[24] D. J. Eisenstein, I. Zehavi, D. W. Hogg, R. Scoccimarro, M. R. Blanton, R. C. Nichol, R. Scranton, H.-J. Seo, M. Tegmark, Z. Zheng, S. F. Anderson, J. Annis, N. Bahcall, J. Brinkmann, S. Burles, F. J. Castander, A. Connolly, I. Csabai, M. Doi, M. Fukugita, J. A. Frieman, K. Glazebrook, J. E. Gunn, J. S. Hendry, G. S. Hennessy, Ž. Ivezić, S. Kent, G. R. Knapp, H. Lin, Y.-S. Loh, R. H. Lupton, B. Margon, T. A. McKay, A. Meiksin, J. A. Munn, A. Pope, M. W. Richmond, D. J. Schlegel, D. P. Schneider, K. Shimasaku, C. Stoughton, M. A. Strauss, M. SubbaRao, A. S. Szalay, I. Szapudi, D. L. Tucker, B. Yanny, and D. G. York. Detection of the Baryon Acoustic Peak in the Large-Scale Correlation Function of SDSS Luminous Red Galaxies. *The Astrophysical Journal*, 633(2):560–574, Nov. 2005.

[25] G. E. Evans. Antenna measurement techniques. *Norwood*, 1990.

[26] X. Fan, C. L. Carilli, and B. Keating. Observational Constraints on Cosmic Reionization. *Annual Review of Astronomy and Astrophysics*, 44(1):415–462, Sept. 2006.

[27] J. A. Frieman, M. S. Turner, and D. Huterer. Dark Energy and the Accelerating Universe. *Annual Review of Astronomy and Astrophysics*, 46(1):385–432, Sept. 2008.

[28] S. R. Furlanetto, S. P. Oh, and F. H. Briggs. Cosmology at low frequencies: The 21 cm transition and the high-redshift Universe. *Physics Reports*, 433(4): 181–301, Oct. 2006. Elsevier B.V.

[29] E. Gaztanaga, A. Cabre, and L. Hui. Clustering of luminous red galaxies - IV. Baryon acoustic peak in the line-of-sight direction and a direct measurement of H(z). *Monthly Notices of the Royal Astronomical Society*, 399(3):1663–1680, Nov. 2009.

[30] K. Glazebrook and C. Blake. Measuring the Cosmic Evolution of Dark Energy with Baryonic Oscillations in the Galaxy Power Spectrum. *The Astrophysical Journal*, 631(1):1–20, Sept. 2005.

[31] A. H. Guth. Inflationary universe: A possible solution to the horizon and flatness problems. *Physical Review D (Particles and Fields)*, 23(2):347–356, Jan. 1981. A&AA ID. AAA029.162.101.

[32] M. Hicken, W. M. Wood-Vasey, S. Blondin, P. Challis, S. Jha, P. L. Kelly, A. Rest, and R. P. Kirshner. Improved Dark Energy Constraints from 100 New CfA Supernova Type Ia Light Curves. *The Astrophysical Journal*, 700(2):1097–1140, Aug. 2009.

[33] J. A. Högbom. Aperture Synthesis with a Non-Regular Distribution of Interferometer Baselines. *Astronomy and Astrophysics Supplement*, 15:417, June 1974.

[34] J. A. Holtzman. Microwave background anisotropies and large-scale structure in universes with cold dark matter, baryons, radiation, and massive and massless neutrinos. *Astrophysical Journal Supplement Series (ISSN 0067-0049)*, 71:1–24, Sept. 1989.

[35] W. Hu and Z. Haiman. Redshifting rings of power. *Physical Review D*, 68(6): 63004, Sept. 2003.

[36] W. Hu and N. Sugiyama. Small-Scale Cosmological Perturbations: an Analytic Approach. *Astrophysical Journal v.471*, 471:542, Nov. 1996.

[37] N. Jarosik, C. L. Bennett, J. Dunkley, B. Gold, M. R. Greason, M. Halpern, R. S. Hill, G. Hinshaw, A. Kogut, E. Komatsu, D. Larson, M. Limon, S. S. Meyer, M. R. Nolta, N. Odegard, L. Page, K. M. Smith, D. N. Spergel, G. S. Tucker, J. L. Weiland, E. Wollack, and E. L. Wright. Seven-year Wilkinson Microwave Anisotropy Probe (WMAP) Observations: Sky Maps, Systematic Errors, and Basic Results. *The Astrophysical Journal Supplement*, 192(2):14, Feb. 2011.

[38] E. Komatsu, J. Dunkley, M. R. Nolta, C. L. Bennett, B. Gold, G. Hinshaw, N. Jarosik, D. Larson, M. Limon, L. Page, D. N. Spergel, M. Halpern, R. S. Hill, A. Kogut, S. S. Meyer, G. S. Tucker, J. L. Weiland, E. Wollack, and E. L. Wright. Five-Year Wilkinson Microwave Anisotropy Probe Observations: Cosmological Interpretation. *The Astrophysical Journal Supplement*, 180(2):330–376, Feb. 2009.

[39] E. Komatsu, K. M. Smith, J. Dunkley, C. L. Bennett, B. Gold, G. Hinshaw, N. Jarosik, D. Larson, M. R. Nolta, L. Page, D. N. Spergel, M. Halpern, R. S. Hill, A. Kogut, M. Limon, S. S. Meyer, N. Odegard, G. S. Tucker, J. L. Weiland, E. Wollack, and E. L. Wright. Seven-year Wilkinson Microwave Anisotropy Probe (WMAP) Observations: Cosmological Interpretation. *The Astrophysical Journal Supplement*, 192(2):18, Feb. 2011.

[40] J. Landon, M. Elmer, J. Waldron, D. Jones, A. Stemmons, B. D. Jeffs, K. F. Warnick, J. R. Fisher, and R. D. Norrod. Phased Array Feed Calibration, Beamforming, and Imaging. *The Astronomical Journal*, 139(3):1154–1167, Mar. 2010.

[41] S. J. Lilly, O. Le Fèvre, A. Renzini, G. Zamorani, M. Scodeggio, T. Contini, C. M. Carollo, G. Hasinger, J.-P. Kneib, A. Iovino, V. Le Brun, C. Maier, V. Mainieri, M. Mignoli, J. Silverman, L. A. M. Tasca, M. Bolzonella, A. Bongiorno, D. Bottini, P. Capak, K. Caputi, A. Cimatti, O. Cucciati, E. Daddi, R. Feldmann, P. Franzetti, B. Garilli, L. Guzzo, O. Ilbert, P. Kampczyk, K. Kovac, F. Lamareille, A. Leauthaud, J.-F. L. Borgne, H. J. McCracken, C. Marinoni, R. Pello, E. Ricciardelli, C. Scarlata, D. Vergani, D. B. Sanders, E. Schinnerer, N. Scoville, Y. Taniguchi, S. Arnouts, H. Aussel, S. Bardelli, M. Brusa, A. Cappi, P. Ciliegi, A. Finoguenov, S. Foucaud, R. Franceschini, C. Halliday, C. Impey, C. Knobel, A. Koekemoer, J. Kurk, D. Maccagni, S. Maddox, B. Marano, G. Marconi, B. Meneux, B. Mobasher, C. Moreau, J. A. Peacock, C. Porciani, L. Pozzetti, R. Scaramella, D. Schiminovich, P. Shopbell, I. Smail, D. Thompson, L. Tresse, G. Vettolani, A. Zanichelli, and E. Zucca. zCOSMOS: A Large VLT/VIMOS Redshift Survey Covering 0 ¡ z ¡ 3 in the COSMOS Field. *The Astrophysical Journal Supplement Series*, 172:70, Sept. 2007. (c) 2007: The American Astronomical Society.

[42] E. V. Linder. Baryon oscillations as a cosmological probe. *Physical Review D*, 68(8):83504, Oct. 2003.

[43] A. Liu and M. Tegmark. A Method for 21cm Power Spectrum Estimation in the Presence of Foregrounds. *Physical Review D*, (1):103006, Mar. 2011. 24 pages, 11 figures; replaced with accepted PRD version (minor editorial changes to text; methods, results, and conclusions unchanged).

[44] A. Liu and M. Tegmark. How well can we measure and understand foregrounds with 21 cm experiments? *arXiv.org*, 1106:7, May 2011. 15 pages, 9 figures, 2 tables; Corrected minor typos and added to acknowledgements.

[45] A. Liu, M. Tegmark, J. Bowman, J. Hewitt, and M. Zaldarriaga. An improved method for 21-cm foreground removal. *Monthly Notices of the Royal Astronomical Society*, 398(1):401–406, Sept. 2009.

[46] A. Liu, M. Tegmark, and M. Zaldarriaga. Will point sources spoil 21-cm tomography? *Monthly Notices of the Royal Astronomical Society*, 394(3):1575–1587, Apr. 2009.

[47] K. W. Masui, P. McDonald, and U.-L. Pen. Near-term measurements with 21 cm intensity mapping: Neutral hydrogen fraction and BAO at z¡2. *Physical Review D*, 81(1):103527, May 2010. (c) 2010: The American Physical Society.

[48] C. J. Miller, R. C. Nichol, and D. J. Batuski. Possible Detection of Baryonic Fluctuations in the Large-Scale Structure Power Spectrum. *The Astrophysical Journal*, 555(1):68–73, July 2001.

[49] B. Y. Mills. The Molonglo Observatory synthesis telescope. *Proceedings of the Astronomical Society of Australia*, 4:156–159, 1981.

[50] M. F. Morales and J. S. B. Wyithe. Reionization and Cosmology with 21-cm Fluctuations. *Annual Review of Astronomy and Astrophysics*, 48:127, Sept. 2010.

[51] P. J. E. Peebles and J. T. Yu. Primeval Adiabatic Perturbation in an Expanding Universe. *Astrophysical Journal*, 162:815, Dec. 1970. A&AA ID. AAA004.162.057.

[52] W. J. Percival, C. M. Baugh, J. Bland-Hawthorn, T. Bridges, R. Cannon, S. Cole, M. Colless, C. Collins, W. Couch, G. Dalton, R. de Propris, S. P. Driver, G. Efstathiou, R. S. Ellis, C. S. Frenk, K. Glazebrook, C. Jackson, O. Lahav, I. Lewis, S. Lumsden, S. Maddox, S. Moody, P. Norberg, J. A. Peacock, B. A. Peterson, W. Sutherland, and K. Taylor. The 2dF Galaxy Redshift Survey: the power spectrum and the matter content of the Universe. *Monthly Notices of the Royal Astronomical Society*, 327(4):1297–1306, Nov. 2001.

[53] W. J. Percival, S. Cole, D. J. Eisenstein, R. C. Nichol, J. A. Peacock, A. C. Pope, and A. S. Szalay. Measuring the Baryon Acoustic Oscillation scale using the Sloan Digital Sky Survey and 2dF Galaxy Redshift Survey. *Monthly Notices of the Royal Astronomical Society*, 381(3):1053–1066, Nov. 2007. (c) 2007 The Authors. Journal compilation © 2007 RAS.

[54] W. J. Percival, B. A. Reid, D. J. Eisenstein, N. A. Bahcall, T. Budavari, J. A. Frieman, M. Fukugita, J. E. Gunn, Ž. Ivezić, G. R. Knapp, R. G. Kron, J. Loveday, R. H. Lupton, T. A. McKay, A. Meiksin, R. C. Nichol, A. C. Pope, D. J. Schlegel, D. P. Schneider, D. N. Spergel, C. Stoughton, M. A. Strauss, A. S. Szalay, M. Tegmark, M. S. Vogeley, D. H. Weinberg, D. G. York, and I. Zehavi. Baryon acoustic oscillations in the Sloan Digital Sky Survey Data Release 7 galaxy sample. *Monthly Notices of the Royal Astronomical Society*, 401(4):2148–2168, Feb. 2010.

[55] J. B. Peterson, K. Bandura, and U.-L. Pen. The Hubble Sphere Hydrogen Survey. *arXiv*, astro-ph, June 2006. Presented at Moriond Cosmology 2006.

[56] J. B. Peterson, R. Aleksan, R. Ansari, K. Bandura, D. Bond, J. Bunton, K. Carlson, T.-C. Chang, F. DeJongh, M. Dobbs, S. Dodelson, H. Darhmaoui, N. Gnedin, M. Halpern, C. Hogan, J.-M. L. Goff, T. T. Liu, A. Legrouri, A. Loeb, K. Loudiyi, C. Magneville, J. Marriner, D. P. McGinnis, B. McWilliams, M. Moniez, N. Palanque-Delabruille, R. J. Pasquinelli, U.-L. Pen, J. Rich, V. Scarpine, H.-J. Seo, K. Sigurdson, U. Seljak, A. Stebbins, J. H. Steffen, C. Stoughton, P. T. Timbie, A. Vallinotto, S. Wyithe, and C. Yeche. 21 cm Intensity Mapping. *eprint arXiv*, 0902:3091, Feb. 2009. White Paper for the Astro2010 Astronomy Decadal Review.

[57] A. G. Riess, L. Macri, S. Casertano, M. Sosey, H. Lampeitl, H. C. Ferguson, A. V. Filippenko, S. W. Jha, W. Li, R. Chornock, and D. Sarkar. A Redetermination of the Hubble Constant with the Hubble Space Telescope from a Differential Distance Ladder. *The Astrophysical Journal*, 699(1):539–563, July 2009.

[58] J. Roy, Y. Gupta, U.-L. Pen, J. B. Peterson, S. Kudale, and J. Kodilkar. A real-time software backend for the GMRT. *Experimental Astronomy*, 28:25, Aug. 2010. (c) 2010: Springer Science+Business Media B.V.

[59] M. Ryle. The mullard radio astronomy observatory. *Electrical Engineers, Journal of the Institution of*, 6(61):14–19, Jan. 1960.

[60] M. Ryle and D. D. Vonberg. Solar Radiation on 175 Mc./s. *Nature*, 158(4): 339–340, Sept. 1946.

[61] F. R. Schwab. Relaxing the isoplanatism assumption in self-calibration; applications to low-frequency radio interferometry. *The Astronomical Journal*, 89: 1076–1081, July 1984.

[62] H.-J. Seo and D. J. Eisenstein. Probing Dark Energy with Baryonic Acoustic Oscillations from Future Large Galaxy Redshift Surveys. *The Astrophysical Journal*, 598(2):720–740, Dec. 2003.

[63] H.-J. Seo, S. Dodelson, J. Marriner, D. Mcginnis, A. Stebbins, C. Stoughton, and A. Vallinotto. A Ground-based 21 cm Baryon Acoustic Oscillation Survey. *The Astrophysical Journal*, 721(1):164–173, Sept. 2010.

[64] L. Staveley-Smith, W. E. Wilson, T. Bird, M. J. Disney, R. D. Ekers, K. C. Freeman, R. F. Haynes, M. W. Sinclair, R. A. Vaile, R. L. Webster, and A. E. Wright. The Parkes 21 CM multibeam receiver. *Publications of the Astronomical Society of Australia*, 13:243–248, Nov. 1996.

[65] R. A. Sunyaev and Y. B. Zeldovich. Small-Scale Fluctuations of Relic Radiation. *Astrophysics and Space Science*, 7:3–19, Apr. 1970.

[66] S. H. Suyu, P. J. Marshall, M. W. Auger, S. Hilbert, R. D. Blandford, L. V. E. Koopmans, C. D. Fassnacht, and T. Treu. Dissecting the Gravitational lens B1608+656. II. Precision Measurements of the Hubble Constant, Spatial Curvature, and the Dark Energy Equation of State. *The Astrophysical Journal*, 711 (1):201–221, Mar. 2010.

[67] G. SWARUP, N. V. G. SARMA, M. N. JOSHI, V. K. KAPAHI, D. S. BAGRI, S. H. DAMLE, S. ANANTHAKRISHNAN, V. BALASUBRAMANIAN, S. S. BHAVE, and R. P. SINHA. Large Steerable Radio Telescope at Ootacamund, India. *Nature*, 230(17):185–188, Apr. 1971.

[68] G. Swenson and Y. Lo. The University of Illinois radio telescope. *IRE Transactions on Antennas and Propagation*, 9(1):9–16, 1961.

[69] M. Tegmark, A. J. S. Hamilton, and Y. Xu. The power spectrum of galaxies in the 2dF 100k redshift survey. *Monthly Notice of the Royal Astronomical Society*, 335(4):887–908, Oct. 2002.

[70] X. Wang, M. Tegmark, M. G. Santos, and L. Knox. 21 cm Tomography with Foregrounds. *The Astrophysical Journal*, 650(2):529–537, Oct. 2006. (c) 2006: The American Astronomical Society.

[71] J. S. B. Wyithe. A method to measure the mass of damped Ly absorber host galaxies using fluctuations in 21-cm emission. *Monthly Notices of the Royal Astronomical Society*, 388(4):1889–1898, Aug. 2008.

[72] J. S. B. Wyithe and A. Loeb. The 21-cm power spectrum after reionization. *Monthly Notices of the Royal Astronomical Society*, 397(4):1926–1934, Aug. 2009.